ABSTRACT

Title of Document: MECHANICAL MANIPULATION AND CHARACTERIZATION OF BIOLOGICAL CELLS.

Anand Pillarisetti
Doctor of Philosophy, 2008

Directed By: Dr. Jaydev P. Desai
Department of Mechanical Engineering
Robotics, Automation, Manipulation, and Sensing (RAMS) Laboratory.

Mechanical manipulation and characterization of an individual biological cell is currently one of the most exciting research areas in the field of medical robotics. Single cell manipulation is an important process in intracytoplasmic sperm injection (ICSI), pro-nuclei DNA injection, gene therapy, and other biomedical areas. However, conventional cell manipulation requires long training and the success rate depends on the experience of the operator. The goal of this research is to address the drawbacks of conventional cell manipulation by using force and vision feedback for cell manipulation tasks. We hypothesize that force feedback plays an important role in cell manipulation and possibly helps in cell characterization. This dissertation will summarize our research on: 1) the development of force and vision feedback interface for cell manipulation, 2) human subject studies to evaluate the addition of force feedback for cell injection tasks, 3) the development of haptics-enabled atomic force

microscope system for cell indentation tasks, 4) appropriate analytical model for characterizing the mechanical property of mouse embryonic stem cells (mESC) and 5) several indentation studies on mESC to determine the mechanical property of undifferentiated and early differentiating (6 days under differentiation conditions) mESC. Our experimental results on zebrafish egg cells show that a system with force feedback capability when combined with vision feedback can lead to potentially higher success rates in cell injection tasks. Using this information, we performed experiments on mESC using the AFM to understand their characteristics in the undifferentiated pluripotent state as well as early differentiating state. These experiments were done on both live as well as fixed cells to understand the correlation between the two during cell indentation studies. Our results show that the mechanical property of undifferentiated mESC differs from early differentiating (6th day) mESC in both live and fixed cells. Thus, we hypothesize that mechanical characterization studies will potentially pave the way for developing a high throughput system with force feedback capability, to understand and predict the differentiation path a particular pluripotent cell will follow. This finding could also be used to develop improved methods of targeted cellular differentiation of stem cells for therapeutic and regenerative medicine.

MECHANICAL MANIPULATION AND CHARACTERIZATION OF BIOLOGICAL CELLS.

By

Anand Pillarisetti.

Dissertation submitted to the Faculty of the Graduate School of the
University of Maryland, College Park, in partial fulfillment
of the requirements for the degree of
Doctor of Philosophy
2008

Advisory Committee:
Dr. Jaydev P. Desai, Chair
Dr. Satyandra K. Gupta
Dr. Carol Keefer
Dr. Ali Mosleh
Dr. Santiago Solares

Dedication

This dissertation is dedicated to my parents

Acknowledgements

I am grateful to numerous people who have shown their help and support during my graduate studies. First, I would like to express my gratitude to my Ph.D. advisor, Dr. Jaydev P. Desai for his enthusiastic guidance and invaluable suggestions during the last five years. I would also like to thank the members of my Ph.D. advisory committee who have guided me in the right direction to complete my thesis. This dissertation would not have been completed without the kind advice and support from Dr. Carol Keefer. She spent tremendous amount of time and effort in preparing the mouse embryonic stem cells (mESC) which were used in my experiments. Drs. Satyandra Gupta and Mosleh Ali have also provided a great amount of support and guidance in completing my dissertation. Finally I would also like to thank Dr. Santiago Solares for serving in my committee.

In addition to the faculty in University of Maryland, I would also like to thank the faculty at Drexel University. I kindly appreciate the advice and support of Dr. Ari D. Brooks in conducting experiments on zebrafish egg cells. I would also like to acknowledge Dr. Bradley Layton for providing the necessary equipment to carry out experiments on zebrafish egg cells. I would especially like to thank Dr. Mun Choi (now Dean of College of Engineering, University of Connecticut) for his motivational speeches and guidance while at Drexel University. Dr. Gary Friedman was also supportive and got me introduced to the field of microelectromechanical systems (MEMS). Some of the courses offered in Drexel helped me a lot in my research. I

would never forget Dr. Paul Oh's brilliant course in controls. Dr. Hongseok Noh also provided an excellent course in microelectromechanical systems (MEMS).

I would also like to thank all my friends and colleagues who were supportive during my graduate studies. The members of the RAMS Lab were friendly and nice during my stay at University of Maryland. I would especially like to thank Hamid Ladjal for helping me in conducting experiments on mouse embryonic stem cells. I would also like to express my sincere appreciation to my previous lab members at Drexel for their friendly nature and suggestions: Teeranoot Chanthasopeephan, James Hing, Tie Hu, Chris Kennedy, Ed Steager, Greg Tholey and Justin Chandler. I would especially like to thank my colleagues/friends: Waqas Anjum and Max Pekarev for providing the necessary help to conduct experiments on fish egg cells. In addition to the lab members, I made a numerous number of close friends during my grad studies. It would not be fair to mention some of them and leave others, so am not mentioning the list.

Finally I would like to thank my family for their soothing support during the past five years. I would especially like to thank my brother (Aravind) for his suggestions and guidance during my graduate studies.

Table of Contents

List of Tables

List of Figures

Chapter 1: Introduction

Cell manipulation is a prevalent process in the field of molecular biology. The process plays an important role in intracytoplasmic sperm injection (ICSI), pronuclei deoxyribonucleic acid (DNA) injection, therapeutic and regenerative medicine, and other biomedical areas. ICSI is one of the assisted reproductive techniques to treat male-factor infertility and involves direct injection of a single immobilized spermatozoon into the cytoplasm of a mature oocyte. Transgenic species are produced by injecting deoxyribonucleic acid (DNA) into the pro-nuclei of an embryo. Stem cells have the unique capability to give rise to different cell types under certain physiological or experimental conditions (differentiation) and hence have the ability to replace damaged cells in the body leading to therapeutic and regenerative medicine. A conventional cell manipulation (e.g. injection) system consists of an injecting pipette mounted on a manual manipulator (figure 1.1). The function of the injecting pipette is to deposit sperm/DNA into a single cell held by another pipette (holding pipette). The holding pipette is mounted on a second manual manipulator. However, conventional manipulation requires long training and the success rate depends on the experience of the operator. Even for an experienced operator, the injection process results in low success rate and poor reproducibility. Further, the current techniques to distinguish between undifferentiated and differentiating stem cells are: (a) time consuming, (b) cannot identify precursor cells (stem cells committed to differentiate into a specialized cell type) and (c) involve genetic manipulation affecting cell characteristics.

1.1 Motivation

The efforts to micromanipulate cells under the microscope date back to the last half of the nineteenth century. The principles of microinjection were developed by Marshall A. Barber, where he developed the "pipette method" to isolate bacterial cells. A detail history of the microinjection process can be found in [1]. A typical cell injection system is shown in figure 1.1. Researchers in the field of biology have conducted experiments using conventional microinjection techniques to understand (a) that the nucleus plays an important role in embryonic differentiation [2], (b) that pronuclei formation from nuclei of a species depends on the activation of egg cytoplasm [3], and (c) that surgically injecting the egg cytoplasm with a spermatozoa of the same species or different species aids in pronuclei development [4, 5].

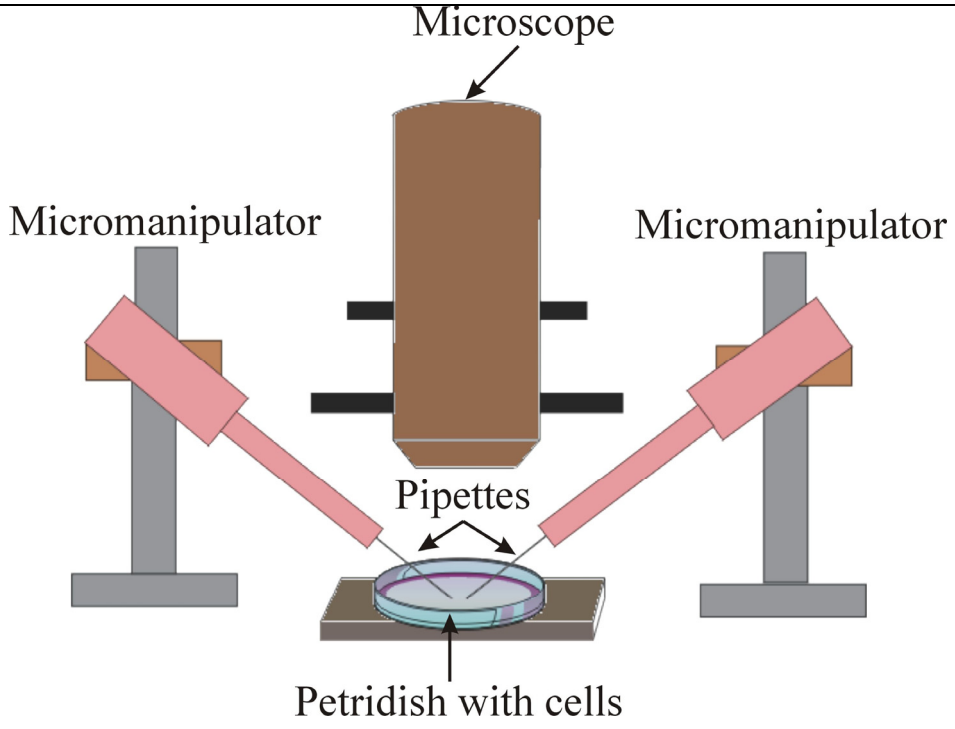

Figure 1.1. Conventional cell injection system

In vitro fertilization (IVF) is an assisted reproductive technique to treat male factor infertility and involves combining an egg cell with sperm cells in a laboratory dish. In this technique, the zona pellucida of the oocyte serves as a major barrier to sperm oocyte interaction. Therefore in severe oligospermia, the sperm may not come in contact with the oocyte, resulting in low fertilization rates [6]. Alternatives to IVF are partial zona dissection (PZD), sub-zonal insemination (SUZI) and intracytoplasmic sperm injection (ICSI). In PZD, a small hole is made in the zona (outer shell of the egg), to assist the sperm in reaching the egg membrane where as in SUZI, the sperm is introduced into the perivitelline space of the oocyte. PZD results in low fertilization rates (less than 27%) in male factor infertility patients [7, 8], where as SUZI achieves fertilization rates of around 30% and less than 8% poor pregnancy rates [9, 10]. However the results obtained by ICSI are promising. Palermo et al [11] reported the first human pregnancies achieved by ICSI, with a fertilization rate of 66%. ICSI ensures high fertilization and pregnancy rates compared with IVF, PZD or SUZI of oocytes [12-14]. However, conventional ICSI involves (a) the risk of mechanical damage to the oocyte and (b) the possibility of injecting foreign substances or contaminants into the oocyte, thus affecting the fertilization rate and viability of an oocyte.

Transgenic techniques have been in use for 20 years for the creation of genetically altered mice. These procedures are straightforward but technically challenging and the transfection rate and survival rate are typically around 20% [15]. Typical transgenic organisms are created by introducing modified genetic material

mechanically, one cell at a time. This method is preferred because it introduces the gene of interest along with the desired regulatory sequences without introducing other potentially confounding elements. The method is tedious and technically challenging even with current mechanical assist devices. Alternatives to this approach for gene delivery include viral vectors, electroporation, and liposomal carriers [16]. These techniques all have the benefit of being able to transfect multiple cells yet their limitations do not make them viable alternatives for the creation of stable transgenic organisms. Viral vectors can carry large DNA or RNA molecules for introduction into the cell and the gene of interest must be packaged within the basic viral genome as part of the vector creation process. Therefore if a stable transgenic organism is created it will have some of the viral genome integrated as well. The use of viral vectors also limits the maximum size of the delivered transgene thereby limiting the amount of flanking DNA and regulatory elements introduced into the cell. The lack of these regions may reduce nuclear localization, chromosomal integration, and expression [17]. In addition, while the infection rate with many viral vectors is very high, a true stable transfection indicating integration into the genome is not the norm. Electroporation is a viable way to introduce genetic material into cells, yet stable transfection is not reliably produced [18]. In addition, the procedure is toxic to a percentage of the cells. Finally, introduction through the use of liposomes or other DNA carriers is less toxic but has the lowest transfection rate [19]. *All three modalities share one other limitation, namely, once delivered to the cell, the genetic material may exist in the cytoplasm as an isolated plasmid, or it may be endocytosed and remain within an intracytoplasmic vesicle, in either case preventing integration*

into the genome within the nucleus as a stable transfection. The direct injection method therefore remains the most reliable approach for creation of transgenic organisms. This method can introduce larger amounts of DNA to include regulatory elements as well as other agents such as restriction enzymes to improve integration. However, current transgenic technology is labor intensive and has relatively low yield. We hypothesize that force feedback plays an important role in increasing the efficiency of conventional cell manipulation systems.

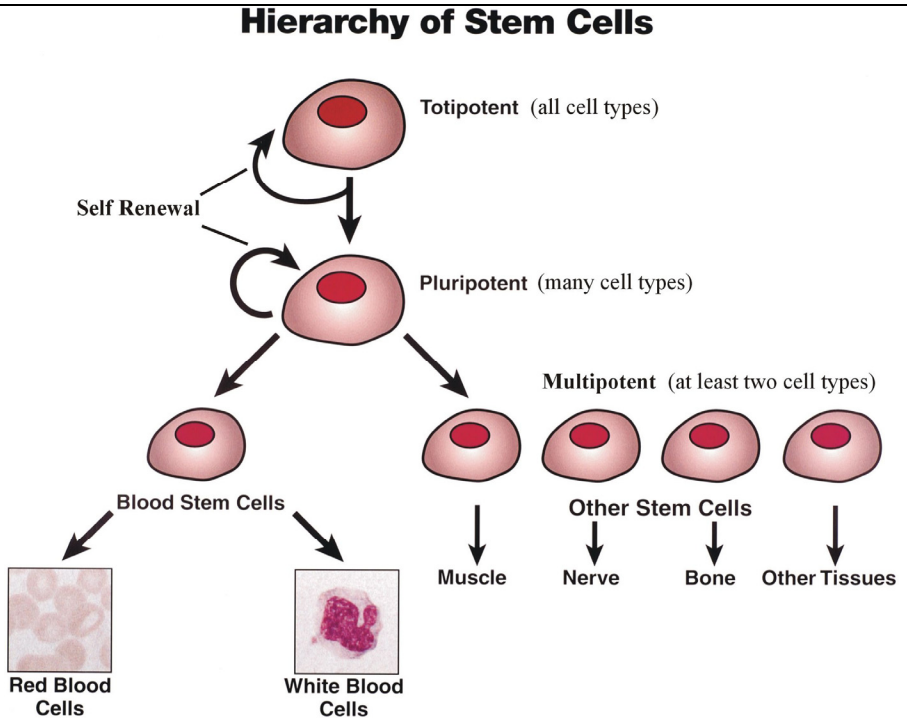

Figure 1.2. Hierarchy of embryonic stem cells. These cells have the capability to self renew and differentiate. The above figure shows stem cells differentiating into blood, muscle, nerve, bone and other cells (http://stemcells.nih.gov/info/media/).

Regenerative therapy is a novel approach to treat injuries and diseases by replacing/repairing damaged tissues/cells with specially grown tissues/cells, laboratory made compounds, and artificial organs. Stem cells have proven to be a

reliable cell type for therapeutic and regenerative medicine [20]. These cells have two essential abilities: (a) they are able to generate identical copies of themselves (self renew) and (b) they give rise to specialized cell types under certain physiological or experimental conditions (differentiation). Stem cells can be classified into two major categories: embryonic and non embryonic (adult) stem cells. The hierarchy of embryonic stem cells is shown in figure 1.2. A fertilized egg (zygote) is a totipotent cell – its daughter cells can become any cell type. As the development proceeds some of the cells become pluripotent cells. These cells are capable of giving rise to most tissues of the organism, except for extra embryonic tissue. Multipotent cells are developed from pluripotent cells and can give rise to limited number of cell types e.g. blood cell, muscle, nerve or bone.

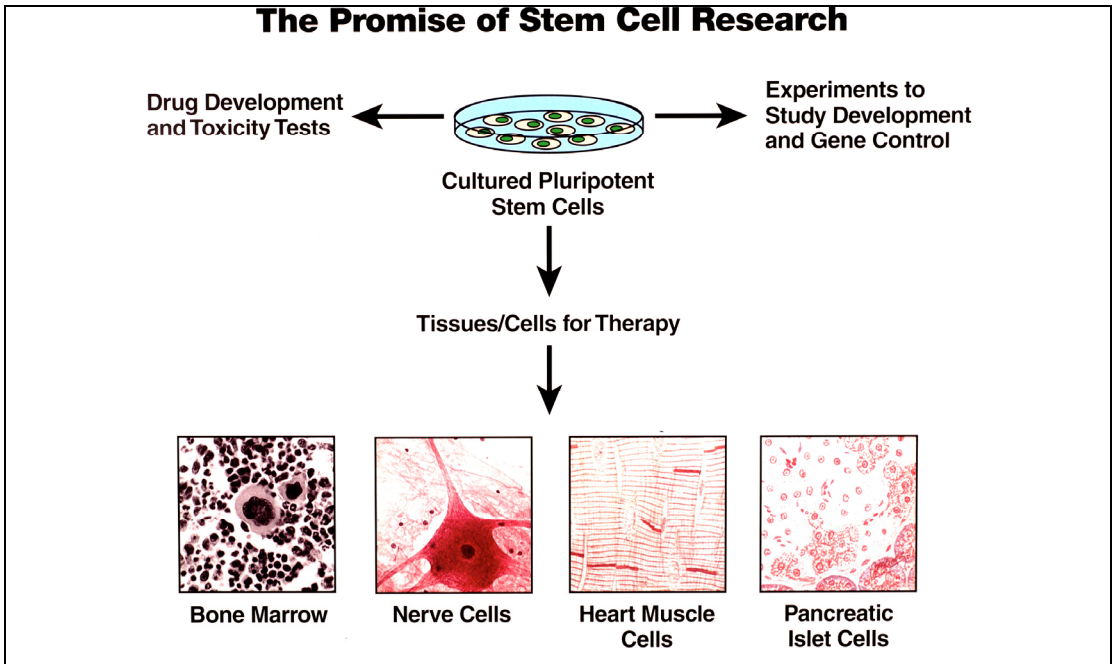

Figure 1.3. Stem cells offer a renewable source of replacement cells/tissues to treat disease and trauma including bone disease, Parkinson's disease, spinal cord injury, heart disease, diabetes etc (http://stemcells.nih.gov/info/media/).

The unique capability of stem cells to differentiate and give rise to specialized cell types makes them an ideal source to replace diseased and damaged cells in the body. Embryonic stem cells can give rise to every cell type in the body unlike adult stem cells and thus have huge therapeutic potential. Stem cell based systems offer a very promising and innovative alternative for obtaining large number of cells for early efficacy and higher toxicity screening (figure 1.3). Stem cell technology provides a new tool for drug development and an insight to better understand mammalian gene function (figure 1.3).

Some of the examples of treatments for major diseases using stem cells are (figure 1.3):

- Diabetes: Pluripotent stem cells instructed to differentiate into particular pancreatic cell could treat diabetes [21, 22].
- Nervous system diseases: Parkinson's disease and spinal cord injury involve death of nerve cells. The individuals with such diseases could be cured by creating a new nerve tissue from pluripotent cells which would restore the normal function of the nervous system [23, 24].
- Heart diseases: The embryonic stem cells could be differentiated to cardiac cells which would repair damaged myocardial tissue thus curing cardiovascular diseases [25, 26].
- Diseases of bone and cartilage: Embryonic stem cells once appropriately differentiated could cure many diseases and degenerative conditions in which bone or cartilage are deficient in number of defective in function [27].

However, the conventional methods to identify state of the cell are:

- Antibody staining: Involves live cell separation and immunocytochemistry. The former is time consuming and expensive while the later involves fixation procedure which kills the cells.
- Morphometric: Cell shape and structure can be used to detect some terminally differentiated cells. However, the method cannot be used to identify precursor cells.
- Transgenics: Cell detection involves specific fluorescent marker proteins which require genetic manipulation of cells, thus changing its characteristics.

1.2 Proposed Solution

Mechanical manipulation and characterization of biological cells is currently one of the promising research areas in the field of medical robotics applied to cellular level interactions. The present research addresses the drawbacks of conventional cell manipulation by using force and vision feedback for cell injection. We carry this work further by providing force feedback for smaller cells during AFM indentation. Finally to enable high throughput screening with force feedback, we have done research on understanding the change in force characterizing different stages of cell differentiation. We have thus done the following:

a) Develop a cell manipulation system with force feedback capability (shown in figure 1.4) to inject egg cells. We chose to perform experiments on zebrafish egg cells (diameter: 600μm – 1mm) because they are sensitive to mutagens and have low spontaneous malignancy rate, which makes it an ideal vertebrate animal model for understanding carcinogenesis, genetic functional screening,

and drug discovery. Moreover, zebrafish have easily accessible eggs, short generation time, high fecundity, rapid development, and external fertilization.

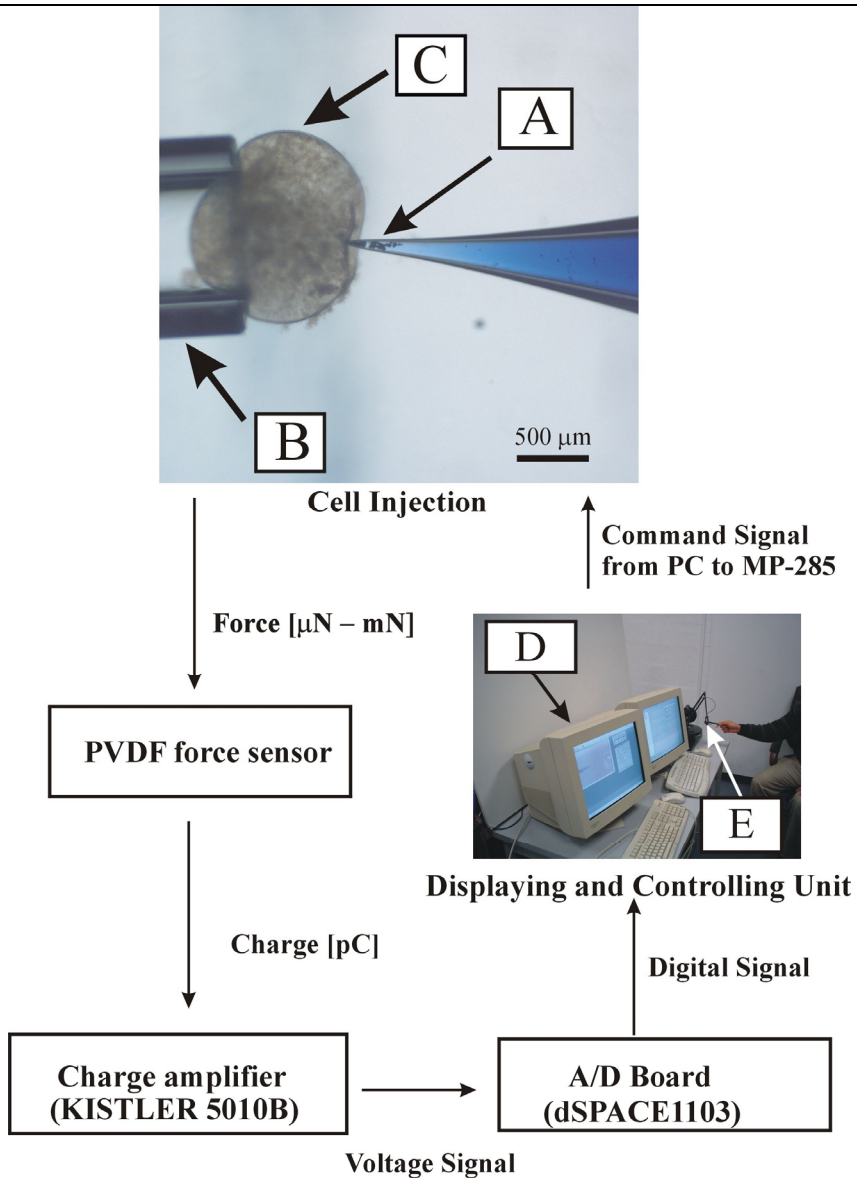

Figure 1.4. Cell injection system with vision and force feedback interface. A: Injecting pipette, B: Holding pipette, C: Zebrafish egg cell, D: Visual Interface, E: PHANToM® haptic interface.

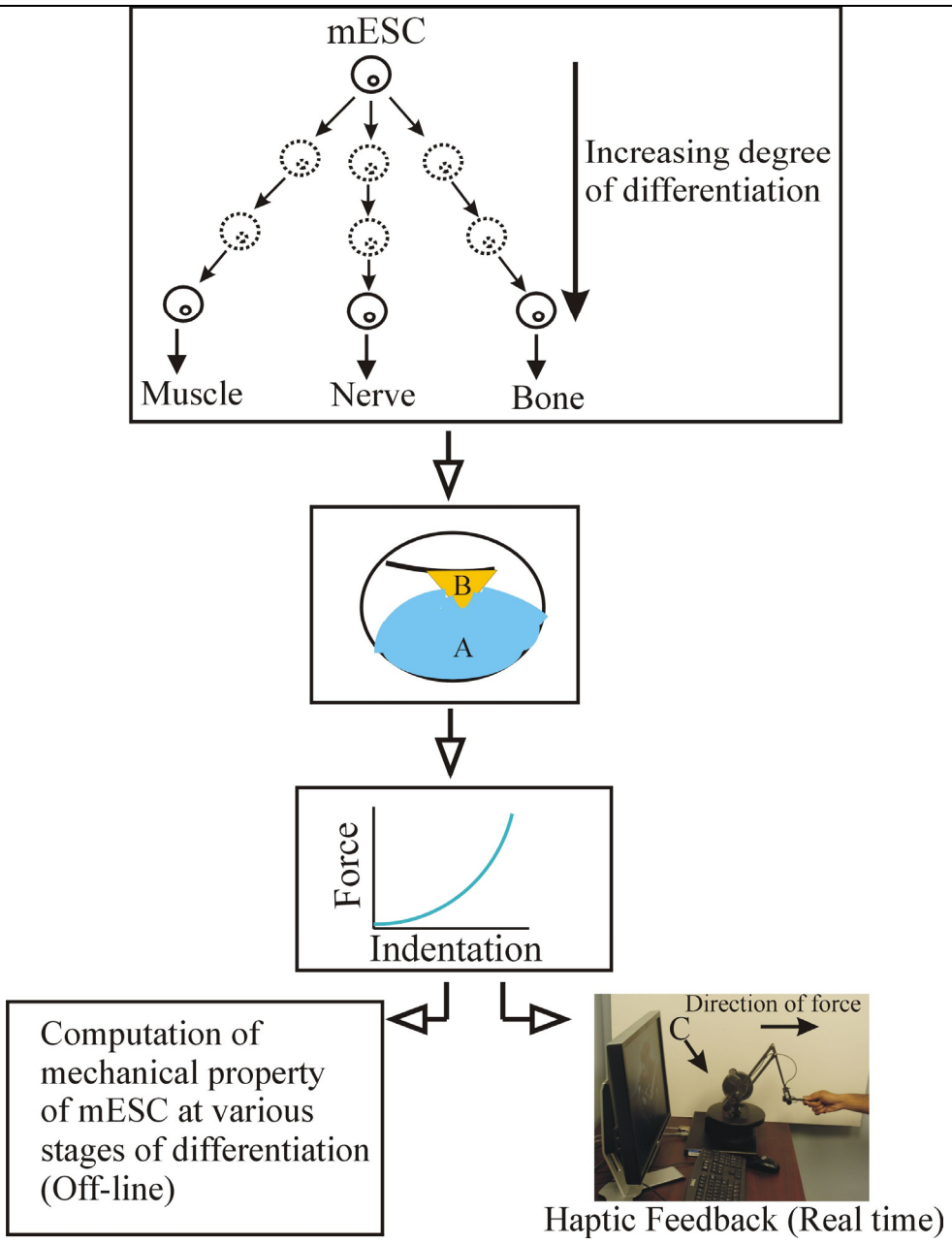

Figure 1.5: Schematic showing our proposed plan to manipulate and characterize an individual mouse embryonic stem cell (mESC) at various stages of differentiation. A: mESC, B: Tip of the AFM cantilever, C: PHANToM haptic feedback interface. AFM is used to obtain force and indentation data from an individual mESC.

b) Conduct human factor studies to evaluate the role of force feedback in cell injection tasks. To our knowledge there have been no human factors studies on evaluating the cell injection outcome with force feedback capability and whether force feedback when combined with vision feedback improves the outcome of cell injection (i.e., maintaining membrane integrity after injection with a pipette). While placing the genetic material in the cytoplasm by mechanical manipulation does not guarantee transgenesis, maintaining membrane integrity after injection is the first requirement.

c) Develop a haptics-enabled atomic force microscopy (AFM) based system that can be used to mechanically manipulate and characterize an individual cell of smaller dimension namely mouse embryonic stem cell (diameter: ~ 10 – 15 μm) as shown in figure 1.5. To our knowledge, there had been no studies to predict whether there exists any difference in mechanical behavior of mouse embryonic stem cell (mESC) at various stages of differentiation towards a particular cell lineage. Hence, we propose to conduct mESC indentation studies at various stages of differentiation using a haptics-enabled atomic force microscopy (AFM) system, where the user could feel the cell indentation forces in real time (figure 1.5) and hence possibly characterize the cell in our future work.

d) Perform a detailed analysis to choose an appropriate analytical model to characterize the mechanical property of mouse embryonic stem cells. We are interested in observing any difference in the mechanical behavior of mESC at

various stages in the differentiation process. The appropriate analytical model will be chosen based on the experimental data (force and indentation) obtained from the haptics-enabled AFM system.

e) Compute the mechanical property of mESC using the haptics enabled AFM system (as shown in figure 1.5) at undifferentiated and early differentiating (6 days under differentiation conditions) states in both live and fixed cells. We conduct indentation studies on mESC to evaluate our research hypothesis that the mechanical property of undifferentiated mESC differs from differentiating mESC in both live and fixed cells. The studies on fixed cells will facilitate its usage when logistics prove difficult to maintain live cells provided the results from live cells parallel that of fixed cells.

Mechanical characterization studies will potentially pave the way for developing a high throughput system with force feedback capability.

1.3 Organization

In chapter 2, we review some of the most common approaches for cell manipulation namely: optic and electric micromanipulation, magnetic micromanipulation, acoustic micromanipulation, micro-electromechanical systems (MEMS) and mechanical micromanipulation, visual servoing and imaging of biological cells and haptic feedback interface for cell manipulation. We discuss the advantages and disadvantages of each of these techniques. In chapter 3, we present the development of a haptic feedback interface for cell injection task including the development of a

force sensor which has the capability to measure forces in μN range. We perform experiments on salmon and flying fish egg cells and evaluate the role of force feedback on zebrafish egg cells. We conduct human factor studies and perform the statistical analysis to confirm our research hypothesis that the use of combined vision and force feedback leads to higher success rate in cell injection task compared to vision feedback alone.

In chapter 4, we present the development of a haptics enabled atomic force microscopy (AFM) to manipulate and characterize mouse embryonic stem cell (mESC). We present the challenges in imaging mESC using AFM and concentrate on obtaining force indentation data from mESC by indentation. We show that the force data obtained using our system is reliable. We conduct preliminary experiments on undifferentiated and differentiating (3^{rd} day) mESC using a haptics-enabled atomic force microscopy (AFM) system, where the user feels the cell indentation forces in real time and characterizes the state of the cell. In chapter 5, we present various analytical models proposed in the literature to characterize the mechanical behavior of an individual biological cell. We begin by presenting each of the analytical models and then present the experimental data obtained from indentation studies on both live as well as fixed mESC in undifferentiated and early differentiating states. The experimental data was used to choose an appropriate analytical model for mESC.

In Chapter 6, we present several indentation studies on mESC (2 different cell lines and two differentiation methods). The goal is to observe any mechanical property

difference between undifferentiated and early differentiating mESC. We use the analytical model chosen in chapter 5 to compute the elastic modulus of mESC. We also present the statistical analysis in detail to evaluate our research hypothesis that the mechanical property of undifferentiated mESC differs from differentiating mESC in both live and fixed cells.

Finally in chapter 7, we make some concluding remarks by mentioning the contributions and limitations of the present work.

Chapter 2: Literature Review

2.1 Introduction

Early efforts have been made to automate the cell injection process. Capillary pressure microinjection (CPM) is one of the supporting technologies for injecting macromolecules into a single living cell. Injection in nuclei or cytoplasm is performed using an ejection system with pressure levels manipulated by a single button, which requires no learning time and the injection rate obtained can be as high as 70 – 80% [28]. A semi-automatic microinjection system has also been developed to increase the cell survival rate in CPM [29]. The introduction of computer control in manipulating biological cells improves the efficiency of the process. A computer controlled microrobotic system with 3 DOF was developed for SUZI in mouse [30]. The sperm injection was successfully completed without damaging any of the mouse ova. Later on piezo driven pipette has been used to perform ICSI in mouse [31], which demonstrated 80% survival rate of sperm-injected oocytes. Yanagida et al [32] used piezo micromanipulator to perform ICSI in humans and obtained superior results compared to conventional ICSI. Different control strategies have also been used to develop a visually servoed microrobotic system. For example Sun and Nelson [33] developed an autonomous embryo pronuclei DNA injection system by implementing a hybrid visual servoing control scheme. In the sections below, we provide a comprehensive overview of the state of the art in biomanipulation. We cover a variety of approaches for biomanipulation, namely: optic and electric micromanipulation, magnetic micromanipulation, acoustic micromanipulation, micro-electromechanical

systems (MEMS) and mechanical micromanipulation, visual servoing and imaging of biological cells followed by haptic feedback interface for cell manipulation.

2.2 Optic and Electric Micromanipulation

Optic micromanipulation technique involves manipulating microscopic objects by optical forces. Ashkin [34] was the first to report the acceleration and trapping of micron sized particles by the forces of radiation pressure from visible laser light. In this setup the laser beam produces an axial force and a radial force on the particle (see figure 2.1).

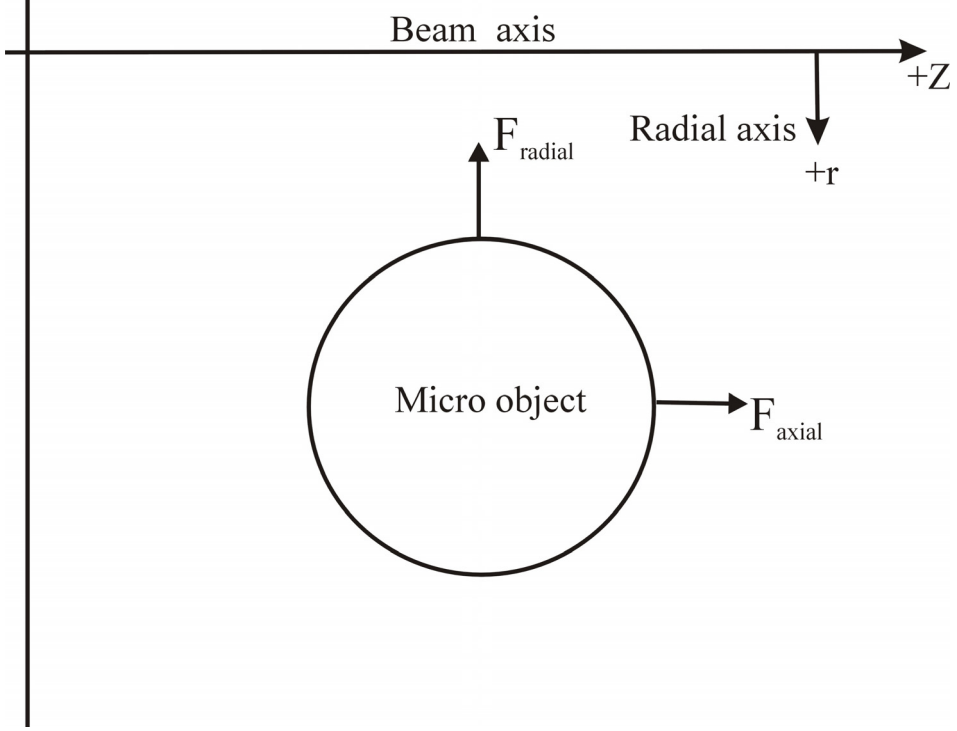

Figure 2.1. Schematic of typical forces experienced by a micro object during laser trapping.

The axial force propels the particle along the axis of the beam and the radial force traps the particle on the beam axis. The optical forces depend on the optical (refractive index and absorption) and geometric properties (shape, composition and surface charge) of the particle. In particular, the axial force on the particle depends on the focal spot size of the laser beam [35]. One of the conditions for optical trapping is that the refractive index of the micro particle (n_1) should be greater than the refractive index of the surrounding medium (n_2) i.e. $n_1 > n_2$. In certain cases, when: (a) $n_1 = n_2$, there is no force acting on the particle, and (b) $n_1 < n_2$, the particle is pushed out of the beam, for example air bubbles in glycerol [34]. Thus a major limitation is the cells should have refractive index contrast with the surrounding medium while using optical forces for biomanipulation. Absorption can increase the temperature of the particle and generate radiometric forces, which are usually larger in magnitude than radiation pressure. In a typical optical micromanipulation set up, the radiometric forces can be eliminated by suspending relatively transparent particle in a relatively transparent media. Ashkin et al [36] was also the first to demonstrate the use of optical traps for biomanipulation. An individual bacterium was manipulated and reproduced within the infrared laser trap [37]. An amoeba was also maneuvered successfully without any physical damage. Continuous wave laser beams have harmful effects on single living cells. The effects include changes in membrane permeability and alterations in cloning efficiency [38]. The photo damage of a living cell depends on the wavelength as well as the power of the light source. Infrared lasers have less detrimental effect on cell viability compared to visible laser light because the cell absorption is lower in the infrared region [37]. Apart from

positioning, laser beam also transports cells over certain distances with certain velocities [39]. A model was proposed to quantify the axial force generated in a single beam optical trap as it acts upon micro particles [35]. However the major limitations of this work are the following assumptions: (a) absorption of light by the particle is negligible, (b) momentum transfer is the same for both the reflected and transmitted beams, (c) the laser beam has Gaussian intensity profile, and (d) the diffraction effects are neglected. Experiments were performed to measure the minimum power required to trap a particle and to measure the effective trapping range over which a particle could be caught and held within the trap. Experimental results were found to be in good agreement with model prediction. The application of laser trapping to cell biology was demonstrated by performing experiments involving chromosome movement in mitotic cells and the trapping of spermatozoa. However, the possibility of sperm damage from absorption and subsequent heating after exposure to trap remained a concern. A detail history and review of optical trapping can be found in [40].

In addition to optical trapping, other non contact manipulation techniques are dielectrophoresis and electrorotation. Dielectrophoresis (DEP) involves manipulation of dielectric particles using non uniform electric fields. Pohl [41] first investigated the phenomenon in 1951. Electrorotation involves manipulation of electrically polarizable objects by controlling the phase and magnitude of electric fields. Rotating electric field was used to distinguish between live and dead cells [42]. Live cells exhibited 2 to 3 response peaks where as dead cells exhibited only one response peak,

when subjected to the field over a frequency of 500 to 700 Hz. Electrorotation was used to determine the dielectric parameters of individual cells [43]. Dielectrophoretic forces can be analyzed using finite element method (FEM) [44]. DEP and electrorotation generated translational and rotational force respectively on living bacteria [45]. The characteristics of the bacteria will play an important role in understanding its mechanism. A new technique called "opt-electrostatic" micromanipulation combines dielectrophoretic force and the optical pressure of the laser beam. The technique achieves more flexible micromanipulation of cells [46]. *Escherichia coli (E.coli)* and *schizosaccharomyces pombe (S. Pombe)* were optically trapped by the laser and subsequently oriented with high frequency electric field by controlling the switching frequency of the AC voltage [47]. Peak of critical rotation frequency (PCRF) characterized the live and dead cells. The knowledge of PCRF can be utilized for the investigation of the dielectric properties of single cells. Another combination technique [48] involved laser scanning manipulator for local position control of a target cell and DEP for exclusion of other cells around the target cell, which proved to be an efficient method of selective separation. Manipulation of cells using DEP and electrorotation involves applying electric field to aqueous solutions. The temperature of the solution and the gas bubble formation (electrolytic process) in the solution increases with an increase in the conductivity of the solution. Therefore applications of DEP and electrorotation are limited to aqueous solution of conductivity between 10^{-6} and 10^{-4} S/m. The other alternative involves reducing the applied voltage by proper arrangement of electrodes because bubble generation by electrolysis will occur at around 2V potential in water. It has been reported that cell

exposure to high frequency electric fields does not cause any harmful effect to cell viability [49].

Group Type	Number of oocytes	Sperm concentration (in sperm cells/mL)	Fertilization rate (in %)	
			Laser drilling	*In vitro* fertilization(IVF)
Group 1	89	10(5)	67	31
Group 2	94	10(6)	90	54

Table 2.1: The fertilization rate of mouse oocytes increases by zona drilling

Laser light can be used to drill hole in the zona pellucida of an oocyte/ embryo. Laser assisted zona drilling increases the fertilization rate of an oocyte *in vitro* and efficiency of embryo biopsy compared to conventional partial zona dissection (PZD) [7, 8] as well as chemical zona drilling [50, 51]. The laser light can be used in contact or non contact mode to create a hole in the zona pellucida. In contact mode, the laser is guided through an optical fiber or glass pipette touching the oocyte/embryo. In non-contact mode, the laser is guided using an optical lens tangential to the oocyte/embryo. The size of the hole depends on the irradiation time. For example, the infrared 1.48 μm diode laser created a hole with diameter 5 -10 μm in 10-15 ms [52]. Larger hole diameter can be obtained by increasing the irradiation time. However laser zona drilling may cause genetic defect to cells. The defect can be prevented by having minimal thermal effect of the laser on the cells and choosing a laser whose wavelength is sufficiently distant from the maximum absorption of DNA. Palanker et al [53] first reported laser assisted zona drilling. An ultraviolet laser emitting at 193 nm was used in contact mode to obtain uniform, circular holes in the zona of mouse oocytes. The zona drilling of mouse oocytes increased the fertilization rate (as high as 90%) compared to conventional IVF at low sperm concentrations [54]. The results are

shown in table 2.1. However, one must be careful in selecting ultra violet radiation for zona drilling, because of its potential harmful mutagenic effect [55].

Sometimes, healthy pre-embryos are not able to hatch from their protective shell i.e. zona pellucida after *in vitro* fertilization. Erbium laser in contact mode was used to create 20 to 30 μm diameter hole in the zona pellucida of human embryo to improve embryo hatching after embryo transfer [56]. The wavelength of erbium-YAG laser is 2.9 μm, which is sufficiently distant from 268 nm, the absorption maximum of DNA [57]. The same laser was used to create holes of 14 μm diameter in the zona pellucida of human oocytes, with a fertilization rate of 30% [58]. A laser operating at wavelength 1.48 μm in non-contact mode is preferred over other laser systems in biomanipulation because water molecules absorb strongly at this wavelength and the cleavage of cellular material is mainly due to heat transfer from water. Therefore the laser system has no mechanical, thermal or mutagenic effects on cells. Researchers reported the use of infrared 1.48 μm diode laser to achieve (a) a high fertilization rate of mouse oocytes [52], (b) an efficient biopsy of human embryos [59] and mouse oocytes [60], and (c) an efficient cryopreservation of single human spermatozoa [61]. Apart from zona drilling of an oocyte, the other condition to achieve high fertilization in ICSI is immobilization of the spermatozoon prior to injection. Conventional immobilization technique involves mechanical breakage of the spermatozoon tail. Immobilization can also be achieved by treating the spermatozoon with a laser [62]. The whole immobilization process i.e. identification, aspiration and injection of a potential spermatozoon took shorter time compared to the conventional technique.

The fertilization rate was same for both techniques. The photodamage of the sperm cell from high optical intensities should be considered during the process. Laser is also used to decrease the thickness of zona pellucida of embryos for assisted hatching. The process commonly known as “laser zona thinning” improved the implantation and pregnancy rate of human embryos compared to embryos with intact zona pellucida [63, 64]. However laser zona manipulation should be carefully evaluated before performing any clinical application [65].

2.3 Magnetic Micromanipulation

The manipulation of micron sized magnetic particles by an external magnetic field is referred as “magnetic micromanipulation”. The concept was first introduced in the field of molecular biology by Crick et al [66]. Biomanipulation using magnetic energy can be used to: (a) study intracellular properties, (b) determine mechanical properties of an individual cell, and (c) separate certain cells labeled with magnetic beads. The magnetic particles are introduced into the cell via phagocytosis, a natural process which does not involve forcible manipulation. Thus the process does not cause physical damage to the cell. The magnetic particles do not affect the rate of growth of cell cultures. Therefore introduction of these particles inside a living cell is a viable process. A constant force can be generated on a magnetic bead by two fields: (a) a large uniform homogeneous magnetic field, and (b) a constant magnetic field gradient. Magnetic manipulation is preferred over optical manipulation when investigating intracellular properties. Optical forces are exerted on microscopic objects when they have refractive index contrast with the surrounding medium.

Optical tweezers cannot always selectively operate in intracellular environment, because of innumerable objects inside a cell. Moreover, in the field of biomanipulation, photodamage of cells from high optical intensities is a major limitation. Magnetic manipulators used for biomanipulation should have a compact size and be able to mount onto the stage of a microscope without intervening with the functionality of the microscope or video acquisition hardware. Two pole magnetic tweezers [67] consist of two magnetic coils. It was used to determine the intracellular properties of a mouse macrophage consisting of four 1.28 μm spherical superparamagnetic particles. Experimental results showed that the bead inside the macrophage did not relax to its original position upon turning off the magnetic field and beads at distinct locations within the same cell responded differently to the magnetic force. Thus the cytoplasm of a macrophage is viscoelastic and inhomogeneous in nature. Three pole magnetic tweezers [68] achieves more flexibility in manipulating magnetic probes within a cell. The tweezers produce high forces in a controllable fashion. The achieved magnetic flux gradient was 8×10^3 T/m and the beads were moved either along a linear path or a triangular path [68]. Beads with diameters of 1 μm and 0.35 μm were manipulated inside a cell and the force-displacement relationship of the beads indicated that the interior of a cell is viscoelastic. The magnetic particles can also be introduced into a living cell via endocytosis into preformed membrane compartments called “magnetic endosome” [69]. Initially the endosome was circular in shape. Under the influence of an external magnetic field the endosome became elliptical in shape. The deformation of the endosome was averaged over a large number of instantaneous shapes. The movement

of magnetic endosomes guided by an external magnetic field within an individual cell could offer signatures of specific molecular mechanisms.

Single DNA molecule is manipulated magnetically by attaching one end of the molecule to a magnetic bead and immobilizing the other end of the molecule by attaching it to a surface (preferably glass). Permanent magnets are used for manipulating DNA because they are portable and do not require power. The elasticity of a single linear DNA molecule was studied [70] by plotting the stretching force (range: 6 fN to 20 pN) versus extension curves for the molecule. It was coiled in a controllable and reversible fashion by the rotation of small magnets. Magnetic tweezers composed of two sets of co-axial electromagnetic coils applied a constant force on a magnetic bead attached to a single DNA molecule [71]. The force-extension curve of a single DNA molecule was obtained by tracking the centroid of the magnetic bead and measuring the applied magnetic force (0.1 pN). Larger forces of the order of 200 pN can be generated on a DNA molecule by a small permanent magnet [72]. The force measurement was performed by three glass micropipettes namely: (a) loading pipette, (b) force measuring pipette, and (c) catching pipette. One end of the DNA molecule was labeled with 3 μm diameter paramagnetic particle and the other end with a non-magnetic particle. The pipettes manipulated the DNA in the following manner: (a) The loading pipette injected the DNA into the sample medium, and (b) The catching pipette grabbed the non-paramagnetic particle attached to the DNA, and transferred it to the force measuring pipette (force constant: 137 pN/μm). The system was also able to measure forces as low as 0.2 pN. However the primary limitation is that permanent magnets cannot control the movement of the bead

precisely and magnetic coils have high coil resistance which generates heat when applying high current. On the other hand, electromagnets offer excellent controllability during operation. 3D manipulation of a DNA molecule was achieved by six electromagnets and a ring trapper [73]. The magnetic bead attached to the DNA molecule was manipulated linearly/angularly by the electromagnets and vertically (out of the plane) by the ring trapper. The measured force-extension relationship for a single DNA molecule was found to be different from the theoretical model. The theoretical model assumed that the molecule is a perfectly, homogeneous, cylinder rod and there are negligible electrostatic interactions between the molecules. A magnetic force transducer composed of two electromagnets was used to measure forces produced by an individual leukocyte during locomotion both *in vivo* and *in vitro* [74]. The cell consisting of nickel magnetic particles was positioned between the two electromagnets and the force produced by the cell was measured in terms of the currents through the two electromagnets. Experiments showed that the extension of a *lamellipod* was always accompanied by an increase in force production. In *in vitro* experiments the resolution of the transducer was 100 pN but for *in vivo,* the resolution was limited to 1 nN due to mechanical noise in tissue. Forces in the range of 1.9 to 10.7 nN were generated by the cells. Such results may be helpful in determining the mechanisms driving locomotion in *leukocytes* and other nonmuscle cells. An electromagnetic tweezer was used to apply focused and quantifiable mechanical stress to individual cells in culture [75]. This technique examines cell mechanics of an individual cell which can play a major role in quantifying the material properties of the integrin-cytoskeleton linkages. Experiments were performed on wild type *F9*

embryonic carcinoma cells and cells from vinculin knock out mouse *F9 Vin (-/-)*. The tensional forces applied to the transmembrane receptors were in the range of 10 pN to greater than 1 nN. Magnetic micromanipulation was also proposed to measure the elasticity of the zona pellucida of oocytes [76]. The set up used a force sensing manipulator to measure forces in the nN range using permanent magnets and diamagnetic material. Thus magnetic energy is used to explore the mechanical properties of individual cells.

Specific cells carrying magnetic beads can be separated from other cells in a cell culture medium by applying an external magnetic field. MiniMACS magnetic separation method (MB42102, Miltenyi Biotec) isolated and purified mouse *primodal germ* cells (PGCs) from 10.5-13.5 days *post cortium* (d.p.c) [77]. Cells sequentially stained with an antibody and superparamagnetic particles were separated on high gradient magnetic columns. With this technique, a maximum of 90% of the PGCs are recovered and the cell viability is never lower than 90%. Yeast cells labeled with magnetic beads were trapped by a microelectromagnet matrix [78]. The unlabelled cells were trapped by microposit matrix generating electric fields. This set up allows the possibility of constructing an efficient microfluidic system for sorting cells. Various other magnetic tools for biomanipulation are magnetic micromanipulator, micromotor and microtweezer [79]. The magnetic micromanipulator was fabricated by winding a 25 μm diameter copper magnet wire around a 50 μm diameter soft-ferromagnetic wire. High field gradient is achieved by etching the soft-ferromagnetic wire into a sharp probe. Experiments on 2.8 μm diameter superparamagnetic beads

demonstrated forces of 10 pN and submicron positioning control. Magnetic micromotor was developed by arranging three micromanipulator coils and tips into an equilateral triangle. This arrangement acted as the three-phase stator of the micromotor placed outside the fluid and the rotor was a cylindrical nickel particle (40 μm long & 1 μm in diameter). The set up demonstrated one full rotation of the motor. Magnetic microtweezer was developed by manipulating magnetic micro wires in aqueous media. However, the usage of magnetic wires for biomanipulation involves power consumption and long period of manipulation can cause local heating possibly damaging the cells [80].

2.4 Micromanipulation using Acoustic Energy

The manipulation of microparticles and biological cells by ultrasonic waves has been investigated by few researchers. The advantage of this technique involves no mechanical contact and non invasiveness. Kozuka et al [81] used acoustic energy to trap and control the position of micro objects in two dimensions. Polystyrene particles (100 to 150 μm in diameter) were trapped at the nodes of the standing waves which were formed by three ultrasonic transducers placed at an angle of 120^0 to each other in the same plane. The position of the particle was controlled by changing the phase of one of the transducers, which caused the particle to be transported along the sound beam axis of phase shifted transducer. 3D manipulation [82] was realized by using four ultrasonic transducers placed at the corners of a regular triangular pyramid. The movement of each particle was captured by two CCD cameras. A theoretical derivation was obtained for the displacement of the particle, which was found to be in

agreement with experimental results. An attempt was made to examine the behavior of micro particles in a short path length chamber formed by a plane transducer and reflector [83]. Conditions for particle concentration into bands and clumps were identified. The system consists of acoustic chambers and microscopy chamber and was tested with 4.6μm diameter yeast cells as well as 2.16μm diameter fluorescent orange beads. The nodes of the standing wave play an important role in manipulating micron sized particles, the position of such nodes could be changed by varying the electronic parameters of the resonator instead of the mechanical parameters [84]. The resonator consists of a fluid filled tube and two piezoelectric transducers. The proposed model of the resonator studied the electronic parameters of piezo devices, and proved its importance in affecting the position of the nodes of standing waves. The advantage of this approach is that there is no mechanical movement which would cause unwanted fluid flow. Kim et al [85] used acoustic forces in an ultrasonic field for concentrating Hela cells and human mesenchymal stem cells (hMSCs). It was demonstrated that 90% of the cells are successfully concentrated into desired patterns. Ultrasonic waves were generated by piezo transducers. The critical voltages for initial cell movement were observed at 5.74 V (AC peak voltage) for HeLa cells and 1.05V for hMSCs. The authors believe that this critical voltage difference reflects adhesion and buoyancy differences of hMSCs and HeLa cells. The cell viability tests suggested that 98% of the hMSCs survived. However the usage of acoustic techniques for determining the characteristics of biological cells has yet to be realized.

2.5 Microelectromechanical systems (MEMS) and Mechanical Micromanipulation

Microelectromechanical systems (MEMS) technology is an important tool to manipulate a single cell or an array of cells. The technology fabricates devices with dimensions in the same order of magnitude as individual cells and allows single cell characterization. MEMS devices used for biomanipulation should be able to operate in aqueous solution without affecting the viability of cells. Electrochemically activated microrobot transported 100 μm glass bead over a distance of about 200 to 250 μm in an aqueous media [86] (see figure 2.2). The robot was fabricated from a conducting polymer, polypyrrole (PPy) in a bi-layer configuration with gold. Apart from manipulating glass bead, the microrobot was not tested on cells. Electro thermally activated polymer (SU-8) microgripper was fabricated to manipulate single Hela cell (diameter ~ 10 μm) in solution [87]. High coefficient of thermal expansion of SU-8 allows in plane activation of the gripper at low voltages (less than 2V) and average temperature changes (less than 32^0 C). Voltages greater than 2 V result in bubble formation due to electrolysis of water and high temperature changes may affect the viability of cells. Chemical etching based process, one of the micro fabrication processes was used to fabricate single cell trapper and sharpened micro injector [88]. A model was developed for the etching of cell trapper and the experiments demonstrated successful injection of a fluorescent dye in *brassica oleracea* (cabbage) protoplast (diameter ~ 50 μm). The limitations of the model are the following assumptions, namely: (a) the etching process is one-dimensional axi-symmetric and (b) the etchant has steady-state concentration distribution.

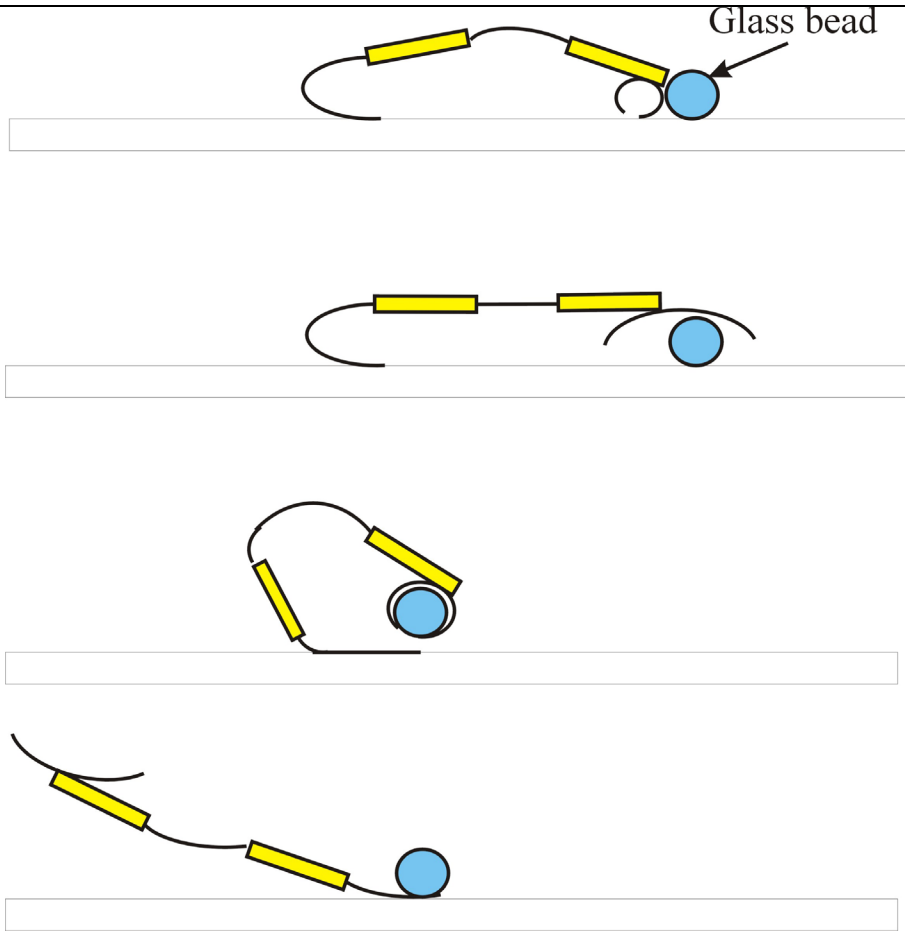

Figure 2.2. Schematic of a glass bead manipulated by a micro-robot developed by Jager et al [86].

MEMS devices are also used to obtain characteristics of single cells. Thermally actuated cantilever array integrated with micro fluidic channels was proposed for individual cell characterization [89]. The device consisted of three cantilevers on the flow channel. The middle cantilever was used to immobilize individual cell and measure its impedance. The other two cantilevers were actuated to open and close the flow of cells. However the set up was not tested on cells and no investigation was

carried out on the viability of cells in high temperature environment. A cell clinic was proposed to perform impedance measurements on a single cell [90]. The clinic consisted of a microvial that can be closed with a lid activated by two polypyrrole (PPy) hinges. The microvial was fabricated with SU8 negative photoresist and has two gold electrodes for impedance measurements. Experiments were performed on *Xenopus leavis* melanophores, but there was no demonstration of automated placement of individual cell in each microvial. The lay out of the cell clinic was improved by integrating each vial with bioamplifiers to form a lab on a chip [91]. The cell clinic prototypes were fabricated on top of custom VLSI circuitry designed to record signals from cells within individual vials. Extracellular signals obtained from bovine aortic smooth muscle cells (BAOSMC) were in the range of μV to mV range. Hence, the lab on a chip offers the following merits over the conventional cell biology studies carried out in petri-dish: (a) ease of use, (b) low consumption of reagent and samples, (c) faster analysis, and (d) High reproducibility. Apart from analyzing single cells, MEMS has the advantage of treating an array of cells, thus reducing the time of operation [92, 93]. The functionality of MEMS devices depends on the size of the cells to be manipulated, hence a single MEMS device can be operated specifically on cells of certain size.

Mechanical micromanipulation commonly referred as contact manipulation is widely used in ICSI, pro-nuclei DNA injection, gene therapy and other biomedical areas. The drawbacks associated with conventional cell manipulation techniques like low success rate due to poor reproducibility and human contamination have motivated

researchers to automate the biomanipulation process. Piezo materials are ideal for actuating micromanipulators because they provide high positional accuracy, high control bandwidth and smart structure design [94-97].

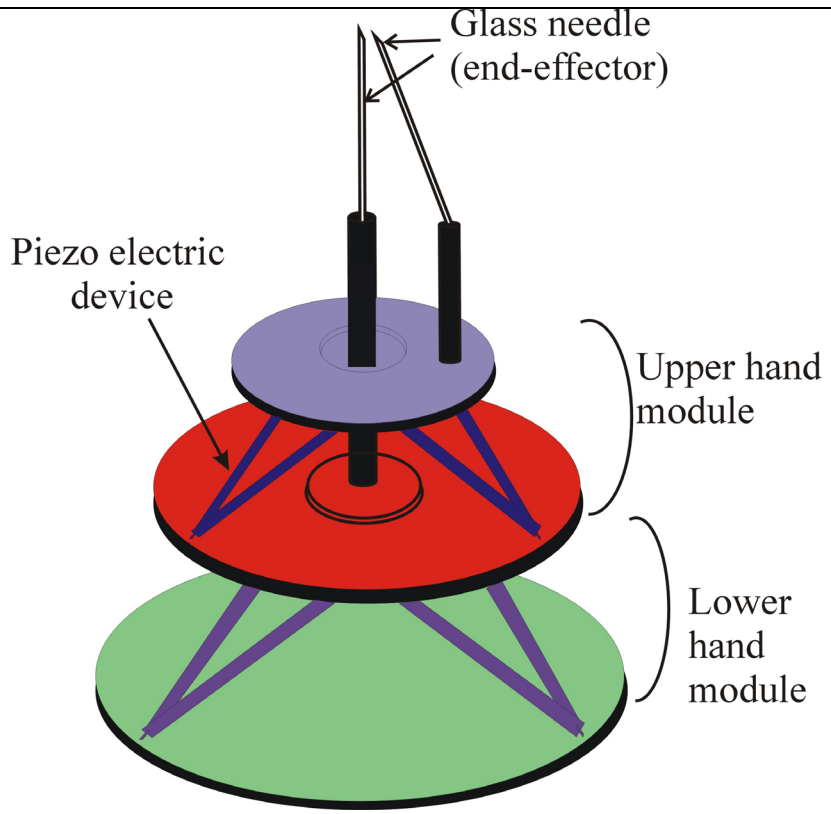

Figure 2.3. Schematic of the micro-hand driven by piezo electric actuators developed by Tanikawa and Arai [98].

A two fingered micro hand was developed to manipulate a microscopic object by simulating chopstick manipulation [98]. The micro hand shown in figure 2.3 is made up of piezo electric actuators has a lower module to provide global motion, while the upper module provides local relative motion of the two finger tips. Apart from

transporting, the micro-hand can also control the orientation of a micro-object. Experiments on human white blood cell (diameter ~ 10 μm) demonstrated successful actuation of the micro-hand. A piezo driven micropipette was used to perform ICSI in mouse [31]. A resolution of 0.5 μm was achieved by piezoelectric actuation. The pipette punctured the cell membrane with minimal distortion of the cell (oocyte). Experiments showed that 80% of sperm injected oocytes survived and 70% of them developed into blastocysts using the piezo driven micropipette. By conventional method only 16% of the oocytes survived. A typical schematic of the cell injection set up is shown in figure 2.4. Direct nuclear injection using piezo drill has been shown to be an efficient method for nuclear transfer between horse and cattle oocytes [99].

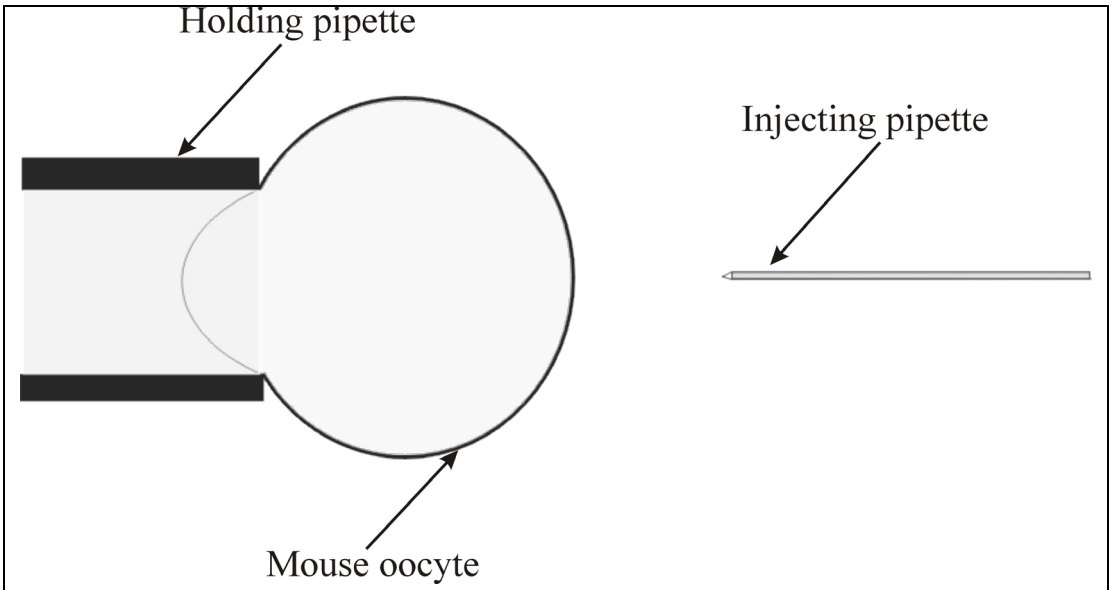

Figure 2.4. Microscopic view of the cell injection set up.

Calibration of micromanipulators has also been proposed to increase the positional accuracy [100, 101]. Apart from significant research carried out in the area of

micromanipulators, some of them are commercially available for example, the DC3-K motorized micromanipulator (manufactured by Stoelting Inc.) offers a highest resolution of 500 nm, the MP-285 nanomanipulator (manufactured by Sutter Inc.) offers a highest resolution of 40 nm, and the HS6-3 micromanipulator (manufactured by WPI Inc.) offers a highest resolution of 10 nm.

2.6 Visual Tracking and Imaging of Biological Cells

Visual servoing and recognition of an individual cell from a group of cells is a challenging task. In order to develop an automated biomanipulation system, active vision techniques have been investigated [102]. The two active vision techniques proposed were: depth from defocus and visual servoing. The depth from defocus technique indicates a repeatability of 8 μm, recovering depth estimates from the limited depth of field exhibited by optical lenses. Sub micron resolution and high speed in mm/sec range is achieved with visual servoing. An improved visual servoing system was developed having a repeatability of 1 μm in x and y direction [103]. The proposed system was used for the assembly of MEMS parts, by generating synthetic microscopic images from CAD drawings. This synthetic image is used to select image processing routines and generate reference features for visual servoing. The experimental results demonstrated the ability to visually servo MEMS parts to a desired location in a plane. An automatic micro manipulation system (AMMS) improved the performance of the vision system in the area of algorithm design and hardware implementation [104]. The accurate position of the micro tube (for holding the oocyte), oocyte, and the micro injector was found out. The oocyte as well as

micro tube was recognized by pattern matching method and the micro injector was recognized by binary morphological operation. Experimental results demonstrated tracking a circle and automatic gene insertion. Visual feedback system using a stereomicroscope was developed for injecting areas in brain [105]. The measurement resolution was 0.0096 mm/pixel for x & z axes and 0.0366mm/pixel for y axis at a magnification of 10.

A visual servoing technique was proposed [106] to position a loop mounted on a micromanipulator to manipulate a protein crystal. The technique used image-based approach which involved the computation of image Jacobian. Experimental results demonstrated positional accuracy beyond 0.1μm. The system could visually isolate individual proteins in a culture. A microshovel was developed to pick up the protein [107]. Vision techniques were presented to automate the entire process. Apart from visual servoing, there had been focus on cell detection algorithms. Sanchez–Marin [108] proposed hotelling transform as well as coordinate functions of contours for object recognition which need not necessarily need the representation of object's shape and eliminates the problems that arise from translation, scaling and rotation. Arambula Cosio [109] presented a neural network based workstation for improved automatic identification of metaphase spreads and nuclei on microscopic slide. Image processing techniques were used to segment the objects on each image. The morphological features were used to characterize each segmented object. The system has been able to classify correctly 91% of the metaphases and stimulated nuclei in a test set of 191 mitosis, 331 nuclei and 387 artefacts obtained from 30 different

microscopic slides. Segmenting cells in cell image analysis is important because it measures the geometric parameters of the cells, which is useful for the pathologists to make diagnostic decisions. An evolutionary tabu search (ETS) was proposed [110], which is a powerful optimization technique for cell segmentation. An elliptical cell contour model is introduced to describe the boundary of the cells and the experimental results showed that the ETS results in good robustness over the traditional tabu search (TS).

The resolution of optical microscopy depends on the nature of the light used. The maximum resolution the photons of light can provide is 0.2 μm. In light microscopy resolution below 0.2 μm is provided by the shorter wavelength of electrons used to generate image in electron microscope, however the specimens to be examined should not contain water, which may not be a suitable environmental condition for cells. Atomic force microscopy (AFM) has turned out be an excellent tool for imaging of living cells. It can image biological specimens in liquid with very high resolution and can monitor cellular dynamic processes. Atomic force microscopy was developed by Binnig and Quate [111] as a combination of scanning tunneling microscope and the stylus profilometer. The basic imaging modes of operation are contact mode, non-contact mode and tapping mode. The detailed principle of operation is presented in [112]. The resolution of the image depends on the geometry of the probe attached to the cantilever. Fritzsche et al [113] provided an overview of application of AFM to visualization of DNA, chromatin and chromosomes. The topographic mode yields the most accurate results for height determination and the

force mode visualizes the changes in deflection directly. The height of biological molecules imaged by SFM is influenced by: (a) sample preparation, (b) elastic behavior of the specimen, (c) lateral friction interactions between the tip and the sample surface. The highest vertical resolution achieved was 3 – 7 nm. However the resolution of the AFM image is hampered with time. This may be due to the result of the smearing of the cantilever tip with living cell associated molecules. This smearing process over time may coat the AFM tip with layers of non- rigid molecules and thus hamper the quality of the image and the resolution. Fragile or weakly bond specimens are more readily visualized by tapping mode at high frequencies [114]. Because of the viscoelastic behavior of the cellular surface the cells effectively harden under such tapping motion and are less susceptible to deformation. The surface structure of the cell is revealed with a spatial resolution of approximately 20 nm. Apart from taking images of static cells, another major application of AFM is the real time monitoring of dynamic events. Haberle et al [115] imaged living monkey-kidney cultured cells under normal growth conditions and showed reproducible features on the 10 nm scale. Cell viability is also an important issue while imaging with AFM. It has been reported that the cells are found to be viable up to 48 hours and no significant cell damage or cell death has occurred [116, 117].

An important limitation imaging with AFM is its temporal resolution, which is limited by the scan rate typically at ~ 50 – 60 sec/image. As a result usual AFM time-lapse imaging cannot capture important cellular events in real time. Few researchers addressed this issue and developed effective methods to increase the scanning speed.

Minne et al [118] reported an automated cantilever array design to operate multiple AFM probes in parallel at high speeds. The scan speed was increased by integrating thin layer of zinc oxide (ZNO) on the base of a piezo resistive cantilever. The ZNO actuation was able to track 2μm high topography at 1 mm/sec. Faster imaging speed of AFM was demonstrated using microcantilevers with integrated piezoelectric actuators [119]. High speed tapping mode image of *e coli* bacteria in saline solution was achieved at 75.5μm/sec using the ZNO actuator. High scanning speed was also obtained by using AFM with a PMN-PT single crystal scanner and a self sensing cantilever [120]. The advantages of this system are: high dynamic stiffness and decoupled XY and Z scanners. The images were obtained under scan rates of 1 Hz and 6 Hz with a corresponding scan speed of 6μm/sec and 36μm/sec. The imaging time of biological samples (like stranded DNA) was reduced by using a high-level control algorithm to steer the tip along the sample [121]. The resolution of image depends on the geometry of the tip of AFM. Commercially available probes consists of microfabricated Si or Si_3N_4 that have an end radii of curvature as small as 10nm, the end radii and the shape of the tips places significant constraint on lateral resolution and the ability to image narrow and deep features. To overcome the limitations, carbon nanotubes (as small as ~4nm diameter) have been reported. Multi-wall carbon nanotube (MWNT) and single-wall carbon nanotube (SWNT) offer high lateral resolution and smaller adhesion forces enabling gentler imaging conditions [122, 123]. Features as small as 0.5 nm in dimension could be extracted with this method. The cylindrical geometry of the carbon nano tubes allows to image deep structures and the nature of buckling above a critical force can prevent damage to

delicate organic and biological samples. The dimensional feature measured while imaging DNA by SWNT was 5 ± 1 nm and by Si tips was 15 ± 3 nm which demonstrated a significant three fold improvement in resolution. Hence, AFM is a promising tool to image and manipulate objects/biological samples having dimensions in the range of μm – nm.

2.7 Haptic Feedback Interface for Cell manipulation

Even though there have been considerable efforts to automate manipulation of biological cells, vision has been the only sensing modality. Recently, there have been efforts aimed at sensing the interaction forces to improve the reliability of biomanipulation tasks [124]. Force sensing in addition to vision would make the manipulation process repeatable and accurate. Few researchers have proposed the concept of "bilateral control", which involves a master- slave set up [125, 126].

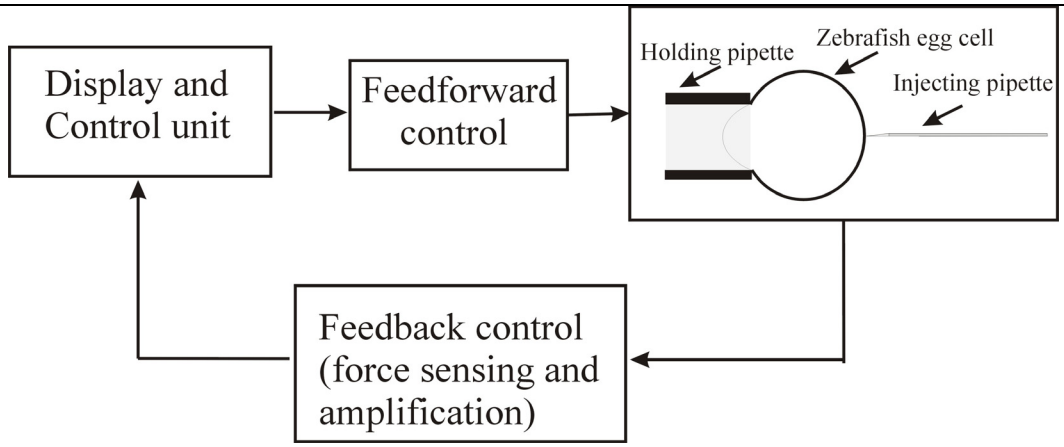

Figure 2.5. Schematic of master-slave teleoperated cell injection system with force feedback capability.

The master manipulator (in the macro world) gives position command to the slave manipulator (in the micro world) and the force sensed by the slave manipulator is communicated to the master manipulator, which allows dexterous manipulation of cells. The bilateral control system takes into account the scaling effect in the micro/macro world and maintains a stable, transparent system. A typical schematic of the master-slave teleoperation setup is shown in figure 2.5. A nanomanipulation system was developed to provide force feedback from biological samples and carbon nanotubes [127]. In this set up the user does not feel the actual forces from the sample, but feels a surface representation that is simultaneously reconstructed during the scan. Vogl et al [128] proposed a spline based surface model for nanomanipulation with 3D visual and force feedback using AFM. However, the spline based model, has not been evaluated on biological systems. Moreover, limited studies have been performed on biological cells using haptics based AFM [129, 130].

2.8 Cell Characterization

Mechanical characterization of cells using atomic force microscopy (AFM) has been studied many researchers. Hoh et al [131] calculated the effective spring constant of Mandin-Darby canine kidney cells (MDCK) fixed by glutaraldehyde. A novel sample preparation method was proposed to measure the elastic properties of β-chitin fibers [132]. A micro-mechanics cell model was developed to determine the mechanical properties of human dentine [133]. However, Hertz model [134-137] has been used extensively to characterize the mechanical property of cells using AFM. The model assumes that the cell is: (a) linear elastic, isotropic and homogeneous, and (b) no adhesion or friction occurs at the tip-cell interface. Hertz model [138] was originally

developed for contact between two spheres. Later, researchers extended the model to various indenter geometries namely: cylinder (Sneddon model) [139], cone (Sneddon model) [140], pyramid (Bilodeau model) [141], blunt cone [142], blunt pyramid [143]. Typically, the Sneddon model has been used by many researchers to determine the elastic modulus of biological entities [134-137]. Although Sneddon model is an extension of Hertz model, it is sometimes referred to as Hertz model. Most of the AFM tips have pyramidal tips which are used to obtain high resolution images and then subsequently probe specific locations of the cell to determine the local mechanical properties of the cell. Bilodeau model has been used to compute the mechanical properties of lung epithelial cell [144] and leukemia cells [145]. However, majority of the AFM pyramidal tips have a spherical shape at the end. The usage of Sneddon or Bilodeau model might result in an incorrect computation of elastic modulus of the sample indented by a blunt tip. Thus, Briscoe et al [142] and Rico et al [143] developed analytical models for blunt conical and pyramidal tip indenters respectively. The blunt conical model was used to estimate modulus of cardiac cells, skeletal muscle cells and the endothelial cell [146]. The blunt pyramidal model was used to compute the elastic modulus of agarose gels and epithelial cells [143]. JKR and DMT models [147] take into account the adhesion between the two elastic spheres. The assumptions made by Hertz theory are applicable in these models. Further, the JKR theory assumes that the adhesion force operates over a short distance within the contact region. On the other hand, DMT theory assumes that the adhesion force operates just outside the contact zone where the surfaces are small distance apart. The JKR theory was found to be valid for the indentation of relatively

compliance materials with probes of relatively large radii and strong adhesive forces [148]. On the other hand, the DMT theory applies to stiff materials and probes with small radii and weak adhesive forces [148]. The JKR and DMT theories were used to characterize the mechanical behavior of cells where there was significant force of adhesion [129, 149]. Apart from solid models, the capsule model was proposed for estimating the mechanical behavior of cells indented by AFM [150]. This model considers that the cell membrane is a thin film and that the inner cytoplasm provides a uniform hydrostatic pressure on the membrane. Further, the model assumes that: (a) cell membrane is linear elastic, (b) cell volume is constant, and (c), the cell is free of initial membrane stress or residual stress.

Danti et al [151] used force modulation microscopy (FMM) to detect variations in mechanical properties of human mesenchymal stem cells (hMSCs). However FMM imaging technique is not quantitative. It can detect only relative and qualitative elastic modulus differences between different cell surfaces. To our knowledge no one has carried out mechanical characterization studies on stem cells, which could lead to effective therapeutic and regenerative medicine. Stem cells are unique because of two essential characteristics: (a) they are able to produce identical copies of themselves (self-renewal); and (b) they give rise to specialized cell types (differentiation). Stem cells are classified into two major categories: embryonic and non-embryonic (adult) stem cells. Embryonic stem cells are pluripotent cells (cells capable of giving rise to most tissues of the organism, except for extra embryonic tissue), isolated from the inner cell mass of the blastocyst-stage mammalian embryo [152, 153]. On the other

hand, adult stem cells are specialized cells found within many tissues of the body. These cells are precursor cells capable of differentiating into limited number of cell types unlike pluripotent cells. Hence embryonic stem cells have huge therapeutic potential compared to adult stem cells. Researchers have shown that embryonic stem cells can be differentiated into a variety of specialized cell types namely: neural [23, 24], cardiac [25, 26], pancreatic [21, 22], and bone [27]. Some of the diseases which could be cured using differentiated stem cells are: diabetes (caused by destruction of insulin producing cells in the pancreas), Parkinson's disease (the death of nerve cells responsible to produce chemical 'dopamine'), cardiovascular disease (damaged myocardial tissue), and osteoarthritis (abnormal wearing of the cartilage). Stem cell based systems offer a very promising and innovative alternative for obtaining large number of cells for early efficacy and higher toxicity screening. Stem cell technology provides a new tool for drug development and an insight to better understand mammalian gene function. Conventionally, differentiated stem cells are distinguished from undifferentiated stem cells by: (a) antibody staining, (b) morphometric (cell shape/structure, and (c) transgenics. Antibody staining involves labeling specific cell lineages with florescent antibodies and then purifying them by fluorescence-activated cell sorting (FACS) [154]. This method is time-consuming and expensive. By morphometric, one can detect some terminally differentiated cells, but cannot identify precursor cells [155]. Transgenics involves cell specific markers which control the expression of marker proteins. This method requires genetic modification of cells [156, 157]. Moreover, there is limited availability of reliable markers for early lineage precursors [20]. Hence, there is a need to develop enabling technologies for

characterizing the state of the cell. This could be achieved by developing a haptics-based cell manipulation system. The system will possibly characterize the state of the cell and enable the development of a high throughput system with force feedback.

2.9 Discussion

There are several promising approaches for biomanipulation of cells. In this chapter we have covered some of the most common approaches for cell manipulation, namely: optic and electric micromanipulation, magnetic micromanipulation, acoustic micromanipulation, micro-electromechanical systems (MEMS) and mechanical micromanipulation, visual servoing and imaging of biological cells and haptic feedback interface for cell manipulation. Each of the above techniques has their own advantages and disadvantages. Further, we presented the various analytical approaches for mechanical characterization of cells using atomic force microscopy (AFM) and the significance of stem cell studies. Optic and magnetic techniques offer the ability to manipulate single cells without contact; however, high optical intensities and long period of manipulation using magnetic wires can cause local heating possibly damaging the cells. The usage of acoustic techniques for characterizing the properties of cells has yet to be realized. Individual cells are characterized using MEMS devices, whose dimensions are in the same order of magnitude as cells. Advances in the field of computer vision algorithms facilitated the integration of robotics with visual servoing control schemes. The integration was a boon to the microrobotics community. However, (a) effective manipulation of an individual cell is yet to be realized through the use of a vision and force feedback interface and has to be evaluated with human factor studies. (b) In addition force feedback could be

used to determine the state (real time) and mechanical property (off-line) of cells. Goals (a) and (b) are explored in this dissertation. We summarize our literature review as follows:

- Large amounts of DNA can be introduced into a cell by the "direct injection method", the most reliable approach to create transgenic organisms compared to viral vectors, electroporation, and liposomal carriers.
- Optical tweezers can harm active biological systems.
- Non-contact lasers are preferred over contact lasers in drilling a hole in the zona pellucida of an oocyte/embryo.
- Magnetic manipulation is an efficient technique to characterize intracellular properties.
- MEMS devices have the ability to manipulate cells effectively as the devices dimensions are in the same order of magnitude as individual cells.
- Piezo actuating micromanipulators increase the efficiency of micromanipulation tasks like ICSI compared to conventional cell manipulation techniques.
- The addition of force feedback to an automated micromanipulation system could increase the success rate of cell injection tasks.
- Mechanical characterization of stem cells at various stages of differentiation using haptics-based cell manipulation system will possibly pave the way for developing a high throughput system with force feedback capability.

Chapter 3: Force and Vision Feedback Interface for Cell Injection

3.1 Introduction

Conventional methods of manipulating individual biological cells have been prevalent in the field of molecular biology. These methods do not have the ability to provide force feedback to an operator. Poor control of cell injection force is one of the primary reasons for low success rates in cell injection and transgenesis in particular. Therefore, there exists a need to incorporate force feedback into a cell injection system. In this chapter, we present a force feedback interface, which has the capability of measuring forces in the range of μN and provide a haptic display of the cell injection forces in real time. Initially, the system was tested on salmon and flying fish egg cells and the user was able to feel the cell injection forces in real time. Our aim is to evaluate the role of force feedback in cell injection tasks. To our knowledge there have been no human factors studies on evaluating the cell injection outcome with force feedback capability and whether force feedback when combined with vision feedback improves the outcome of cell injection (i.e., maintaining membrane integrity after injection with a pipette). While placing the genetic material in the cytoplasm by mechanical manipulation does not guarantee transgenesis, maintaining membrane integrity after injection is the first requirement. Hence, we conducted human factors studies to evaluate if the cell membrane maintained its integrity and did not collapse after injection. We performed our experiments on zebrafish eggs cells. These cells are transparent in nature which makes it an ideal vertebrate animal

model for understanding carcinogenesis, genetic functional screening, and drug discovery.

3.2. Development of Force Sensor

A key component in the development of a haptic feedback interface is the force sensor. Since we are developing the interface for cell manipulation tasks, the sensor should be able to measure forces in μN range. In addition, the force sensor should have high sensitivity and high signal to noise ratio. Force sensors can be based on the following principles: piezoresistive, capacitive and piezoelectric. Ando et al [125] used a force sensor based on piezoresistive principle for micromanipulation. However, the force sensor has low resolution (~ 8 mN). Capacitive based force sensors are non-linear meaning that the force varies non-linearly with the change in capacitance [158, 159]. This affects the sensitivity of the sensor and is not desirable for our application. On the other hand, piezoelectric sensor has high sensitivity, high compliance and high signal to noise ratio [160-162]. In this section, we show our approach in developing the piezoelectric force sensor.

A piezoelectric sensor generates an electric charge when mechanically deformed. We used a PVDF (polyvinylidene fluoride) film (model: LDT1-028K of Measurement Specialties, Inc., Hampton, VA) for our application. The dimensions of the film are 0.0414m in length, 0.0162 in width and 28 μm in thickness. The PVDF film has a high frequency range (0.001 Hz to 10^9 Hz). The high sensitivity is given by the piezo strain constant $d_{31} = 23 \times 10^{-12}$ C/N.

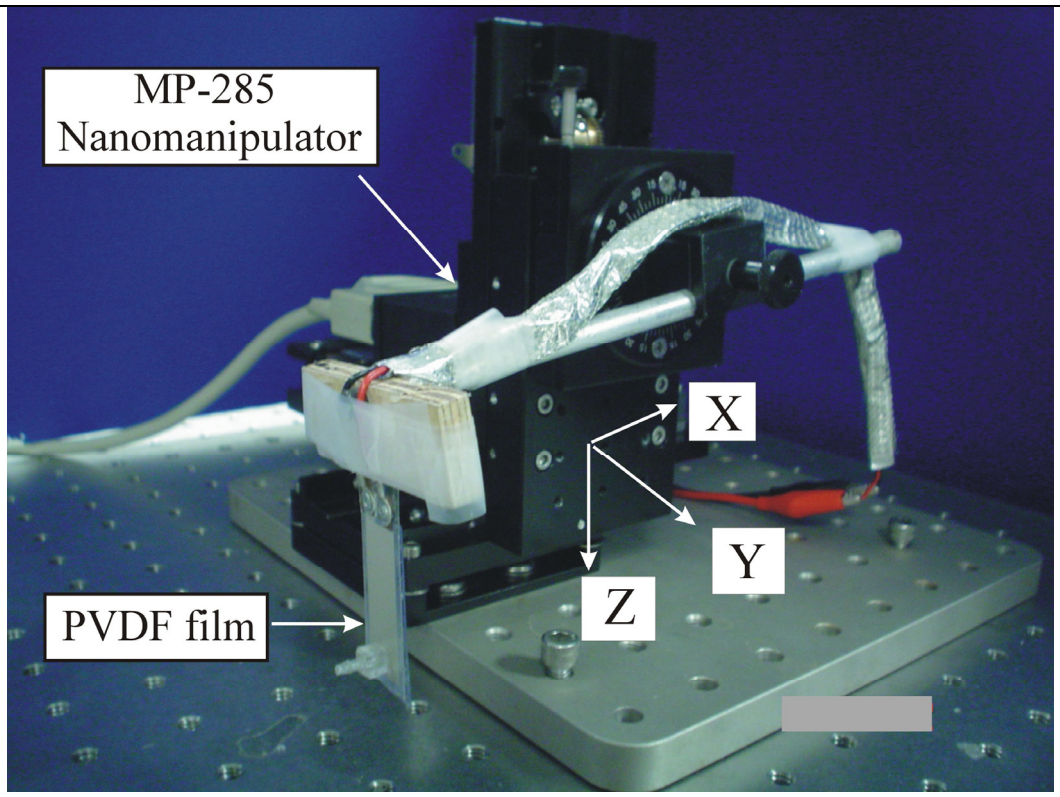

Figure 3.1. Integration of the PVDF film with the nanomanipulator

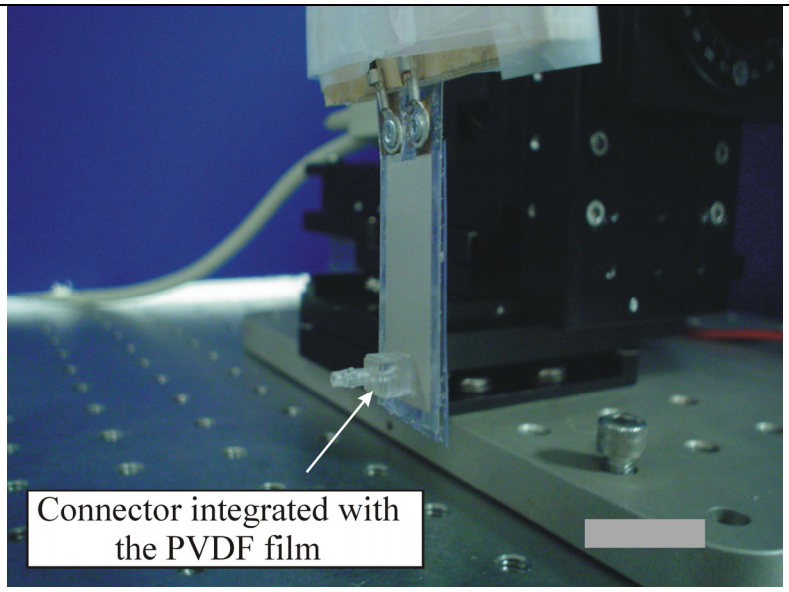

Figure 3.2: Connector integrated with the PVDF film

Figure 3.1 shows the overall setup on the biomanipulation side, which consists of a nanomanipulator (Model: MP-285, Sutter Instrument, Novato, CA) holding the PVDF force sensor and the pipette holding apparatus. The nanomanipulator has three degrees of freedom in x, y, and z direction and an additional fourth degree of freedom for the diagonal advancement of the pipette in the XZ plane (refer to figure 3.1). The travel range is 25 mm in all three axes. The lowest resolution is 0.02 μm/step and highest resolution is 40 nm/step. The glass micropipette is integrated to the PVDF film (thickness: 28 μm) with the help of a connector as shown in the figure 3.2. This setup allows the easy removal and replacement of the micropipette (TIP5TW1, World Precision Instruments, Inc., Sarasota, Florida) if the tip of it gets damaged during micromanipulation (5 μm ID).

3.2.1 Theoretical Model for the Force Sensor

A theoretical model for the PVDF film is developed using the methodology proposed in [163], however with a modification that the resistance R_p of the PVDF film is not considered in our analysis since it is very high and the contribution to the charge developed is correspondingly low. The PVDF film was used in a configuration shown in figure 3.3, such that the stress occurred along the x-axis. The film was not mounted on any substrate. This configuration is recommended for sensing of low frequency signals (< 100 kHz) [162].

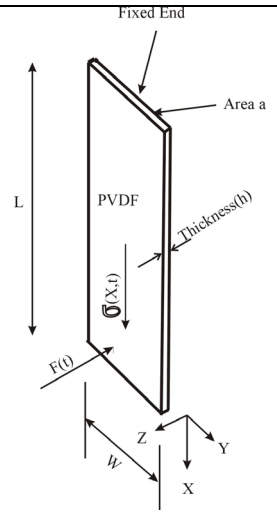

Figure 3.3: PVDF film as a force sensor

The following parameters will be used in the analysis:

W: width of PVDF Film

h: thickness of PVDF film

L: length of PVDF Film

A: surface Area (L * W)

a: cross-sectional area (W * h)

Q (t): charge produced (PVDF Film)

I (t): current produced (PVDF film)

V (t): voltage across the PVDF Film

C_P: capacitance of the PVDF Film

F (t): contact force (such as cell injection force)

I_{xx}: inertial moment of cross sectional area, a

σ (x, t): unit stress

d_{31}: piezoelectric coefficient of PVDF film

ε_{33}^{T}: dielectrical factor of the PVDF film

From the theory of mechanics of materials, for a cantilever beam (see figure 3.3):

$$\sigma(\mathrm{x, t}) = \frac{F(t)x\frac{h}{2}}{I_{xx}} \tag{3.1}$$

Equation (3.1) is valid under the assumption that the neutral axis of the bending deflection of beam is assumed to pass through the centroid of cross sectional area. The total charge generated on the surface of the PVDF film due to the stress, $\sigma(x, t)$ is given by:

$$Q(t) = \int_0^L d_{31}\sigma(x,t)dA + \varepsilon_{33}^T E_3(t)A \tag{3.2}$$

where $dA = Wdx$ (elemental surface area)

Modeling the PVDF film as a charge source in parallel with a capacitor C_P, the output charge $Q(t)$ and the output current $I(t)$ are given by:

$$Q(t) = C_P V(t) \tag{3.3}$$

$$I(t) = \frac{dQ}{dt} = C_p \frac{dV}{dt} \tag{3.4}$$

The resistance R_P, of the PVDF film is neglected, since it is very high (10^{13}ohms). The electrical field $E_3(t)$ is given by:

$$E_3(t) = -\frac{dV(t)}{dh} \tag{3.5}$$

Assuming a uniform electric field over the cross-sectional thickness, h, we can write $E_3(t)$ as:

$$E_3(t) = -\frac{V(t)}{h} \tag{3.6}$$

Substituting equations 3.1, 3.3, 3.5 and $C_P = \frac{\varepsilon_{33}^T A}{h}$ (capacitance of the PVDF film) in equation 3.2, we get the generated voltage *V (t)* across the PVDF film based on the contact force *F (t)*:

$$V(t) = BF(t) \text{ and } B = \frac{Ad_{31}hL}{8I_{xx}C_P}. \tag{3.7}$$

Since the voltage output from the charge amplifier is proportional to the current input (produced by the external force applied to the PVDF film), we have:

$$V_{out}(t) = GI(t) \tag{3.8}$$

Substituting equation (3.4) and (3.7) in (3.8), we get:

$$F = \frac{1}{GBC_p}\int V_{out}\, dt \tag{3.9}$$

where *G* is a constant. The above equation shows that there exists a linear relationship between the force applied to the PVDF film and the corresponding integral of the output voltage from the charge amplifier.

3.2.2 Experimental Calibration for the Force Sensor

The PVDF Film is calibrated with the load cell (Model: GSO-10 of Transducer Techniques®, Temecula, CA, Maximum measurement range: 98.1 mN and accuracy of 50 μN). The load cell is mounted on a stationary platform and the PVDF film is mounted on the MP-285 Nanomanipulator. The experimental calibration setup is shown in figure 3.4.

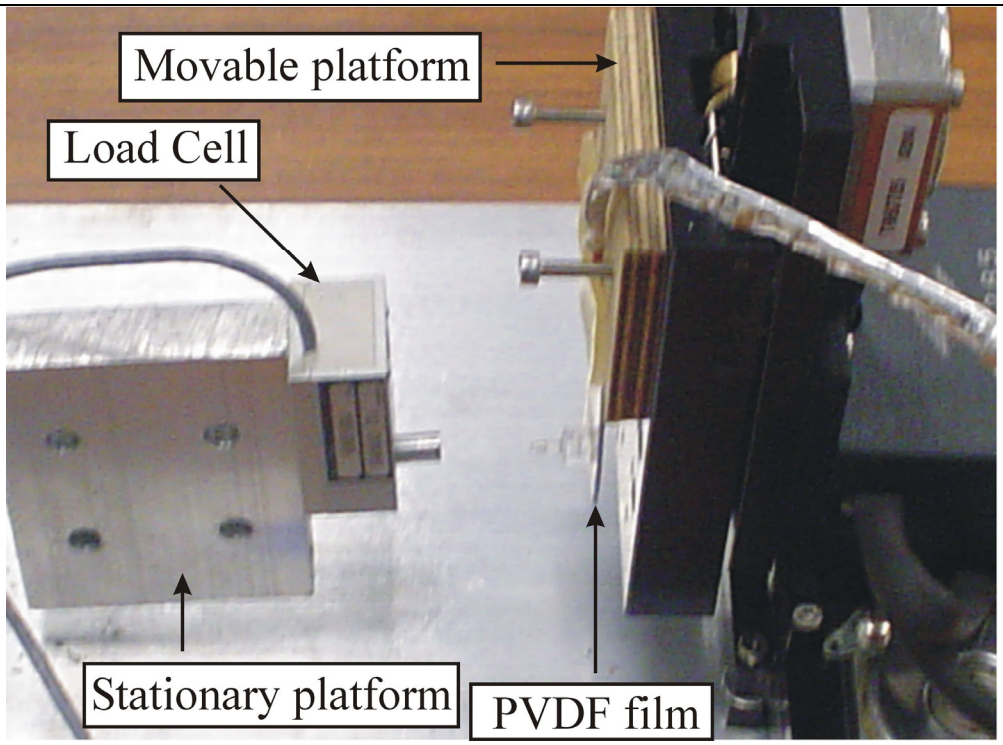

Figure 3.4. Overview of calibration set up for the PVDF force sensor.

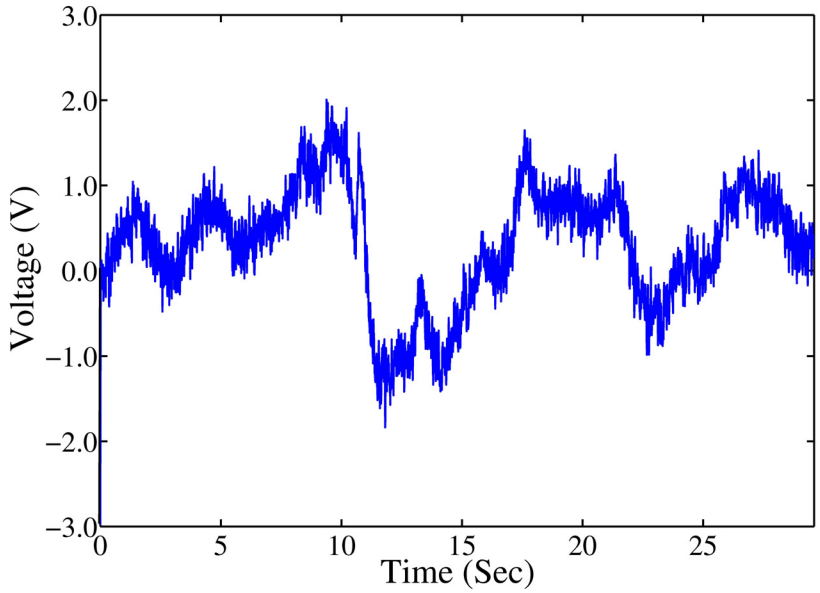

Figure 3.5. Noise signal from PVDF sensor without any applied force.

The signal conditioning circuit for the sensor consisted of a charge amplifier (Model: 5010B, Kistler Instrument Corp., Amherst, NY) and a low pass filter (cut off frequency: 4 Hz) to get an amplified voltage signal, which is measured, through a data acquisition board (model: dSpace 1103, dSpace Inc., Wixom, MI). However, we observed significant noise in the signal without any applied force on the PVDF sensor as shown in figure 3.5.

During calibration, the PVDF approaches the load cell and the connector contacts the load cell as shown in figure 3.6, which leads to charge generation across the PVDF film. But we observe that the signal to noise ratio is poor as shown in figure 3.7.

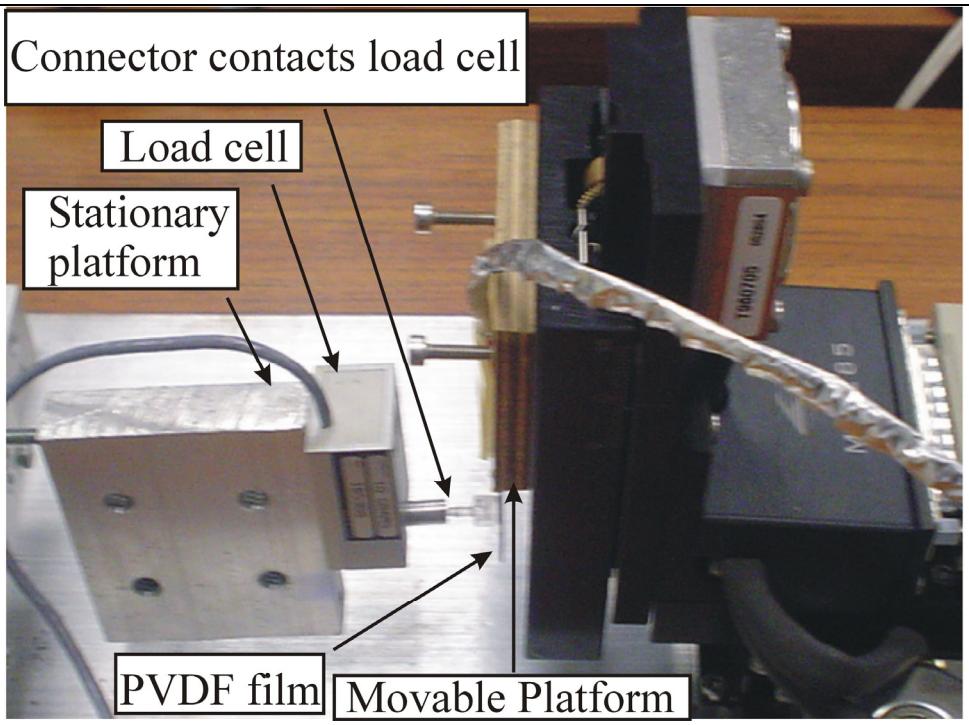

Figure 3.6. The connector contacts the load cell during calibration.

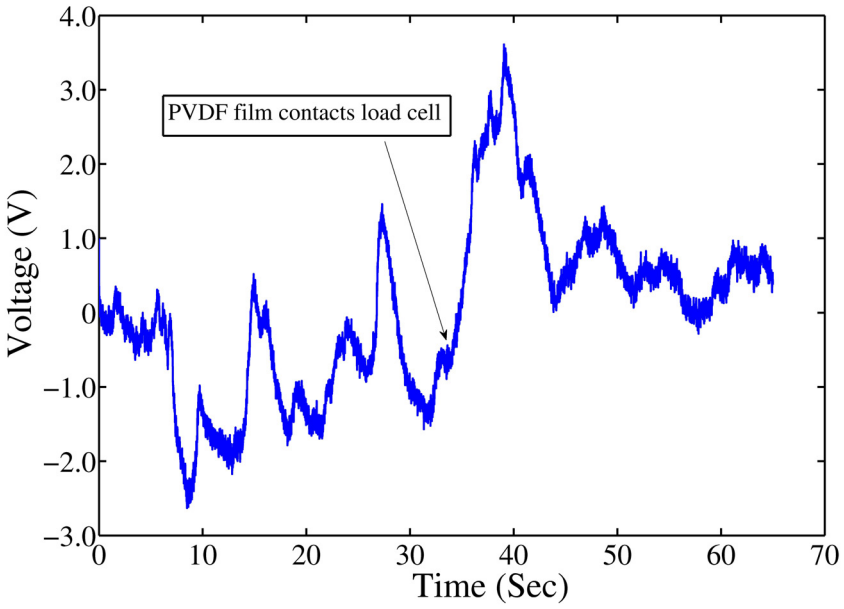

Figure 3.7. The signal to noise ratio is low for the PVDF sensor.

(a)

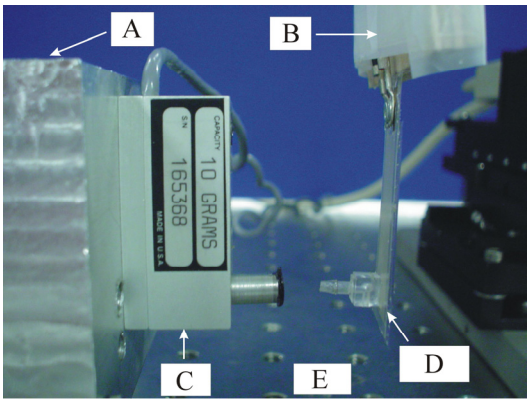

(b)

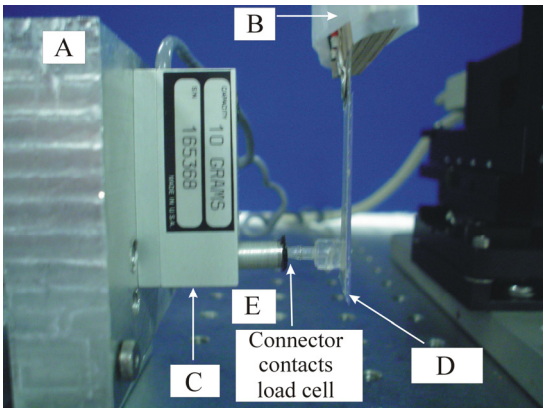

Figure 3.8 Overview of calibration set up with vibration isolation table (E)

A: Stationary platform, B: Movable platform, C: Load cell, and D: PVDF film

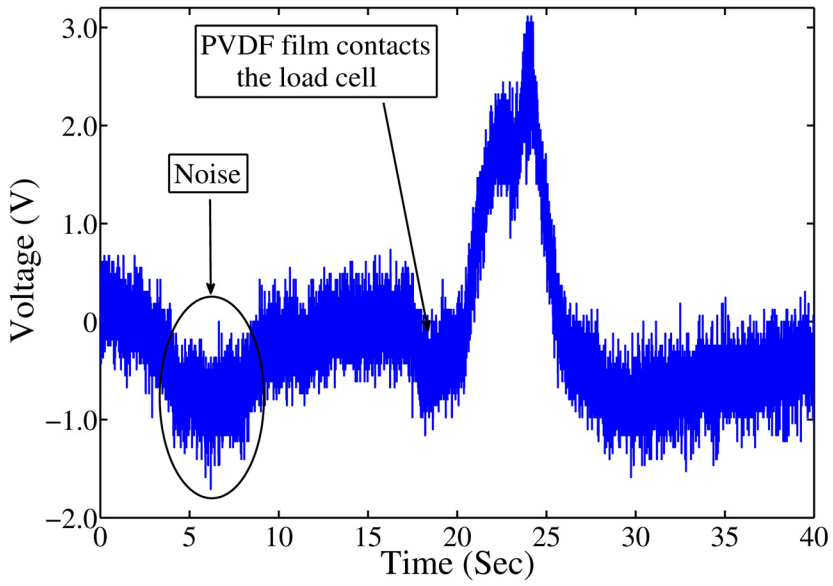

Figure 3.9. The voltage signal from the PVDF film. The ground vibrations were removed by vibration isolation table. However we still observed significant noise in the signal.

The noise observed in figures 3.5 and 3.7 may be due to external disturbances e.g. ground vibrations, hence we decided to use a vibration isolation table in our set up (figures 3.8). We repeated the calibration experiment and voltage signal is shown in figure 3.9. However we still observed significant noise in the signal. Piezoelectric sensors have a wide dynamic range and hence are sensitive to low frequency external disturbances. After repeated trials, we figured out that the noise observed in figure 3.9 was due to acoustic waves and hence we used an acoustic enclosure in our calibration set up (figure 3.10).

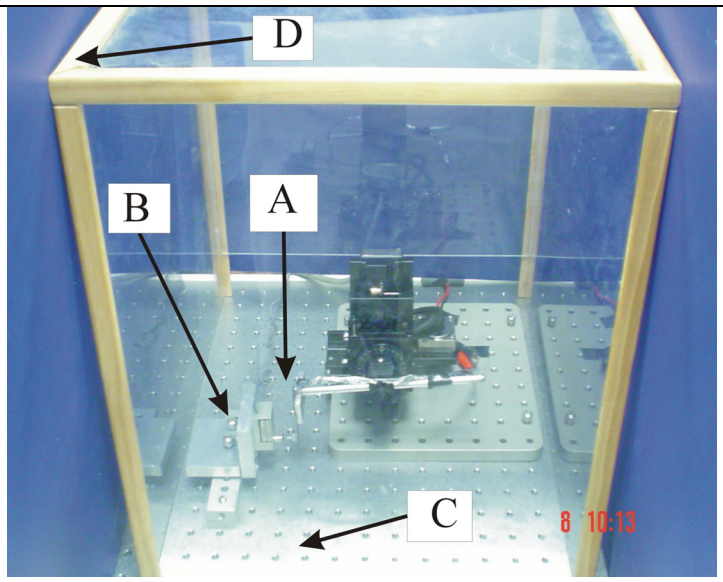

Figure 3.10. Overview of calibration set up with acoustic enclosure (D), vibration isolation table (C), load cell set up B) and the PVDF film (A)

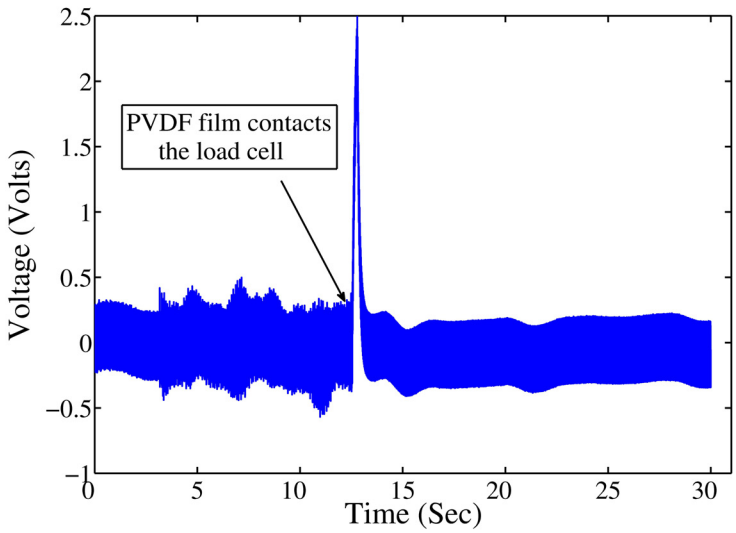

Figure 3.11. The output from the PVDF sensor has a high signal to noise ratio, upon reducing the external disturbances by a vibration isolation table and an acoustic enclosure.

During calibration, when the PVDF film contacted the load cell, the voltage signal ramped up ad has a high signal to noise ratio as shown in figure 3.11. The connector contacts the load cell at different velocities and range of distances, so the PVDF film bends depending on the distance traversed by the nanomanipulator. Due to different velocities and range of distances traveled by the PVDF film, the strain developed in the PVDF film will result in a generation of different voltage signals from the amplifier. We observed that the peak of the integrated voltage signal from the PVDF film corresponds to the peak of the force signal from the load cell as shown in figure 3.12.

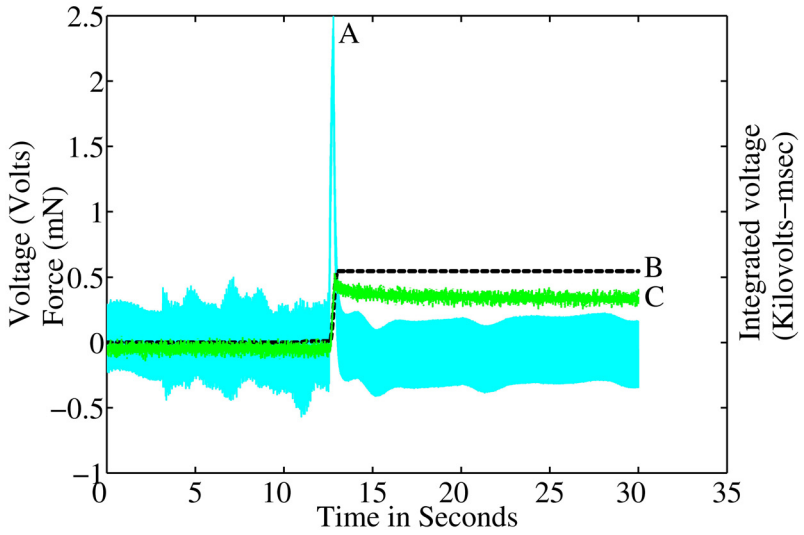

Figure 3.12. Plot showing the peaks of the voltage, the integrated voltage, and the force profile for a typical calibration measurement: A: Voltage signal from the PVDF film in volts; B: The integrated voltage signal from the PVDF film in kilovolts-sec; C: The force signal from the load cell in mN.

We performed several measurements to derive the experimental calibration curve shown in figure 3.13. The experimental calibration curve is given by:

$$F = 0.0007216 \int V_{out}\, dt + \ 0.00439 \qquad (3.10)$$

where, F: Force applied to the PVDF film in mN, $\int V_{out}\, dt$: Integrated voltage output from the PVDF film in volt-msec.

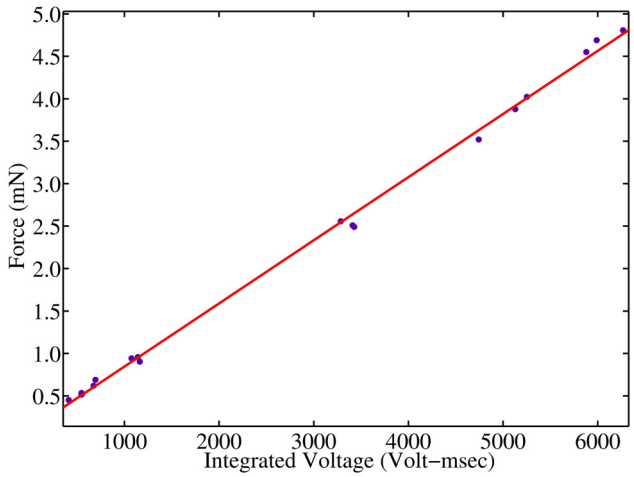

Figure 3.13. Calibration curve showing a linear relationship between the force measured by the load cell and the integrated voltage from the PVDF film.

A comparison of equations (3.9) and (3.10) shows that there is a linear relationship between the applied force and the corresponding integral of the voltage output from the charge amplifier. The offset in the experimental calibration curve could possibly be due to pyroelectric effects (they have not been considered in the derivation) as well the effect of acoustic waves and ground vibration (even though a vibration isolation table and an enclosure were used). The ground vibrations and acoustic waves cannot be completely eliminated from the experimental setup.

3.3 Haptic Feedback Interface for Salmon and Flying Fish Egg Cells

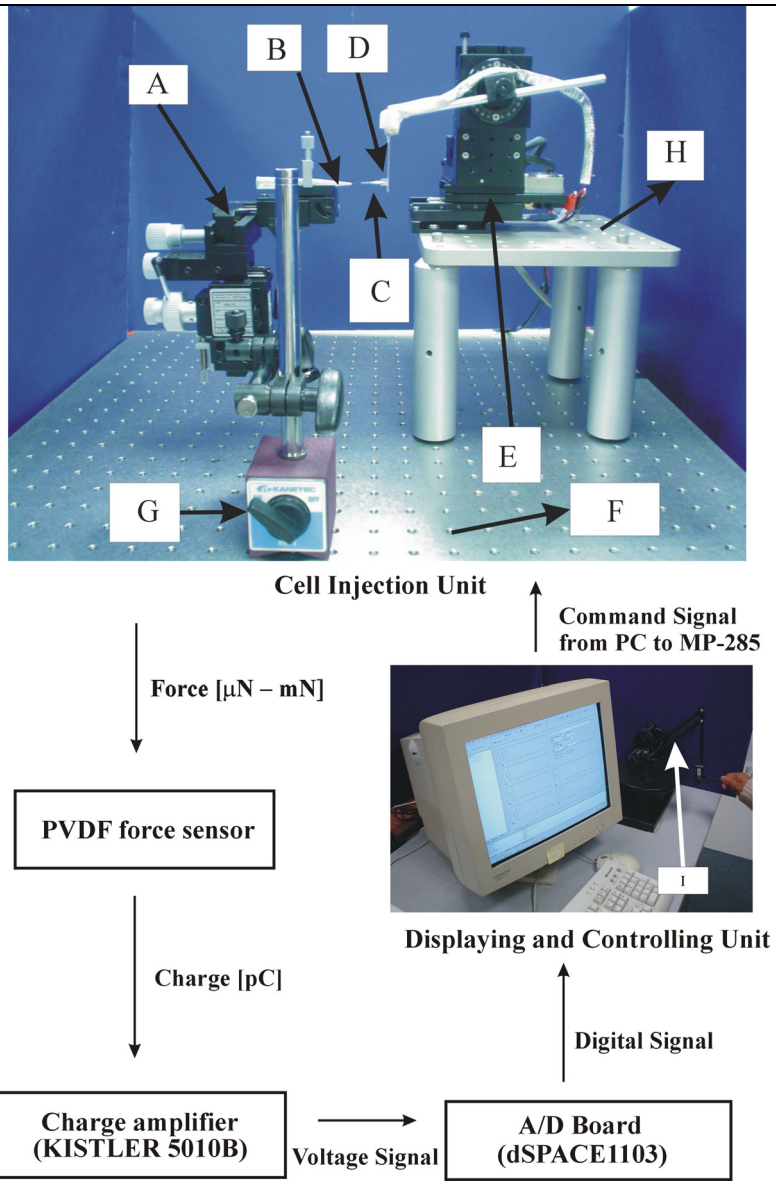

Figure 3.14. The experimental set up for injecting egg cells: A: MMJR-Manual manipulator; B: Holding pipette; C: Injecting pipette; D: PVDF film; E: MP-285 Nanomanipulator; F: Vibration isolation table; G: Magnetic base; H: Manipulator Stand; I: The PHANToM haptic interface.

We tested our force feedback interface for cell injection on two different types of egg cells, namely, salmon fish egg cell and flying fish egg cell. The experimental setup consisted of the PVDF film, nanomanipulator, micropipette (Tip ID: 5 μm) inserted into the hollow connector, and the PHANToM® haptic interface device (SensAble Technologies, Inc., Woburn, MA). A plastic micropipette holds the egg cells. The holding micropipette is mounted on to the MMJR, manual manipulator (World Precision Instruments, Inc., Sarasota, Florida) which has three degrees of freedom in x, y, and z-direction. The travel range is 37 mm in X-axis, 20 mm in Y-axis and 25 mm in Z-axis. The resolution is 0.1 mm in all three axes. The cell manipulation system has a total of six degrees of freedom (3 DOF for holding pipette and 3 DOF for the injection pipette) as shown in figure 3.14. A magnetic base is used for the positioning and holding of the manual manipulator. The whole set up is mounted on a vibration isolation table and covered by an enclosure (not shown in figure 3.14). The egg cells are sucked inside the holding pipette, which facilitate the penetration of the injection pipette into the egg cell.

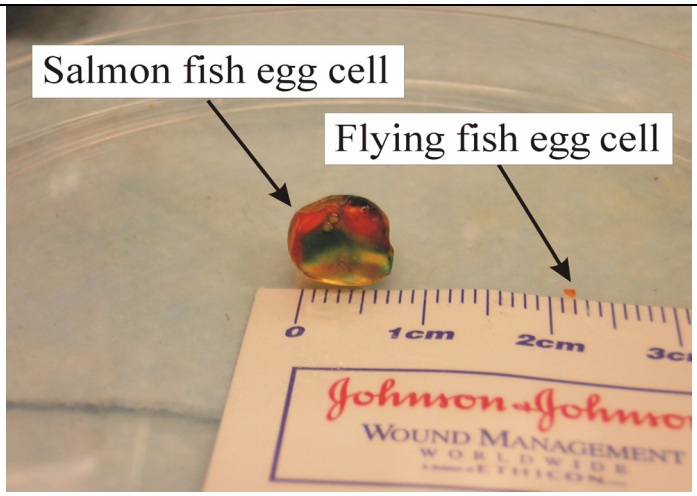

Figure 3.15. Comparison of salmon and flying fish egg cell.

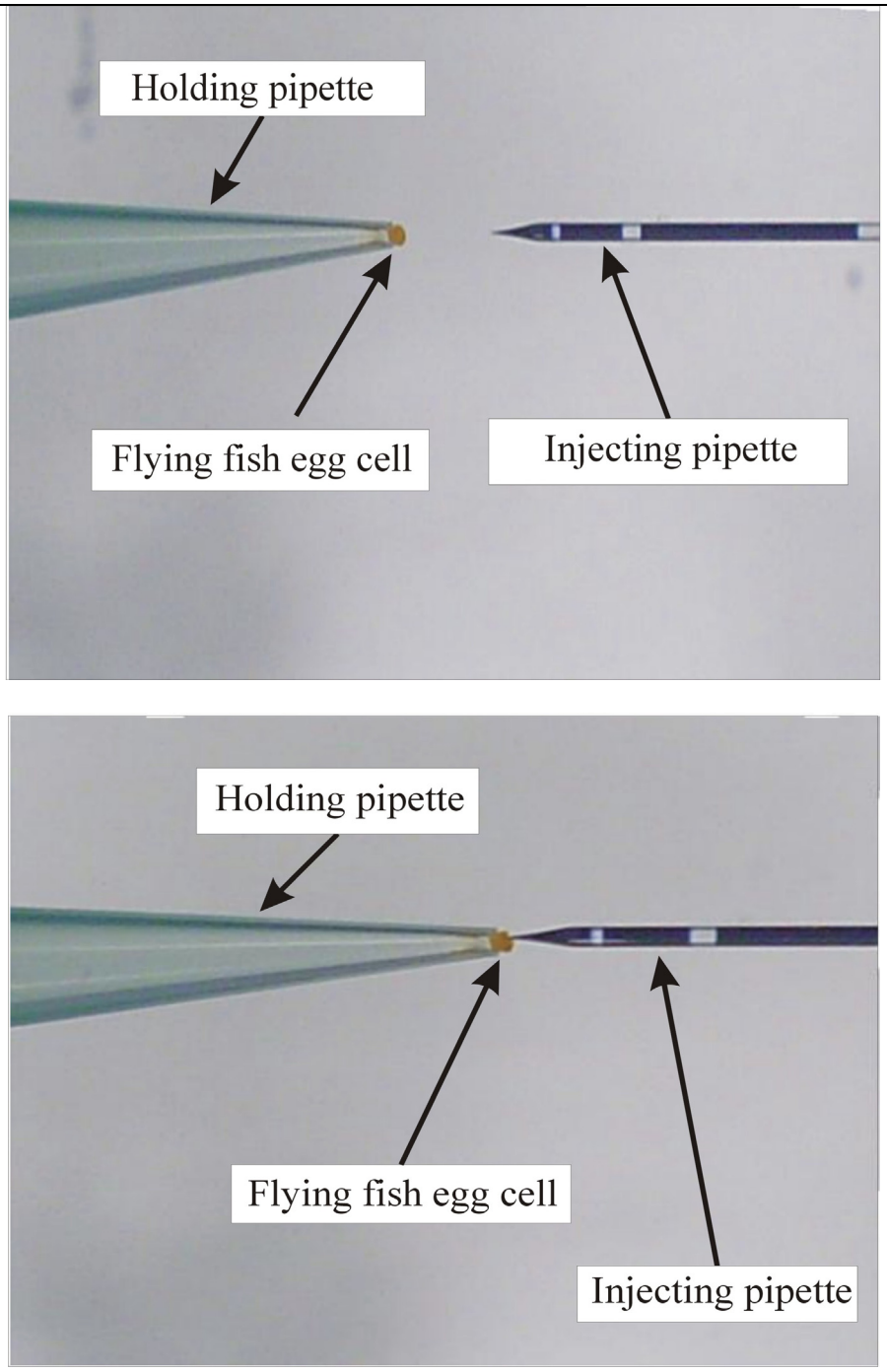

Figure 3.16. The figure on the top shows the injecting pipette approaching the flying fish egg cell and the figure on the bottom shows the injecting pipette penetrating into the egg cell.

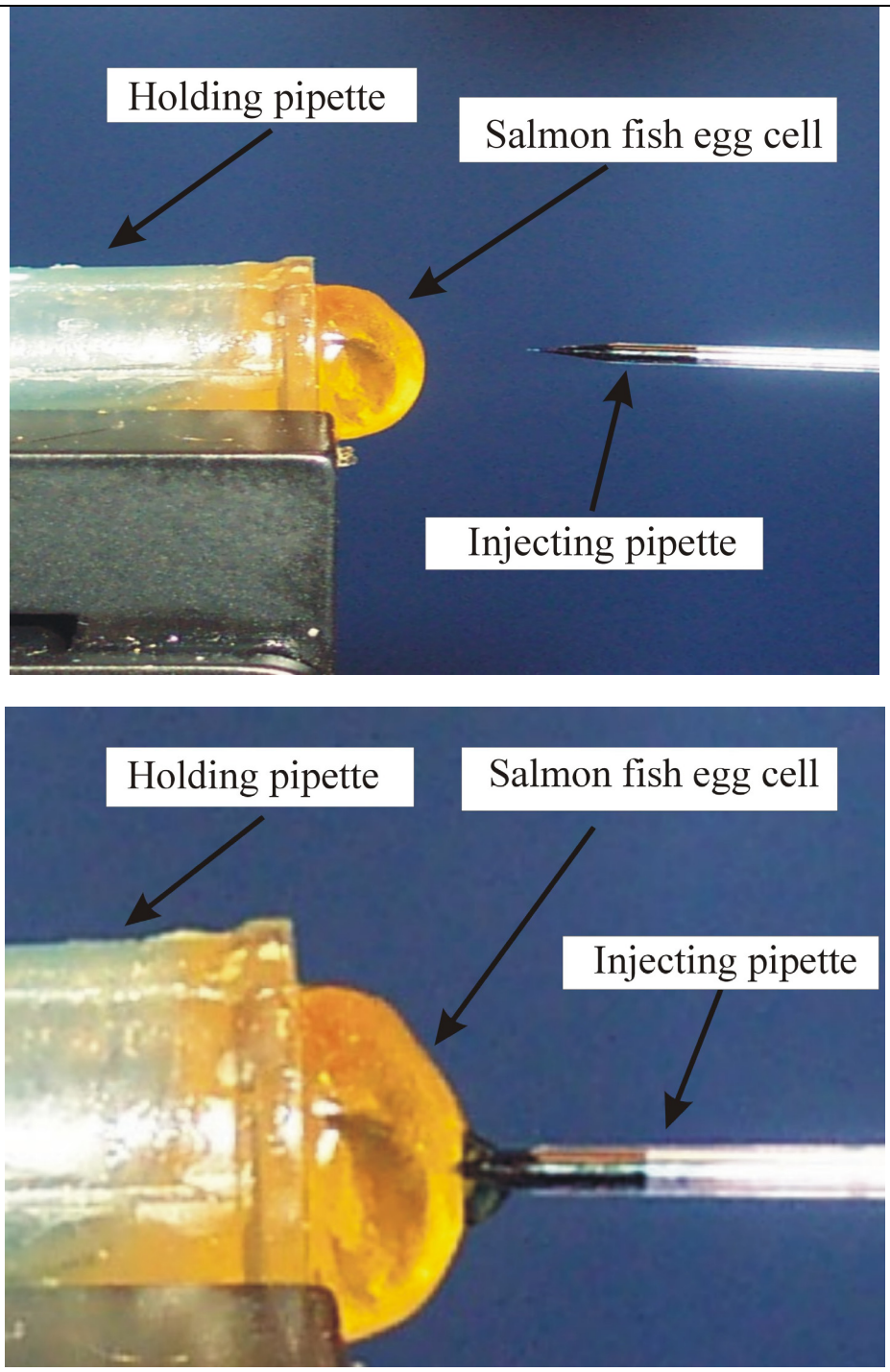

Figure 3.17. The figure on the top shows the injecting pipette approaching the salmon fish egg cell and the figure on the bottom shows the injecting pipette penetrating into the egg cell.

The diameter of salmon fish egg cell is around 4mm - 6mm and the diameter of the flying fish egg cell is around 700 µm – 1 mm as shown in figure 3.15. The velocity of the manipulator during injection is 120 µm/sec. Before performing the experiment the holding pipette is aligned with the injection pipette, which facilitates the injection pipette to penetrate into the egg. The injecting and holding pipette are aligned by controlling the 6 DOF of the cell manipulation system in such a manner that the tip of the injecting pipette contacts the center of the egg cell. While performing the experiment the injection pipette is moved towards the egg cell with the help of MP-285 nanomanipulator, where as the manual manipulator is held stationary. To track down the pipette tip it is filled with a dye as shown in figure 3.16. Visible light is used for illumination. Using light of different wavelengths, in particular lower wavelengths, may cause some physical damage to the cell. As the egg cells are transparent in nature, the dark colored dye can be seen when the pipette penetrates the egg cell as shown as shown in figures 3.16 and 3.17. There is no noticeable effect of the dye on the egg cells (non-living).

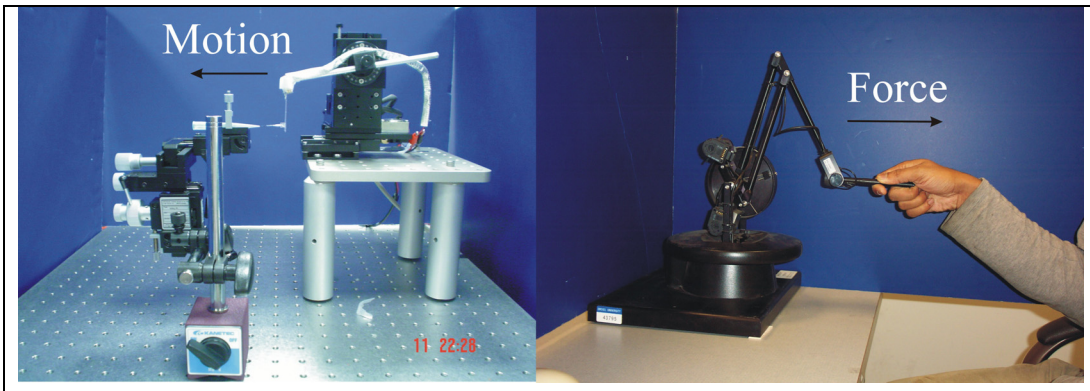

Figure 3.18. Force feedback is achieved in real time through the PHANToM.

Though the PHANToM is capable of providing force feedback along three principal directions, in our experimental setup, the force was felt only in the direction opposite to the motion of the pipette (see figure 3.18). The forces measured during cell injection are amplified and displayed to the user in real-time. As a result, the user can perceive the cell injection as an apparent drop in injection force after puncture.

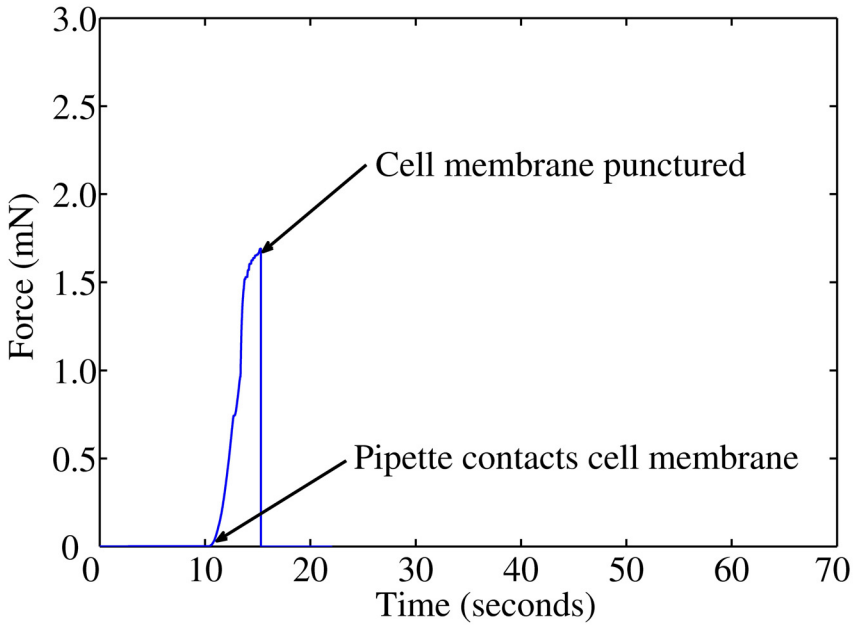

Figure 3.19. Variation of force with time during membrane puncture of a flying fish egg cell. The puncturing force was 1.69 mN.

The experiments were performed on 10 samples of each egg cell. From figure 3.18, it can be observed that there is a gradual increase in the force prior to puncture of the membrane. The maximum force is recorded when the cell membrane is punctured. From figure 3.19, the puncturing force for one of the flying fish egg cell was observed to be 1.69 mN. Based on 10 different samples of the flying fish egg cell, the

average puncturing force was found to be 1.6057 mN with a standard deviation of 0.33 mN. The puncturing force values obtained for injecting 10 flying fish egg cells is shown in figure 3.20.

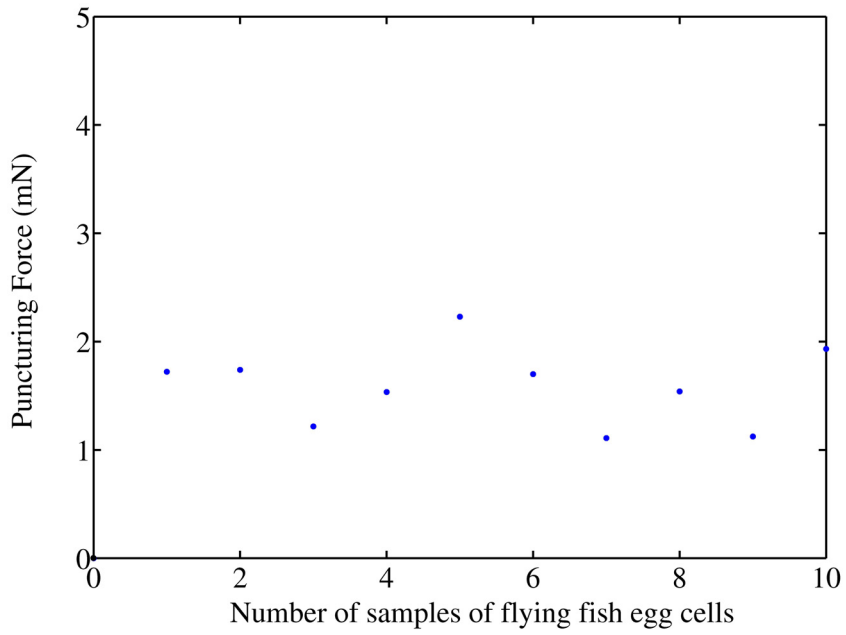

Figure 3.20. Variation of the puncturing force for 10 samples of flying fish egg cells. The average puncturing force was 1.6057 mN.

During each of these cell injections, force feedback was provided to the user through the PHANToM and the user was able to discern when the pipette penetrated the egg cell. Similarly the typical force profile obtained for puncturing the membrane of the salmon fish egg cell is shown in figure 3.21. The puncturing force for one of the salmon fish egg cell was observed to be 2.38 mN.

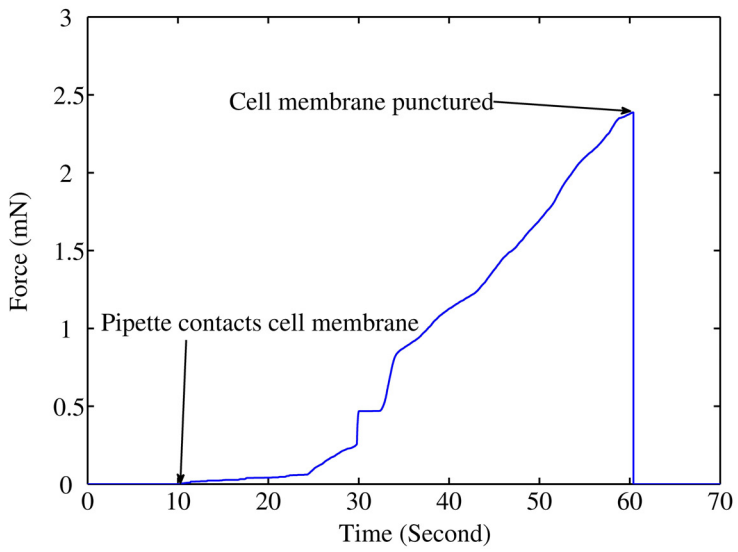

Figure 3.21. Variation of force with time during membrane puncture of a salmon fish egg cell. The puncturing force is 2.38 mN.

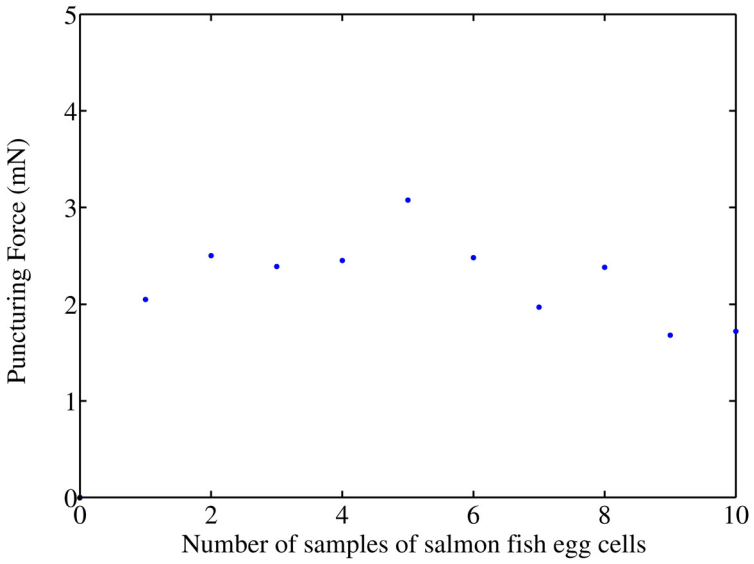

Figure 3.22. Variation of the puncturing force for 10 samples of salmon fish egg cells. The average puncturing force was 2.2694 mN.

In all the trials, we observed that the slope of the force vs. time curve was less steep for the salmon fish egg cell compared to the flying fish egg cell. This indicated that the salmon fish egg cell underwent more deformation than flying fish egg cell, before its membrane was punctured. The average force for puncturing the salmon fish egg cell for 10 different samples was 2.2694 mN with a standard deviation of 0.41 mN. The puncturing force values obtained for injecting 10 salmon fish egg cells are shown in figure 3.22. In all these experiments the measured forces were scaled by a factor of 200 when they were displayed to the user.

3.4 Haptic Feedback Interface for Zebrafish Egg Cells

We used the PVDF film (mentioned in the previous section) as a force sensor to measure the zebrafish egg cell injection forces. The biomanipulation system (see figure 3.23(a)) consists of a MP- 285 nanomanipulator forming the cell injection unit and a micromanipulator (Model: TransferMan NK2, Eppendorf, Inc., Westbury, NY) forming the cell holding unit. The nanomanipulator as well as the micromanipulator has 3-DOF each and the inverted microscope (Model: IX81, manufactured by Olympus, Inc., Center Valley, PA) has a 2-DOF stage for positioning the sample. The travel range for MP-285 nanomanipulator (computer controlled) is 25 mm along all three axes (X, Y & Z) with lowest resolution of 0.02 μm/step and highest resolution of 40 nm/step. The travel range for TransferMan NK2 micromanipulator (joystick controlled) is 20 mm in all three axes with a resolution of 40 nm per step. Figure 3.23(b) shows the magnified view of the cell injection system.

(a)

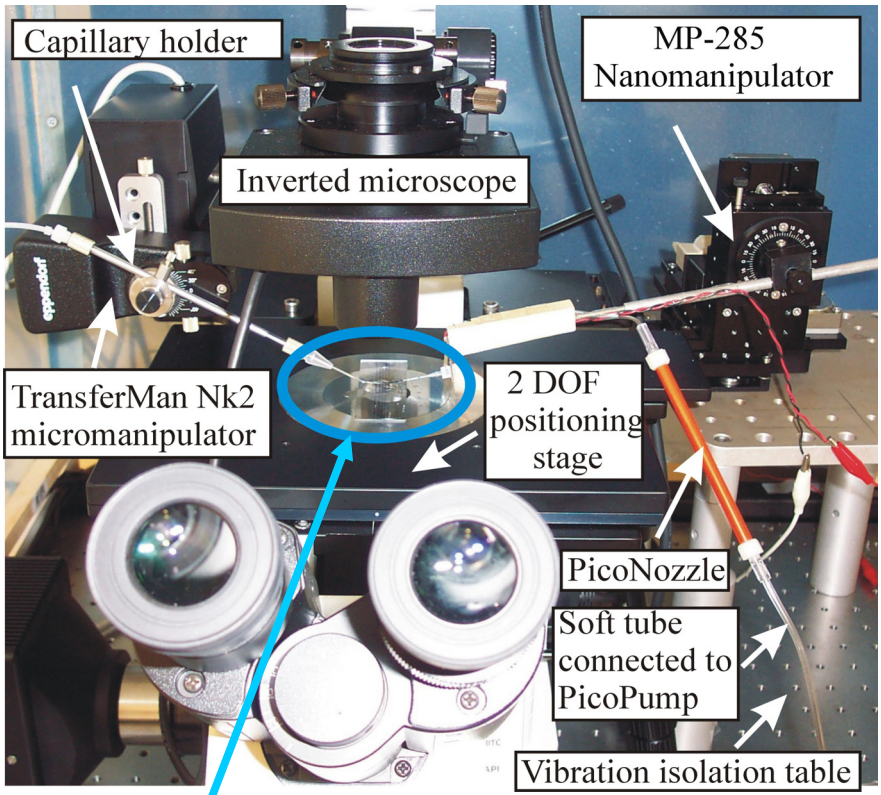

(b)

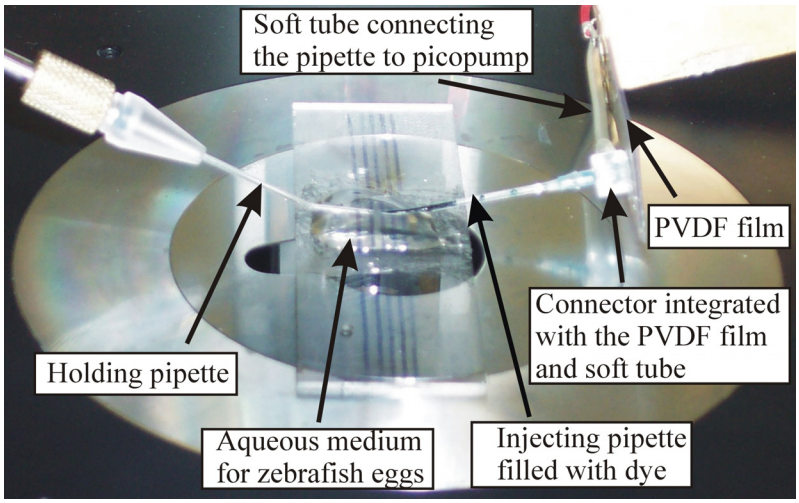

Figure 3.23. (a) Experimental system for injecting zebrafish egg cells. (b) Magnified view of the cell injection system.

As shown in figure 3.24, the glass micropipette is integrated onto the PVDF film with the help of a connector. This set up allows easy removal and replacement of the micropipette if its tip (5 µm ID) gets damaged during micromanipulation. The injecting pipette is connected to a pneumatic PicoPump (Model: PV830, World Precision Instruments, Inc., Sarasota, Florida) for the purpose of injecting blue dye into the cell (refer to figure 3.25). A manual piston pump (Model: CellTram Air, Eppendorf, Inc., Westbury, NY) is used to apply suction for reliable holding of suspended zebrafish egg cells.

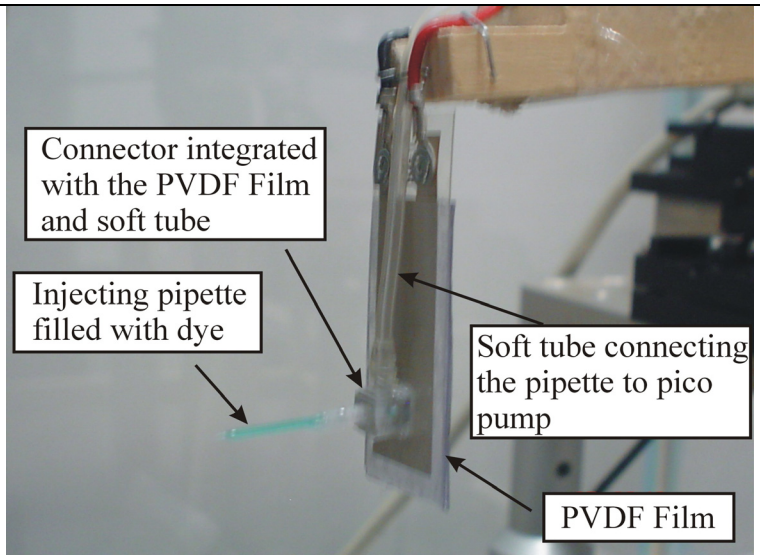

Figure 3.24. Connector integrated with the PVDF film and soft tube

Figure 3.25. The pneumatic PicoPump regulates air pressure for injecting dye into cell.

3.4.1 Experimental calibration for the force sensor

The previous section described the calibration set up for the force sensor with the load cell. The same calibration curve was re-plotted for forces less than 1 mN as shown in figure 3.26. Experimental calibration shows that the sensitivity of the PVDF sensor is 1.3858 volt-msec/ μN. The linearity of the sensor is 2% of the rated peak output (850 μN), as shown in figure 3.26.

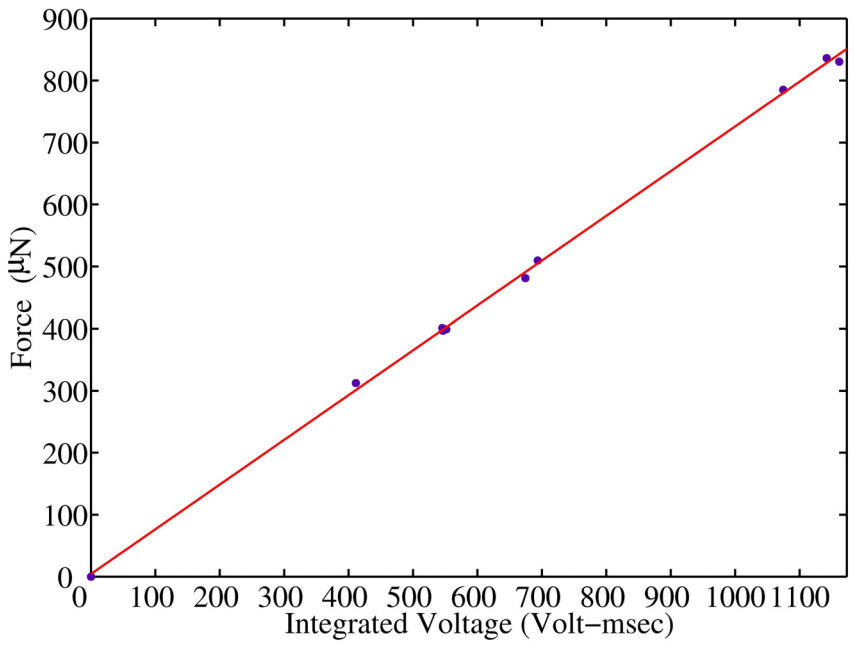

Figure 3.26. Calibration curve showing a linear relationship between the force measured by the load cell and the integrated voltage from the PVDF film.

The hysteresis plot of the PVDF sensor is shown in figure 3.27. Hence we observe that the PVDF sensor has negligible hysteresis. During the experiments, the velocity of the manipulator was 120 μm. The calibration experiments and the experiments

with zebrafish egg cells were performed at room temperature (~25^{0}C) which lies in the operating temperature range of the PVDF film (-40^{0}C to 100^{0}C). Any pyroelectric effects have not been considered in the calibration experiments, since the drift was very minimal over several calibration trials and we also do not have the necessary experimental facility to be able to make these thermal drift measurements. The minimal offset in the experimental calibration curve (equation 10) could possibly be due to pyroelectric effects as well as the effect of acoustic waves and ground vibration (even though a vibration isolation table and an enclosure were used). The ground vibrations and acoustic waves cannot be completely eliminated from the experimental setup. The cell injection system is integrated with vision and haptic interface as shown in figure 3.28.

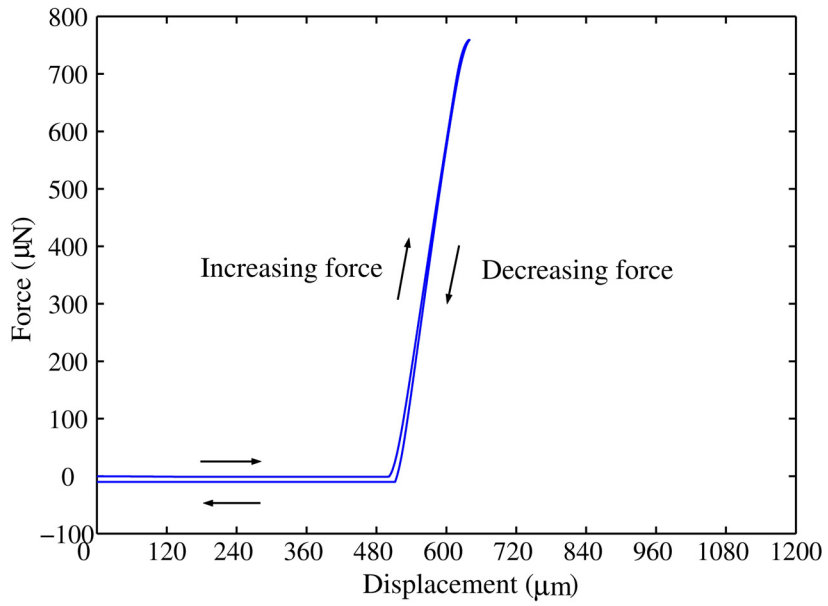

Figure 3.27. Hysteresis loop of the PVDF sensor.

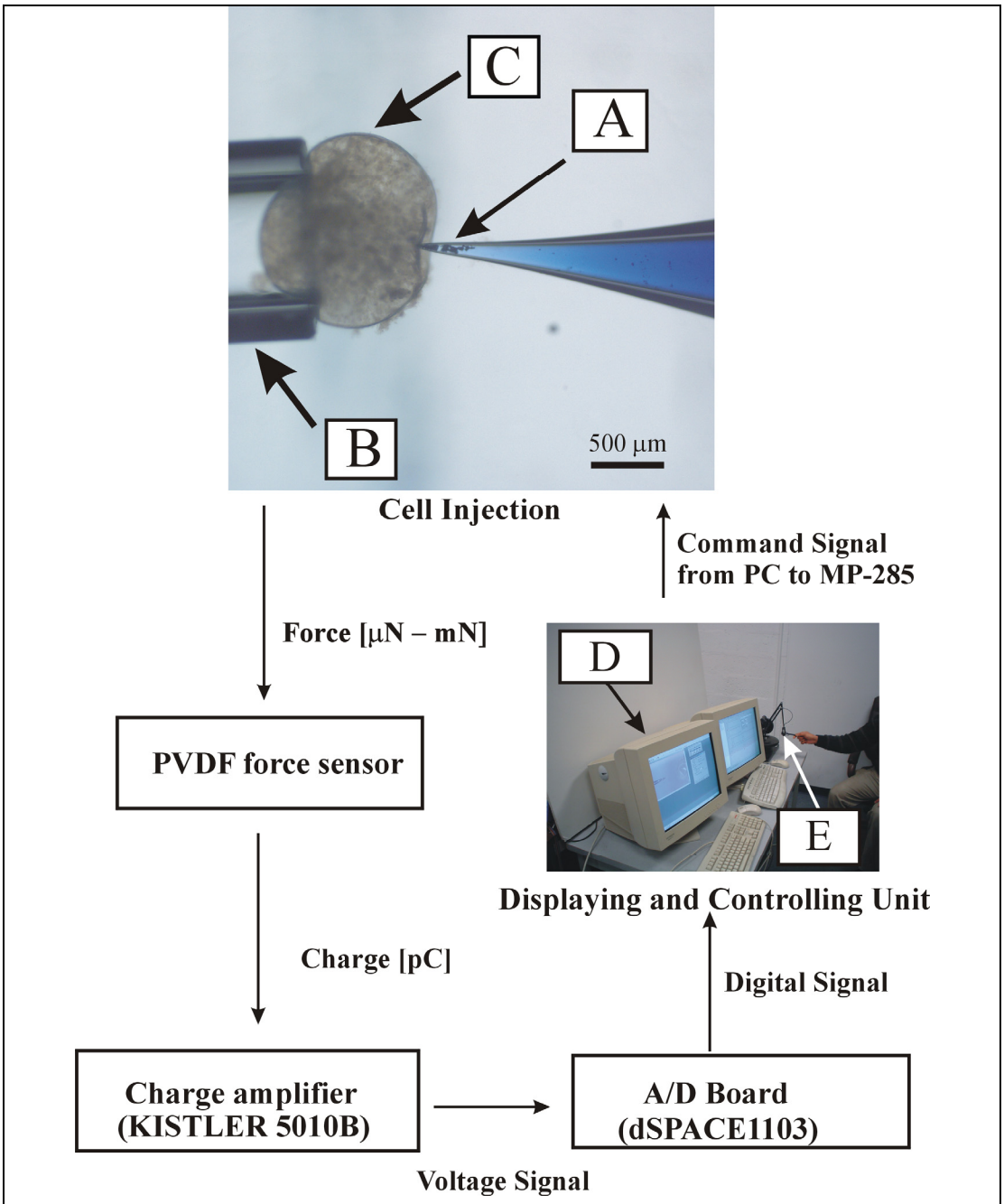

Figure 3.28. The Cell injection system with vision and force feedback interface. A: Injecting pipette, B: Holding pipette, C: Zebrafish egg cell, D: Visual Interface, E: PHANToM haptic interface.

3.4.2 Zebrafish egg cell preparation

Zebrafish (Danio rerio) were selected as an animal model because of their easily accessible eggs, short generation time, high fecundity, rapid development, external fertilization and translucent embryos [164]. Zebrafish egg cell are sensitive to mutagens and have low spontaneous malignancy rate, which make it an ideal vertebrate animal model for understanding carcinogenesis, genetic functional screening, and drug discovery. Changes in this organism can be observed *in vivo* over time and unlike mouse models, do not require multipoint sacrifice. Moreover, they develop solid organ malignancies analogous to human tumors. Zebrafish were obtained from "Scientific Hatcheries" (Huntington Beach, CA) and were maintained under standard conditions. The following standard procedures were followed to maintain zebrafish in the laboratory:

- After arrival of adult female fish in the laboratory, they were maintained in 10 gallon aquaria. 25 fish were maintained per aquarium.
- The fish were maintained in tap water at 25 – 28°C. The temperature of the water was monitored daily.
- The pH of the water was maintained at 6.5 – 7.8 and was monitored twice per week.
- Desired bright illumination (14/10 hour day night cycle) was maintained with lamp and timer placed on aquaria.
- The aquaria were maintained at optimal hygienic conditions and the fish were fed twice a day.

- Sick fish were separated as soon as possible to maintain healthy colony in the aquaria. The sick fish were euthanized with immersion in tricane solution.

Zebrafish egg harvesting is a very short procedure and it causes minimum distress even if it is performed without anesthesia. Adult female zebra fish were caught and immersed in beaker containing 100 ml of aquarium water and 4.2 ml of 0.2 % tricaine solution for 5-10 seconds. After confirming anesthesia, fish were removed and placed in a petri dish where eggs were expressed by gentle compression. After getting eggs, the zebrafish were placed in a recovery tank for 10- 20 minute. Recovery from anesthesia was confirmed by the movement of gills. After recovery, the zebrafish were placed back in the aquaria. The fish were marked (sharpie marker) with the date and time of egg harvest. Freshly harvested eggs were used for each component of the experiment. The diameter of an egg is approximately 600 μm – 1 mm.

3.5 Evaluation of force feedback interface

We were interested in evaluating the role of force feedback in cell injection. The outcome of a transgenesis task depends not only on successful delivery of the desired gene into the cell but also on the successful integration of the genetic material into the genome within the nucleus as a stable transfection. Successful delivery of desired material into the cytoplasm is itself a challenging task. To judge the outcome of the injection process (success or failure), we chose to inject trypan blue dye in zebrafish egg cell. We chose to inject the dye and not a genetic material or fertilize the egg because genetic modification and change in the cell structure depends on various

other biochemical factors once the genetic material is placed within the cytoplasm. Since in mechanical manipulation techniques, injection of the membrane and the consequent integrity of the membrane are crucial, we focused on human factors studies on evaluating the membrane integrity after injection using only vision feedback and vision + force feedback. We created two different scenarios in our experiment: (a) S_1: the subject was prohibited from seeing the dye being injected and (b) S_2: the subject was allowed to see the dye being injected. In a practical situation, the first scenario (S_1) corresponds to injecting non-transparent cells whereby it is impossible to ascertain the presence of the injected material (colored or colorless) in the cell and the second scenario (S_2) would correspond to injecting transparent cells (zebrafish eggs, for example) with a colored dye. Since we are working with only one type of egg, namely, zebrafish, which are transparent, we created experimental conditions for scenarios S_1 and S_2 by differentiating whether the subject cannot see (S_1) or can see (S_2) the injected colored dye within the cell. Since in conventional biomanipulation tasks, the cell may or may not be transparent, our experimental scenarios S_1 and S_2 described above cover the most general cases to study the effect of force feedback in biomanipulation tasks. We had 40 human subjects perform the experiments with vision (V) feedback alone and combined vision + force (V+F) feedback, with 20 subjects allocated for S_1 and 20 subjects allocated for S_2. All the subjects had no previous experience in cell injection tasks. Each subject performed 5 trials with vision (V) feedback alone and 5 trials with vision + force (V+F) feedback. Details for both the (V) and (V+F) feedback protocol are presented in the following subsections.

3.5.1 Vision (V) Feedback Protocol

The first part of the experiment consisted of only vision feedback to perform the cell injection task. The subject was able to view injecting pipette through the eyepiece of the inverted microscope. An operator applied suction and fixed the zebrafish egg cell. At this moment, center of the egg was not aligned with the tip of the injecting pipette. With the help of the joystick (TransferMan NK2) the subject controlled the movement of the holding pipette and aligned the egg with the tip of injecting pipette. The egg and the tip of injecting pipette were maintained at a fixed distance apart by the subject. For the first test, a practice session was given to familiarize the subject with the alignment task. The subject was then able to view the alignment on a video screen and moved the injecting pipette forward with the help of computer controlled nanomanipulator. The subject observed the injecting pipette penetrating the egg membrane on a video screen and stopped the motion of injecting pipette when he/she was confident that pipette has penetrated the cell membrane. At this moment, trypan blue dye was injected by the operator by depressing the foot pedal switch. The injection was deemed successful, when the dye remained inside the cell and the cell did not collapse on removing the pipette. Since the dye is blue in color, it was straight forward to determine if the dye remained inside the cell after injection. The volume of dye injected was approximately 0.001 times the volume of the egg cell. Completion time for the injection task (including alignment task) was recorded. The process was repeated for five trials for each scenario S_1 and S_2.

3.5.2 Vision and Force (V + F) Feedback Protocol

The second test was conducted by using both vision and force feedback to perform the cell injection task. This test was performed in the same way as the vision test, with the addition of force feedback. For this experiment the subject used the PHANToM haptic interface device by holding its stylus. The forces were amplified by a factor of 800. The direction of the force feedback was horizontal and was acting towards the subject. The operator controlled the movement of the injecting pipette with the help of computer controlled nanomanipulator. If the subject contacted the cell membrane and pressed against it, he/she would perceive an apparent increase in force followed by a drop in force when the membrane was punctured. A typical force profile for cell membrane penetration is shown in figure 3.29.

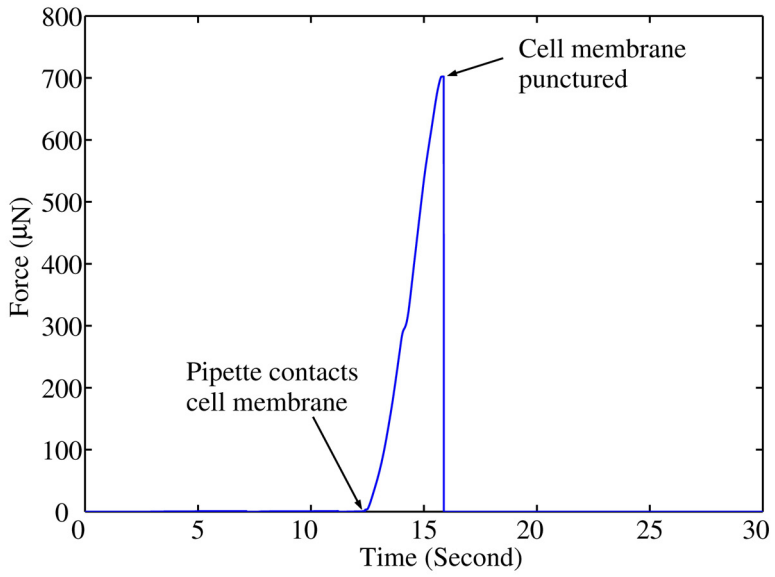

Figure 3.29. Variation of force with time during membrane puncture of a zebrafish egg cell. The puncturing fore was 700 μN.

During cell injection, the PVDF film is subjected to a force which increases with time until the cell membrane is punctured. After feeling the drop in force, the subject communicated to the operator to stop the motion of the injecting pipette. The operator injected trypan blue dye after the subject confirmed that the cell membrane was punctured. The criteria mentioned in the vision test were used to judge the outcome of the injection process. Completion time for the injection task (including alignment task) was recorded. The process was repeated for five trials for each scenario S_1 and S_2.

3.6 Statistical Analysis

The experiment was performed by 40 subjects (20 subjects for each scenario S_1 and S_2) for a total of 400 trials (5 trials each for V and V+F; hence 10 trials by each subject). The data were collected in a qualitative fashion with cell injections characterized as either "success" or "failure" and denoted by a value 1 or 0 respectively since trypan blue dye is easily observed under the microscope. The data were then analyzed using a non-parametric equivalent of the paired t-test i.e. Wilcoxon test. The test generates a p-value (probability) for the null hypothesis (H_0) and thus a probability for the research hypothesis (H_1) to be tested. The lower the p-value, the smaller the probability for the null hypothesis to be true and consequently higher is the probability that there is a significant statistical difference between the data sets (or the research hypothesis H_1 is true). The level of significance (α-value) for our statistical analysis was chosen to be 0.05, meaning that our research hypothesis would be considered true if $p < \alpha$.

3.6.1 Results

We performed the experiments to test the validity of our research hypothesis, namely, providing vision + force feedback simultaneously leads to higher success rate in cell injection task than only vision feedback ((V + F) > V). The ">" sign denotes "is better than" in the hypothesis. Vision feedback alone was tested before combined vision + force feedback because of the presence of more than one sensory cue. If the above approach is not followed, the subjects may link the drop in force to the visual cue of cell membrane puncture and that may contribute to a learning effect. The trials were, thus, presented in the following order: vision feedback alone followed by vision + force feedback.

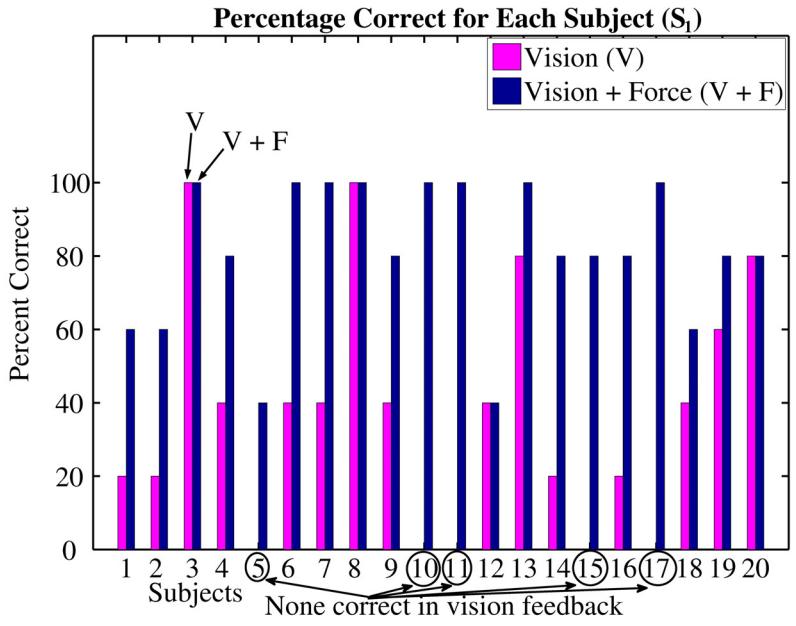

Figure 3.30 The percentage of successful cell injection for each individual using (V) and (V+F) feedback for S_1 where the subject was not allowed to see the dye being injected.

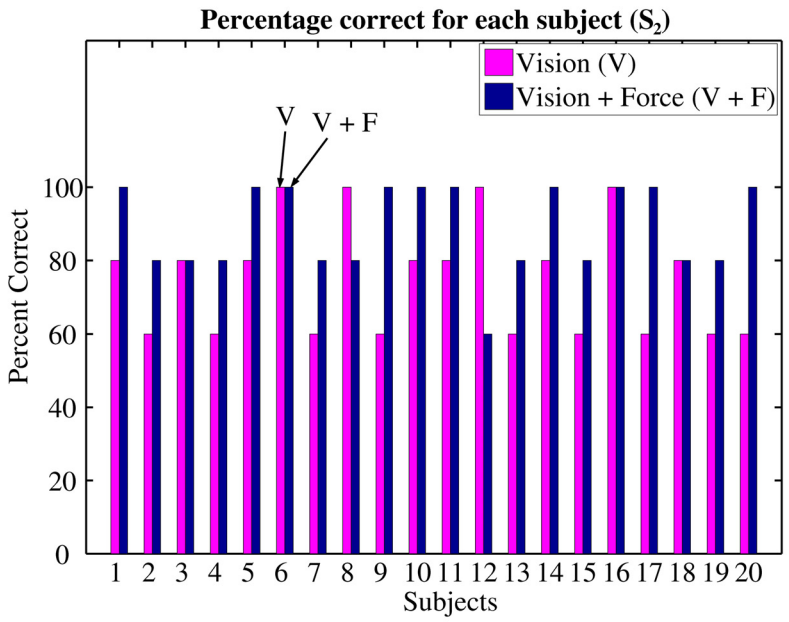

Figure 3.31. The percentage of successful cell injection for each individual using (V) and (V+F) feedback for S_2 where the subject was allowed to see the dye being injected.

The individual results for each subject performing the cell injection task in each of the 2 methods (V and V + F) for two different scenarios, S_1 and S_2, are shown in figure 3.30 and 3.31 respectively based on the research protocol. As seen from the figures, the outcome of cell injection with combined vision + force feedback is superior to vision feedback alone for each subject. The effect of learning is shown in figure 3.33 (S_2). As observed from the figures, there is a significant learning effect using vision feedback in S_2 compared to using combined vision + force feedback. There was no learning effect observed in S_1 for both V and V + F feedback. We have incorporated the learning phase data of the subjects in our analysis.

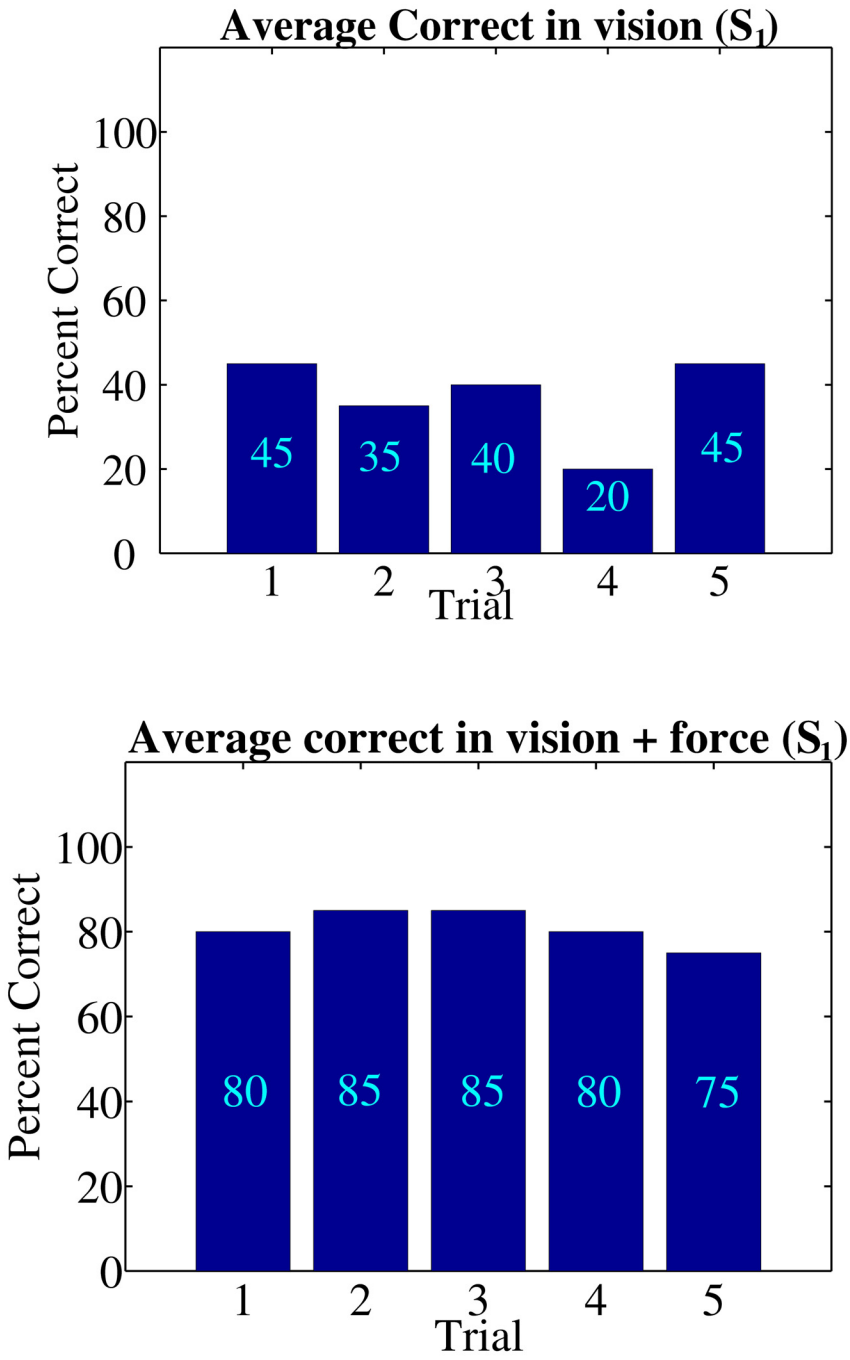

Figure 3.32. Percentage of successful injections for all five trials using only vision feedback and using combined vision + force feedback for S_1 where the subject was not allowed to see the dye being injected.

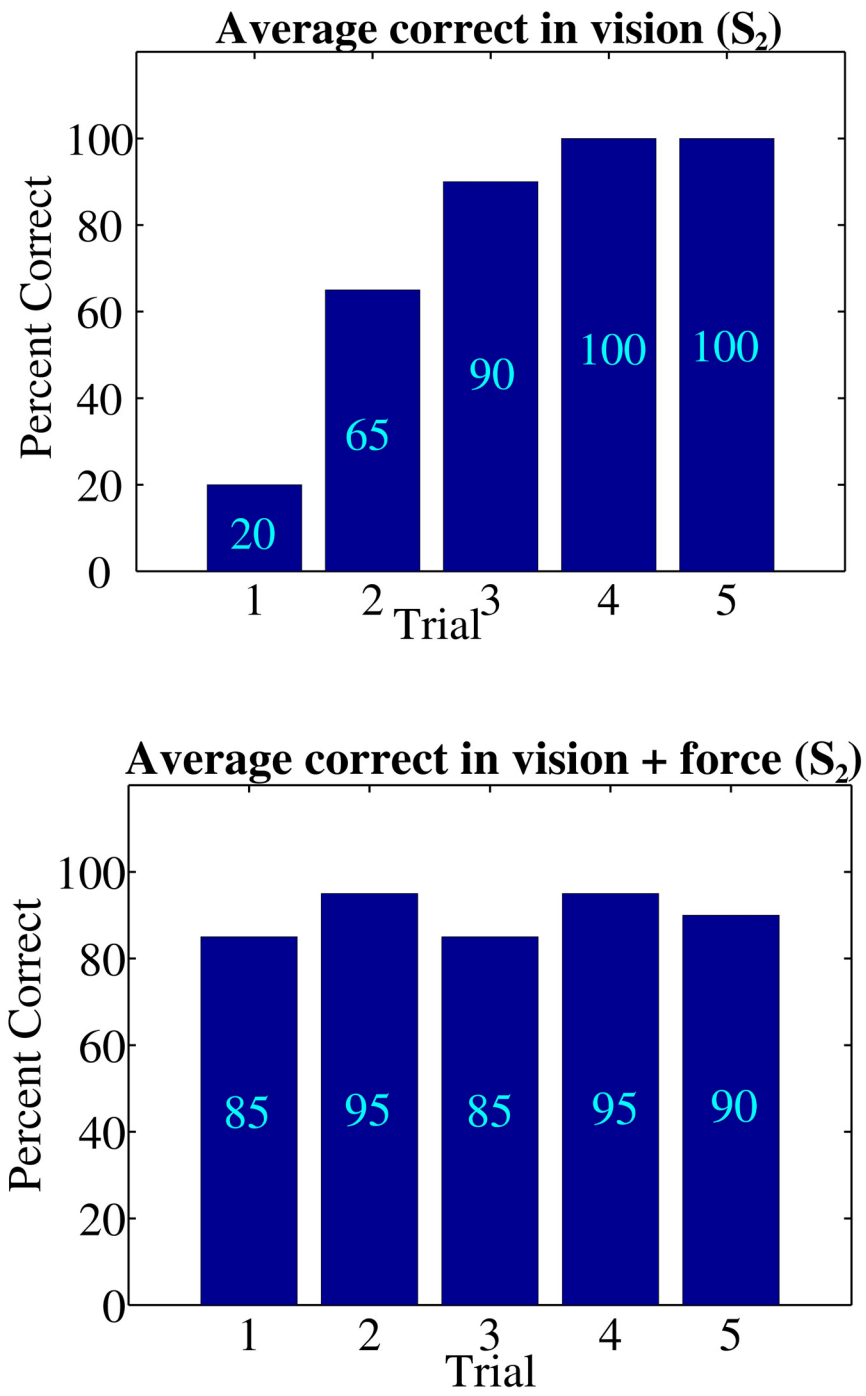

Figure 3.33. Percentage of successful injections for all five trials using only vision feedback and using combined vision + force feedback for S_1 where the subject was not allowed to see the dye being injected.

(a)

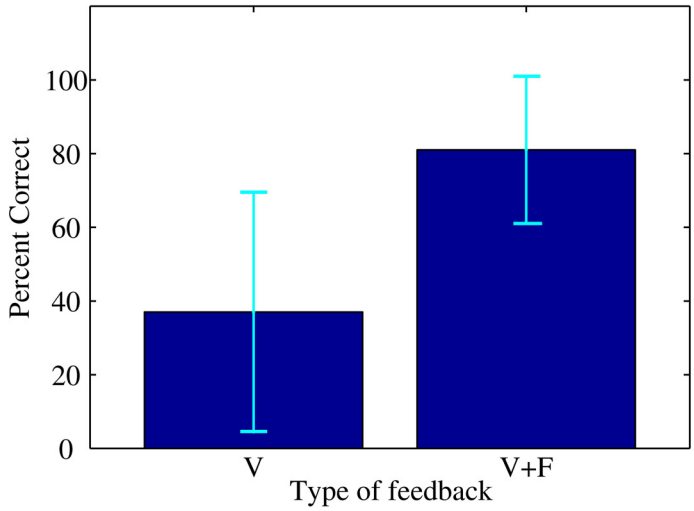

(b)

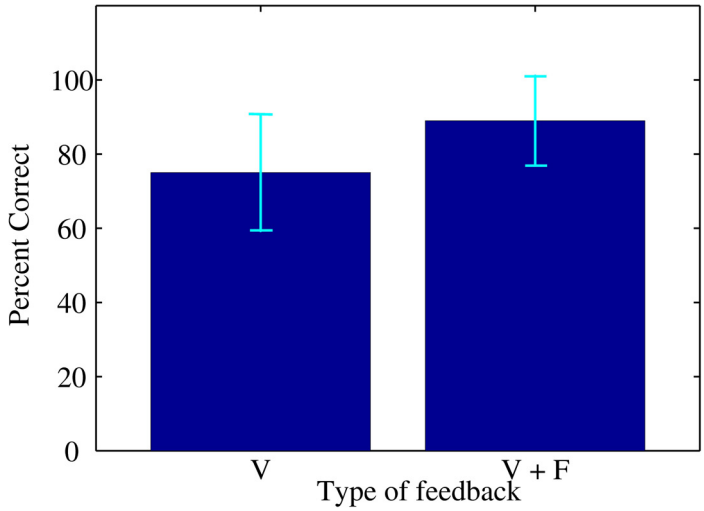

Figure 3.34. In two experimental scenarios, S_1 and S_2, the percentage of successful cell injection for all 20 subjects. (a) For S_1: Average success using only vision feedback (37%) and vision + force (V + F) feedback (81%). (b) For S_2: Average success using only vision feedback (75%) and vision + force (V + F) feedback (89%).

(a) S_1

Trial	p value
1	**0.017***
2	**0.001***
3	**0.0065***
4	**0.0005***
5	**0.030***

Average success	**< 0.0001***

(b) S_2

Trial	p-value
1	**0.0005***
2	**0.017***
3	0.32
4	0.15
5	0.07

Average success	**0.005***

Table 3.1. The p-value generated when comparing the two data sets (V & V+F) for each trial and average success for: a) S_1 and b) S_2 (* indicates $p < \alpha$, where $\alpha = 0.05$)

From figure 3.33, we observe that success with vision + force (V+F) feedback is less than vision (V) feedback for trials 3, 4, and 5 in S_2. One of the reasons for such observation could be that the subject was not able to react to the force feedback in time and stop the movement of the pipette. This might have lead to the collapse of the cell on removing the pipette, even though the trypan blue dye remained inside the cell. Thus, the injection task was deemed unsuccessful based on the criteria mentioned in the vision feedback protocol (section 3.5.1). Overall the average success for S_1 and S_2 is shown in figure 3.34. Paired t-test was performed to evaluate whether

there was significant difference in each trial between 2 data sets (V and V + F) for different scenarios S_1 and S_2. Table 3.1 shows the p-value generated when comparing the data sets for each trial and average success, for scenarios S_1 and S_2. The p-value was less than α-value (0.05) for all trials in S_1 and for trials 1 & 2 in S_2. Thus comparing the 2 data sets (V & V+F) in S_1 for each trial and in S_2 for trials 1 & 2, there exists a probability of greater than 95%, that there was a significant difference between the two data sets. There was no significant difference when comparing the data sets for trials 3, 4 & 5 in S_2, which shows that the subjects had a learning effect. The p-value obtained when comparing the average success for the two data sets for S_1 and S_2 was less than 0.0001 and equal to 0.005 respectively, leading to a probability of greater than 99.95 % that there was a significant difference between the data sets. Hence, there was a significant improvement in success rate using combined vision + force feedback compared to using vision feedback alone for S_1 as compared to S_2. Also there is a large standard deviation in vision feedback alone for S_1 as compared to S_2. Thus force feedback plays a major role in improving the success rate while injecting non transparent egg cells with a color/colorless dye or injecting transparent egg cells with colored material (trypan blue dye). Figure 3.35 shows one of the injection tests which was unsuccessful and figure 3.36 shows one of the injection tests which was successful based on the feedback protocol. In most of the unsuccessful cell injection tasks the subjects perceived that they had penetrated the cell membrane while in reality they had not. Obviously the range of pipette movement by the subject cannot be very large since that could lead to cell rupture or the pipette reaching the other end of the cell membrane. The obvious advantage of force feedback is the

perceived drop in injection force after the membrane is punctured, which resulted in a successful cell injection task.

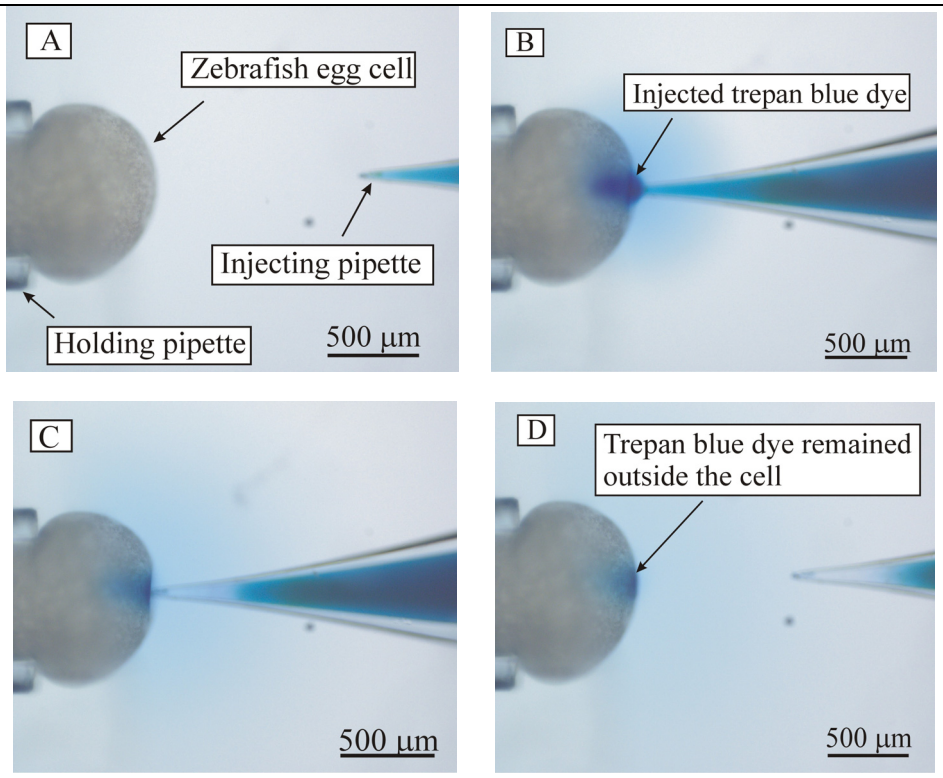

Figure 3.35. Example of an unsuccessful injection of zebrafish egg cell.

(A) The injecting pipette approaching the cell.

(B) The subject stopped the forward motion of the pipette being certain that the cell membrane is punctured, at this moment trypan blue dye was injected into the cell.

(C) The pipette being withdrawn.

(D) The trypan blue dye remained outside the cell.

The average completion time taken by each subject to perform experiments with V and V+F feedback for S_1 and S_2 scenarios is shown in figure 3.37. As seen from the

figure there was no significant difference in the completion time for each subject in V and V+F feedback. However there was a significant variation in completion time across subjects.

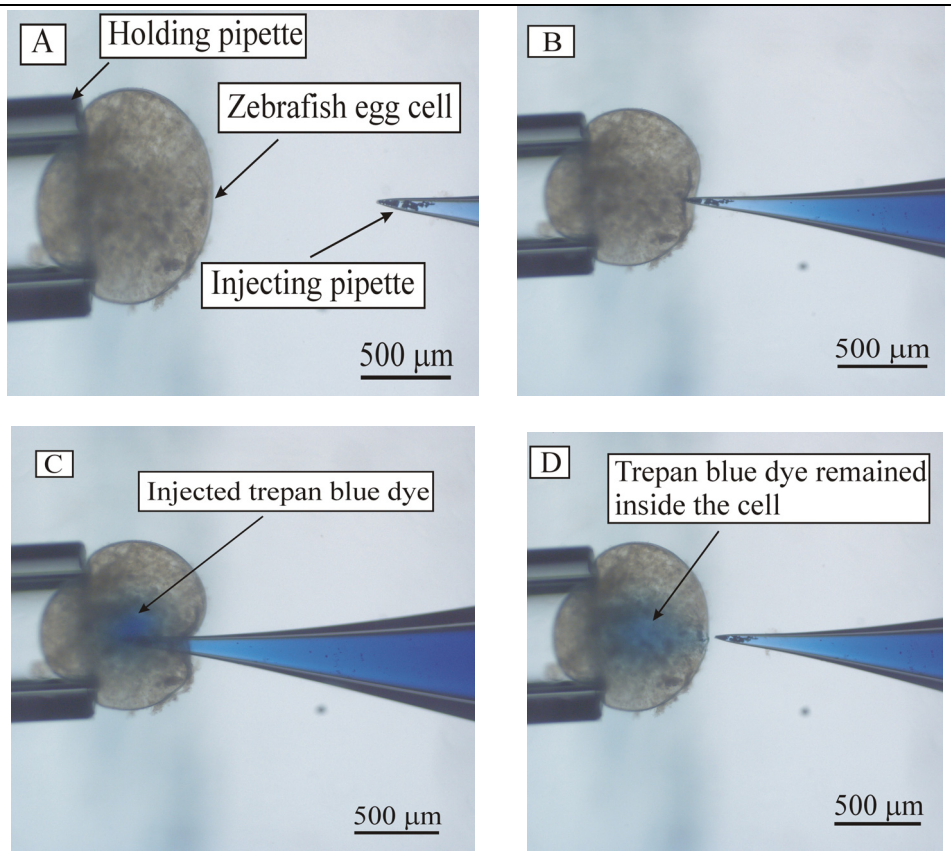

Figure 3.36. Example of a successful injection of zebrafish egg cell.

(A) The injecting pipette approaching the cell.

(B) The injecting pipette in contact with the cell membrane.

(C) The subject stopped the motion of the pipette when perceiving an apparent drop in force; at this moment trypan blue dye was injected into the cell.

(D) The trypan blue dye remained inside the cell.

(a)

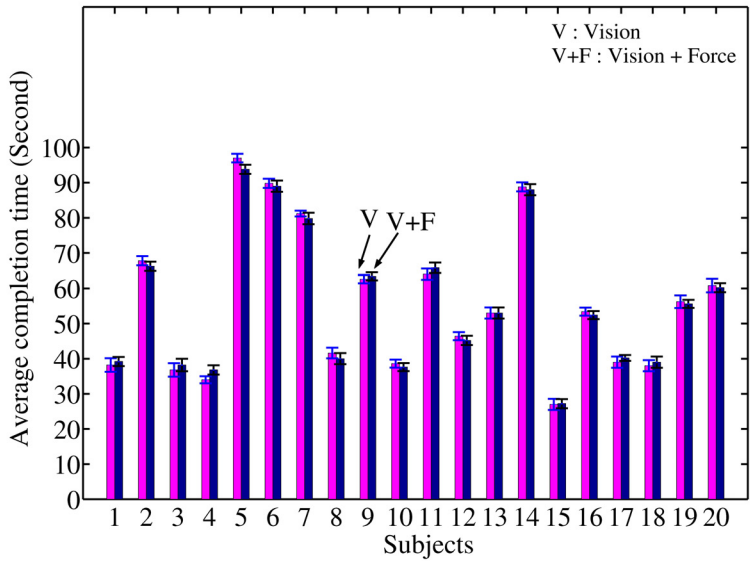

(b)

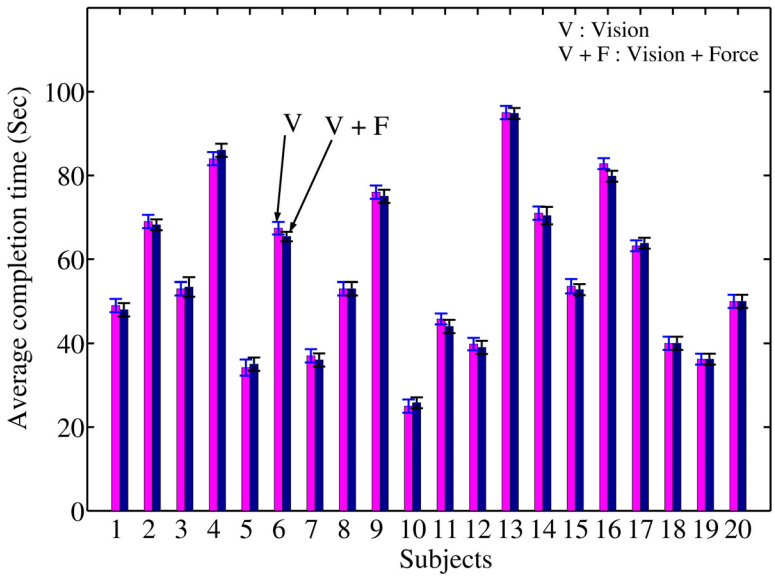

Figure 3.37. The average completion time taken by each subject to perform cell injection with vision (V) feedback and vision + force (V+F) feedback for: a) S_1 and b) S_2

3.7 Discussion

In this chapter, the development of a haptic feedback interface for cell injection task has been presented. The force sensing system is capable of measuring forces in the μN – mN range. The successful implementation and calibration of the force sensor has been discussed in detail. We performed experiments on three different types of egg cells namely: salmon fish, flying fish and zebrafish. The force values obtained for puncturing the outer membrane of salmon fish, flying fish and zebrafish egg cells was 2.2694mN, 1.6057mN and 0.70 mN respectively. During all membrane puncture tasks the user was clearly able to discern when the membrane was punctured through a rapid drop in the force felt through the PHANToM. The role of force feedback was evaluated on zebrafish egg cells (since it is an excellent model for vertebrate studies). As we performed experiments only on zebrafish egg cells (transparent), we created two different scenarios: S_1 and S_2, which covered the most general cases in biomanipulation tasks. The outcome of cell injection task for each individual subject with combined vision + force (V+F) feedback was superior compared to vision feedback (V) alone for both S_1 and S_2. We have incorporated the learning phase data of the subjects in our analysis. Overall, the p-value for the two data sets (V and V+F) for S_1 and S_2 was less than 0.0001 and equal to 0.0005 leading to a probability of greater than 99.95% that that there was a significant difference between V and V+F feedback. Our results confirm that subjects had a higher degree of success in injecting the desired material (trypan blue dye) into the cell with simultaneous vision + force feedback compared with vision feedback alone. Overall, considering all 40 subjects, the research hypothesis was validated through our experimental results. Statistical

analysis proved that there is a significant difference between the 2 data sets (V and V+F). Our findings confirm that a system with force feedback capability when combined with vision feedback can lead to potentially higher success rates in transgenesis, specifically where mechanical manipulation techniques are involved. The limitations of the work presented in this chapter are:

- The force feedback interface developed for cell manipulation system can only perform cell injection. The system cannot perform other manipulation tasks e.g. grasping [165].
- The force feedback interface cannot be directly applied to inject smaller cells in the range of 10 – 50 μm diameter [166].

In the field of cell biology most experiments involve cells with dimensions less than 100 microns. Thus the next chapter focuses on the development of a haptics-enabled atomic force microscopy system which has the capability to manipulate (indent) cells (< 100 microns in dimension) and measure forces in nN range.

Chapter 4: Haptics-enabled Atomic Force Microscopy

4.1 Introduction

As presented in chapter 3, one of the ways to improve the efficiency of cell manipulation tasks is the inclusion of haptic feedback. In addition, the force feedback obtained from an individual biological cell (e.g. stem cell) could be a potential mechanical marker to characterize its state. Stem cells have the unique capability to give rise to different cell types (differentiation) under certain physiological or experimental conditions.

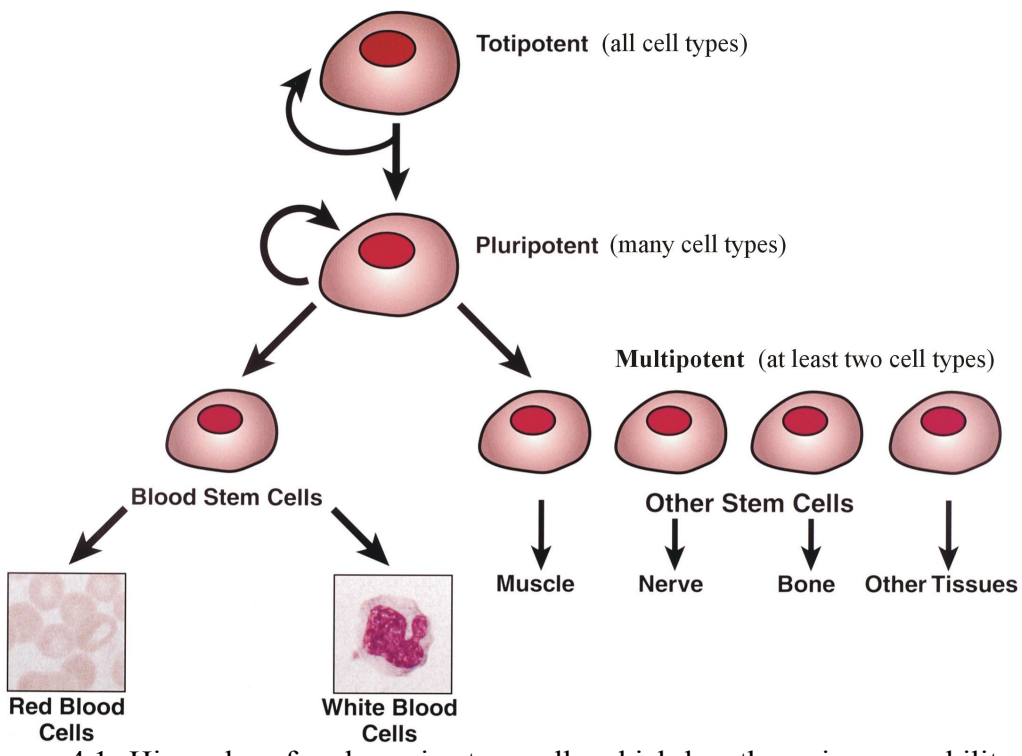

Figure 4.1: Hierarchy of embryonic stem cells which has the unique capability to differentiate into specialized cells types e.g. blood, muscle, nerve or bone (http://stemcells.nih.gov/info/media/).

There are two kinds of stem cells: embryonic stem cells and adult stem cells. Embryonic stem cells have huge therapeutic potential because they can give rise to every cell type in the body. On the other hand, adult stem cells can give rise to a limited range of cell types. Figure 4.1 shows the hierarchy of embryonic stem cells differentiating into different cell/tissue types. Thus stem cells have the ability to replace damaged cells in the body and could be used in therapeutic and regenerative medicine as shown in figure 4.2. In addition, stem cells allow drug testing in a wider range of cell types, thus assisting in drug development.

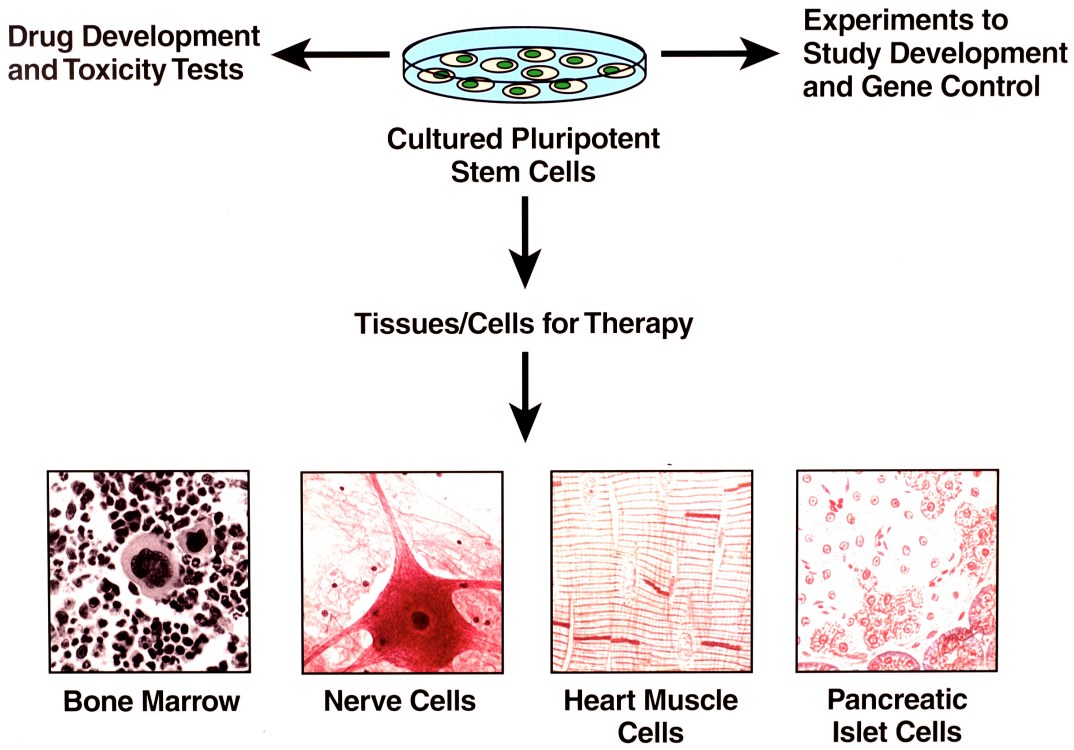

Figure 4.2. Stem cells offer a renewable source of replacement cells/tissues to treat disease and trauma including bone disease, Parkinson's disease, spinal cord injury, heart disease, diabetes etc (http://stemcells.nih.gov/info/media/).

Some of the examples of treatments for major diseases using stem cells are:

- Diabetes: Pluripotent stem cells instructed to differentiate into particular pancreatic cell could treat diabetes.
- Nervous system diseases: In Parkinson's disease and spinal cord injury, nerve cells are lost or die. The individuals with such diseases could be cured by creating a new nerve tissue from pluripotent cells which would restore the normal function of the nervous system.
- Heart diseases: The embryonic stem cells could be differentiated to cardiac cells which would repair damaged myocardial tissue thus curing cardiovascular diseases.
- Diseases of bone and cartilage: Embryonic stem cells once appropriately differentiated could cure many diseases and degenerative conditions in which bone or cartilage are deficient in number of defective in function.

However, the conventional methods to detect state of the cell are:

- Antibody staining: Involves live cell separation and immunocytochemistry. The former is time consuming and expensive while the later involves fixation procedure which kills the cells.
- Morphometric: Cell shape and structure can be used to detect some terminally differentiated cells. However, the method cannot be used to identify precursor cells.
- Transgenics: Cell detection involves specific fluorescent marker proteins which require genetic manipulation of cells, thus changing its characteristics.

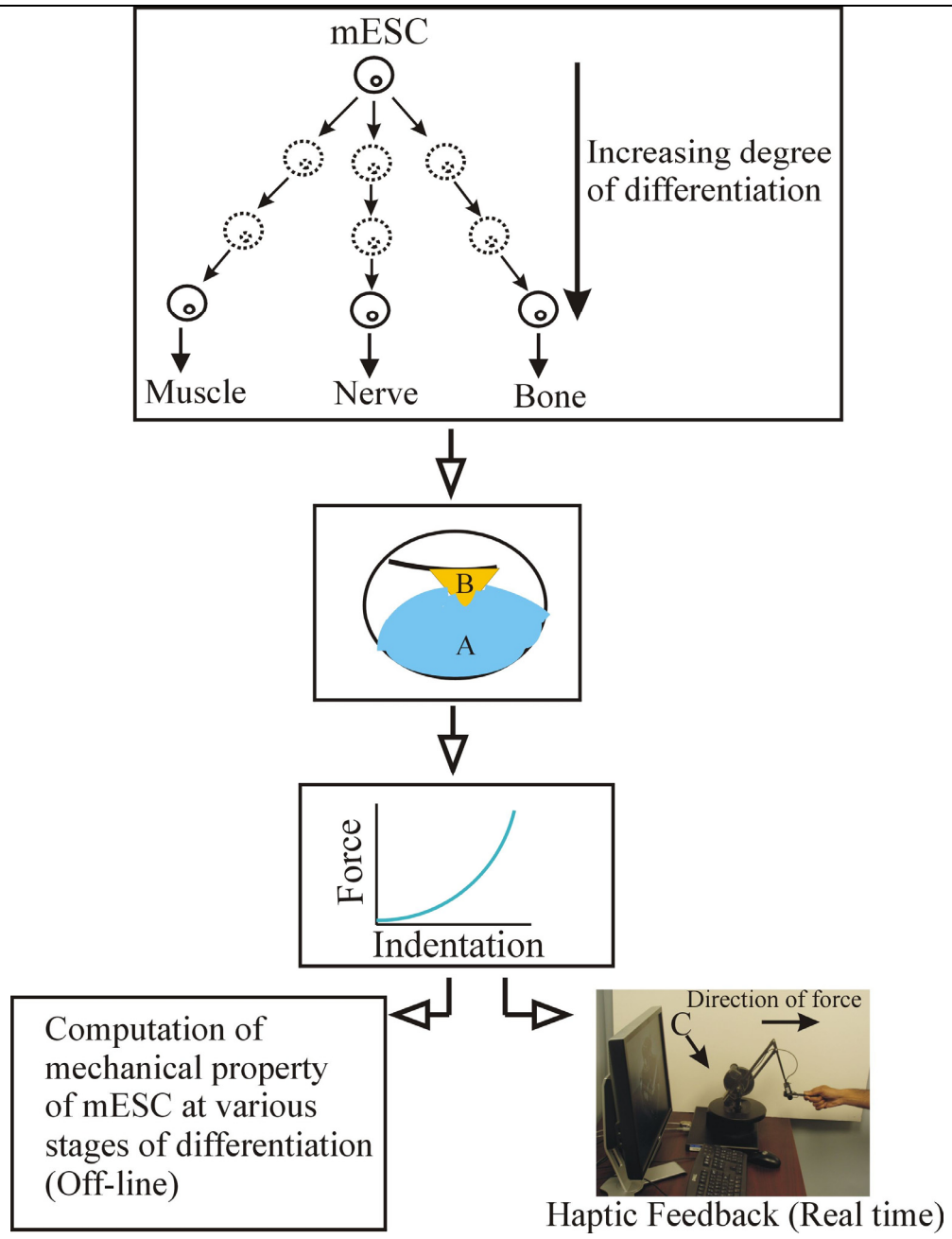

Figure 4.3: Schematic showing our proposed plan to manipulate and characterize an individual mouse embryonic stem cell (mESC) at various stages of differentiation. A: mESC, B: Tip of the AFM cantilever, C: PHANToM haptic feedback interface. AFM is used to obtain force and indentation data from an individual mESC.

Hence, there is a need to develop enabling technologies for characterizing the state of the cell. Consequently, we propose to develop haptics-enabled atomic force microscopy (AFM) based system that can be used to mechanically manipulate and haptically characterize an individual cell (figure 4.3). Mechanical characterization of cells will potentially pave the way for developing a high throughput system with force feedback capability. Since stem cells (diameter ~ 10 – 15 μm) have the potential applications in therapeutic and regenerative medicine, we chose to perform studies on mouse embryonic stem cells (mESC). Thus, we focus on performing experiments on cells with dimensions less than 100 μm compared to zebrafish egg cells (chapter 3) whose dimensions are 600 μm – 1mm. In this thesis, we attempt to provide haptic display of cell indentation forces in real time while manipulating mESC at various stages of differentiation. We also characterize the mechanical property of mESC at various stages of differentiation (off-line).

AFM, primarily developed as an imaging tool [167] has also emerged as a unique force sensor with nanometer resolution [112]. It has been used extensively to study the mechanical properties of biological materials [168]. On the other hand, Robotics researchers have proposed new human machine interfaces and models to manipulate biological cells. Vogl et al [128] proposed a spline based surface model for nanomanipulation with 3D visual and force feedback using AFM. Another AFM based nanorobotics system was developed by Sitti et al [169]. Small autonomous robot (MICRON) based on AFM was developed for cell manipulation applications [170]. However, the spline based model, the nanorobotics system, and the MICRON

have not been evaluated on biological systems. A nano-manipulation system consisting of an AFM and a haptic device has also been developed to provide force feedback from biological samples and carbon nanotubes [127]. In this set up the user does not feel the actual forces from the sample, but feels a surface representation that is simultaneously reconstructed during the AFM scan. Limited studies have been performed on biological cells using haptics based AFM [129, 130]. To our knowledge, there had been no studies to predict whether there exists any difference in mechanical behavior of mESC at various stages of differentiation towards a particular cell lineage. Hence, we propose to conduct mESC indentation studies at various stages of differentiation using a haptics-enabled atomic force microscopy (AFM) system, where the user could feel the cell indentation forces in real time (figure 4.3) and hence possibly characterize the state of the cell. In addition, we also followed an analytical approach (chapter 5) to compute the mechanical property of mESC at various stages of differentiation (figure 4.3). Both the approaches could be used to develop improved methods of targeted cellular differentiation of embryonic/adult stem cells for therapeutic and regenerative medicine. We have performed experiments on live as well as fixed mESC. When the logistics prove difficult to maintain live cells, then we can perform experiments only on fixed cells, provided the results obtained with live cells parallel with fixed cells. Thus, to validate the correlation we initially performed experiments on live as well as fixed cells. We also propose that the mechanical property of undifferentiated mESC differs from differentiating mESC. We have conducted several indentation studies on mESC to confirm our research hypothesis (chapter 6).

4.2 AFM Studies on Cells

In this section, we present the various challenges encountered in developing a haptics-enabled atomic force microscopy (AFM) system for mechanical characterization of mouse embryonic stem cells (mESC). We describe in detail the procedure to obtain the spring constant of the AFM cantilever and the force-indentation data. We also mention the challenges faced to obtain image of mESC and the selection of an AFM cantilever of appropriate stiffness to perform experiments on live and fixed mESC.

4.2.1 Determination of Spring Constant of AFM Cantilever

The spring constant of the AFM cantilever is determined by the equipartition technique also known as the thermal method [171]. It is very crucial to determine the spring constant of cantilever before experimentation even though the manufacturers mention the theoretical value of the spring constant. This is because the dimensions of the tip may not be exactly same as the theoretical values and may vary from tip to tip. Thus using theoretical spring constant would lead to erroneous force plots. Computation of spring constant by the thermal method involves determination of: (a) sensitivity (nm/V) and (b) resonant frequency of the cantilever. A step-by step process is described below (for details refer to the manual [172]):

- The cantilever was engaged in "contact" mode (figure 4.4) on a clean, hard surface (set point ~ 0.3 to 1.0 V and integral gain ~ 3 to 5)
- The 'force' tab of the 'master panel' (figure 4.4) was chosen and a force distance of 0.5 to 1μm was selected (figure 4.5).

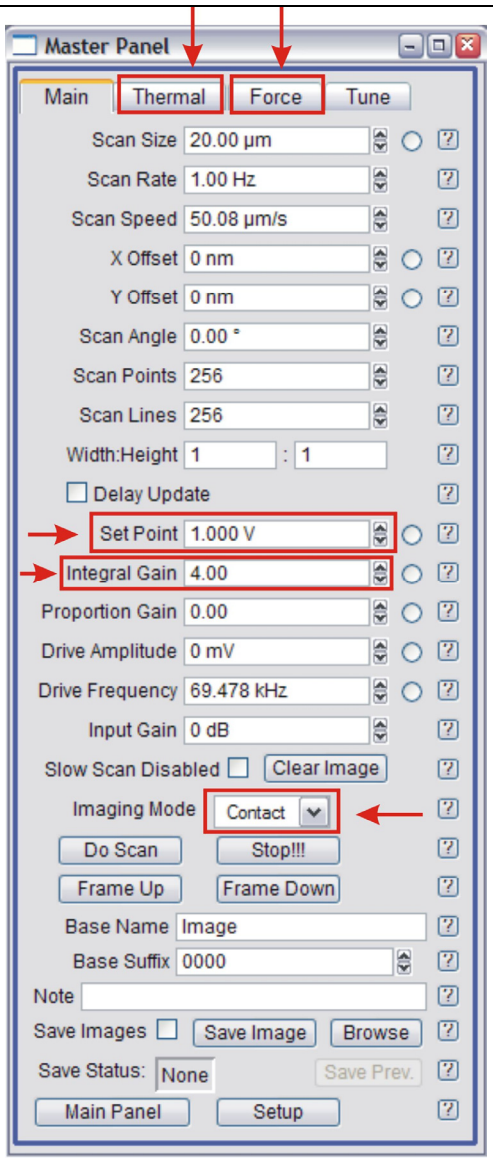

Figure 4.4. The master panel from MFP 3D™ software. The 'contact mode' imaging, the set point, the integral gain, thermal tab and the force tab are highlighted in the figure.

- "DeflVolts" (figure 4.5) was chosen from the "trigger channel" pull down menu with a value of approximately 0.2 – 1.0 V.

- "Single force" button (figure 4.5) was clicked, which gave the deflection versus piezo position (*z*) profile (figure 4.7).

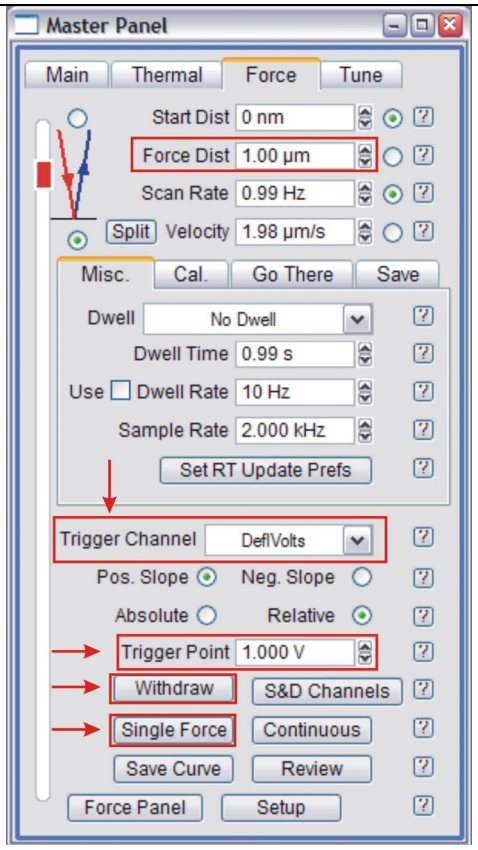

Figure 4.5. The force panel showing 'force distance' 'trigger channel (DeflVolts)', 'trigger point', 'single force' and 'withdraw' tab.

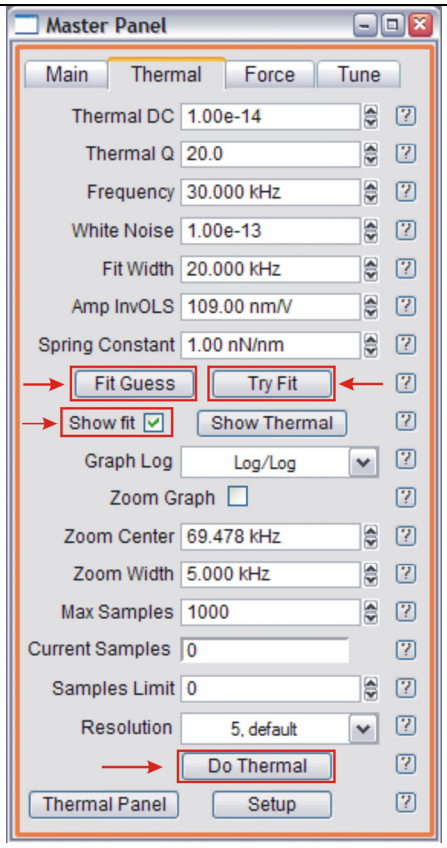

Figure 4.6. The thermal panel showing 'Do thermal', 'Show fit', 'Fit Guess' and 'Try Fit'.

- The inverse optical sensitivity (InVOLS in nm/V) was determined from the force curve (figure 4.7).
- The tip was disengaged by clicking the "withdraw" button in the force tab.
- The 'thermal' tab was selected on the master panel (figure 4.4).

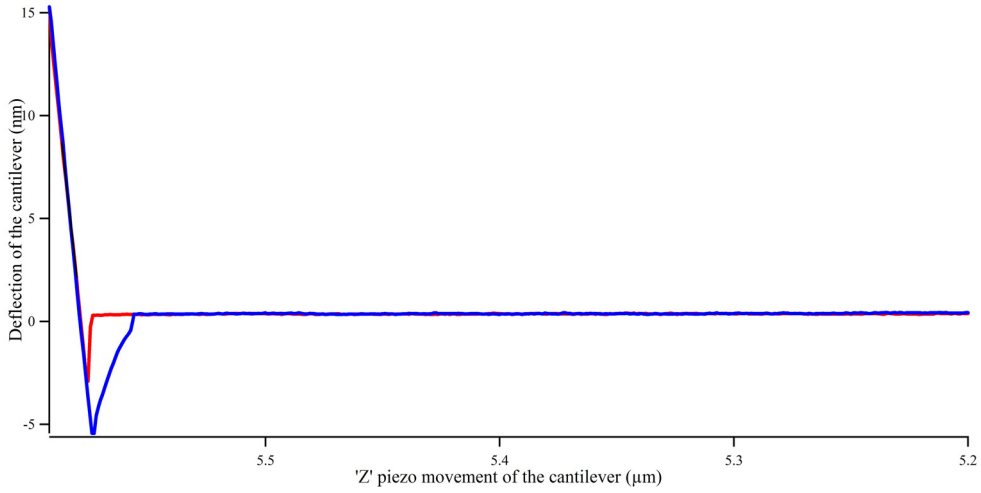

Figure 4.7. Deflection versus the piezo movement of the cantilever (z).

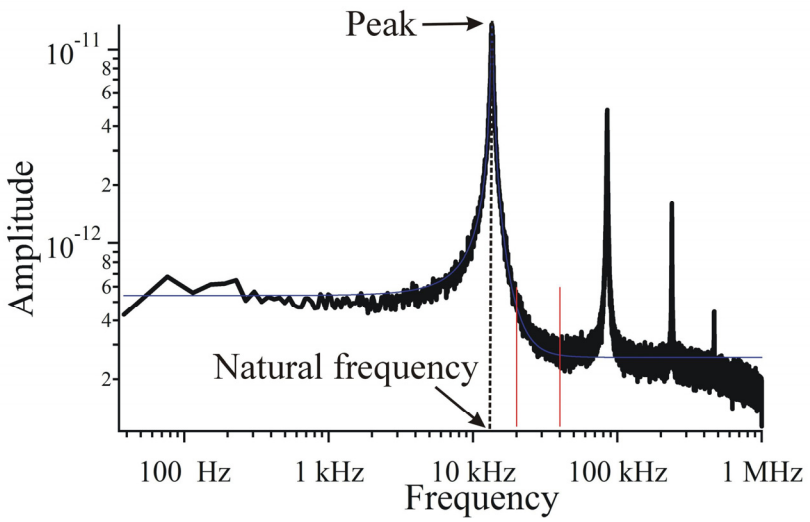

Figure 4.8. The peak amplitude determines the natural frequency of the cantilever.

- The 'Do thermal' (figure 4.6) button was clicked in the thermal tab. This determined the natural frequency of the cantilever by performing an iterative sweeps and averaging them.
- 'Stop thermal' was clicked when the resonance plot looked smooth (figure 4.8)

- A perfect fit was determined by clicking on the 'show fit', 'fit guess' followed by 'try fit' button.
- The software (MFP3D^{TM}) automatically determined the spring constant and updated the resonant frequency.

4.2.2 AFM imaging of mESC

We attempted to obtain images of fixed mESC in liquid using AFM. Fixation of the cell using cross linking agents such as formaldehyde might prevent cell damage due to the sharp pyramidal tip or detachment by the scanning tip. Initially, we used silicon nitride cantilevers (TR400PB and TR800PB, k = 0.02 N/m and 0.16 respectively, Asylum Research, Santa Barbara, CA) for imaging in 'AC mode'. In AC mode, the cantilever is oscillated at or close to its resonant frequency. When the cantilever hits the sample surface, the oscillation amplitude is damped. By recording the feedback signal required to keep the amplitude constant, the topography of the sample can be obtained. However, the cell moved away from the tip of the cantilever as it approached the cell surface (figures 4.9 and 4.10). We tried the 'contact mode imaging'. In contact mode, the deflection of the cantilever is kept constant by the feedback system while the tip scans the surface. Images are created by recording the piezo-vertical position. However, the cell stuck to the tip of the cantilever. One of the reasons for improper tip-cell contact may be due to the height of the tip (~ 2.9 μm, TR400PB and TR800PB) being less than the height of the cell (~ 10 – 15 μm). This might have caused the end of the cantilever (not the tip) to touch the cell surface and push it along during scanning.

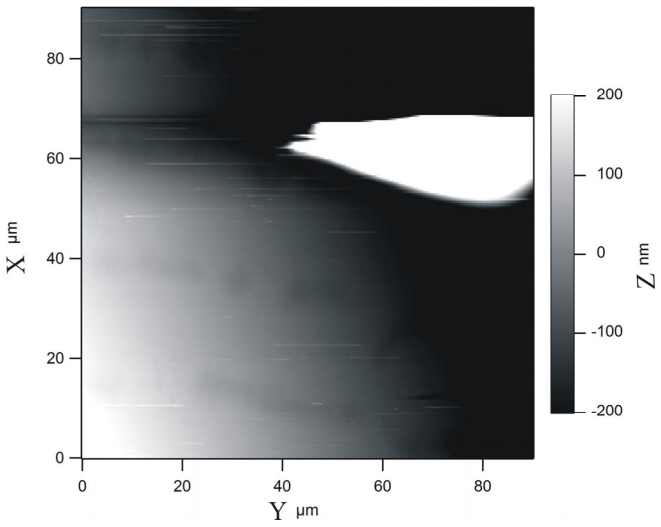

Tip geometry of
TR 400PB and
TR 800PB

www.olympus.co.jp/probe

Figure 4.9. AC mode image of a fixed mESC (cantilever TR400PB, k = 0.02 N/m). The AFM was not able to scan the entire cell surface as the cell moved away from the cantilever tip.

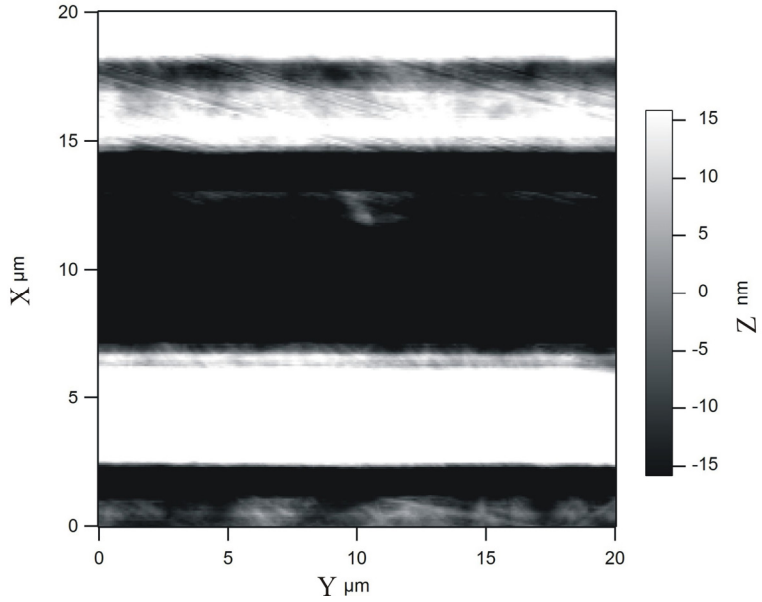

Figure 4.10. The AFM was not able to scan the cell surface as the cell moved away from the cantilever tip and we were not able to obtain the image of the cell (cantilever TR800PB, k = 0.16 N/m)

Hence, we used another silicon nitride cantilever whose tip height is 7 µm (Biolever, k = 0.027 N/m, Asylum Research), but the problem of tip-cell contact still persisted (figure 4.11).

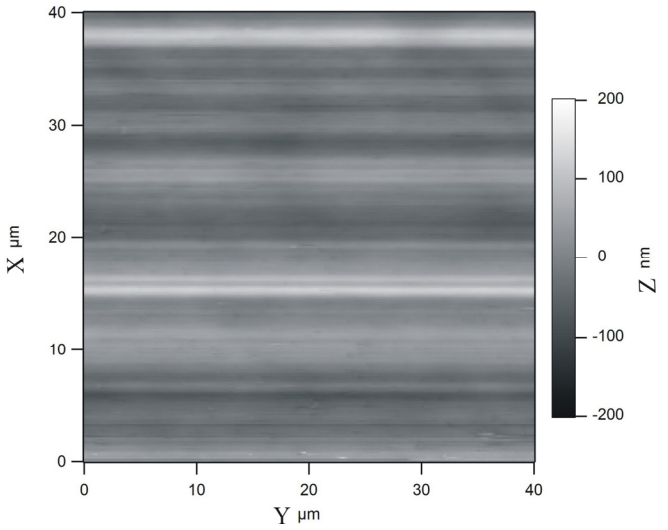

Tip geometry of Biolever

www.olympus.co.jp/probe

Figure 4.11. The AFM tip-cell contact persisted with cantilever of tip height 7 µm. Thus, we were not able to obtain the image of the cell.

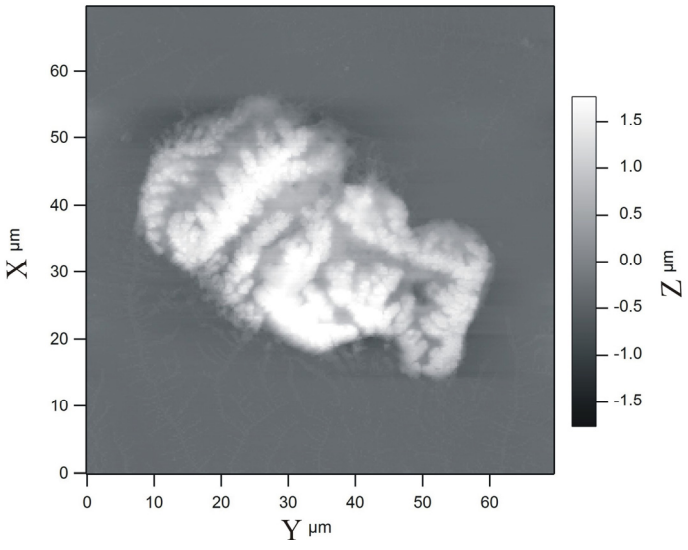

Tip geometry of PNP-DB

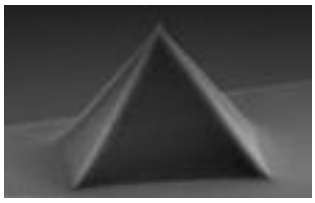

www.nanoworld.com

Figure 4.12 Contact mode image of mESC colony (PNP-DB, k = 0.48 N/m)

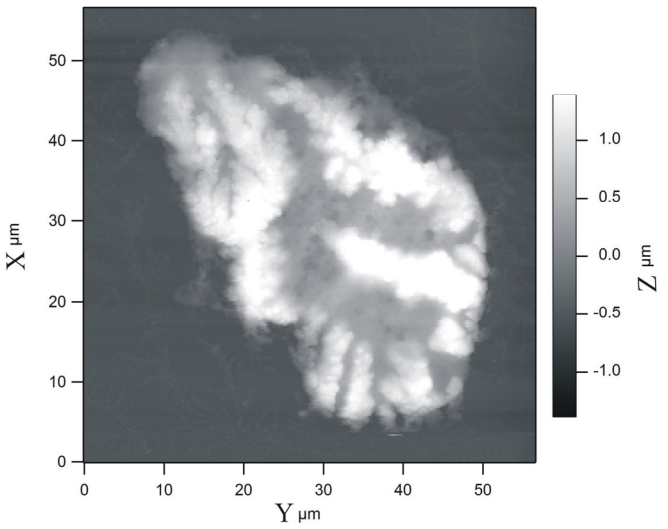

Tip geometry of PPP-BSI

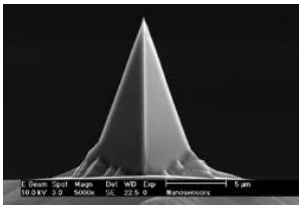

www.nanosensors.com

Figure 4.13 Contact mode image of mESC colony (PPP-BSI, k = 0.1 N/m)

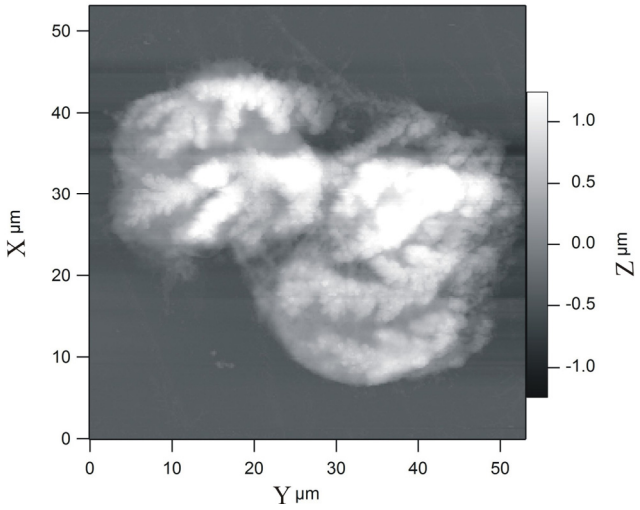

Tip geometry of SiNi

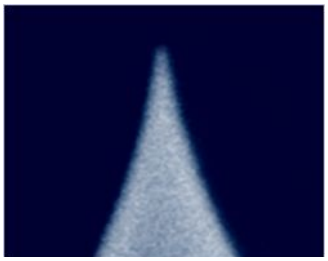

www.budgetsensors.com

Figure 4.14 Contact mode image of mESC colony (SiNi, k = 0.06 N/m)

After obtaining unsuccessful results with fixed mESC in liquid, we decided to conduct studies on fixed mESC in air. Contact mode images of mESC colony in air are shown in figures 4.12 - 4.14 obtained by the following cantilevers: (a) A v-shaped Pyrex Nitride cantilever (PNP-DB, NanoWorld AG, Neuchâtel, Switzerland) (k = 0.48 N/m), (e) silicon cantilever (PPP-BSI, Nanosensors™, Neuchâtel, Switzerland),

(k = 0.1 N/m) and (f) a v-shaped silicon nitride cantilever (SiNi, Budget Sensors, Sofia, Bulgaria) (k = 0.06 N/m). We obtained good images in air compared to liquid. However, the studies on mESC have to be conducted in cell culture (liquid), which would reflect its true topography and mechanical properties. Also cell culture (liquid) is a crucial component for maintaining live cells. The tip-cell contact during AFM scanning in liquid is a major concern due to the cells dislodging from the substrate. The adherence of the cell to the substrate depends on the type of the substrate [173]. Coating the substrate with certain materials (e.g. collagen, polylysine) may enhance immobilization of the cell [174]. However, our primary goal is to obtain force signature from mESC and characterize its mechanical property, thus we concentrate on obtaining the force/indentation data from mESC rather than obtaining the AFM image. We plan to perform indentation studies on mESC without obtaining its image. This is possible by initially obtaining a force curve (figure 4.15) on a hard surface near the cell. Such a curve has a steep slope and negligible hysteresis. We then move the cantilever tip on the cell and expect that the tip will contact the cell upon movement of the cantilever. If the tip contacts the cell surface, then we obtain a force curve shown in figure 4.16 which does not have a steep slope and has hysteresis. Thus we confirm that the tip is on the cell surface and the force measurement method is reliable. From figures 4.15 and 4.16, we can determine the height of the cell given by (h):

$$h = h_0 - h_1 \tag{4.1}$$

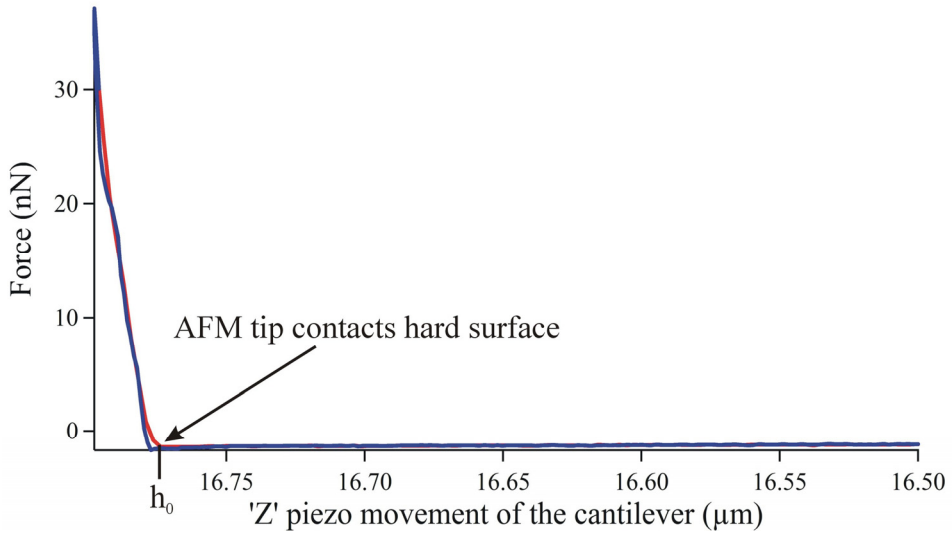

Figure 4.15. Force (*F*) versus piezo movement of the cantilever (Z) on a hard surface. The cantilever tip contacts the hard surface at a z value given by h_0. The red and blue lines represent loading and unloading curves respectively

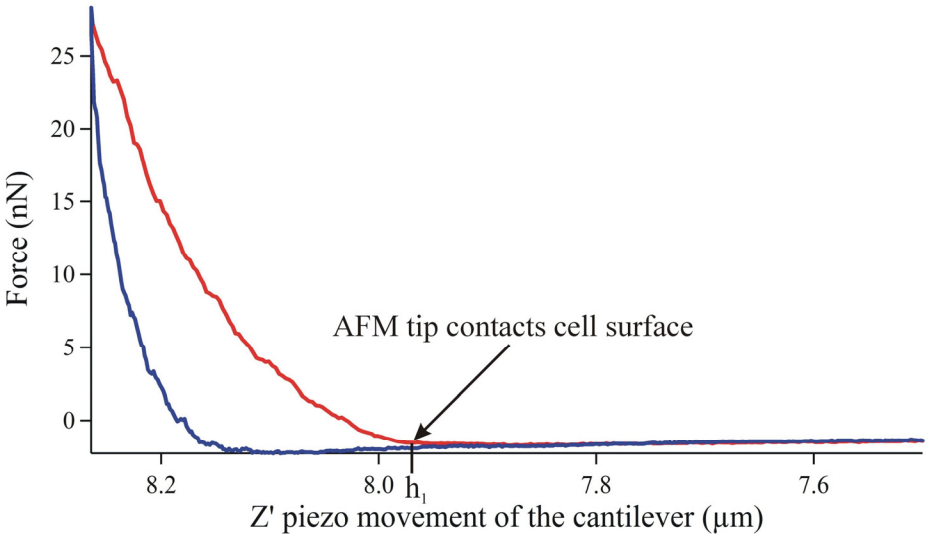

Figure 4.16. Force (*F*) versus piezo movement of the cantilever (Z) on a cell surface. The cantilever tip contacts the cell surface at a z value given by h_1. The red and blue lines represent loading and unloading curves respectively

4.2.3 Force-Indentation data

The AFM system is used to obtain force and cell deformation data from biological samples. The cantilever is moved by the piezoelectric scanner in the z direction towards the cell. The deflection of the cantilever is detected by a photodiode when the tip comes in contact with the cell. When the tip of the cantilever is in contact with the cell, the initial cantilever deflection, d_0, and initial cantilever movement in z direction, z_0, are obtained (see figure 4.17(a)). As the cantilever moves in the z direction and deforms the cell, the final cantilever deflection, d_1, and the cantilever movement, z_1, are obtained (see figure 4.17(b)).

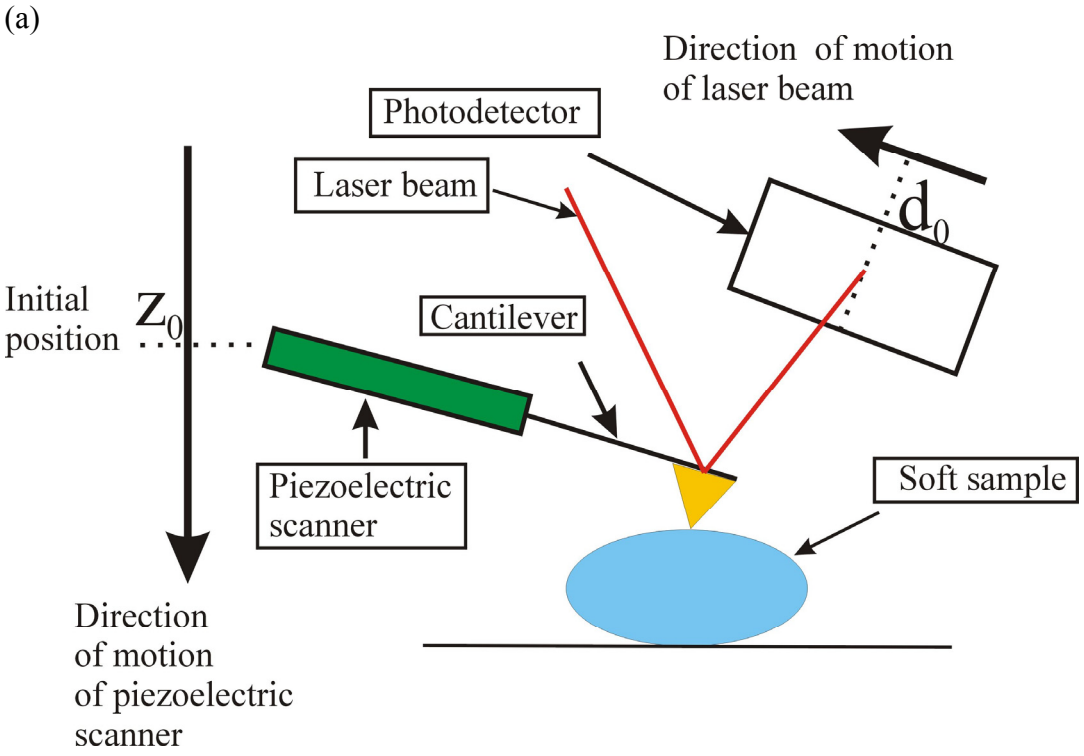

Figure 4.17 (a) Schematic of AFM cantilever interacting with a cell. Point of contact: d_0 and z_0 represent the initial cantilever deflection and movement respectively.

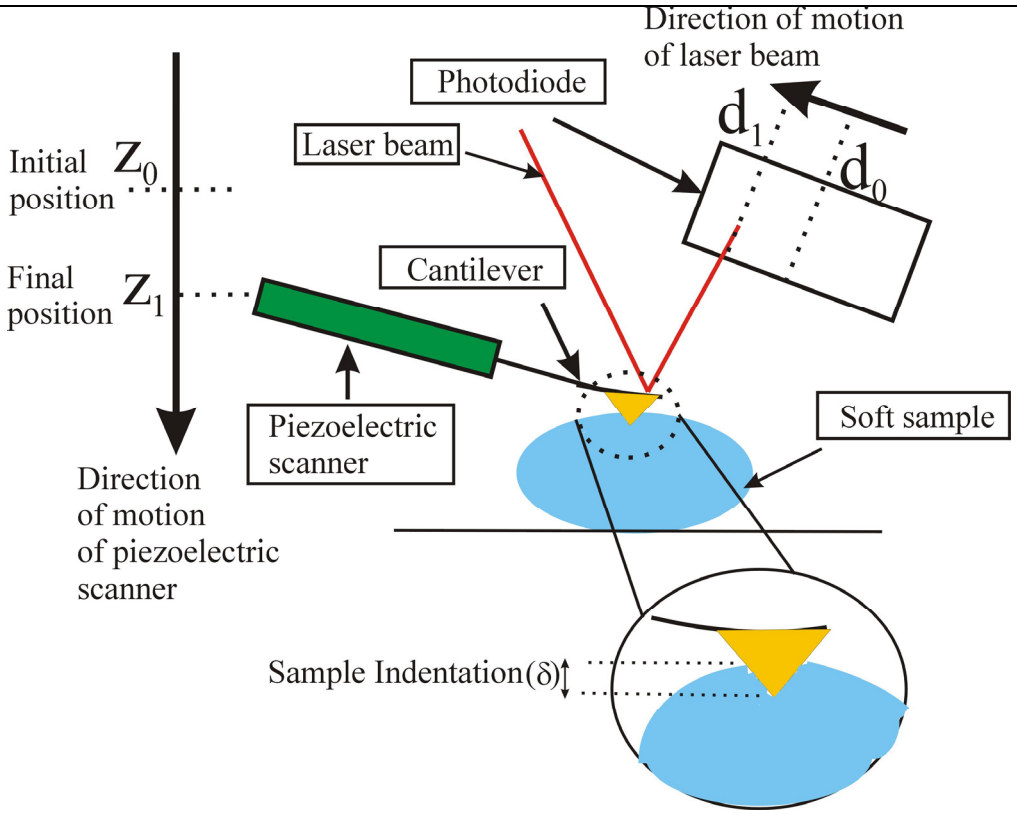

Figure 4.17 (b) Cell indentation: the cantilever further moves from the point of contact and indents the cell. d_1 and z_1 represent the final cantilever deflection and movement respectively.

The actual cantilever deflection, d, and the movement, z, are given by:

$$d = d_0 - d_1 \tag{4.2}$$

$$z = z_0 - z_1 \tag{4.3}$$

The difference between the actual cantilever movement, z, and actual cantilever deflection, d, represents the cell indentation, δ, and is given by (see figure 4.17(b)):

$$\delta = z - d \tag{4.4}$$

Substituting (4.2) and (4.3) in (4.4) we get:

$$\delta = (z_1 - z_0) - (d_1 - d_0) \tag{4.5}$$

Thus the cell indentation, δ, can be used to compute the elastic modulus of the cell based on an analytical model (chapter 5 and 6). The force exerted on a biological cell and the corresponding deformation predicts its mechanical behavior.

4.2.3.1 Force and Indentation Trigger

In AFM, the force curve can be obtained by setting a maximum loading force to be exerted on the sample by the cantilever (force trigger). Initially we performed experiments by choosing the force trigger (section 4.5) as shown in figure 4.18.

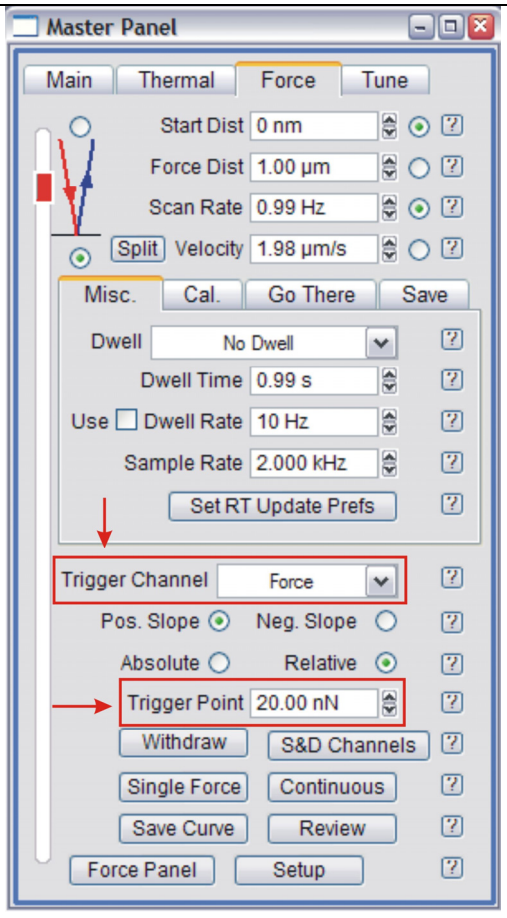

Figure 4.18. The force panel showing force as the trigger parameter set at 20 nN.

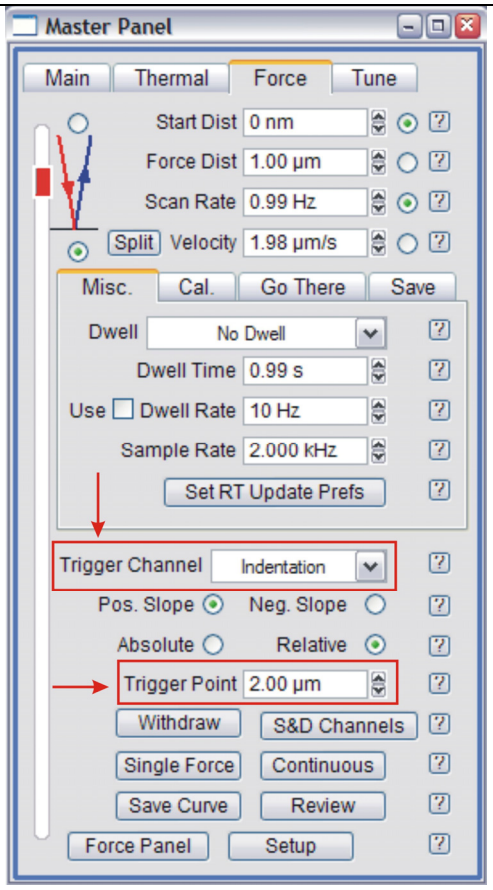

Figure 4.19. The force panel showing indentation as the trigger parameter set at 2 µm.

In order to standardize the experimental procedure we have to determine the force trigger for a particular mESC (differentiating and undifferentiated) and then perform the experiments. This involves an extra step and is time consuming. Moreover, a certain force value (force trigger) may indent a particular state of mESC (undifferentiated/differentiating) by negligible amount compared to another state of mESC (undifferentiated/differentiating). The force-indentation data obtained by the former may not reflect the true mechanical property of mESC compared to the later. Hence we decided to use the indentation trigger (custom made by Asylum Research, based on our proposed requirement) in our experiments. Indentation trigger (figure 4.19), standardizes the experimental procedure for undifferentiated and differentiating mESC by indenting each one of them by a constant value (~ 2 µm).

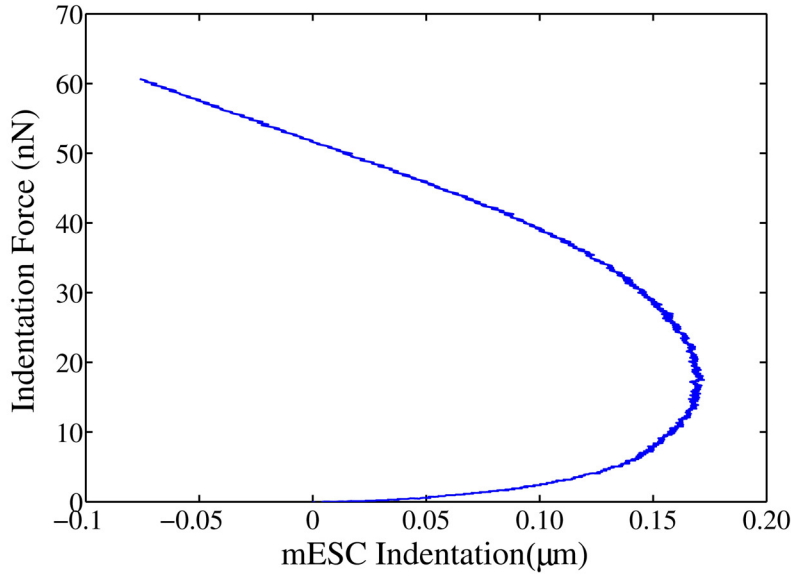

Figure 4.20. Force versus indentation for first sample of fixed mESC. The AFM cantilever (k = 0.06 N/m) was not stiff enough to achieve an indentation of 2 µm.

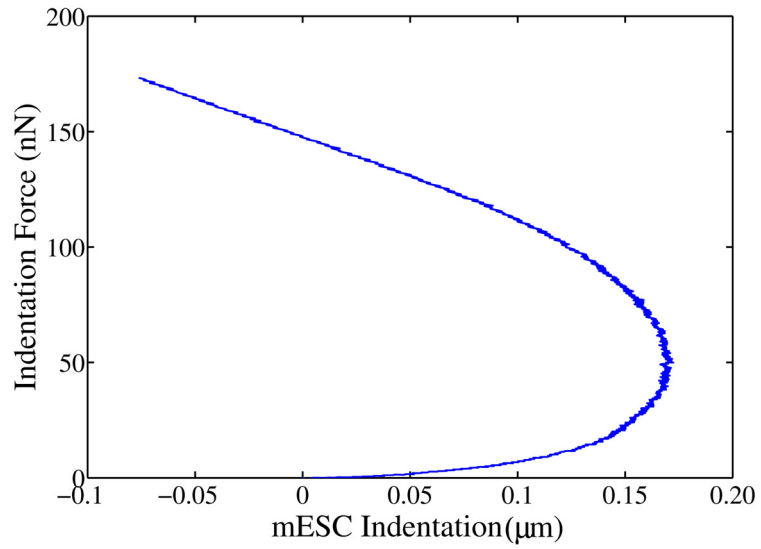

Figure 4.21. Force versus indentation for second sample of fixed mESC. The AFM cantilever (k = 0.06 N/m) was not stiff enough to achieve an indentation of 2 μm.

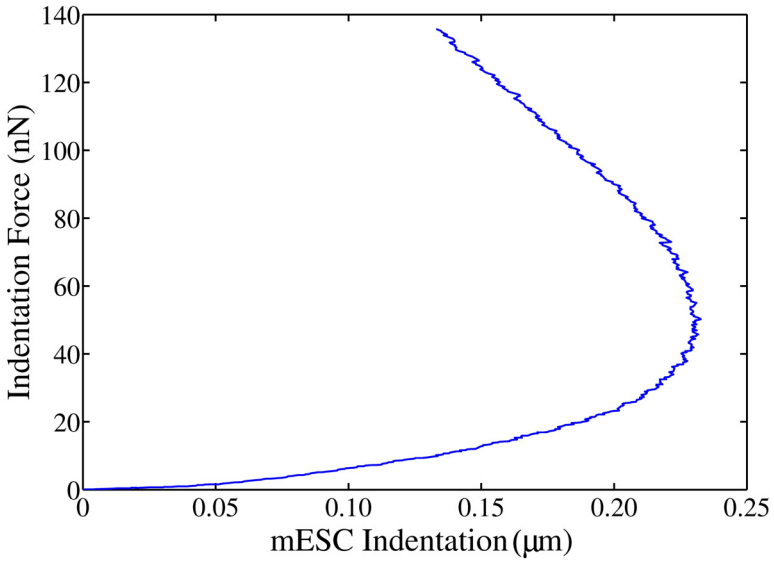

Figure 4.22. Force versus indentation for third sample of fixed mESC. The AFM cantilever (k = 0.06 N/m) was not stiff enough to achieve an indentation of 2 μm.

To test the indentation trigger, we performed experiments on fixed mESC with a silicon nitride cantilever (PNP-DB, long cantilever: k = 0.06 N/m). The force-indentation plots are shown in figures 4.20 – 4.22. We observed that the force profiles curl up implying that the cantilever was not stiff enough to indent the cell and it reached the maximum deflection before indenting the sample to 2 μm. The cantilever withdraws from the sample once it reaches the maximum deflection. Hence we obtained unconventional force-indentation profile. Thus the cantilever stiffness plays an important role in measuring forces on a particular sample. Later, we conducted experiments on fixed mESC for cell indentation range of 2 – 2.5 μm with a stiffer cantilever (AC240TS, Asylum Research, originally manufactured by Olympus Inc) which has a spring constant of 2 N/m. The force-indentation plots are shown in figures 4.23 – 4.25.

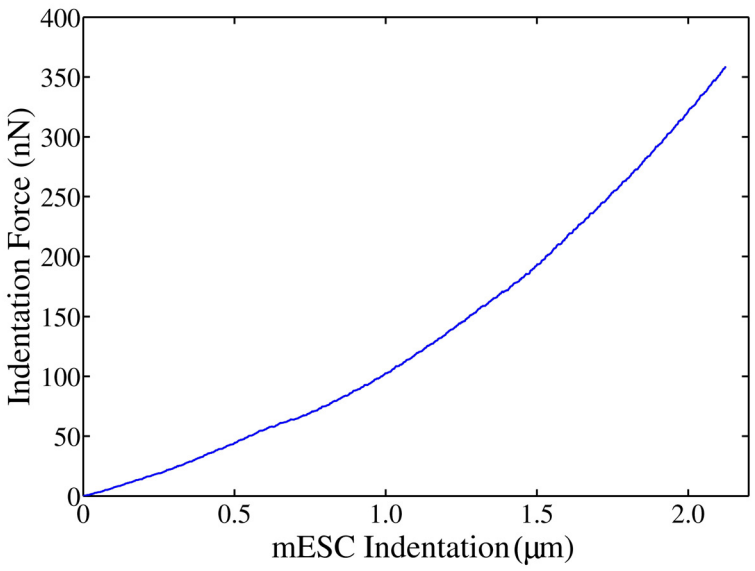

Figure 4.23. Force versus indentation for first sample of fixed mESC obtained with a cantilever of stiffness 2 N/m.

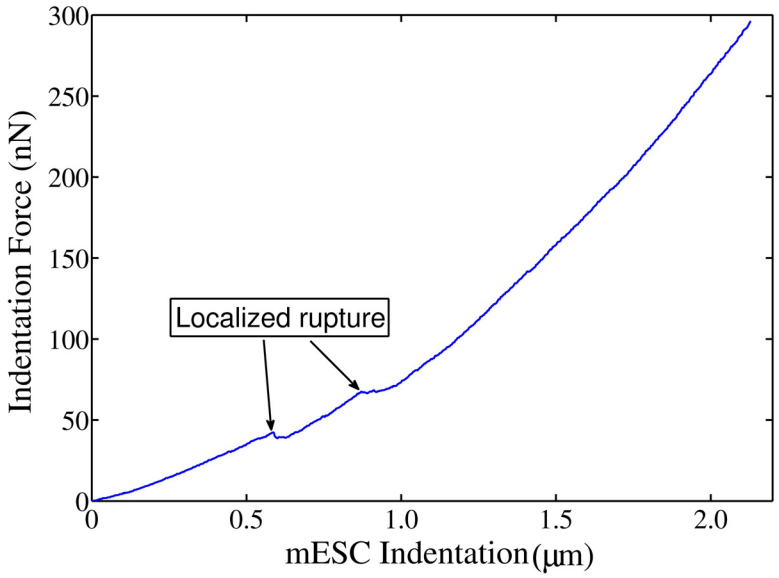

Figure 4.24. Force versus indentation for second sample of fixed mESC obtained with a cantilever of stiffness 2 N/m.

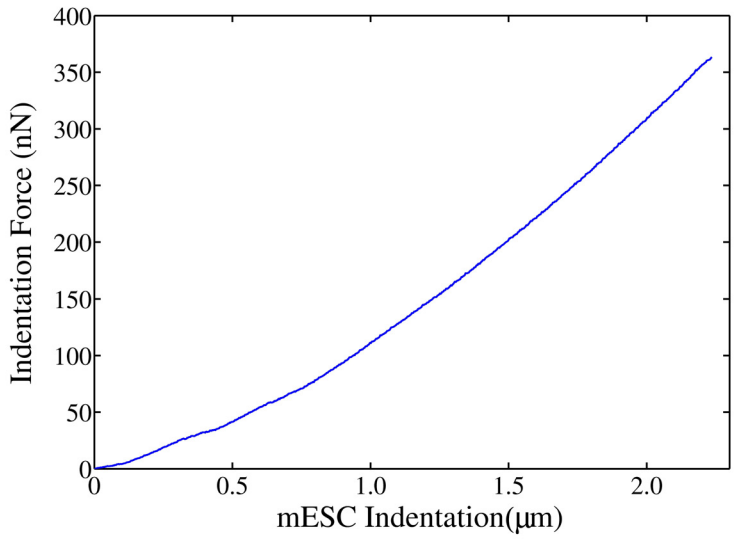

Figure 4.25. Force versus indentation for third sample of fixed mESC obtained with a cantilever of stiffness 2 N/m.

We obtained convincing plots which showed that the cantilever with a stiffness of 2 N/m was ideal for performing indentation studies (~ 2 – 2.5 µm) on fixed mESC. We also performed indentation studies (~ 2 – 2.5 µm) on live mESC with a cantilever of spring constant 0.06 N/m and obtained convincing force plots. The localized rupture in the force-indentation profile from the second sample (figure 4.24) might be due to the local rupture of the cell membrane. *Hence, we chose an AFM cantilever depending on the stiffness of the sample, which was achieved by conducting several trials.*

4.3 Haptic Feedback Interface

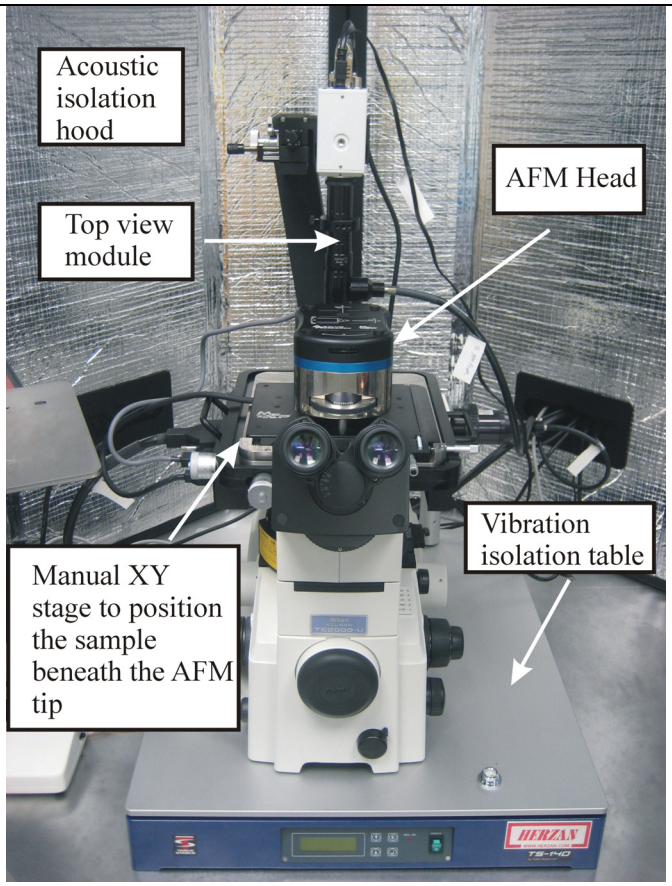

Figure 4.26. Experimental set up for mESC indentation studies

We have developed haptics-enabled atomic force microscopy (AFM) system to perform indentation studies on mouse embryonic stem cells (mESC). The haptic feedback interface consists of an Atomic Force Microscope (MFP-3D-BIO™, Asylum Research, Santa Barbara, CA) and the PHANToM haptic feedback device. The main part of AFM is the scan head, which is integrated with a top view module and mounted on a active vibration isolation table manufactured by Herzan (Laguna Hills, CA) (see figure 4.26).

The top view module enables viewing of cells and easy alignment of the laser beam on the AFM cantilever. XY stage (manual) allows the user to position the cell beneath the cantilever tip of AFM. The entire AFM set up is enclosed in an acoustic isolation chamber to prevent acoustic noise from interfering with the AFM measurements. The x and y-axes range of the scan head is 90 µm. The z-axis scan range is 40 µm. The AFM has the capability to measure forces in the range of pN-nN.

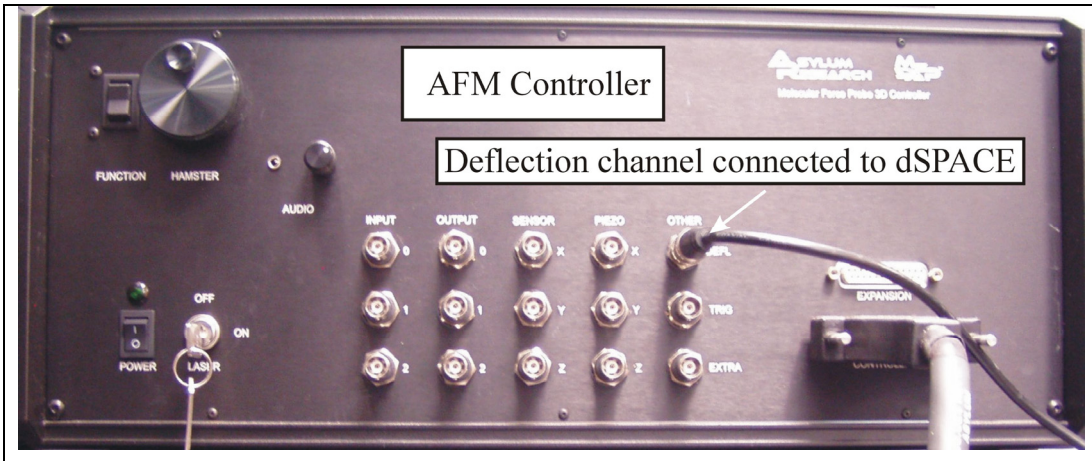

Figure 4.27. The deflection channel of the AFM controller was connected to the data acquisition board.

The AFM is integrated with the PHANToM as shown in figure 4.27. The deflection channel of the AFM controller was connected to a data acquisition board (model: DS1103, dSPACE Inc, Wixom, MI). A C-code was written to compute the force and display it on the PHANToM. Modeling the system (AFM cantilever and the sample) as two linear springs in series, the force experienced by the cell is given by the product of effective spring constant (k') of the system and the cell indentation (δ). However, the force experienced by the cell is equal to the force exerted on the cantilever. Hence the force transmitted to the haptic feedback device is given by:

$$F = kd \tag{4.5}$$

where k is the spring constant of the cantilever obtained initially through the IGOR software after exciting the AFM scanning tip in various modes (section 4.2.1). Substituting (4.1) in (4.5), we get:

$$F = k(d_1 - d_0) \tag{4.6}$$

Thus, our haptics-enabled AFM system obtains the relationship between the force exerted on the cell and the corresponding deformation. The force detected by the AFM during cell contact is acquired by a data acquisition board in real-time (model: dSPACE DS1103). The AFM is integrated with the PHANToM haptic feedback device as shown schematically in figure 4.28. The interface allowed the user to feel the cell indentation force in real time. The force was amplified by a factor of 10^7 for the human operator to perceive the change in force during cell indentation by the AFM cantilever. Thus, haptics-enabled AFM monitoring provides real time force information from an individual cell. This information can be used as a mechanical marker to characterize state of the cell.

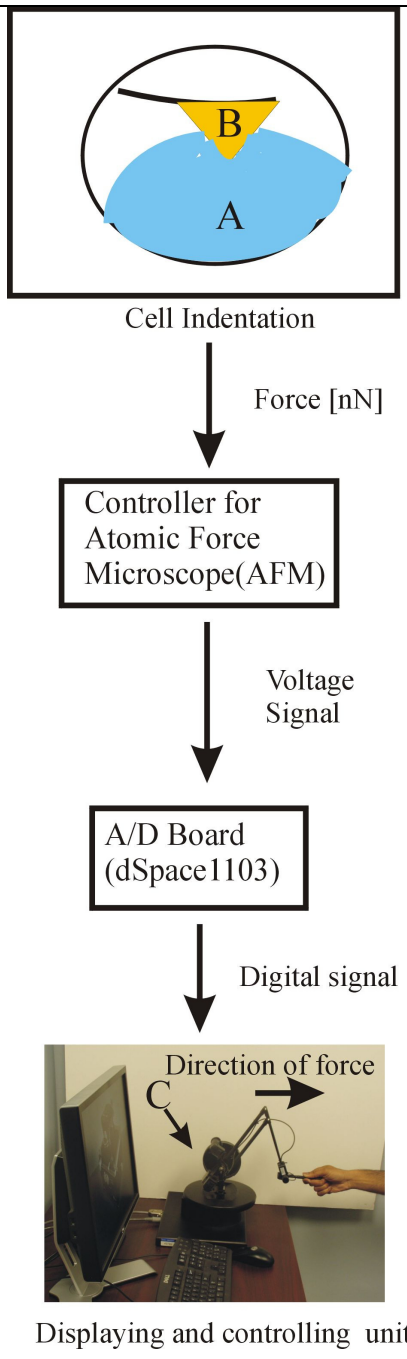

Figure 4.28. Cell manipulation system comprising of AFM and force feedback interface. A: mESC, B: Cantilever tip, C: PHANToM haptic feedback interface. When the tip indents mESC, the operator can feel the indentation force in real-time. The direction of force is towards the user.

4.4 Mouse Embryonic Stem Cell Preparation

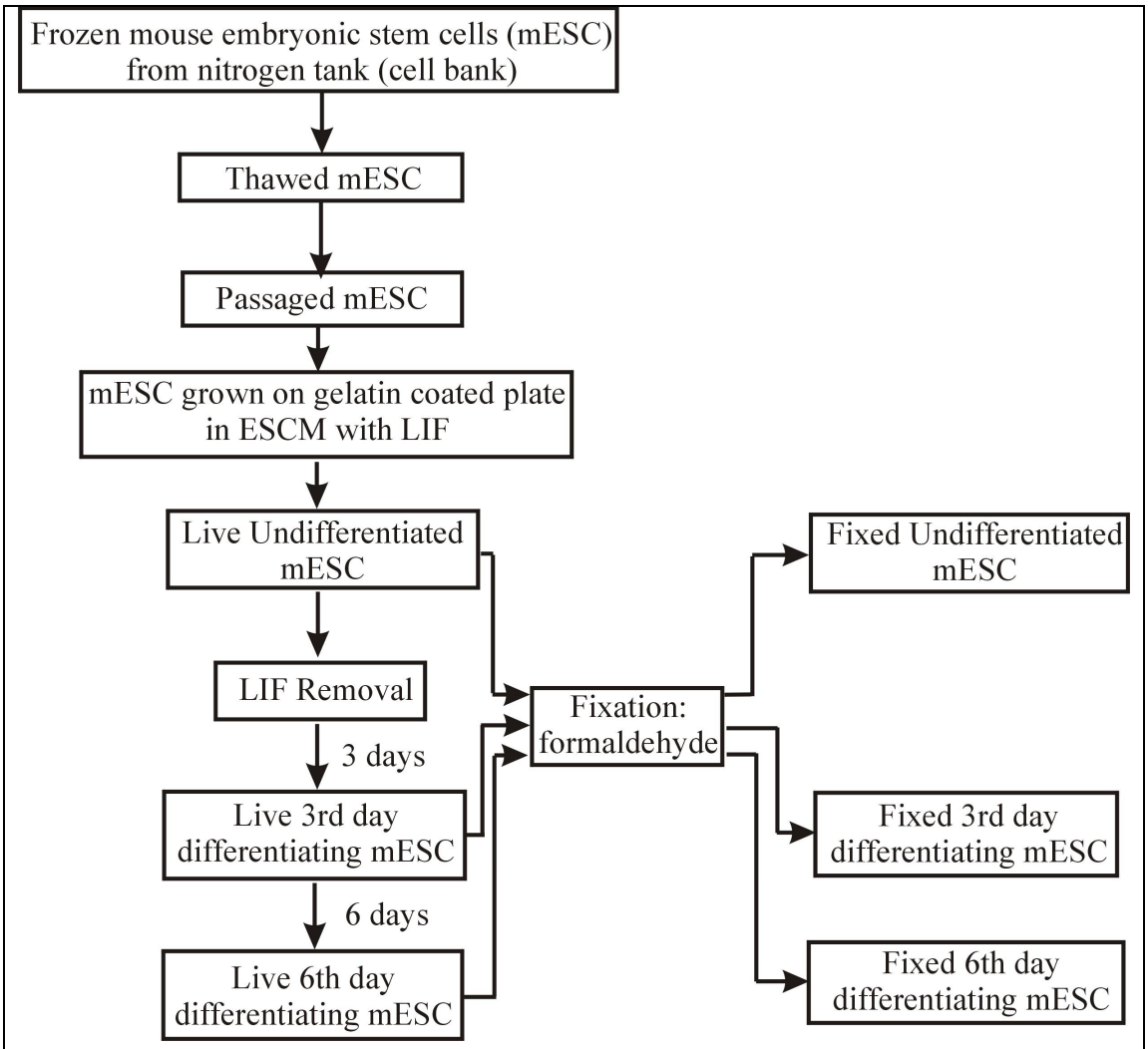

Figure 4.29: Flow chart showing the preparation of mouse embryonic stem cells: undifferentiated and differentiating by: (a) leukemia inhibitory factor (LIF) removal and (b) ascorbic acid treatment.

Mouse embryonic stem (ES) cells R1 (SCRC-1011, American Type Culture Collection [ATCC], Manassas, VA) and D3 (CRL-11632, American Type Culture Collection) were grown on 0.1% gelatin-coated plates in the absence of feeder cells. The embryonic stem cell medium (ESCM) consisted of 1000 U/ml leukemia

inhibitory factor (LIF, ESGRO, Chemicon, Temecula, CA), 15% fetal bovine serum (FBS) (Invitrogen), and basic medium that included Knockout Dulbecco's modified Eagle's medium (Invitrogen), 2 mM L-glutamine, 1x non-essential amino acids, and 0.1 mM mercaptoethanol. Differentiation was induced by the removal of LIF from the medium for R1 and D3 cell lines. Differentiation was also induced by treating R1 cell line with 10^{-4} M ascorbic acid towards cardiac cells [175]. Live 3rd day differentiating and live 6th day differentiating mESC were achieved by allowing the cells to differentiate for 3 days and 6 days respectively (figure 4.29). Prior to experiments, cells were dispersed using trypsin to obtain single cells and were plated on 60 mm tissue culture petri dish. Fixed mouse ES cells were obtained by treating the live mouse ES cells with 4% formaldehyde for 10 minutes and were stored in phosphate buffered saline (PBS). The live undifferentiated mESC were fed everyday and passaged in 2-3 days. The live differentiating mESC were passaged depending on the density of the cells in the petridish.

4.5 Preliminary Studies on Mouse Embryonic Stem Cells (mESC)

We conducted our preliminary studies on live and fixed mESC in undifferentiated and differentiating (3rd day) states. A v-shaped Pyrex Nitride cantilever (PNP-DB, NanoWorld AG) was used in our experiments. The spring constant of the cantilever was determined experimentally for each tip used in our studies using the IGOR software interface supplied by Asylum Research (section 4.2.1). The typical radius of curvature of the cantilever tip is below 10 nm. Through our preliminary studies, we have determined that undifferentiated mESC has a more supple membrane. Figure

4.30 (a) and (b) shows the force trigger curves for mESC where indentation force versus the cell indentation, δ, for differentiating (3rd day) and undifferentiated cells is shown for live and fixed mESC respectively.

(a)

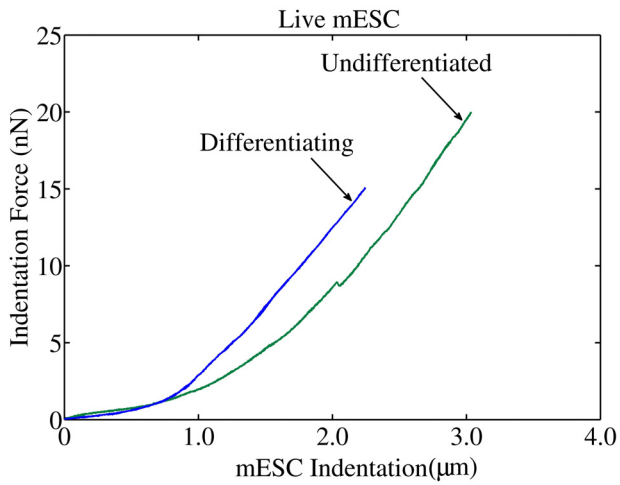

(b)

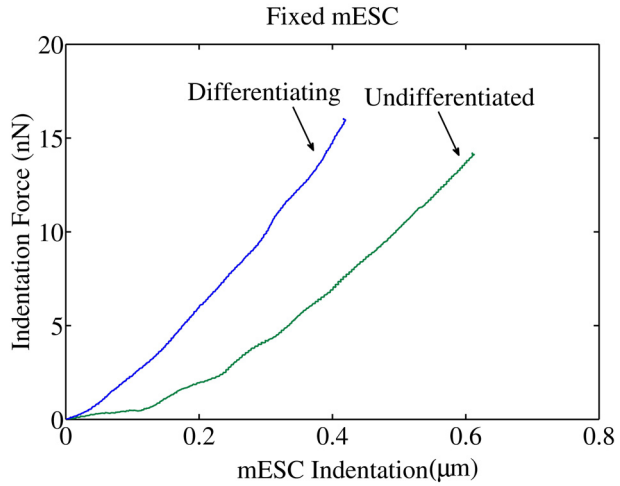

Figure 4.30. Force trigger curves for mESC where indentation force versus the cell indentation for differentiating (3rd day) and undifferentiated cells is shown for a) live mESC and b) fixed mESC.

From the figure it is clear that undifferentiated mESC is supple compared to differentiating (3rd day) mESC. These studies were done for a controlled 1 μm deflection of the AFM tip during cell indentation. Using the peak trigger force for 1 μm deflection of the AFM tip, we performed several mESC indentation tasks using the peak trigger force as the trigger value in AFM studies. Through our haptic feedback interface described in section 4.3, we are able to provide force feedback to the user in real-time and "feel" the change in the cell stiffness as the AFM tip indents on the cell surface.

4.5.1 Live Cells

Figure 4.31 and figure 4.32 shows the force versus cell indentation, δ, for live undifferentiated and differentiating (3rd day) mESC respectively.

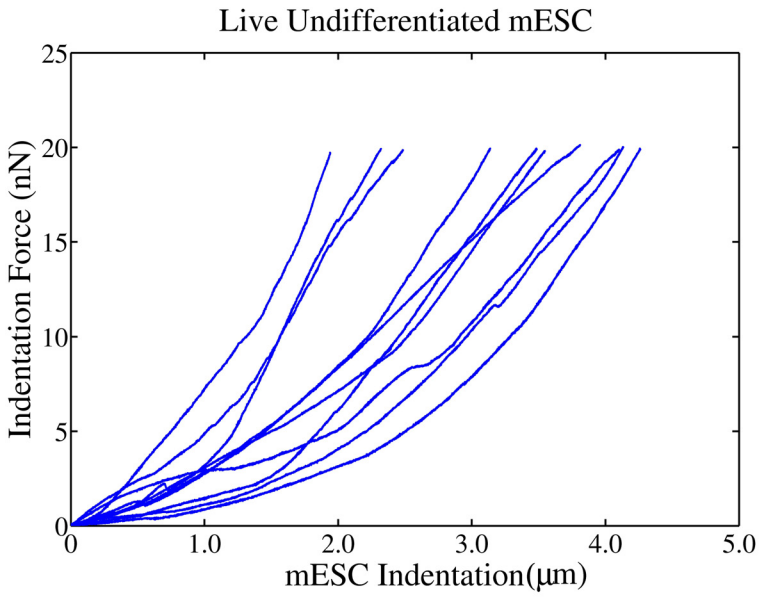

Figure 4.31: Force (F) versus cell indentation (δ) for live undifferentiated mESC.

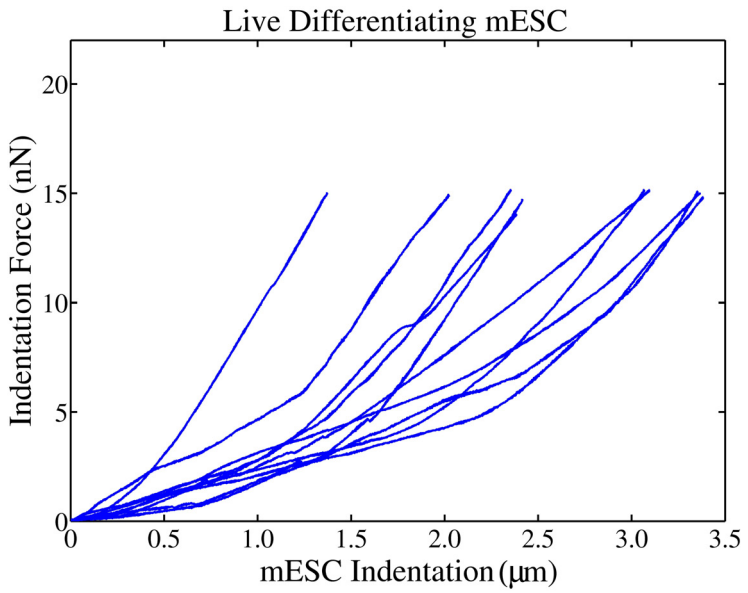

Figure 4.32: Force (F) versus cell indentation (δ) for live differentiating (3rd day) mESC.

4.5.2 Fixed Cells

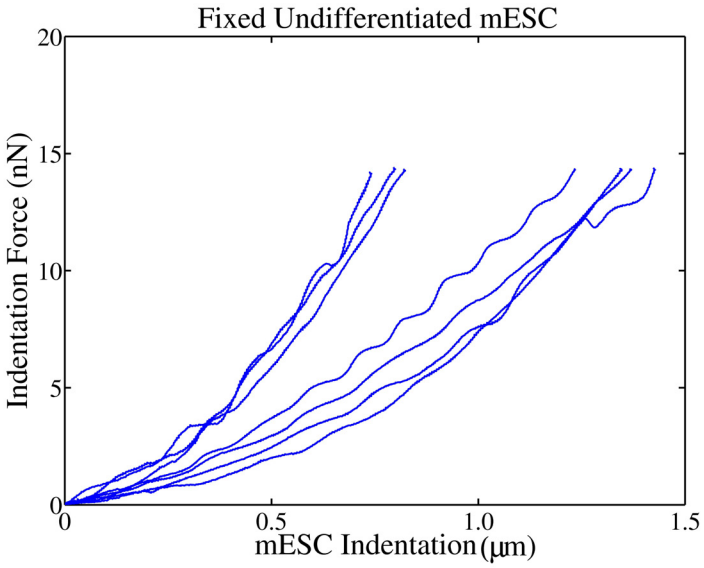

Figure 4.33: Force (F) versus cell indentation (δ) for fixed undifferentiated mESC.

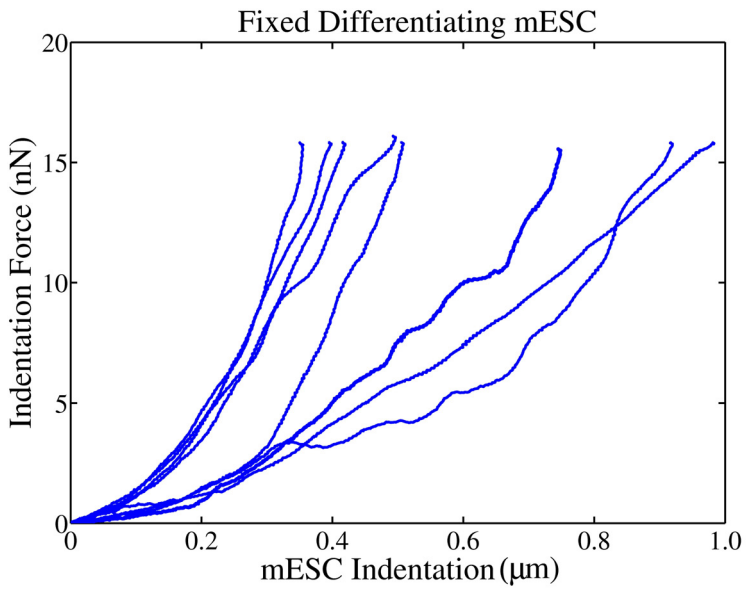

Figure 4.34: Force (F) versus cell indentation (δ) for fixed differentiating mESC.

Figure 4.33 and figure 4.34 shows the force versus cell indentation, δ, for fixed undifferentiated and differentiating (3rd day) mESC respectively. The force (F) and indentation (δ) was used to compute the mechanical property of live and fixed mESC in differentiating (3rd day) and undifferentiated states using an appropriate analytical model (please refer to chapters 5 and 6).

4.6 Discussion

We have developed a haptics-enabled atomic force microscopy system to manipulate and haptically characterize mouse embryonic stem cell (mESC). Stem cells have the unique capability to differentiate into specialized cell types e.g. bone, heart, nerve etc. Thus these cells could be used for therapeutic and regenerative medicine. However, the current techniques to detect the state of the cell are time consuming, harmful, and

may only identify precursor cells. Hence, we conducted preliminary experiments on undifferentiated and differentiating (3rd day) mESC using a haptics-enabled atomic force microscopy (AFM) system, where the user could feel the cell indentation forces in real time and characterize the cell. We observed that the undifferentiated mESC is supple compared to differentiating mESC in both live and fixed states. We have attempted to image mESC using AFM, but were unsuccessful because the cells dislodged from the substrate. Thus, we concentrated only on obtaining force indentation data from mESC by indenting (~ 2μm) the cell. The stiffness of the cantilever plays a crucial role in indenting the sample. As fixed cells are stiffer compared to live cells, we chose to perform further indentation studies (please refer to chapter 5 and 6) on fixed cells using a cantilever of stiffness 2 N/m. The slope of the force versus cantilever movement (z) curve (figure 4.16) obtained on the cell surface is less compared to that obtained on the hard surface (figure 4.15). The profiles can also be used to determine the height of the cell. Hence the force data obtained from the cell using our haptics-enabled AFM is reliable.

However, we were not able to obtain the AFM image of the cell in liquid (cell culture). The image would facilitate force measurements at various specific locations on the cell surface. We did obtain the image of an individual cell with optical microscopy. However, it was not possible to position the tip at specific locations on the cell surface because the end of the cantilever obstructs the clear visibility of the cell surface, when the tip is positioned on the cell. Force measurements at various specific locations on the cell surface could possibly determine the heterogeneity of

the cell surface. The next step is to quantify the mechanical property of mESC in undifferentiated and early differentiating (6 days under differentiation condition) states using the force (F) and indentation (δ) data obtained from the experiments. Thus chapter 5 focuses on the various analytical models existing in literature and chooses the appropriate analytical model for mESC followed by further indentation studies on mESC to validate our research hypothesis that the mechanical property of undifferentiated mESC differs from early differentiating mESC.

Chapter 5: Analytical Models for Biological Cells

5.1 Introduction

One of the goals of this thesis is to characterize the mechanical property of mouse embryonic stem cells (mESC). To achieve this goal, it is important to study the various models proposed by researchers for characterizing the mechanical behavior of biological cells. Cell is a complex structure comprising of cell membrane, cytoplasm, cytoskeleton and nucleus as shown in figure 5.1. It is practically impossible to model all the components of a cell with perfection. However, one can get preliminary information regarding the cell mechanics by following an analytical approach. To our knowledge, there had been no studies to predict whether there exists any difference in mechanical behavior of mESC at various stages of differentiation towards a particular cell lineage. Thus, the present chapter considers various analytical models proposed in the literature for characterizing the mechanical property of an individual biological cell followed by an exhaustive analysis to choose an appropriate model for mESC. The chapter does not focus on complex mechanical and finite element models, because the first step is to observe whether there exists any difference in the mechanical behavior of mESC at various stages in the differentiation process. This could be achieved by following an analytical approach and calculating the elastic modulus of mESC. Upon successful achievement of this goal, we would focus on much more detailed analysis of an individual cell (future work). Thus, the review of complex mechanical and finite element models for biological cells is beyond the scope of the present work.

(a)

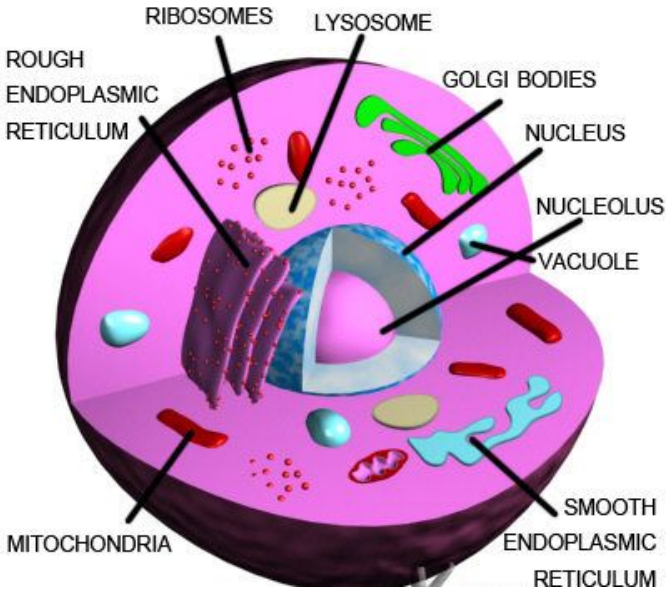

(b)

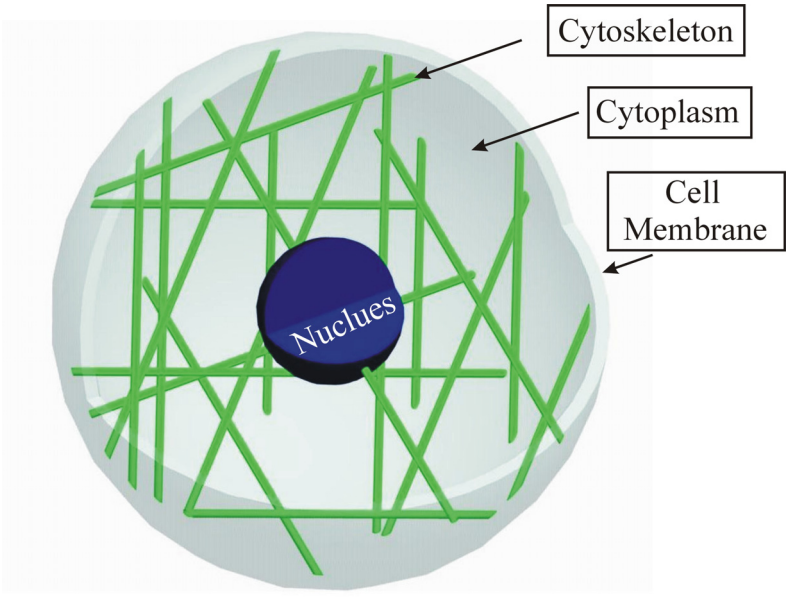

Figure 5.1 (a) Schematic of a biological cell

(Source: http://www.turbosquid.com/FullPreview/Index.cfm/ID/252419);

(b) Schematic of the cell from modeling perspective showing: cytoskeleton, cytoplasm and the nucleus

Since the past decade, researchers have used/proposed different analytical models to determine the mechanical properties of biological entities using AFM. Hertz and Sneddon contact models has been used extensively by physicists to quantify the mechanical property of biological samples using AFM [134-137, 150, 176]. The force-indentation relationship of a biological cell depends on the geometry of the tip. Solid contact models have been proposed in the literature for various tip geometries: sphere [138], cylinder [139], cone [140], pyramid [141], blunt cone [142], blunt pyramid [143]. Also JKR and DMT theories [147] proposed analytical models for adhesive contact between two spherical bodies. The JKR theory was extended to a blunt conical indenter by Sun et al [177]. A capsule model was also proposed to model the mechanical behavior of a cell membrane. The model was proposed for cylindrical [166] and spherical tip [178]. We describe each of the above mentioned models in this chapter in sections 5.2 – 5.7 followed by a detailed analysis in section 5.8 to choose an appropriate model for mESC.

5.2 Hertz Theory: Contact of Spheres

In 1881, Hertz solved the problem of contact between two spherical solids [138]. In this section we present a brief description of the model. It considers two elastic spheres of radii R_1 and R_2 as shown in figure 5.2. If no force is applied between the two spheres, the contact occurs only at point O (figure 5.2a). When one sphere is pressed on the other with a force F, the centers of the two spheres approach by a quantity δ (figure 5.2b) and the contact is achieved on a circle of radius a.

(a)

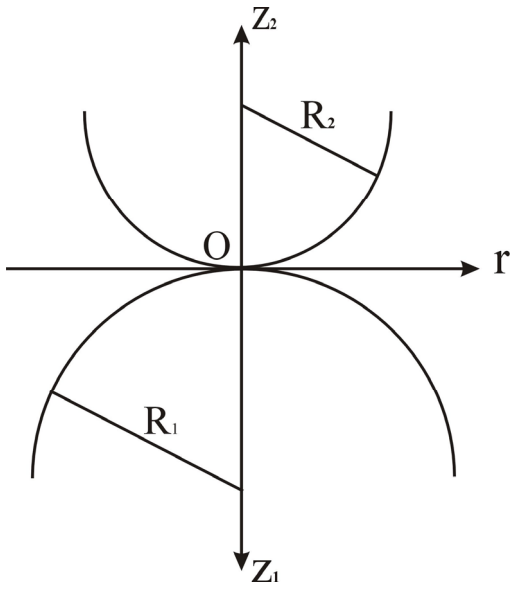

(b)

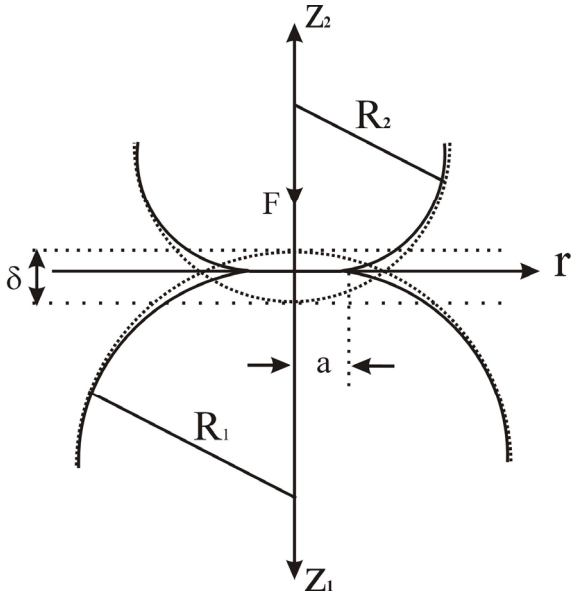

Figure 5.2 (a) Two spheres in contact: (a) at a single point O; (b) by a circle of contact of radius *'a'*. The broken lines in (b) show the surfaces as they would be in the absence of any deformation, while the continuous lines show the surfaces of deformed bodies.

The assumptions of Hertz model can be summarized as follows:

- The spheres are elastic, isotropic and homogeneous.
- The strains are small, i.e. $a << R$, where 'a' is the contact radius and 'R' is the relative radius of curvature given by equation (5.3).
- No adhesion and friction occurs at the interface.
- The contact geometry is assumed to be axisymmetric and the force 'F' applied along the axis of symmetry.

The force (F) versus indentation (δ) relationship is given by [138]:

$$F = \frac{4}{3} E^* R^{1/2} \delta^{3/2} \tag{5.1}$$

where, E^* is the combined modulus of sphere 1 and 2 given by:

$$\frac{1}{E^*} = \frac{1-\nu_1^2}{E_1} + \frac{1-\nu_2^2}{E_2} \tag{5.2}$$

R is the relative curvature of the sphere 1 and 2 given by:

$$\frac{1}{R} = \frac{1}{R_1} + \frac{1}{R_2} \tag{5.3}$$

E_1, ν_1, and R_1 represent the elastic modulus, Poisson's ratio, and the radius of sphere 1. Similarly E_2, ν_2, and R_2 represent the elastic modulus, Poisson's ratio, and the radius of the sphere 2. The radius of contact is 'a' given by [138]:

$$a = (R\delta)^{1/2} \tag{5.4}$$

The Hertz model has been used by researchers to characterize the mechanical behavior of various biological entities [136, 150].

5.3 Sneddon Theory

Sneddon extended the Hertz theory and studied the contact mechanics between a cylindrical indenter and a flat sample of infinite thickness [139]. He also developed a force-indentation relationship for a conical tip indenting a flat sample of infinite thickness [140]. Since it is an extension of Hertz Theory, it is sometimes called as Hertz-Sneddon Theory. The assumptions made in the Hertz theory are applicable in this analysis. We present a brief description of the Sneddon theory for cylindrical and conical indenter in the following sub sections.

5.3.1 The Cylindrical Indenter

Consider a flat cylindrical indenter of radius '*a*' indenting an infinite elastic half space. A loading force (*F*) causes an indentation (δ) as shown in figure 5.3.

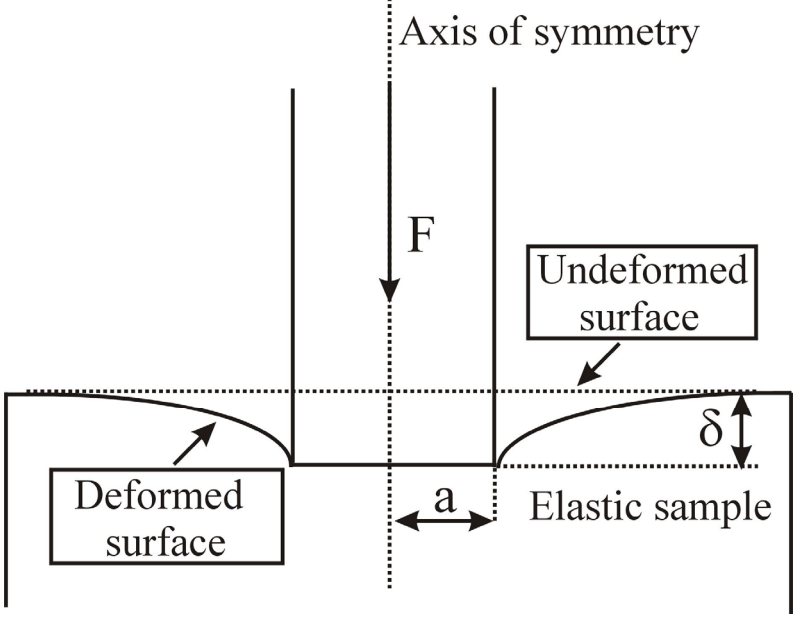

Figure 5.3. Cylindrical indenter deforming an infinite elastic half-space, where *F* is the loading force and δ is the indentation.

The force (F) versus indentation (δ) relationship is given by [139]:

$$F = 2E^{*}a\delta \tag{5.5}$$

where, E^{*} is the combined modulus of the cylinder and the sample given by equation (5.2), where subscript 1 refers to the cylinder and 2 to the specimen. As seen from figure 5.3, the radius of contact is given by '*a*' (the radius of the cylinder). Hence the contact radius remains constant over the entire indentation process.

The cylindrical indenter model is seldom used by AFM researchers to predict the mechanical behavior of biological entities. One of the reasons is that most AFM tips are either pyramidal or spherical in shape, thus eliminating the possibility of using the model.

5.3.2 The Conical Indenter

Consider a sharp conical indenter with a semi-angle α indenting an infinite elastic half space as shown in figure 5.4.

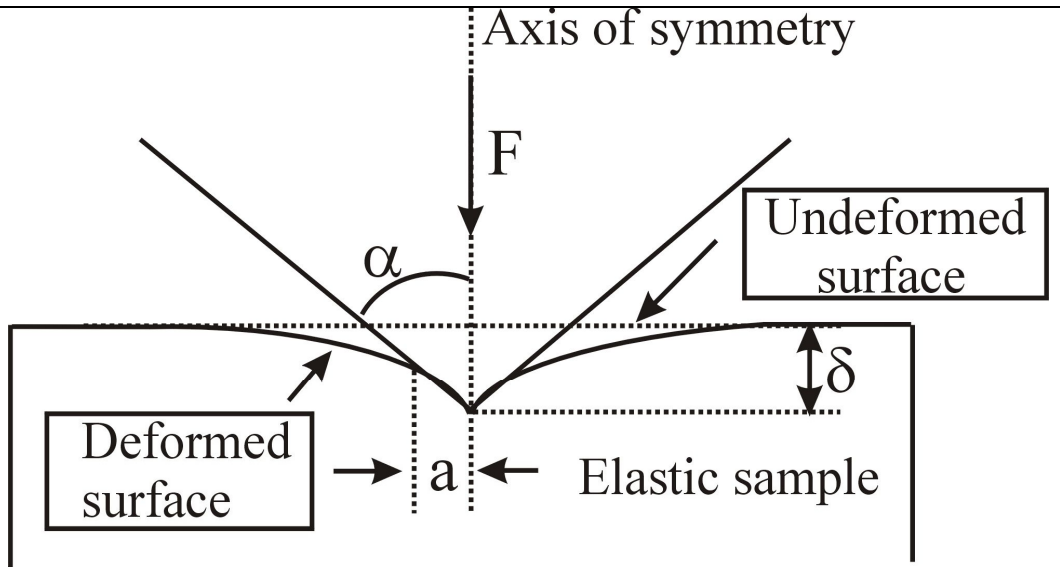

Figure 5.4. Conical indenter deforming an infinite elastic half-space, where F is the loading force and δ is the indentation.

The general expression for the loading force (F) is given by [140]:

$$F = \frac{\pi}{2} a^2 E^* \cot\alpha \tag{5.6}$$

where, E^* is the combined modulus of the cone and the sample given by equation (5.2), where subscript 1 refers to the cone and 2 to the specimen. '*a'* is the contact radius.

The depth of penetration of the apex of the indenter beneath the specimen free surface (shown as dotted line in figure 5.4) is given by [140]:

$$u_z = (\frac{\pi}{2} - \frac{r}{a}) a \cot\alpha \tag{5.7}$$

Substituting $r = 0$ in the above equation, we get the maximum depth of penetration represented by *'δ'* given by:

$$\delta = \frac{\pi}{2} a \cot\alpha \tag{5.8}$$

From equations (5.6) and (5.8), the force (F) versus indentation (δ) relationship is given by:

$$F = \frac{2E^* \tan\alpha}{\pi} \delta^2 \tag{5.9}$$

The above relationship had been used extensively by the AFM community to deduce the elastic modulus of biological entities [134, 135, 137, 176]. The primary reason is that most of the AFM cantilevers have pyramidal tips which are used for imaging and subsequently probe different parts of the cell to obtain force-indentation relationship.

5.4 The Pyramidal Indenter

A solid contact model for a regular pyramid indenting an infinite elastic half space has been numerically developed by Bilodeau [141]. The assumptions made in the Hertz and Sneddon theories are applicable here. Unlike conical indenter, the stress distribution for the pyramid has singularities produced by the lateral edges joining each face of the pyramid. The lateral faces of the pyramid are isosceles triangles and the base is an *n*-sided polygon. The boundary of the contact area is assumed to be a polygon of the same type as the base of the pyramid. Thus, the polygons corresponding to tetrahedral and quadrilateral pyramid are triangle and square respectively.

For a tetrahedral pyramid (n = 3), the force (F) – indentation (δ) relationship is given by [141]:

$$F = \frac{8E^* \tan(\theta)}{9}(\delta^2) \tag{5.10}$$

where *'θ'* is the vertex angle of the triangle face. The contact area *'A'* in terms of the indentation *'δ'* is given by:

$$A = 1.895\delta^2 \tan^2 \theta \tag{5.11}$$

For a quadrilateral pyramid ($n = 4$), the force (F) – indentation (δ) relationship is given by [141]:

$$F = \frac{3E^* \tan(\theta)}{4}(\delta^2) \tag{5.12}$$

The contact area *'A'* in terms of the indentation *'δ'* is given by:

$$A = 1.579\delta^2 \tan^2 \theta \tag{5.13}$$

Most of the AFM cantilever tips are pyramidal in shape rather than a cone. Hence the pyramidal indenter model best describes the contact mechanics compared to conical indenter model during AFM-cell interaction. The pyramidal model has been used to compute the mechanical properties of lung epithelial cells [144] and leukemia cells [145].

5.5 Blunt Indenters

In the previous sections we have considered the mechanical interaction of a sharp tip with an infinite elastic half space. However, most of the AFM cantilevers have a spherical shape (radius < 10 nm) at the end that merges smoothly with the tip geometry. Also the possibility of tip damage cannot be ruled out at nanoscale, which will result in truncated tip geometry. The inevitable tip defects of sharp indenters might result in an incorrect computation of elastic modulus of the sample. Briscoe et al [142] were the first to address these concerns and developed an analytical model for blunt conical indenter. Later, Rico et al [143], developed a contact model taking into account the blunt geometry of a pyramidal indenter. We will give a brief description of each model in the following subsections.

5.5.1. Blunt Conical Indenter

Consider a blunt cone indenting an infinite elastic half space as shown in figure 5.5. The assumptions made by Sneddon model for a sharp conical indenter are applicable here. The model calculates the elastic modulus of the specimen without estimating the contact area between the tip and the specimen.

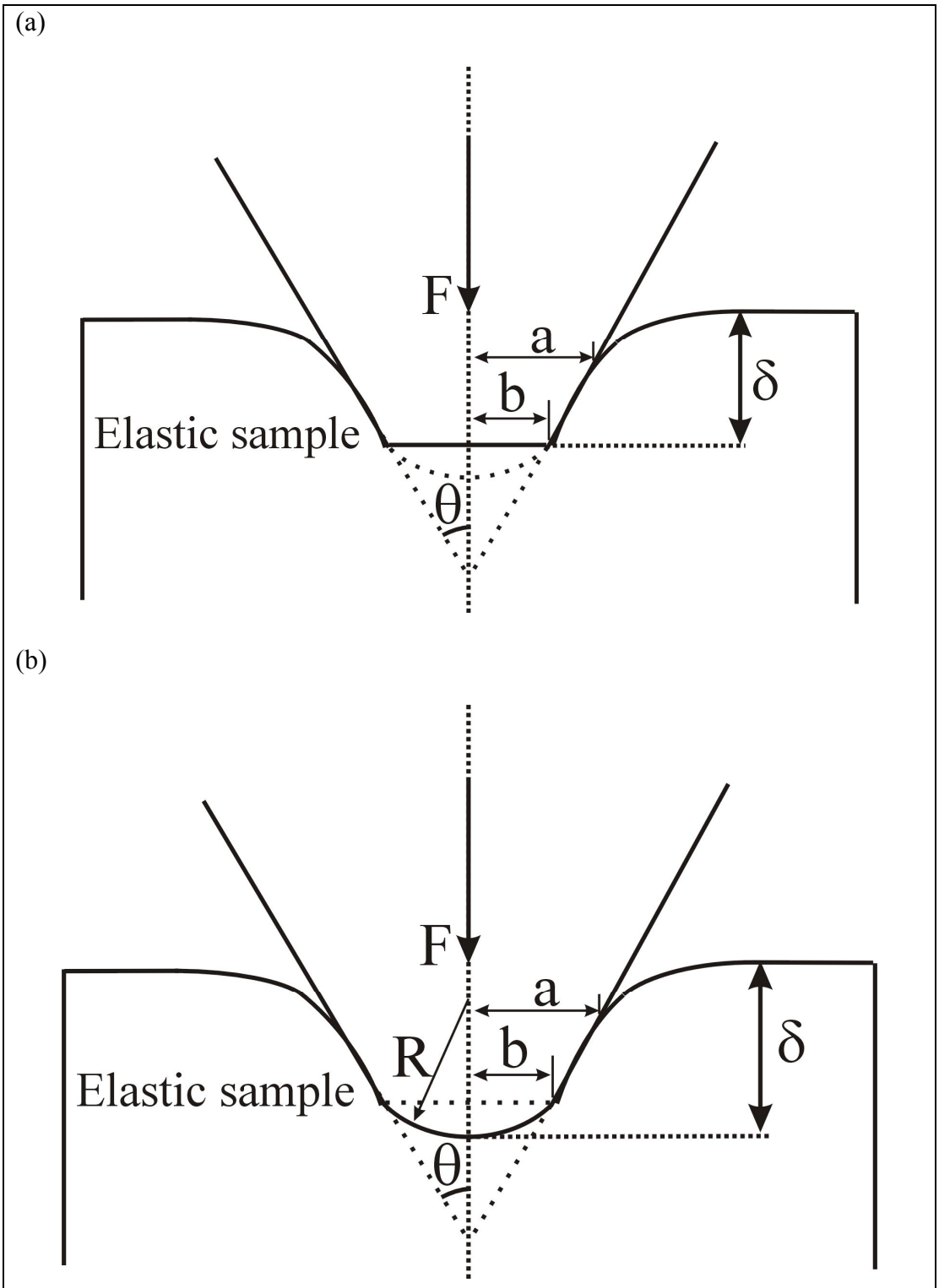

Figure 5.5 Geometric model for: (a) a truncated cone, and (b) a cone with a spherical tip indenting an infinite elastic half space

The relationship between loading force (F) and indentation (δ) is given by (as shown in figure 5.5) [142]:

$$P = 2E^* \left\{ a\delta - \frac{a^2}{2\tan\theta}\left[\frac{\pi}{2} - \arcsin\left(\frac{b}{a}\right)\right] - \frac{a^3}{3R} + \left(a^2 - b^2\right)^{1/2}\left(\frac{b}{2\tan\theta} + \frac{a^2 - b^2}{3R}\right)\right\} \quad (5.14)$$

The radius of contact *'a'* can be derived from the following expression [142]:

$$\delta + \frac{a}{R}((a^2 - b^2)^{1/2} - a) - \frac{a}{\tan\theta}\left[\frac{\pi}{2} - \arcsin\left(\frac{b}{a}\right)\right] = 0 \quad (5.15)$$

Two special cases of the blunt cone are considered here:

Truncated Cone: For a truncated cone (figure 5.5a), R $\rightarrow \infty$. Substituting it in the general expression for the loading force (5.14), we get:

$$P = \frac{2E^*}{\tan\theta}\left\{\delta a \tan\theta - \frac{a^2}{2}\left[\frac{\pi}{2} - \arcsin\left(\frac{b}{a}\right)\right] + \frac{b}{2}(a^2 - b^2)^{1/2}\right\} \quad (5.16)$$

An expression involving the radius of contact, a is given by the same condition ($R \rightarrow \infty$), substituted in (5.15):

$$\delta \tan\theta - a\left[\frac{\pi}{2} - \arcsin\left(\frac{b}{a}\right)\right] = 0 \quad (5.17)$$

Substituting $b = 0$ in (5.16) and (5.17), we obtain the force-indentation relationship for a sharp cone as:

$$F = \frac{2E^* \tan\alpha}{\pi}\delta^2 \quad (5.18)$$

The above relationship is the same as obtained by Sneddon for a sharp conical indenter shown in equation (5.9). Substituting $b = a$ in equation (5.16), we get the force-indentation relationship for a cylindrical indenter:

$$F = 2E^{*} a\delta \tag{5.19}$$

The above relationship is the same as obtained by Sneddon for a cylindrical indenter as shown in equation (5.5).

Cone with a spherical tip: The geometry of an AFM cantilever tip can be described as a spherical tip merging smoothly with the body of a cone (figure 5.5b). The profile of the tip is defined by *'R'* and the corresponding value of *'b'* in equations (5.14) and (5.15) is given by:

$$b = R\cos\theta \tag{5.20}$$

Briscoe et al [142] used the blunt conical indenter model to compute the elastic modulus of poly(isobutylene) rubber. Later on, the model was used to estimate the elastic modulus of cardiac cells, skeletal muscle cells and the endothelial cells [146].

5.5.2. Blunt Pyramidal Indenter

Consider a blunt n-sided regular pyramid of semi-included angle *'θ'*, tip defect *'h'* and spherical radius *'R'* indenting a sample (infinite elastic half space). A section of the blunted pyramid and the indentation can be represented by figure 5.5b. The assumptions made by Bilodeau model [141] are applicable here. However, the cross section area at any indentation depth is approximated to be circular with the center of the circle on the axis of the pyramid. The radius of the circle is represented by *'a'*. The blunt pyramid was modeled as a spherical tip that transforms smoothly into an n-sided pyramid (figure 5.5b). For this case, the radial distance *'b',* is given by (5.20).

A general relationship between loading force *(F)* and indentation *(δ)* for a n-sided blunt pyramid indenting a sample is given by [143]:

$$F = \frac{2E}{1-\nu^2}\left\{\delta a - A - \frac{a^3}{3R} + B\right\} \tag{5.21}$$

where,

$$A = \frac{n}{\pi}\sin\left(\frac{\pi}{n}\right)\frac{a^2}{2\tan\theta}\left(\frac{\pi}{2} - \arcsin\frac{b}{a}\right) \tag{5.22}$$

$$B = \left(a^2 - b^2\right)^{1/2}\left[\frac{n}{\pi}\sin\left(\frac{\pi}{n}\right)\frac{b}{2\tan\theta} + \frac{\left(a^2 - b^2\right)}{3R}\right] \tag{5.23}$$

The effective contact radius *'a'* can be obtained from the following relationship [143]:

$$\delta - \frac{a}{\tan\theta}\frac{n}{\pi}\sin\left(\frac{\pi}{n}\right)\left(\frac{\pi}{2} - \arcsin\frac{b}{a}\right) + \frac{a}{R}\left[\left(a^2 - b^2\right)^{1/2} - a\right] = 0 \tag{5.24}$$

For a regular 4-sided pyramid (quadrilateral), (5.21) and (5.24) simplify to:

$$F = \frac{2E}{1-\nu^2}\left\{\delta a - A_1 - \frac{a^3}{3R} + B_1\right\} \tag{5.25}$$

where,

$$A_1 = \frac{2^{1/2}}{\pi}\frac{a^2}{\tan\theta}\left(\frac{\pi}{2} - \arcsin\frac{b}{a}\right) \tag{5.26}$$

$$B_1 = \left(a^2 - b^2\right)^{1/2}\left[\frac{2^{1/2}}{\pi}\frac{b}{\tan\theta} + \frac{\left(a^2 - b^2\right)}{3R}\right] \tag{5.27}$$

$$\delta - \frac{a}{\tan\theta}\frac{2^{3/2}}{\pi}\left(\frac{\pi}{2} - \arcsin\frac{b}{a}\right) + \frac{a}{R}\left[\left(a^2 - b^2\right)^{1/2} - a\right] = 0 \tag{5.28}$$

Substituting $b \to 0$ in equation (5.25) and (5.28), Rico et al [143] obtained the force-indentation relationship and the effective radius of contact respectively for a sharp 4-sided pyramid:

$$F = \frac{1}{2^{1/2}} \frac{E \tan\theta}{(1-\nu^2)} \delta^2 \tag{5.29}$$

$$a = \delta \tan\theta / 2^{1/2} \tag{5.30}$$

Similarly, the force-indentation relationship and the effective contact radius for a truncated n-sided pyramid is obtained by substituting R $\rightarrow \infty$ in (5.21) and (5.24) respectively followed by for a truncated 4-sided pyramid in equations (5.25) and (5.28) respectively. Rico et al [143] used the blunt pyramid model to compute the elastic modulus of agarose gels and A549 alveolar epithelial cells. They found that the elastic modulus values were lower than that obtained with spherical tip fitted with Hertz model.

5.6 Capsule Model

A capsule model considers the biological cell to be composed of a cell membrane and cytoplasm [166, 178]. The model assumes that the cell membrane is a thin film and that the inner cytoplasm provides a uniform hydrostatic pressure on the membrane. Sun et al [166], developed a capsule model for characterizing the mechanical properties of mouse oocyte and embryo zona pellucida. The model assumes the following:

- The cell membrane is linear elastic
- The deformation of the cell membrane is caused by stretching and the bending is neglected
- The cell volume is constant
- The cell is free of initial membrane stress or residual stress

Consider a cylindrical indenter of radius *c* which exerts a force *F* on the membrane, creating a dimple with radius *a* and depth δ and semicircular curved surface with radius *R* as shown in figure 5.6.

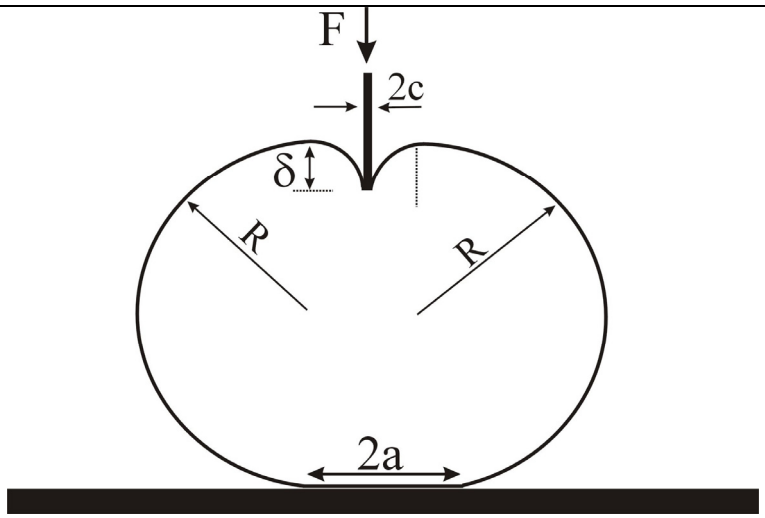

Figure 5.6. A cylindrical indenter deforming a cell considered as a capsule. *F* and δ are the loading force and indentation respectively.

The force (*F*) versus indentation (δ) relationship is given by [166]:

$$F = \frac{2\pi Eh\delta^3}{a^2(1-\nu)}\left[\frac{3-4\zeta^2+\zeta^4+2\ln\zeta^2}{\left(1-\zeta^2\right)\left(1-\zeta^2+\ln\zeta^2\right)^3}\right] \tag{5.31}$$

where $\zeta = c/a$. Also *E*, *v,* and *h* are the elastic modulus, Poisson's ratio and thickness of the cell membrane respectively. By volume conservation, the following relationship is obtained between *a,* w_d, and *R,* where R is the radius of the cell after indentation (figure 5.6) [166]:

$$4R^3 + 3\pi aR^2 + 6a^2R = 4R_0^3 + \frac{3\delta}{2}\left[\frac{a^2(1-\zeta^2)^2}{1-\zeta^2+\ln\zeta^2}\right] \tag{5.32}$$

In the above equation, R_0, is the radius of the cell before indentation.

Lulevich et al [178] developed an analytical expression for the capsule model indented by a sphere. The assumptions listed by Sun et al [166] are applicable here. However, the present model considers stretching as well as bending of the cell membrane. In addition, the model assumes that the shape of the cell (capsule) is spherical except in the contact regions as shown in figure 5.7.

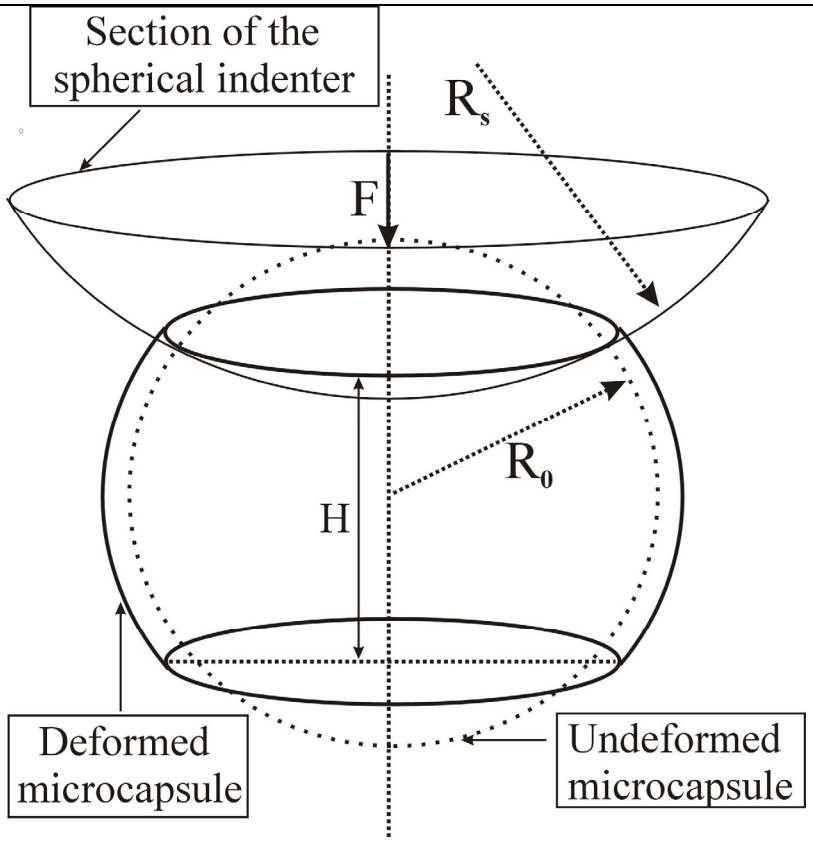

Figure 5.7. Schematic of the microcapsule indented by a sphere with a loading force *F*.

The relationship between the loading force, *F*, and the relative deformation, *ε*, is given by [178]:

$$F = 2\pi \frac{E}{1-\nu} h R_0 \frac{\left[1 + R_0/(2R_s)\right]^2}{\left(1 + R_0/R_s\right)^4} \varepsilon^3 + \frac{\pi}{2(2)^{1/2}} E h^2 \varepsilon^{1/2} \qquad (5.33)$$

where *E, v,* and *h* are the elastic modulus, Poisson's ratio and thickness of the capsule membrane. R_0 and R_s is the radius of the capsule and the spherical indenter respectively. ε is the relative deformation of the capsule given by [178]:

$$\varepsilon = 1 - H / 2R_0 \tag{5.34}$$

where, *H* is the height of the capsule after indentation as shown in figure 5.7.

The first and the second term in (33) represent the force causing stretching and bending of the capsule membrane respectively. The model was used to calculate the elastic modulus of live cells [150].

5.7 JKR and DMT Theory: Contact of spheres with adhesion

The JKR and DMT [147] contact models were proposed which take into account the adhesion between two elastic spheres. The JKR theory modifies the Hertz theory by introducing an apparent Hertz load or the equivalent load in the absence of adhesion that produces the enlarged contact area. The model assumes that the adhesion force operates over a short distance within the contact region. According to this theory, contact radius *a*, indentation δ, and pull-off force P_{off}, are represented by the following equations [147]:

$$a^3 = \frac{3R}{4E^*}\left(F + 3\pi Rw + \sqrt{6\pi RwF + (3\pi Rw)^2} \right) \tag{5.35}$$

$$\delta = \frac{a^2}{R} - \sqrt{\frac{2\pi wa}{E^*}} \tag{5.36}$$

$$P_{off} = \frac{3}{2}\pi Rw \tag{5.37}$$

where, E^* and *R* are the combined elastic modulus of the specimen (equation 5.2) and

relative radius of curvature (equation 5.3) given in Hertz Theory. F is the loading force, and w is the adhesion energy.

Substituting $w = 0$, in equations (5.35) and (5.36) and combining we get:

$$F = \frac{4}{3} E^* R^{1/2} \delta^{3/2} \tag{5.38}$$

The above equation represents the force-indentation relationship derived by Hertz. Hence, in the absence of adhesion, the JKR theory reduces to classical Hertz theory. A Hertzian contact and a JKR contact under the same load F are compared schematically in figure 5.8. In the later case, the area of contact and the indentation are larger.

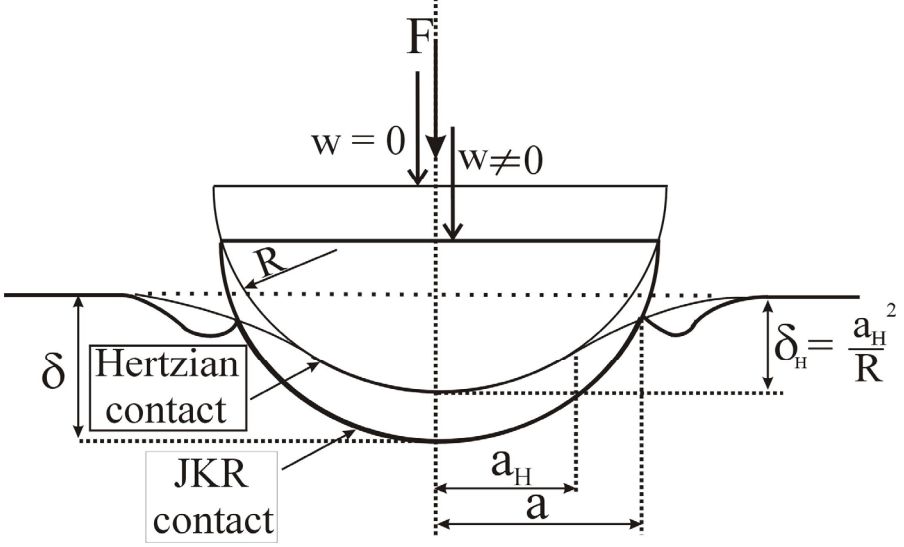

Figure 5.8. Comparison between a JKR contact ($w \neq 0$) and a Hertzian contact ($w = 0$). a and δ are the contact radius and indentation for a JKR contact respectively. a_H and δ_H are the contact radius and indentation for a Hertzian contact respectively.

In 1975, Derjaguin, Muller, and Toporov [147] gave their theory (the DMT theory) which takes into account the adhesion force between two spheres. Unlike JKR theory,

the deformed surface profile is assumed to follow Hertz model. The DMT theory assumes the adhesion force operates just outside the contact zone where the surfaces are small distance apart. According to the DMT model, contact radius a, indentation δ and pull-off force P_{off} are represented by the following equations [147]:

$$a^3 = \frac{3R}{4E^*}\left(F + 2\pi R w\right) \tag{5.39}$$

$$\delta = \frac{a^2}{R} \tag{5.40}$$

$$P_{off} = 2\pi R w \tag{5.41}$$

Tabor [148] identified the applicability of the JKR and DMT theories to opposite extremities of the relationship between sample stiffness and the range of adhesive force. The JKR theory was found to be valid for the indentation of relatively compliance materials with probes of relatively large radii and strong adhesive forces. On the other hand, the DMT theory applies to stiff materials and probes with small radii and weak adhesive forces. The two theories have been used to predict the mechanical behavior of cells [129].

5.7.1 Extension of JKR Theory to a Blunt Conical Indenter

The JKR theory was extended by Sun et al [177] to a blunt conical indenter of tip radius R and semi vertical angle α. The assumptions made by JKR theory are applicable here.

The loading force F and indentation δ are given by the following equations:

$$F = \frac{2E}{1-\nu^2}\left[\frac{A}{2R}(aA + \frac{a^2 - A^2}{2}X - aY)\right] \tag{5.42}$$

$$\delta = \frac{aA}{2R} X - Y \tag{5.43}$$

where

$$X = \left(\frac{\pi}{2} + \arcsin \frac{(a/A)^2 - 1}{(a/A)^2 + 1} \right) \tag{5.44}$$

$$Y = \left(\frac{2a\pi(1-\nu^2)\gamma_{12}}{E} \right)^{1/2} \tag{5.45}$$

The above model is suitable for characterizing the mechanical behavior of cells indented by AFM cantilever (pyramidal tip). Sun et al [177] used the model to calculate the elasticity of PDMS polymers with different degrees of cross-linking.

5.8 Appropriate Model for mESC

We hypothesize that the mechanical property of undifferentiated mESC differs from differentiating mESC. To address this hypothesis, we conducted single indentation studies on live and fixed mESC: undifferentiated and differentiating. In particular, we chose to perform indentation studies on undifferentiated, third day differentiating and sixth day differentiating mESC for both live as well as fixed cells. Initial experiments were performed with a pyramidal tip followed by a spherical tip. It induces lower stress concentration compared to a pyramidal tip. Also, the spherical tip has a large area of contact with the cell which results in averaging local variation in elastic modulus compared to that measured with a regular pyramidal tip. Thus, the spherical tip computes an average elastic modulus over a large area compared to local modulus computed by the pyramidal tip. (For details, please refer to chapter 6).

In this section, we present a thorough analysis to find an appropriate analytical model for mESC. We go through each of the analytical models mentioned in sections 5.2 –

5.7 and find out the model which appropriately describes the force versus indentation relationship for mESC. The appropriate model would compute the elastic modulus and give a preliminary insight regarding the mechanics of mESC. We will test the following models based on the geometry of the tip used in our experiments:

- Bilodeau model for undifferentiated, 3rd day differentiating and 6th day differentiated mESC indented by a pyramidal tip.
- Hertz model and capsule model for undifferentiated, 3rd day differentiating and 6th day differentiating mESC indented by a spherical tip.

mESC State	Number of Undifferentiated	Number of 3rd Day Differentiating	Number of 6th Day Differentiating
Live	10	10	10
Fixed	10	10	10

Table 5.1: Distribution of 60 mESC considered for experiments with (a) pyramidal tip, and (b) spherical tip. Hence, single indentation studies were performed on 120 mESC.

In addition, we also present the force (loading and unloading) versus time profiles for each mESC indentation and determine whether force of adhesion exists between the tip and the sample. Accordingly we would also use the JKR and DMT theory based on the geometry of the tip. Single indentation studies were performed on 120 mESC: (a) 60 mESC with a pyramidal tip, and (b) 60 mESC with a spherical tip. The distribution of 60 mESC considered for experiments with each tip is shown in table 5.1.

Some of the analytical models described in the sections 5.2 – 5.7 can be represented by the following relationship:

$$F = g\delta^n \tag{5.46}$$

where F is the loading force, δ is the indentation, g is a geometrical factor and n is the index of deformation. Both g and n are functions of indenter geometry. They also depend on the model i.e. solid/capsule. Table 5.2 gives a summary of the models which can be represented by (5.46). From the table, it can be seen that the value of n is 2 for both conical and pyramidal indenter. In fact, it has been shown that the force-indentation relationship for a pyramidal indenter with infinite sides is similar to a conical indenter [141].

Model	Indenter geometry	Value of n
Solid	Sphere (Hertz model)	1.5
	Cylinder (Sneddon model)	1.0
	Cone (Sneddon model)	2.0
	Pyramid (Bilodeau model)	2.0
Capsule	Cylinder	3.0

Table 5.2: The value of n (index of deformation) for few indenter geometries and models.

5.8.1 Indentation Studies with Pyramidal Tip

The force-indentation relationship obtained with a pyramidal indenter cannot be described by the following models because of the geometry of the indenter: Hertz theory (spherical indenter), Sneddon theory (cylindrical and conical indenter), and

capsule model (cylindrical and spherical indenters). We used a sharp pyramidal tip in all our experiments, therefore the blunt conical and pyramidal indenter models will not be applicable. These models will be chosen when we use a blunt tip for experiments. Tetrahedral and quadrilateral pyramidal indenters were used for fixed and live mESC respectively. Figure 5.9 and 5.10 show the geometry of the indenters. Hence, we chose Bilodeau model to determine whether it appropriately predicts the force-indentation relationship of mESC obtained with a pyramidal indenter. We also present the force (loading and unloading) versus time profiles and determine whether force of adhesion exists between the tip and the sample. Accordingly we would also use the JKR theory (blunt conical indenter).

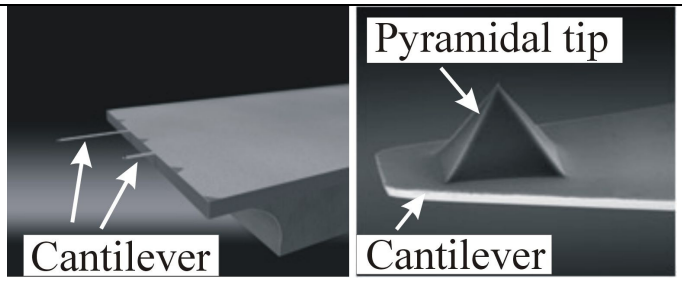

Figure 5.9. PNP-DB Pyrex Nitride probe (quadrilateral tip) for live mESC studies (figure modified from the website: http://www.nanoworld.com)

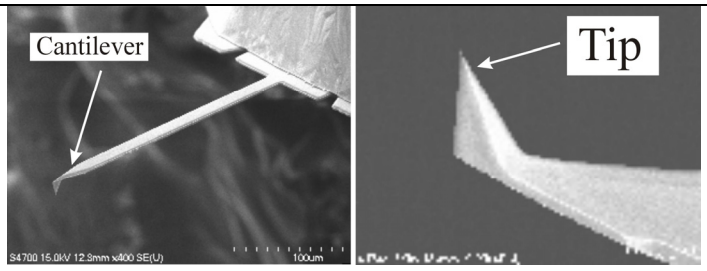

Figure 5.10. AC240TS silicon cantilever (tetrahedral tip) for fixed mESC studies (Source: http://probe.olympus-global.com/en/en/specsisoftE.html)

5.8.1.1 Live mESC – Pyramidal Tip

In this section we present the force-indentation profiles for live undifferentiated, 3rd day differentiating and 6th day differentiating mESC indented by a pyramidal tip. The cell indentation range was 2 – 2.5 µm. The profiles are described by Bilodeau model with the corresponding R^2 values. We also show the force (loading and unloading) versus time profiles for each live mESC.

LIVE UNDIFFERENTIATED mESC

(a)

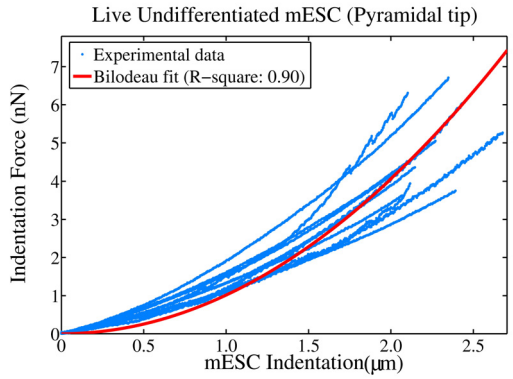

(b)

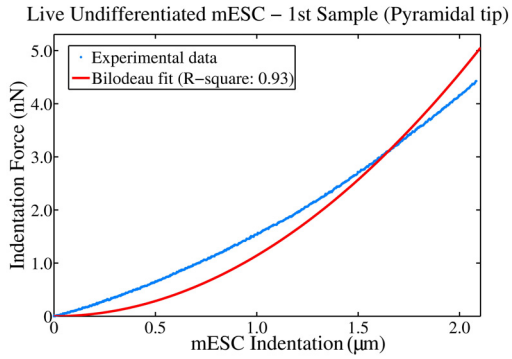

Figure 5.11: Force (F) versus cell indentation (δ) for live undifferentiated mESC: (a) 10 samples; (b) first sample

(a)

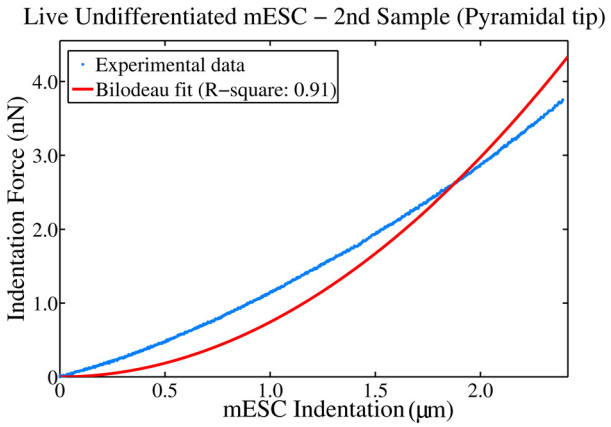

(b)

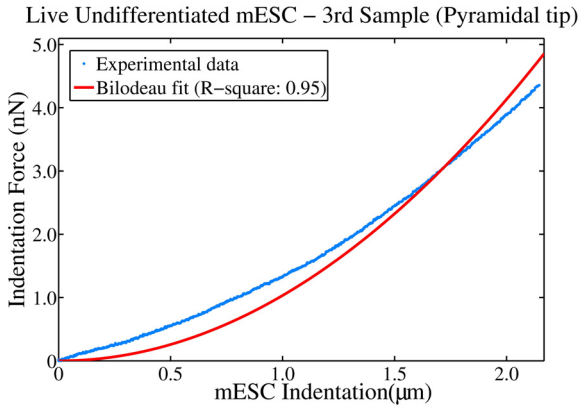

Figure 5.12: Force (F) versus cell indentation (δ) for live undifferentiated mESC (a) second sample; (b) third sample

Sample	1	2	3	4	5	6	7	8	9	10
R^2	0.93	0.91	0.95	0.91	0.92	0.94	0.97	0.99	0.99	0.95

Table 5.3: R^2 value obtained with the Bilodeau fit for 10 samples of live undifferentiated mESC.

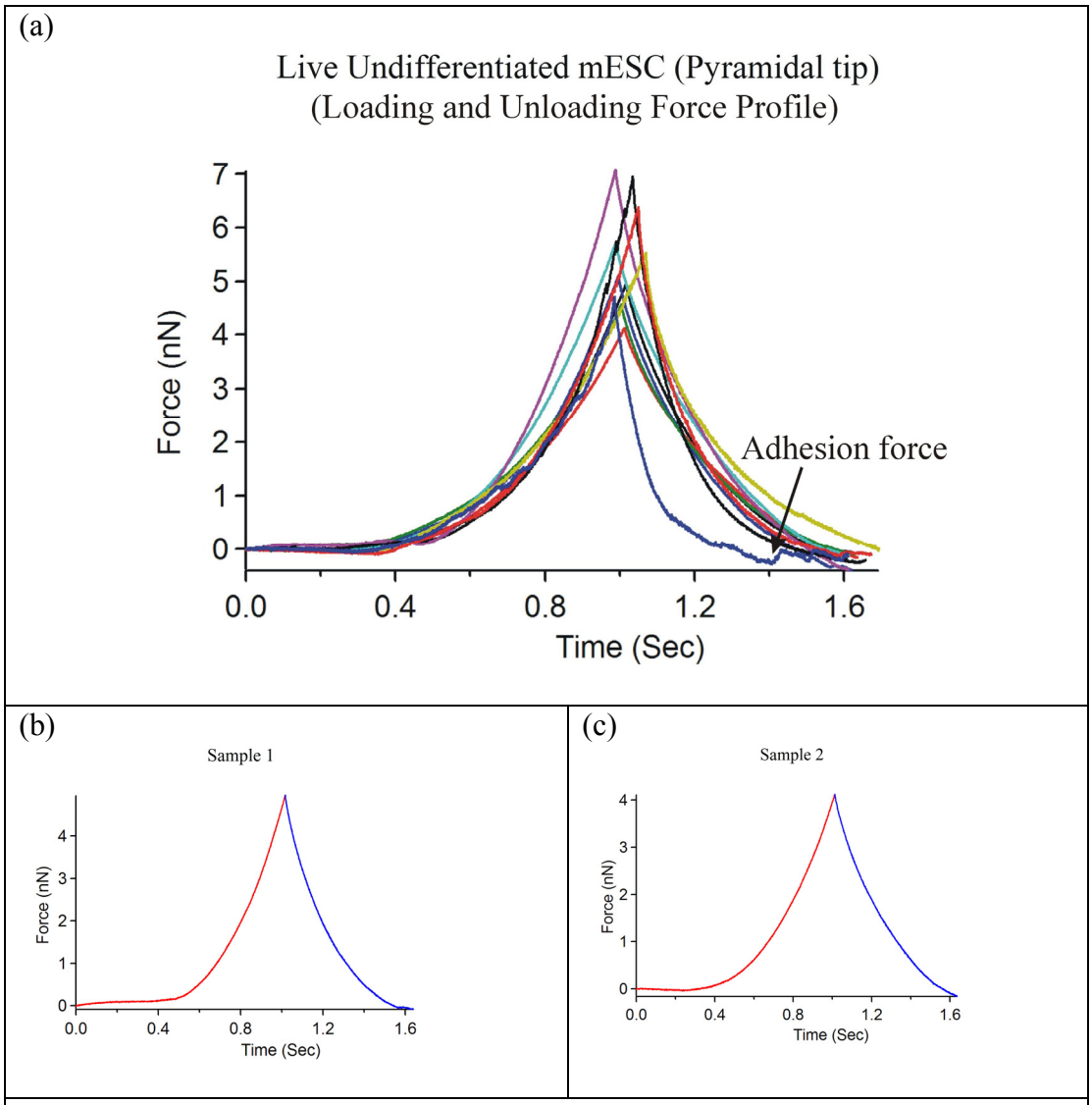

Figure 5.13: Force (loading and unloading) versus time profile obtained for: (a) 10 samples of live undifferentiated mESC. As observed from the figure, force of adhesion does not exist between the tip and the sample except for one of them, (b) sample 1, and (c) sample 2.

We observe that the force of adhesion exists only for one sample (figure 5.13a). One of the reasons for the adhesion force could be due to the wear of the pyramidal tip [179]. Hence, in this case we cannot use the JKR theory applicable to blunt conical

indenter. From figures 5.11 and 5.12, we observe that the force-indentation curves of live undifferentiated mESC can be appropriately described by the Bilodeau model. The R^2 values obtained with: (a) the fit for each live undifferentiated mESC is always greater than 0.90 as shown in table 5.3 (for best fit: $R^2 = 1$) and, (b) the average fit for all the 10 samples is 0.90 (figure 5.11a). Thus, we infer from the above analysis that the force-indentation curves for live undifferentiated mESC probed by a pyramidal indenter is best described by Bilodeau model.

LIVE DIFFERENTIATING (3rd Day) mESC

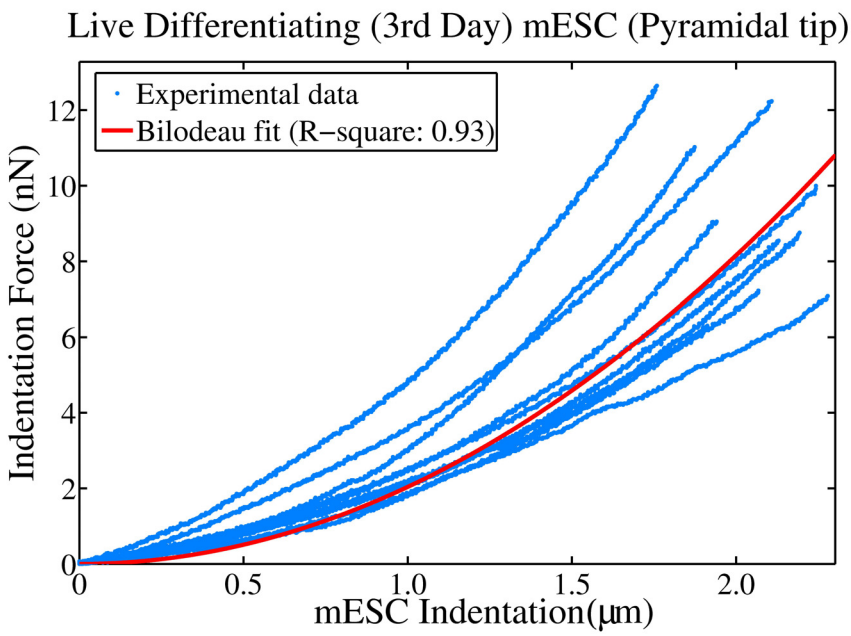

Figure 5.14: Force (F) versus cell indentation (δ) for 10 samples of live differentiating (3rd day) mESC.

Sample	1	2	3	4	5	6	7	8	9	10
R^2	0.99	0.97	0.99	0.97	0.98	0.99	0.97	0.99	0.98	0.97

Table 5.4: R^2 value obtained with the Bilodeau fit for 10 samples of live differentiating (3rd day) mESC.

(a)

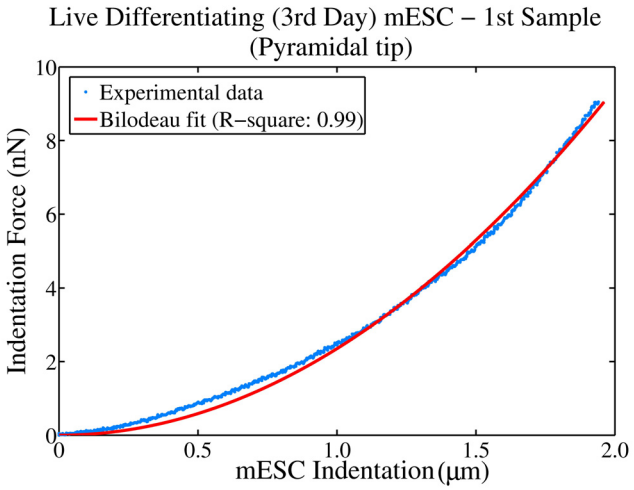

(b)

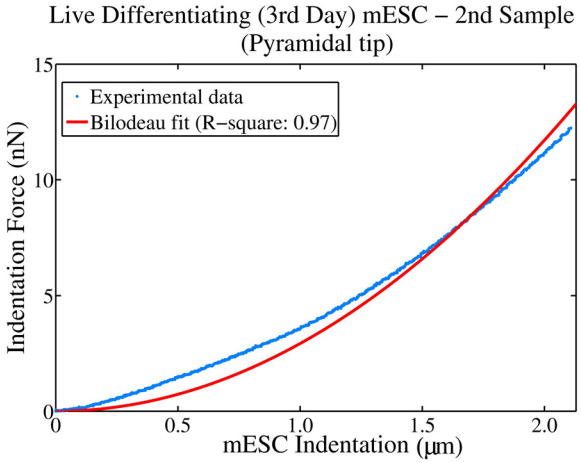

Figure 5.15: Force (F) versus cell indentation (δ) for live differentiating (3rd day) mESC (a) first sample; (b) second sample

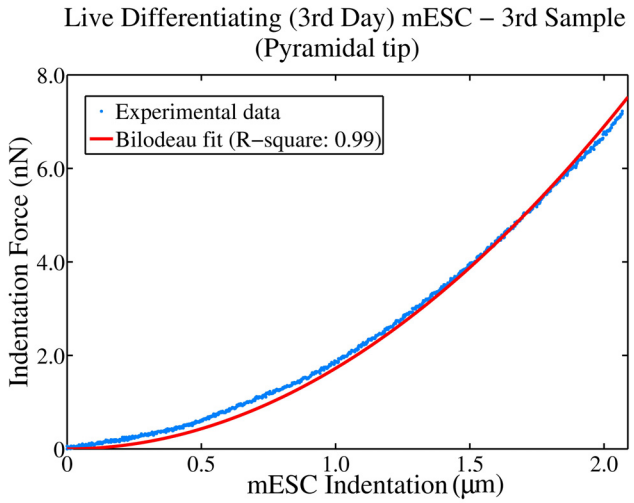

Figure 5.16: Force (F) versus cell indentation (δ) for third sample of live differentiating (3rd day) mESC.

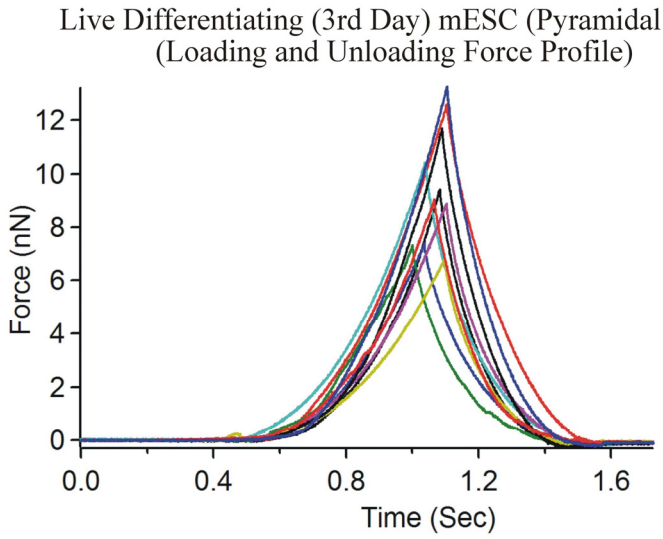

Figure 5.17: Force (loading and unloading) versus time profile obtained for 10 samples of live differentiating (3rd day) mESC. As observed from the figure, force of adhesion does not exist between the tip and the sample

(a)

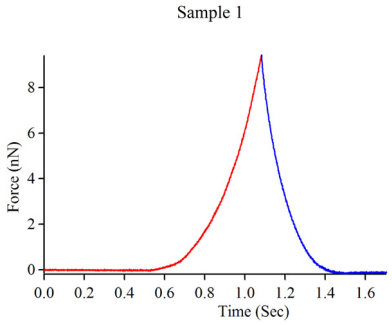

(b)

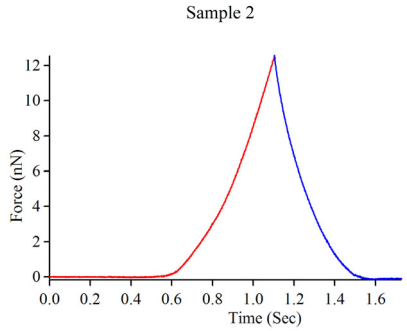

Figure 5.18 Force (loading and unloading) versus time profile obtained for: (a) sample 1, and (b) sample 2 of live differentiating (3rd day) mESC

We observe that the force of adhesion does not exist between the tip and the sample (figure 5.17). Hence, in this case we cannot use the JKR theory applicable to blunt conical indenter. From figures 5.14 – 5.16, we observe that the force-indentation curves of live differentiating (3rd day) mESC can be appropriately described by the Bilodeau model. The R^2 values obtained with: (a) the fit for each live differentiating (3rd day) mESC is always greater than 0.90 as shown in table 5.4 (for best fit: $R^2 = 1$) and, (b) the average fit for all the 10 samples is 0.93 (figure 5.14). Thus, we infer

from the above analysis that the force-indentation curves for live differentiating (3rd day) mESC probed by a pyramidal indenter is best described by Bilodeau model.

LIVE DIFFERENTIATING (6th Day) mESC

(a)

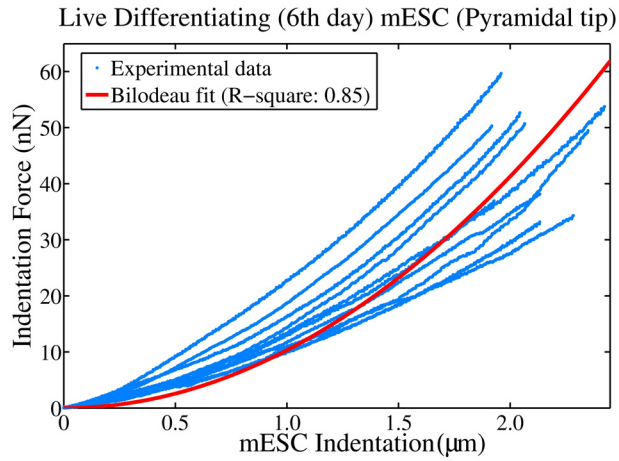

(b)

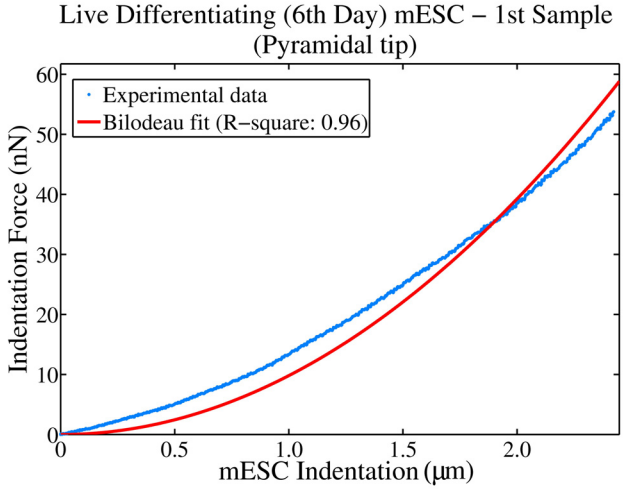

Figure 5.19: Force (F) versus cell indentation (δ) for live differentiating (6th day) mESC: (a) 10 samples; (b) first sample

(a)

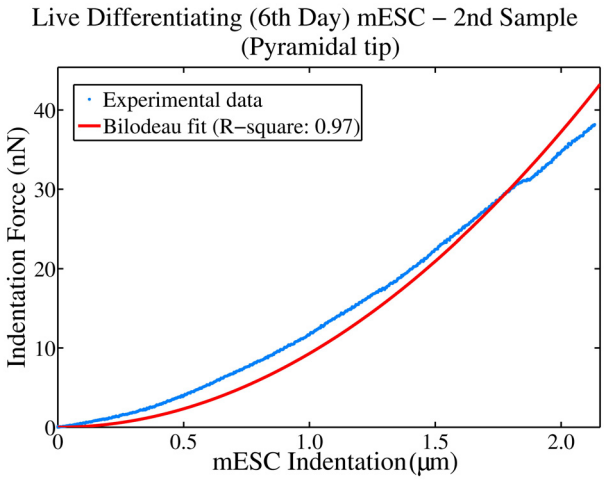

(b)

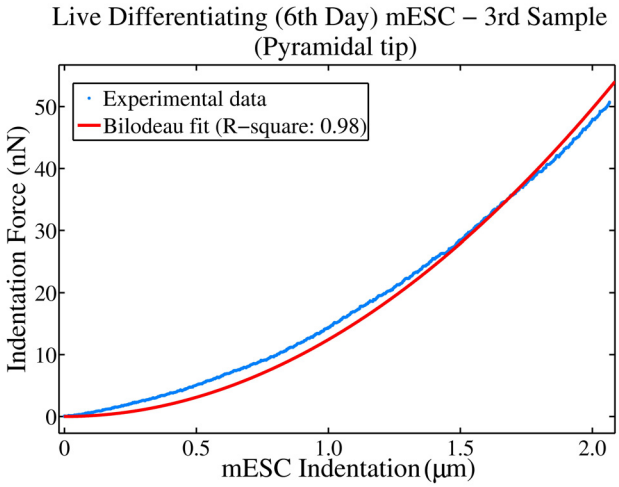

Figure 5.20: Force (F) versus cell indentation (δ) for live differentiating (6^{th} day) mESC (a) second sample; (b) third sample

Sample	1	2	3	4	5	6	7	8	9	10
R^2	0.96	0.97	0.98	0.96	0.99	0.95	0.91	0.97	0.93	0.97

Table 5.5: R^2 value obtained with the Bilodeau fit for 10 samples of live differentiating (6^{th} day) mESC.

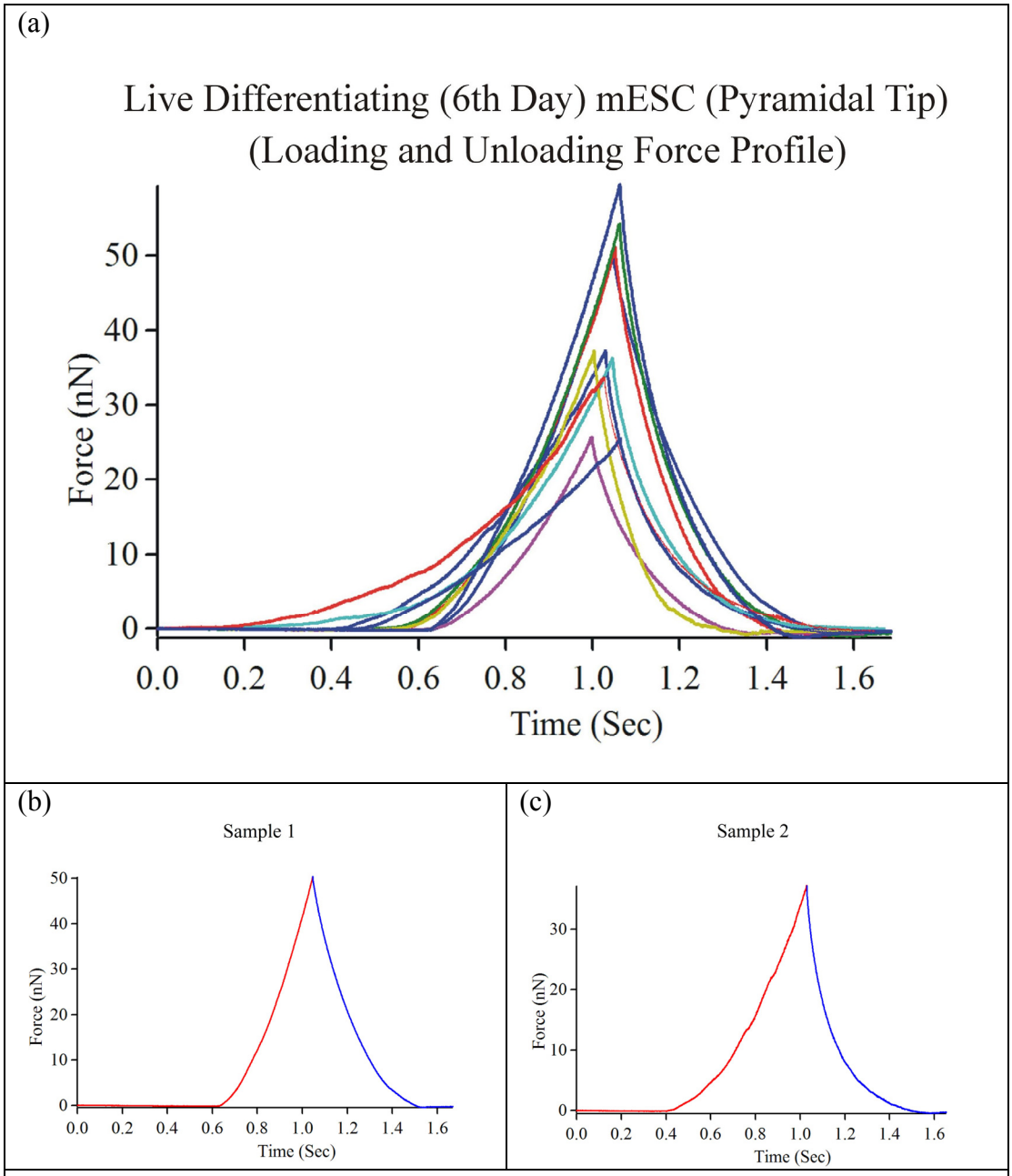

Figure 5.21. Force (loading and unloading) versus time profile obtained for: (a) 10 samples of live differentiating (6^{th} day) mESC. As observed from the figure, force of adhesion does not exist between the tip and the sample, (b) sample 1, and (c) sample 2.

We observe that the force of adhesion does not exist between the tip and the sample (figure 5.21). Hence, in this case we cannot use the JKR theory applicable to blunt conical indenter. From figures 5.19 – 5.21, we observe that the force-indentation curves of live differentiating (6^{th} day) mESC can be appropriately described by the Bilodeau model. The R^2 values obtained with: (a) the fit for each live mESC is always greater than 0.90 as shown in table 5.5 (for best fit: $R^2 = 1$) and, (b) the average fit for all the 10 samples is 0.85 (figure 5.19a). As a first approximation, we infer from the above analysis that the force-indentation curves for live differentiating (6^{th} day) mESC probed by a pyramidal indenter are best described by Bilodeau model.

5.8.1.2 Discussion

We observe that the force-indentation curves of live mESC indented by a pyramidal tip can be appropriately described by the Bilodeau model. The R^2 values obtained with the fit for: (a) each live mESC is always greater than 0.9 (for best fit: $R^2 = 1$) and (b) the average fit for all 10 samples is 0.90, 0.93 and 0.85 for live undifferentiated, 3^{rd} day differentiating and 6^{th} day differentiating mESC respectively. In addition, the force of adhesion between the tip and the sample was observed for only one sample of live undifferentiated mESC (see figure 5.13) and was not observed for all other samples of undifferentiated, 3^{rd} day differentiating and 6^{th} day differentiating mESC. Thus the JKR model does not describe the mechanical behavior of live mESC. We observe that the average maximum force attained for indenting (2 – 2.5 μm) 10 samples of live undifferentiated, 3^{rd} day differentiating and 6^{th} day differentiating mESC sample is approximately 5 nN, 10nN and 44 nN respectively. Computation of

elastic modulus and statistical analysis is presented in chapter 6. *As a first approximation, we conclude from the above analysis that the force-indentation curves for live mESC probed by a pyramidal indenter are best described by Bilodeau model.*

5.8.1.3 Fixed mESC – Pyramidal Tip

In this section we present the force-indentation profiles for fixed undifferentiated, 3rd day differentiating and 6th day differentiating mESC indented by a pyramidal tip. The profiles are described by the Bilodeau model with the corresponding R^2 values. The range of cell indentation was 2 – 2.5 μm. In addition, we show the force (loading and unloading) versus time profiles for each fixed mESC.

FIXED UNDIFFERENTIATED mESC

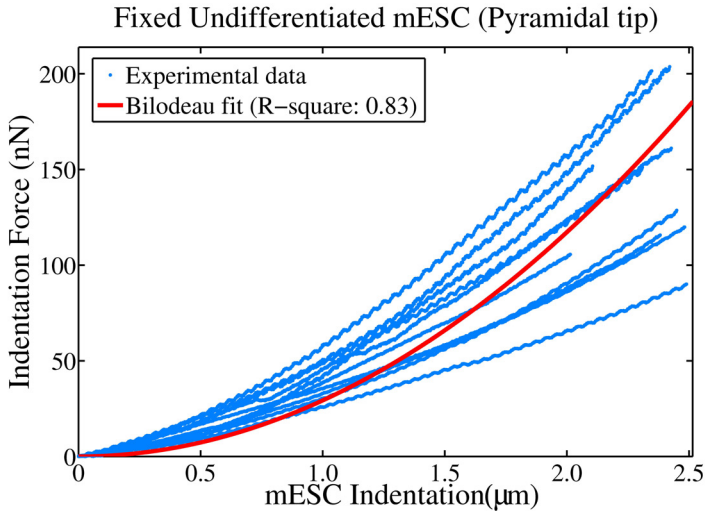

Figure 5.22: Force (F) versus cell indentation (δ) for 10 samples of fixed undifferentiated mESC.

(a)

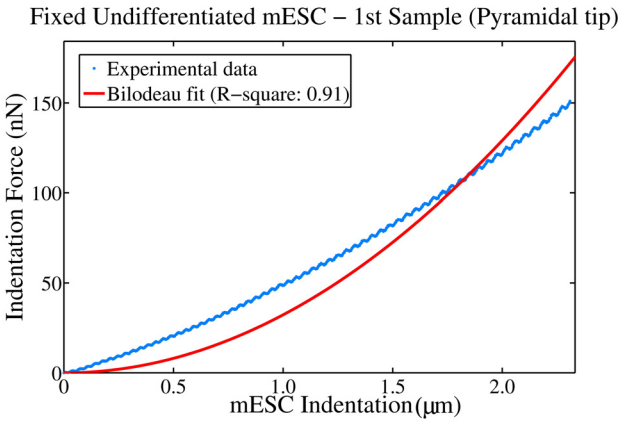

(b)

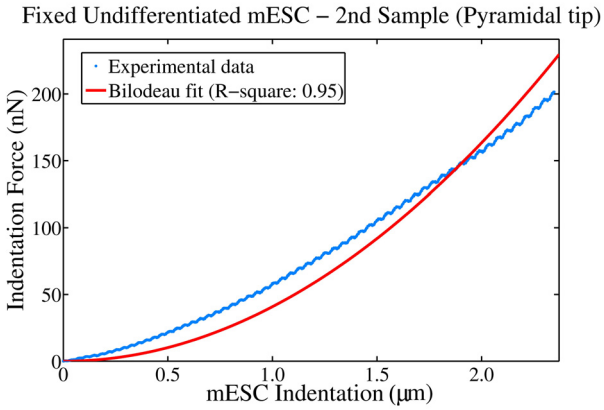

Figure 5.23: (a) Force (F) versus cell indentation (δ) for fixed undifferentiated mESC: (a) first sample; (b) second sample

Sample	1	2	3	4	5	6	7	8	9	10
R^2	0.91	0.95	0.92	0.93	0.95	0.97	0.90	0.99	0.98	0.97

Table 5.6: R^2 value obtained with the Bilodeau fit for 10 samples of fixed undifferentiated mESC.

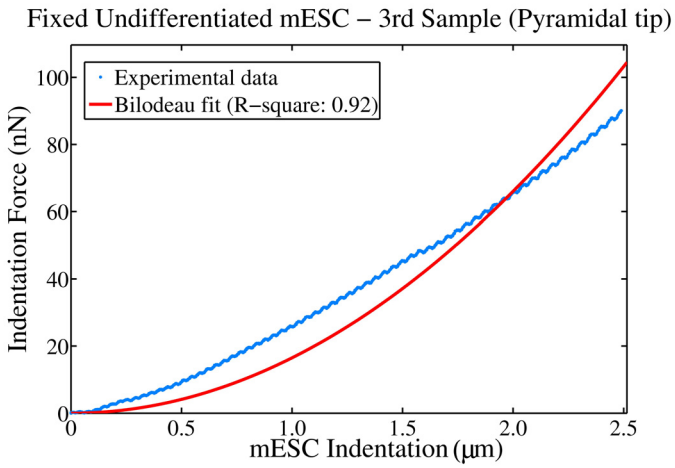

Figure 5.24: Force (F) versus cell indentation (δ) for third sample of fixed undifferentiated mESC

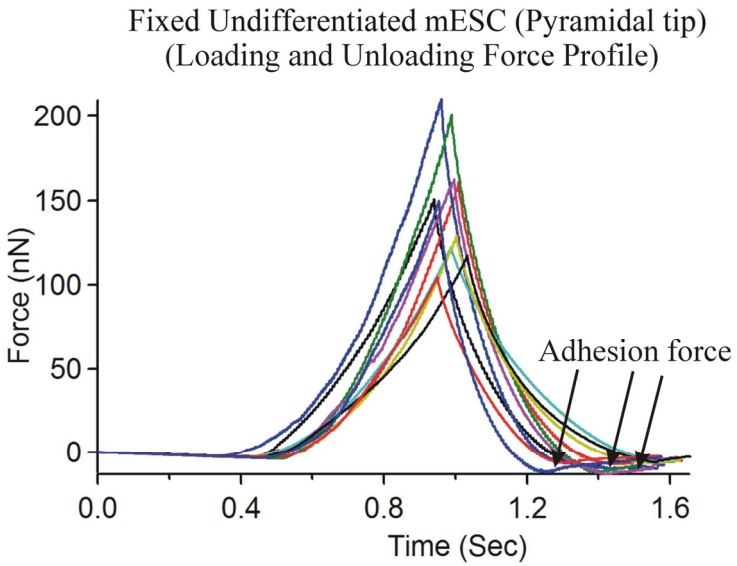

Figure 5.25. Force (loading and unloading) versus time profiles obtained for 10 samples of fixed undifferentiated mESC. Adhesion force exists between the tip and three samples.

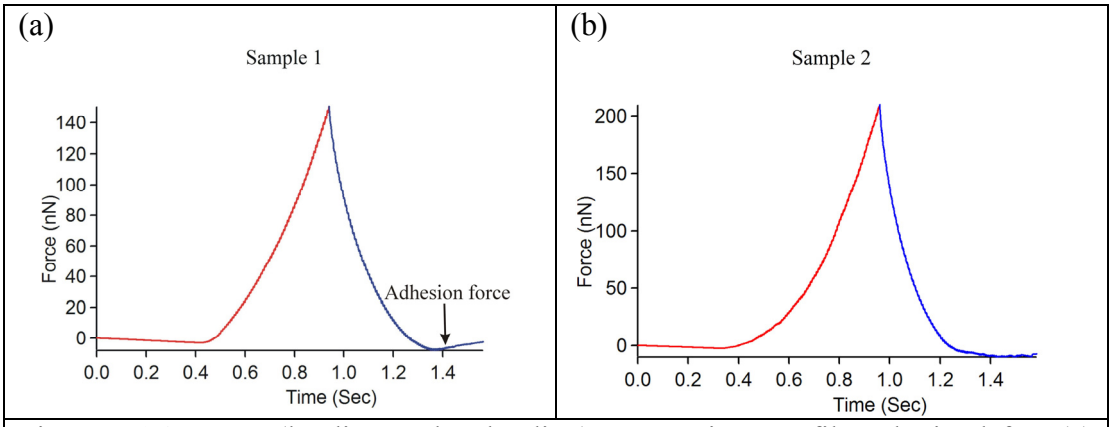

Figure 5.26. Force (loading and unloading) versus time profiles obtained for: (a) first sample and (b) second sample of fixed undifferentiated mESC. The adhesion force in (a) is 4.5 nN.

We observe that the force of adhesion exists for three samples (figure 5.13a). The adhesion force is negligible (less than 0.05 times the maximum indentation force) compared to the adhesion force (more than 0.1 times the maximum indentation force) observed by others for the JKR theory to be applicable [129, 149, 179]. The adhesion could be due to the wear of the pyramidal tip [179]. Hence, in this case we cannot use the JKR theory applicable to blunt conical indenter. From figures 5.22 - 5.24, we observe that the force-indentation curves of fixed undifferentiated mESC can be appropriately described by the Bilodeau model. The R^2 values obtained with: (a) the fit for each fixed undifferentiated mESC is always greater than 0.90 as shown in table 5.6 (for best fit: $R^2 = 1$) and, (b) the average fit for all the 10 samples is 0.83 (figure 5.22). Thus, we infer from the above analysis that the force-indentation curves for fixed undifferentiated mESC probed by a pyramidal indenter is best described by Bilodeau model.

FIXED DIFFERENTIATING (3rd day) mESC

(a)

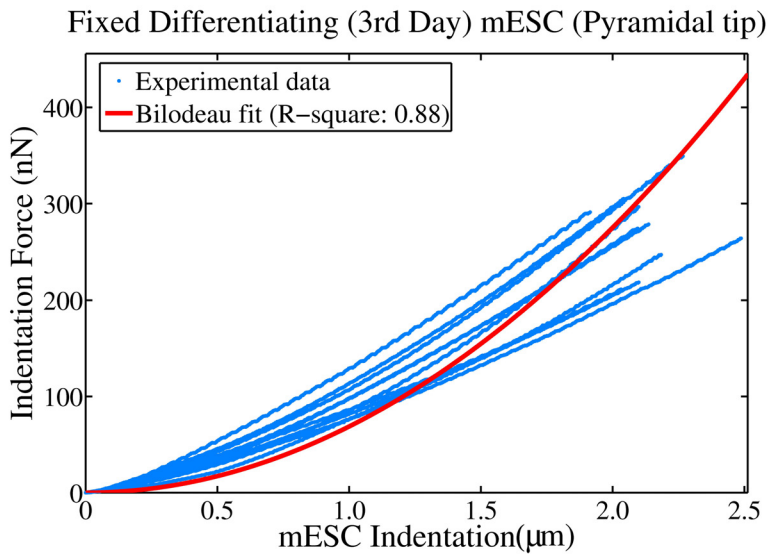

(b)

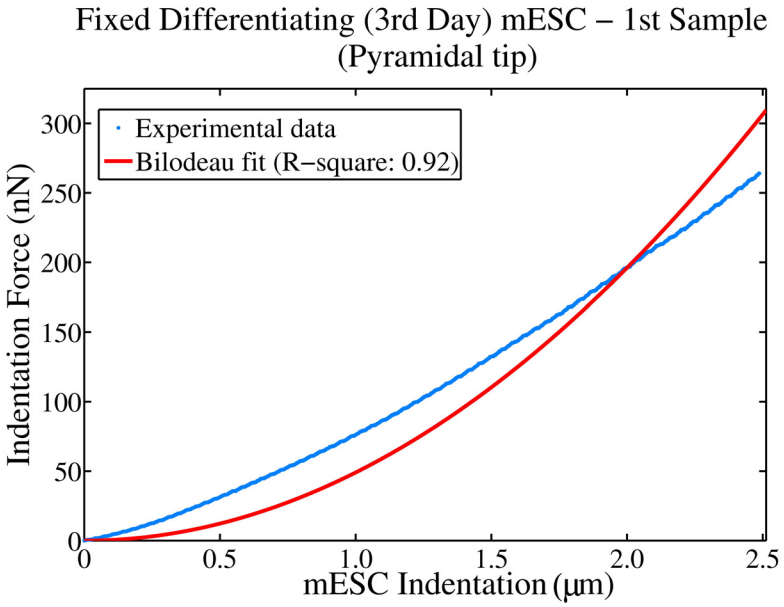

Figure 5.27: Force (F) versus cell indentation (δ) for fixed differentiating (3rd day) mESC: (a) 10 Samples; (b) first sample.

(a)

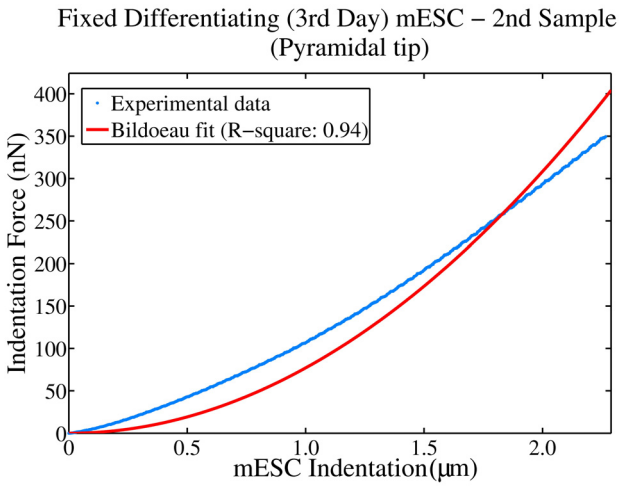

(b)

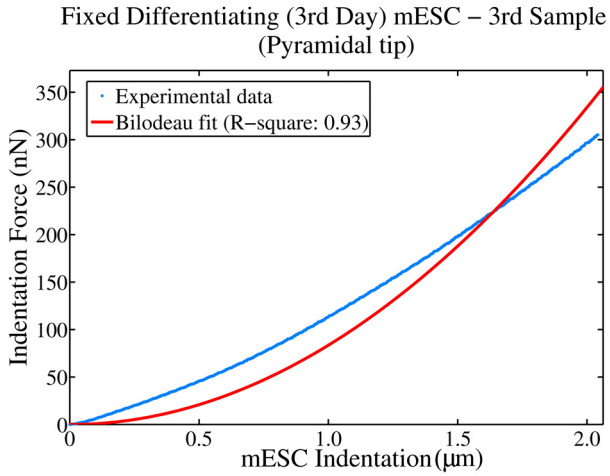

Figure 5.28: Force (F) versus cell indentation (δ) for fixed differentiating (3rd day) mESC (a) second sample; (b) third sample

Sample	1	2	3	4	5	6	7	8	9	10
R^2	0.92	0.94	0.93	0.91	0.98	0.93	0.87	0.94	0.96	0.89

Table 5.7: R^2 value obtained with the Bilodeau fit for 10 samples of fixed differentiating (3rd day) mESC.

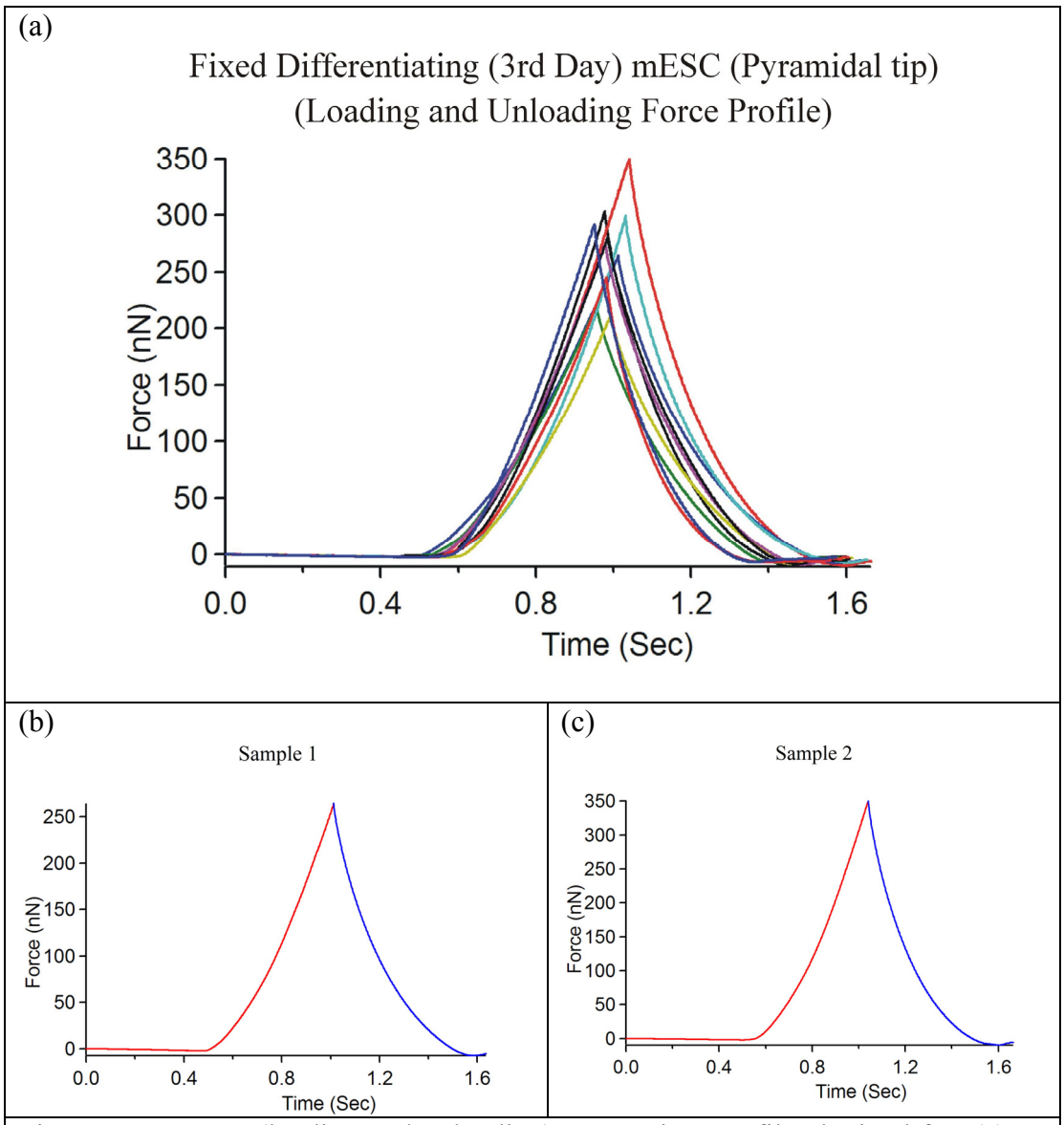

Figure 5.29. Force (loading and unloading) versus time profile obtained for: (a) 10 samples, (b) first sample, and (c) second sample of fixed differentiating (3rd day) mESC

We observe that the force of adhesion does not exist between the tip and the sample (figure 5.29). Hence, in this case we cannot use the JKR theory applicable to blunt conical indenter. From figures 5.27 and 5.28, we observe that the force-indentation

curves of fixed differentiating (3rd day) mESC can be appropriately described by the Bilodeau model. The R^2 values obtained with: (a) the fit for each fixed differentiating (3rd day) mESC is always greater than 0.88 as shown in table 5.7 (for best fit: $R^2 = 1$) and, (b) the average fit for all the 10 samples is 0.85 (figure 5.27a). Thus, we infer from the above analysis that the force-indentation curves for fixed differentiating (3rd day) mESC probed by a pyramidal indenter are best described by Bilodeau model.

FIXED DIFFERENTIATING (6th day) mESC

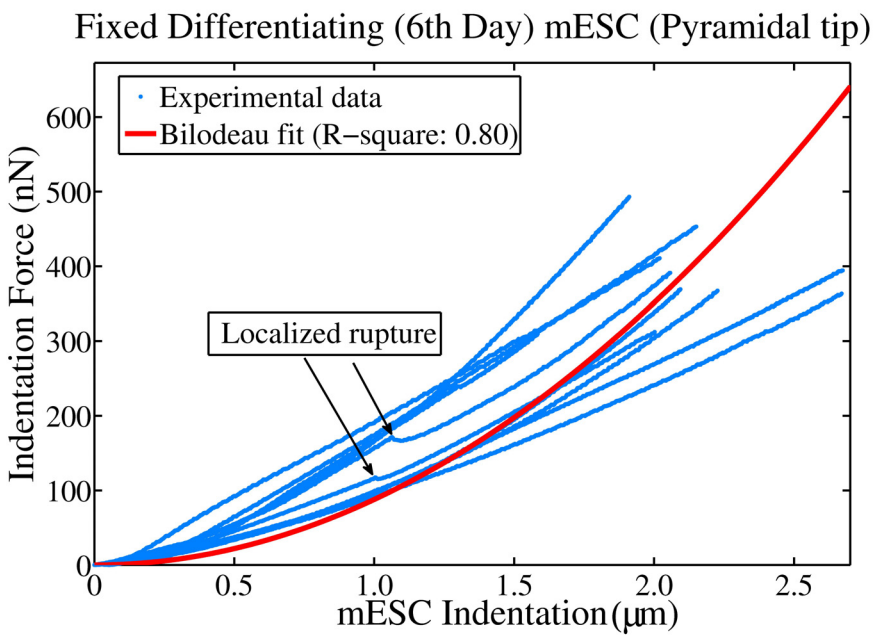

Figure 5.30: Force (F) versus cell indentation (δ) for 10 samples of fixed differentiating (6th day) mESC

(a)

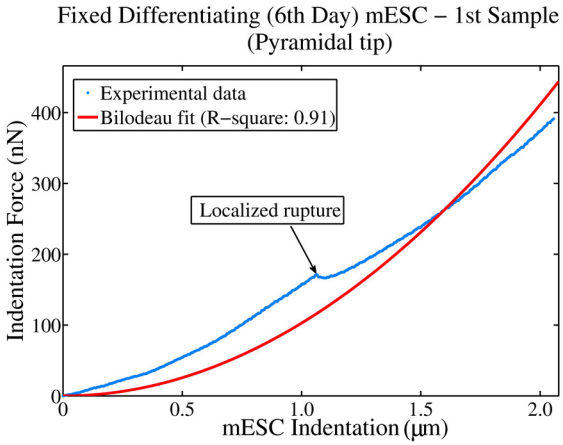

(b)

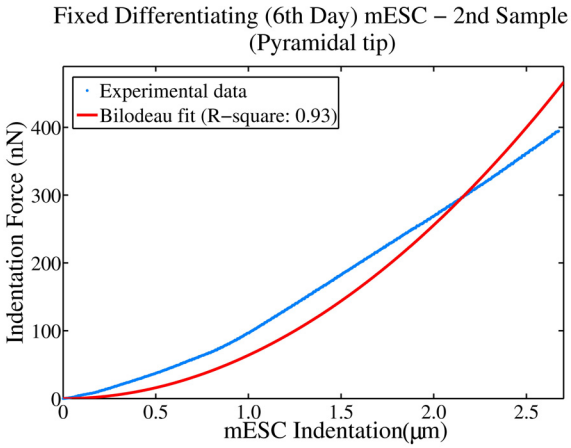

Figure 5.31: (a) Force (F) versus cell indentation (δ) for fixed differentiating (6th day) mESC: (a) first samples; (b) second sample

Sample	1	2	3	4	5	6	7	8	9	10
R^2	0.91	0.94	0.93	0.80	0.90	0.93	0.94	0.99	0.98	0.98

Table 5.8: R^2 value obtained with the Bilodeau fit for 10 samples of fixed differentiating (6th day) mESC.

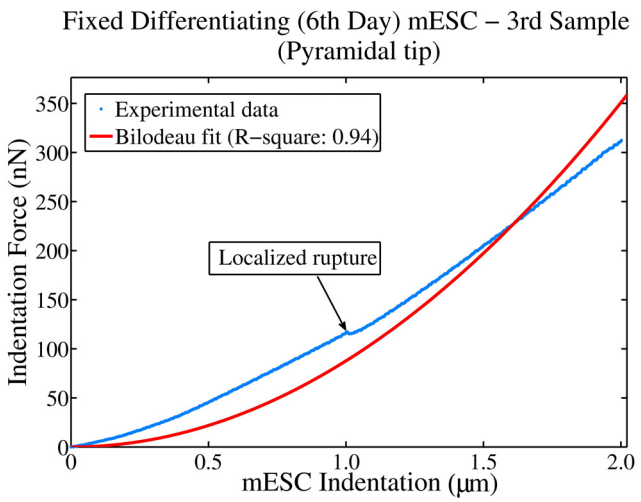

Figure 5.32: Force (F) versus cell indentation (δ) for third sample of fixed differentiating (6^{th} day) mESC.

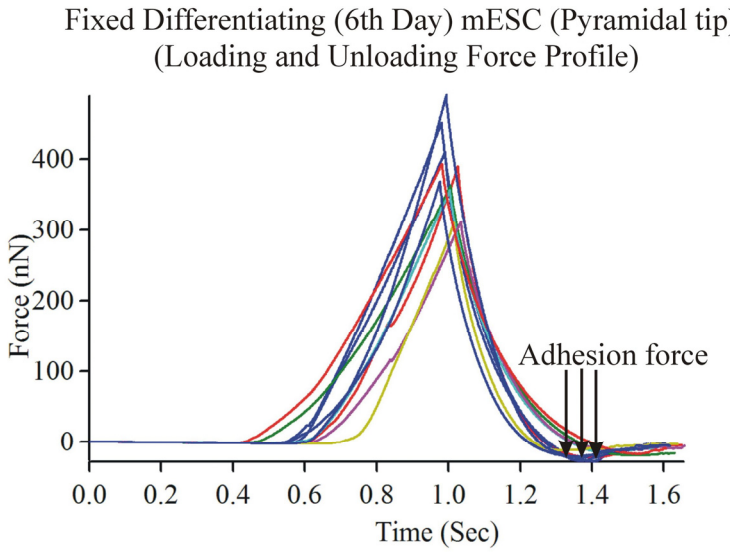

Figure 5.33: Force (loading and unloading) versus time profiles obtained for 10 samples of differentiating (6^{th} day) mESC. Adhesion force exists between the tip and three samples.

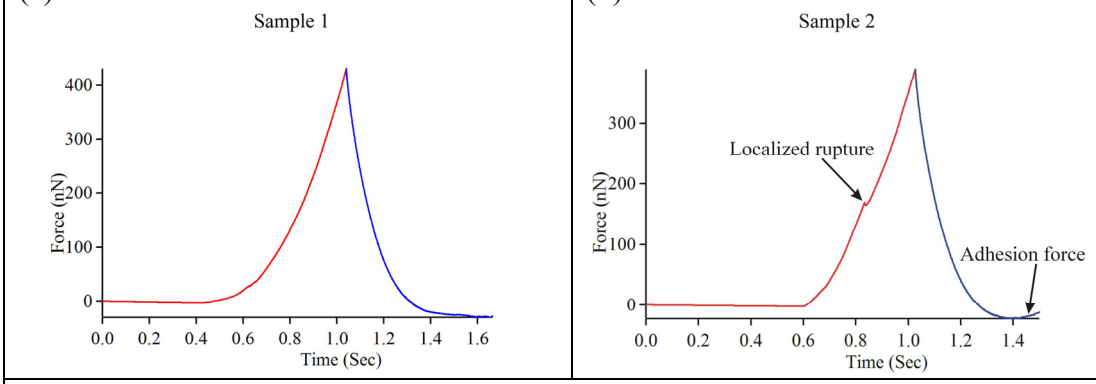

Figure 5.34. Force (loading and unloading) versus time profiles obtained for: (a) first sample, and (b) second sample of fixed differentiating (6^{th} day) mESC.

We observe that the force of adhesion exists for three samples (figure 5.33). The adhesion force is negligible (less than 0.05 times the maximum indentation force) compared to the adhesion force (more than 0.1 times the maximum indentation force) observed by others for the JKR theory to be applicable [129, 149, 179]. The adhesion could be due to the wear of the pyramidal tip [179]. Hence, in this case we cannot use the JKR theory applicable to blunt conical indenter. We observe a small dip in force while indenting the first and the third sample (figures: 5.30, 5.31a and 5.32). This may be due to local rupture of the cell membrane. From figures 5.30 - 5.32, we observe that the force-indentation curves of fixed differentiating (6^{th} day) mESC can be appropriately described by the Bilodeau model. The R^2 values obtained with: (a) the fit for each fixed differentiating (6^{th} day) mESC is always greater than 0.90 (except for sample 4) as shown in table 5.6 (for best fit: $R^2 = 1$) and, (b) the average fit for all the 10 samples is 0.80 (figure 5.30). Thus, we infer from the above analysis that the force-indentation curves for fixed differentiating (6^{th} day) mESC probed by a pyramidal indenter are best described by Bilodeau model.

5.8.1.4 Discussion

We observe that the force-indentation curves of fixed mESC indented by a pyramidal tip can be appropriately described by the Bilodeau model. The R^2 values obtained with the fit for: (a) each mESC is approximately 0.9 (for best fit: $R^2 = 1$) and (b) the average fit for all 10 samples is 0.83, 0.88 and 0.80 for fixed undifferentiated, 3rd day differentiating and 6th day differentiating mESC respectively. In addition, the force of adhesion between the pyramidal tip and the sample was negligible. Thus the JKR model applicable to conical indenter does not describe the mechanical behavior of fixed mESC. We observe that the average maximum force attained for indenting (2 – 2.5 μm) 10 samples of fixed undifferentiated, 3rd day differentiating and 6th day differentiating mESC sample is approximately 140nN, 277nN and 390nN respectively. Computation of elastic modulus and statistical analysis is presented in chapter 6. *As a first approximation, we conclude from the above analysis that the force-indentation curves for fixed mESC probed by a pyramidal indenter are best described by Bilodeau model.*

5.8.2 Indentation Studies with Spherical Tip

We performed single indentation studies with a spherical tip on 60 mESC: 30 fixed and 30 live cells. Table 5.1 shows the distribution of cells. We employed two types of cantilevers attached with a spherical probe (5 μm in diameter): (a) silicon nitride cantilever with a spring constant of 0.06 N/m (Novascan Technologies, Inc., Ames, IA) for live cells, (b) silicon cantilever with a spring constant of 1.75 N/m (Novascan Technologies, Inc) for fixed cells (figure 5.29). The force-indentation relationship obtained with a spherical indenter cannot be described by the Sneddon theory

(cylindrical and conical indenter) and the Bilodeau model (Pyramidal tip) because of the indenter geometry. In addition, the blunt conical and pyramidal indenter models are also not applicable. Initially we chose Hertz model to determine whether it appropriately predicts the force-indentation relationship of mESC obtained with a spherical indenter. Capsule model for a spherical indenter was also used to predict the force-indentation relationship. After an exhaustive comparison between the two models: Hertz and Capsule model, we chose an approach which appropriately describes the mechanical behavior of mESC. We also present the force (loading and unloading) versus time profiles and determine whether force of adhesion exists between the tip and the sample.

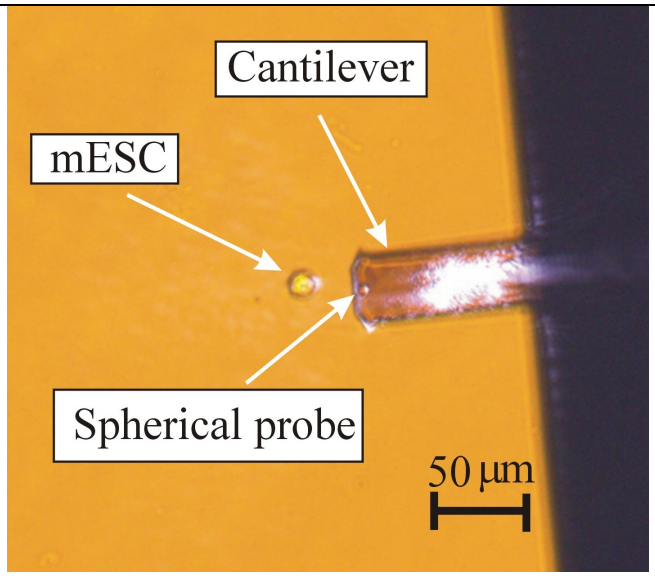

Figure 5.35: Silicon cantilever with a spherical probe (diameter: 5 µm)

5.8.2.1 Live mESC – Spherical Tip

In this section we present the force-indentation profiles for live undifferentiated, 3rd day differentiating and 6th day differentiating mESC indented by a spherical tip. The cell indentation range was 2 – 2.5 µm. The profiles are described by the Hertz model

followed by the capsule model with the corresponding R^2 values. We also show the force (loading and unloading) versus time profiles for each live mESC.

LIVE UNDIFFERENTIATED mESC

(a)

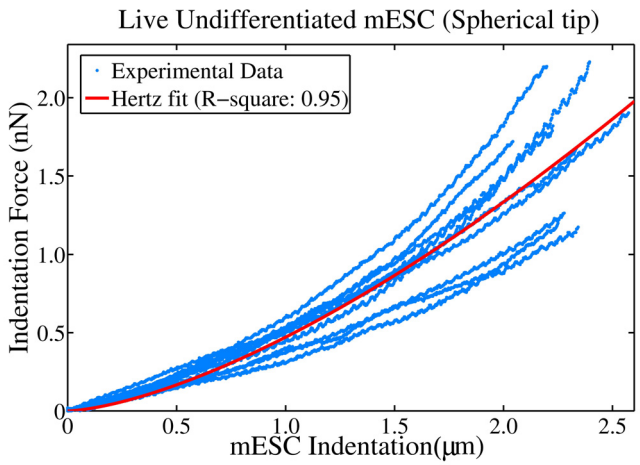

(b)

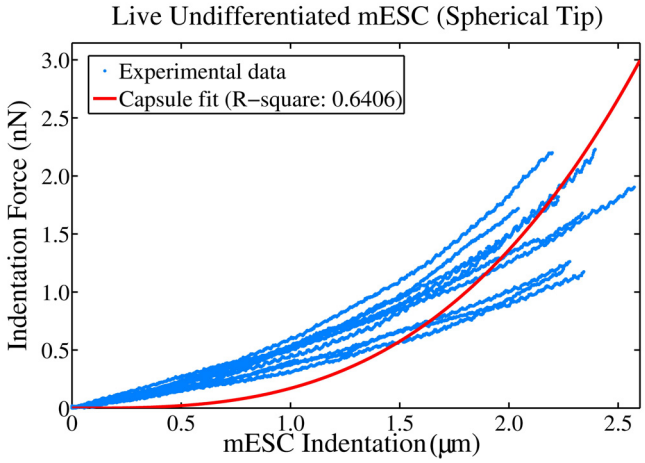

Figure 5.36: Force (F) versus cell indentation (δ) for 10 samples of live undifferentiated mESC: (a) Hertz fit; (b) Capsule fit. The R^2 value obtained with Hertz fit (0.95) is greater than capsule fit (0.64)

(a)

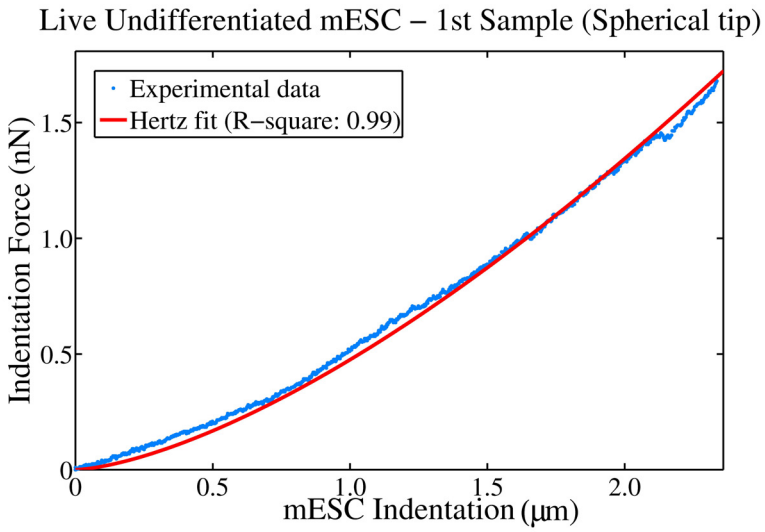

(b)

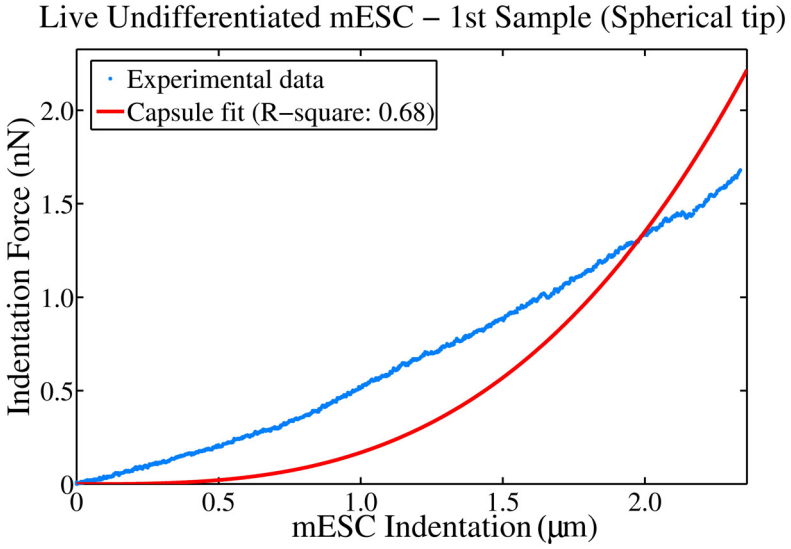

Figure 5.37: Force (F) versus cell indentation (δ) for 1st sample of live undifferentiated mESC: (a) Hertz fit; (b) Capsule fit. The R^2 value obtained with Hertz fit (0.99) is greater than capsule fit (0.68).

(a)

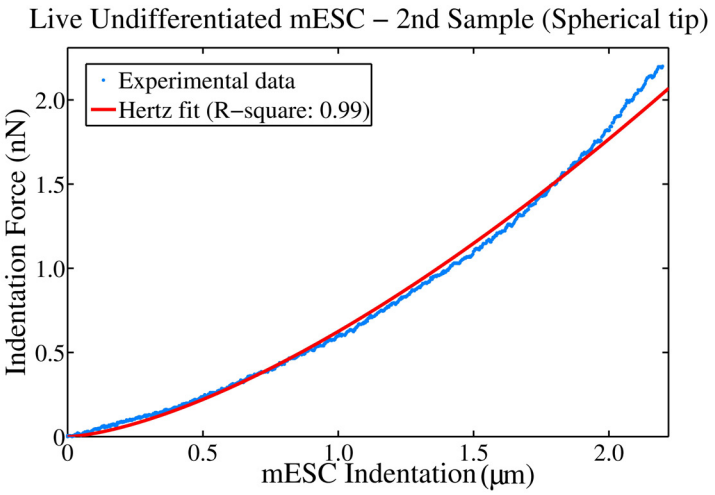

(b)

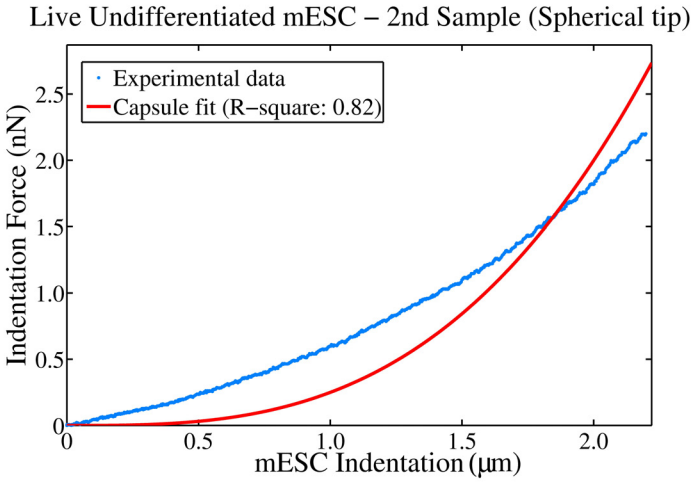

Figure 5.38: Force (F) versus cell indentation (δ) for 2nd sample of live undifferentiated mESC: (a) Hertz fit; (b) Capsule fit. The R^2 value obtained with Hertz fit (0.99) is greater than capsule fit (0.82).

(a)

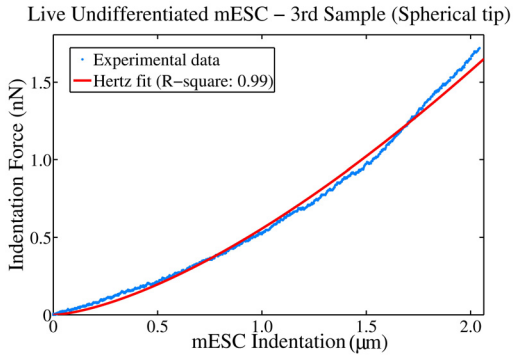

(b)

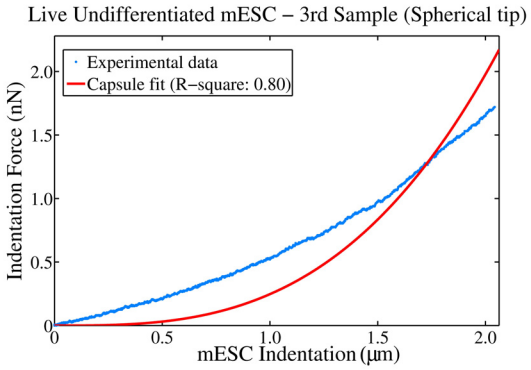

Figure 5.39: Force (F) versus cell indentation (δ) for 3rd sample of live undifferentiated mESC: (a) Hertz fit ; (b) Capsule fit. The R^2 value obtained with Hertz fit (0.99) is greater than capsule fit (0.80)

Sample	1	2	3	4	5	6	7	8	9	10
R^2 (H)	0.99	0.99	0.99	0.99	0.99	0.99	0.99	0.98	0.98	0.98
R^2 (C)	0.68	0.82	0.80	0.68	0.79	0.74	0.73	0.90	0.64	0.65

Table 5.9: R^2 value obtained with the Hertz fit represented by R^2 (H) and capsule fit represented by R^2 (C) for 10 samples of live undifferentiated mESC. The R^2 value obtained with Hertz fit is greater than capsule fit.

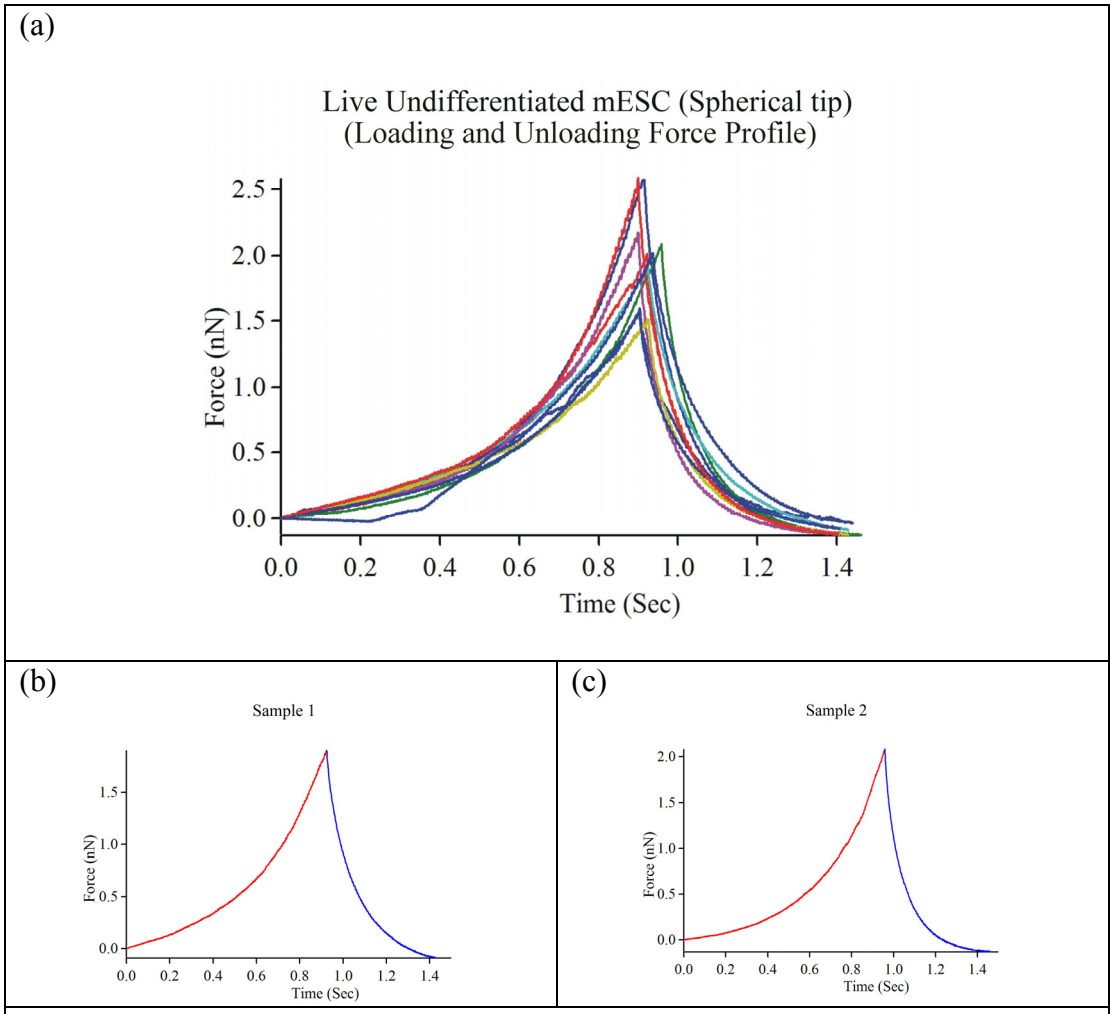

Figure 5.40. Force (loading and unloading) versus time profile obtained for: (a) 10 samples, (b) first sample, and (c) second sample of live undifferentiated mESC.

We observe that the force of adhesion does not exist between the tip and the sample (figure 5.40). Hence, in this case we cannot use the JKR and DMT theory applicable to spherical indenter. From figures 5.36 – 5.39, we observe that the force-indentation curves of live undifferentiated mESC can be appropriately described by the Hertz model compared to the capsule model. The R^2 value obtained with the Hertz fit is always greater than the capsule fit for any force versus indentation profile (table 5.9).

Thus, we infer from the above analysis that the force-indentation curves for live undifferentiated mESC probed by a spherical indenter is appropriately best described by Hertz model.

LIVE DIFFERENTIATING (3rd day) mESC

(a)

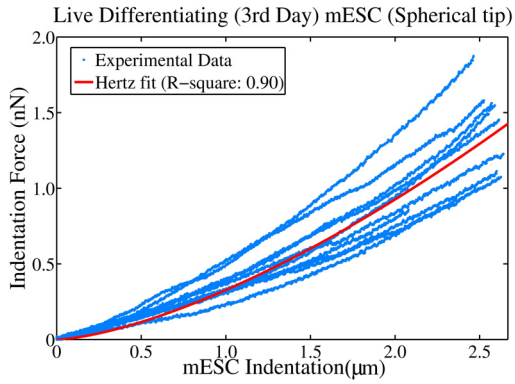

(b)

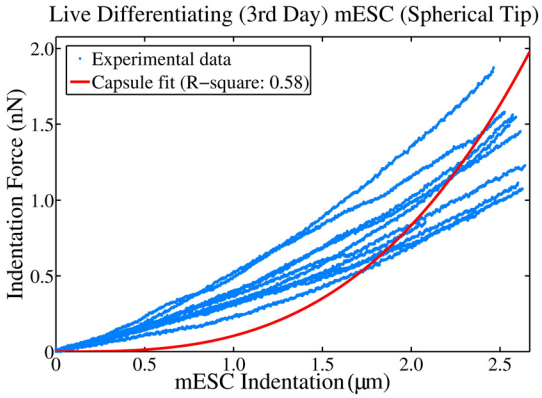

Figure 5.41: Force (F) versus cell indentation (δ) for 10 samples of live differentiating (3rd day) mESC: (a) Hertz fit; (b) Capsule fit. The R^2 value obtained with Hertz fit (0.90) is greater than capsule fit (0.58)

(a)

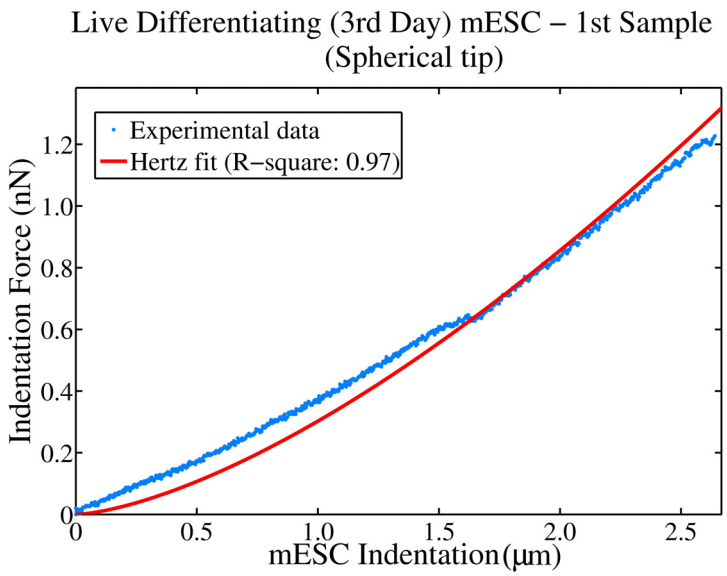

(b)

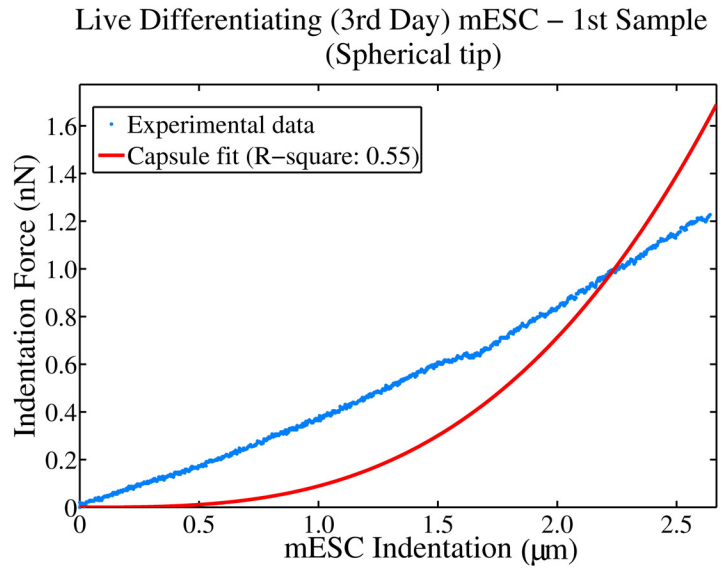

Figure 5.42: Force (F) versus cell indentation (δ) for 1st sample of live differentiating (3rd day) mESC: (a) Hertz fit; (b) Capsule fit. The R^2 value obtained with Hertz fit (0.97) is greater than capsule fit (0.55)

(a)

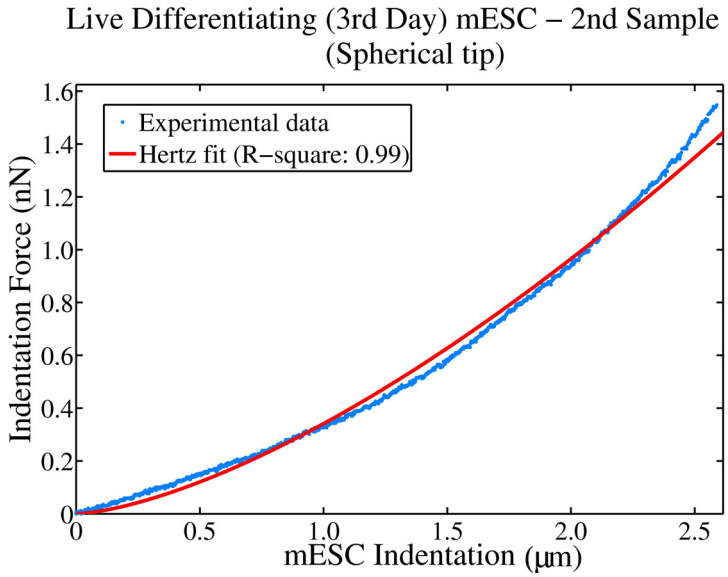

(b)

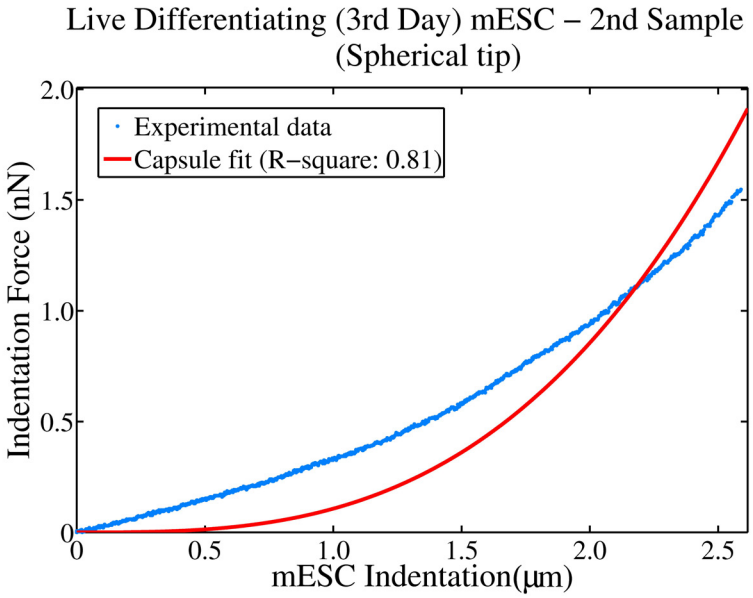

Figure 5.43: Force (F) versus cell indentation (δ) for 2nd sample of live differentiating (3rd day) mESC: (a) Hertz fit; (b) Capsule fit. The R^2 value obtained with Hertz fit (0.99) is greater than capsule fit (0.81)

(a)

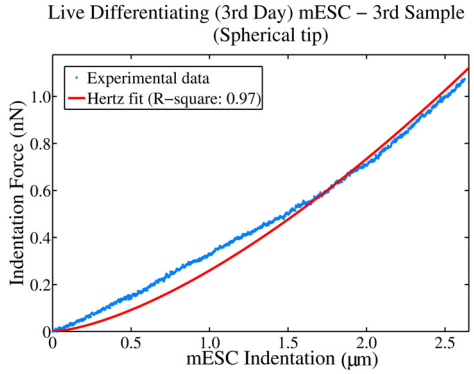

(b)

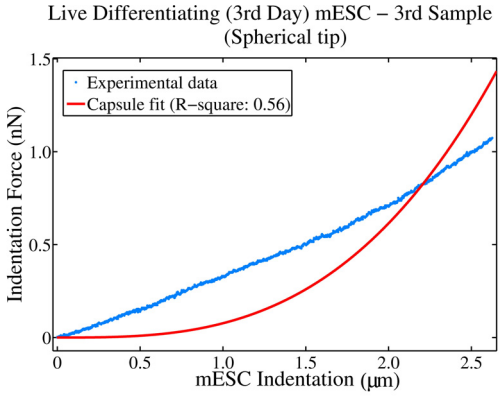

Figure 5.44: Force (F) versus cell indentation (δ) for 3rd sample of live differentiating (3rd day) mESC: (a) Hertz fit; (b) Capsule fit. The R^2 value obtained with Hertz fit (0.97) is greater than capsule fit (0.56)

Sample	1	2	3	4	5	6	7	8	9	10
R^2 (H)	0.97	0.99	0.97	0.99	0.98	0.99	0.99	0.98	0.99	0.97
R^2 (C)	0.55	0.81	0.56	0.64	0.62	0.79	0.71	0.63	0.71	0.52

Table 5.10: R^2 value obtained with the Hertz fit represented by R^2 (H) and capsule fit represented by R^2 (C) for 10 samples of live differentiating (3rd day) mESC. The R^2 value obtained with Hertz fit is greater than capsule fit.

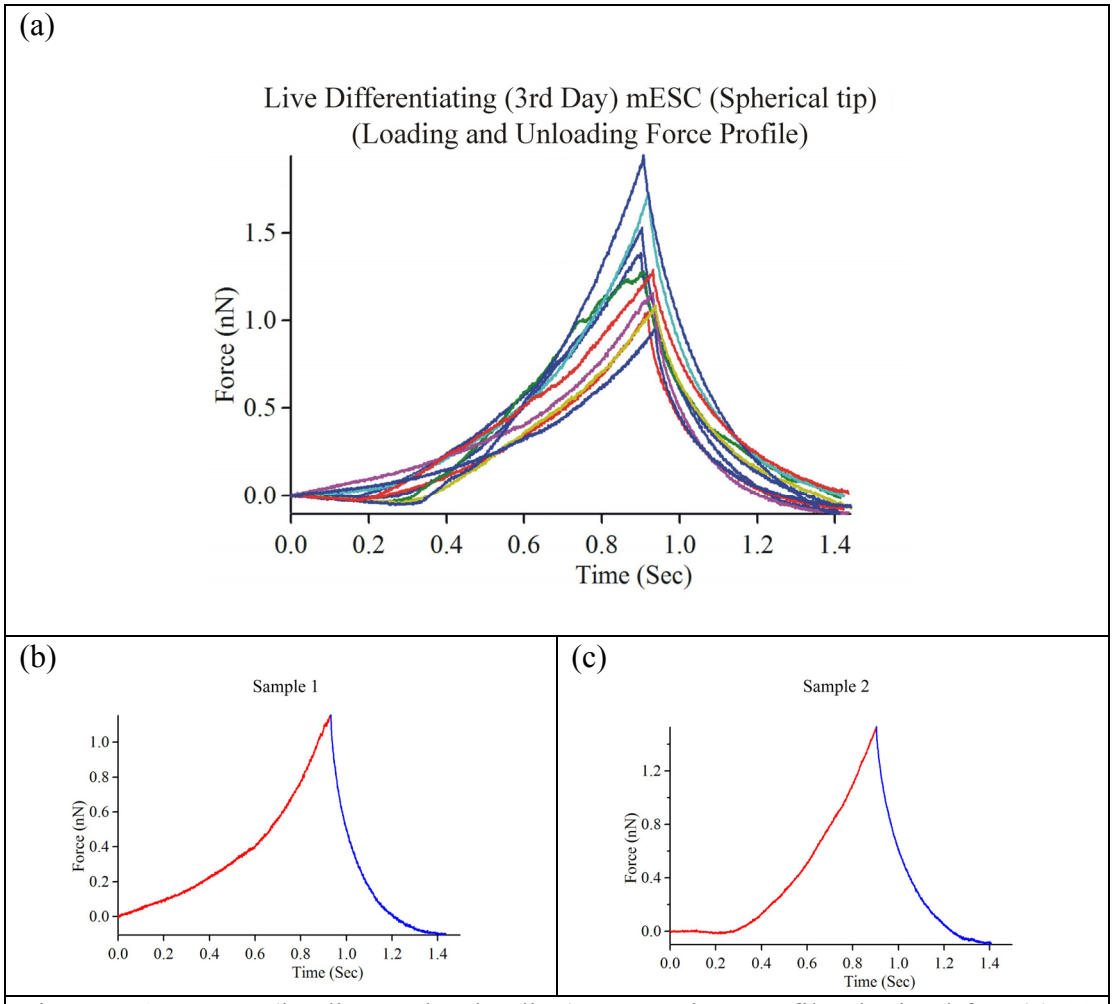

Figure 5.45. Force (loading and unloading) versus time profile obtained for: (a) 10 samples, (b) 1st sample, and (c) 2nd sample of live differentiating (3rd day) mESC

We observe that the force of adhesion does not exist between the tip and the sample (figure 5.45). Hence, in this case we cannot use the JKR and DMT theory applicable to spherical indenter. From figures 5.41 – 5.44, we observe that the force-indentation curves of live differentiating (3rd day) mESC can be appropriately described by the Hertz model compared to the capsule model. The R^2 value obtained with the Hertz fit is always greater than the capsule fit for any force versus indentation profile (table

5.10). As a first approximation, we infer from the above analysis that the force-indentation curves for live differentiating (3rd day) mESC probed by a spherical indenter are best described by Hertz model.

LIVE DIFFERENTIATING (6th day) mESC

(a)

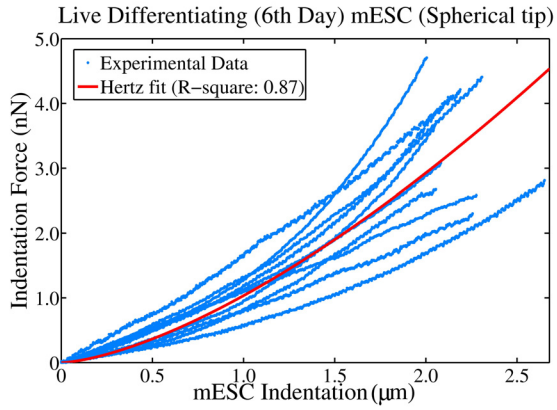

(b)

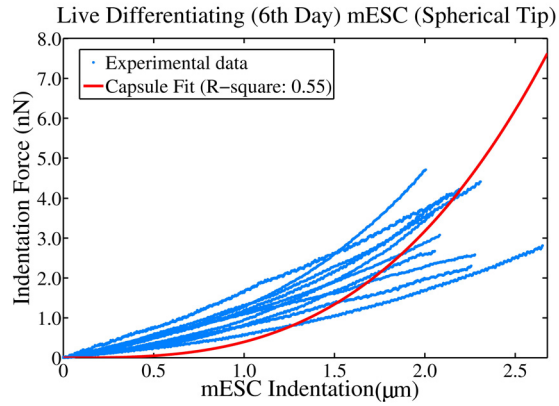

Figure 5.46: Force (F) versus cell indentation (δ) for 10 samples of live differentiating (6th day) mESC: (a) Hertz fit; (b) Capsule fit. The R^2 value obtained with Hertz fit (0.87) is greater than capsule fit (0.55)

(a)

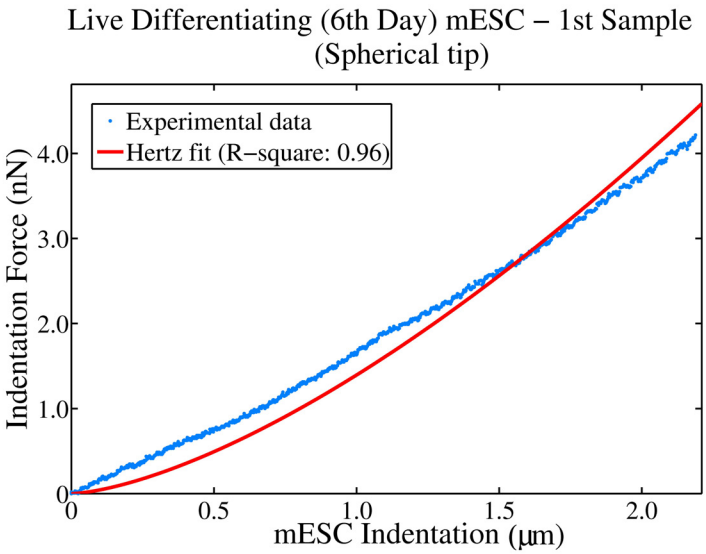

(b)

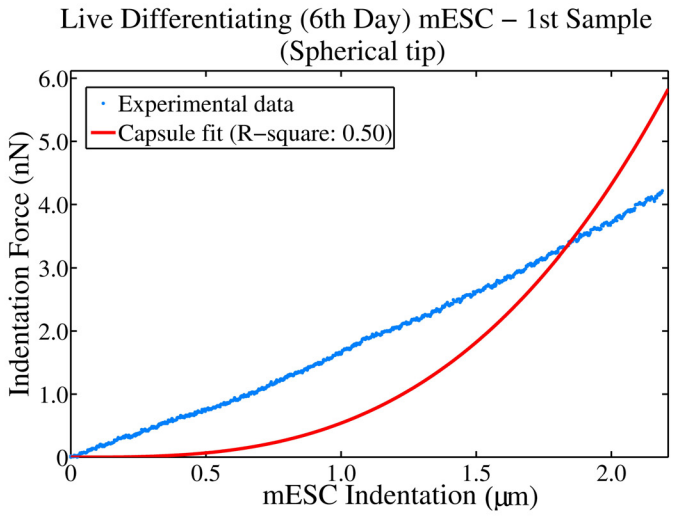

Figure 5.47: Force (F) versus cell indentation (δ) for 1st sample of live differentiating (6th day) mESC: (a) Hertz fit; (b) Capsule fit. The R^2 value obtained with Hertz fit (0.96) is greater than capsule fit (0.50)

(a)

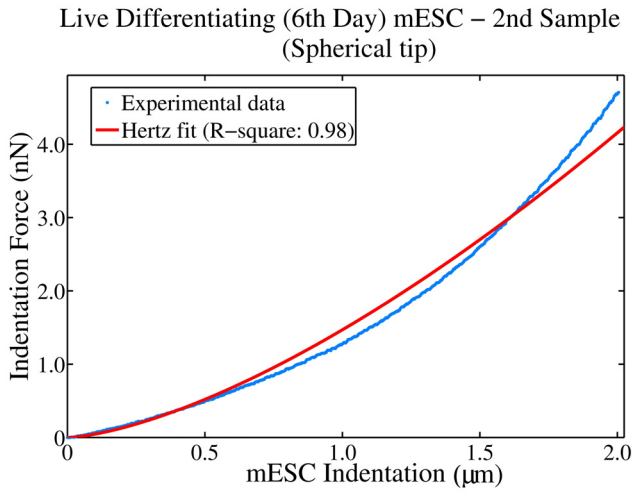

(b)

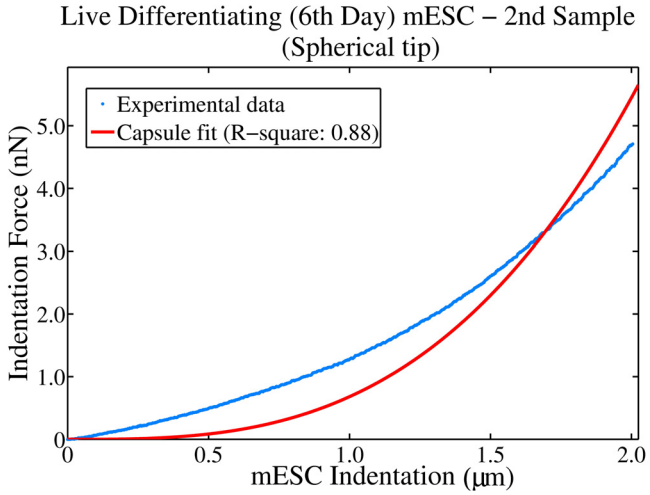

Figure 5.48: Force (F) versus cell indentation (δ) for 2nd sample of live differentiating (6th day) mESC: (a) Hertz fit; (b) Capsule fit. The R^2 value obtained with Hertz fit (0.98) is greater than capsule fit (0.88)

(a)

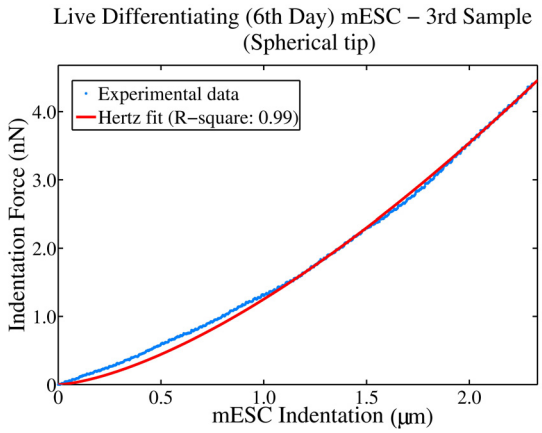

(b)

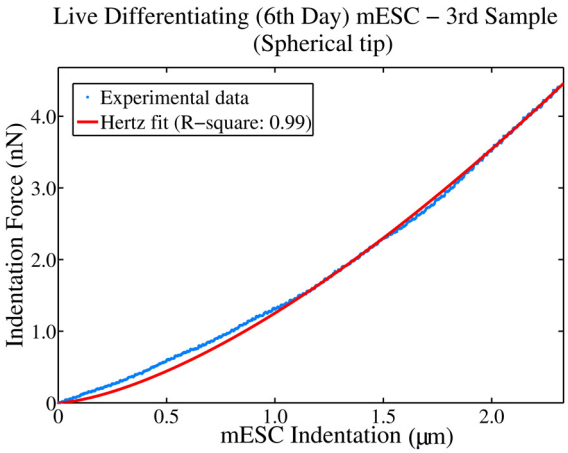

Figure 5.49: Force (F) versus cell indentation (δ) for 3rd sample of live differentiating (6th day) mESC: (a) Hertz fit; (b) Capsule fit. The R^2 value obtained with Hertz fit (0.99) is greater than capsule fit (0.71)

Sample	1	2	3	4	5	6	7	8	9	10
R^2 (H)	0.96	0.98	0.99	0.99	0.99	0.99	0.98	0.92	0.98	0.98
R^2 (C)	0.50	0.88	0.71	0.82	0.81	0.83	0.61	0.33	0.64	0.87

Table 5.11: R^2 value obtained with the Hertz fit represented by R^2 (H) and capsule fit represented by R^2 (C) for 10 samples of live differentiating (6th day) mESC. The R^2 value obtained with Hertz fit is greater than capsule fit.

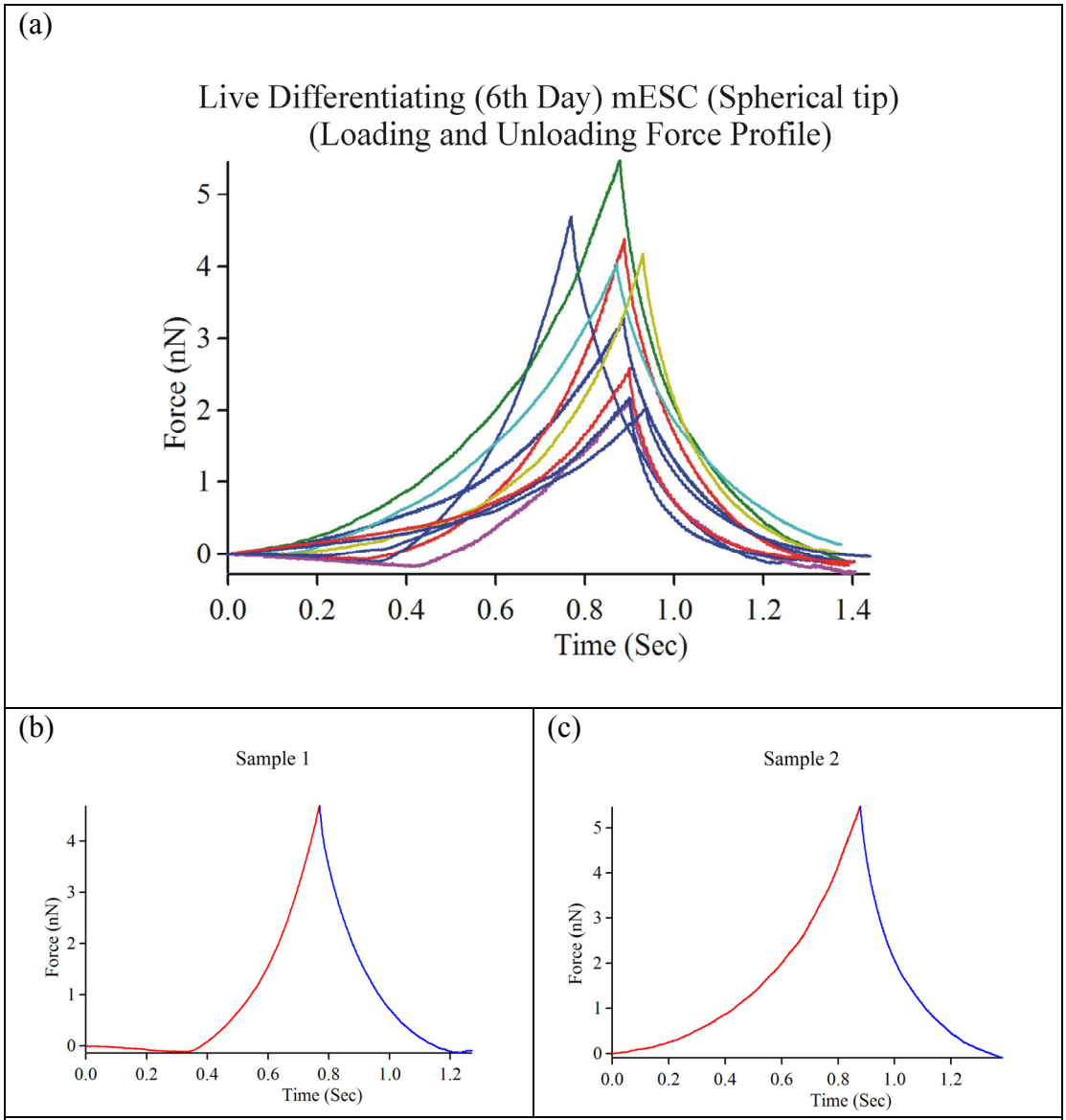

Figure 5.50. Force (loading and unloading) versus time profile obtained for: (a) 10 samples, (b) 1st sample, and (c) 2nd sample of live differentiating (6^{th} day) mESC.

We observe that the force of adhesion does not exist between the tip and the sample (figure 5.50). Hence, in this case we cannot use the JKR and DMT theory applicable to spherical indenter. From figures 5.46 – 5.49, we observe that the force-indentation curves of live differentiating (6^{th} day) mESC can be appropriately described by the

Hertz model compared to the capsule model. The R^2 value obtained with the Hertz fit is always greater than the capsule fit for any force versus indentation profile (table 5.11). Thus, we infer from the above analysis that the force-indentation curves for live differentiating (6^{th} day) mESC probed by a spherical indenter is best described by Hertz model.

5.8.2.2 Discussion

We observe that the force-indentation curves of live mESC indented by a spherical tip can be appropriately described by the Hertz model compared to the capsule model. The R^2 value obtained with the Hertz fit is always greater than the capsule fit for any force versus indentation profile. In addition, the force of adhesion does not exist between the tip and the sample. Thus the JKR and DMT models applicable to spherical indenter do not describe the mechanical behavior of live mESC. We observe that the average maximum force attained for indenting (2 – 2.5 μm) 10 samples of live undifferentiated, 3^{rd} day differentiating and 6^{th} day differentiating mESC sample is approximately 1.6 nN, 1.3 nN and 3.4 nN respectively. The maximum force values are less that that obtained with pyramidal tip. This is in agreement with the theory that the pyramidal tip induces high stress concentration compared to spherical tip. Also the spherical tip attains large contact area with the cell during indentation thus, averaging the local variation in forces across the cell surface. Computation of elastic modulus and statistical analysis are presented in chapter 6. *As a first approximation, we conclude from the above analysis that the force-indentation curves for live mESC probed by a spherical indenter are best described by Hertz model.*

5.8.2.3 Fixed mESC – Spherical Tip

In this section we present the force-indentation profiles for fixed undifferentiated, 3rd day differentiating and 6th day differentiating mESC indented by a spherical tip. The cell indentation range was 2 – 2.5 µm. The profiles are described by the Hertz model followed by the capsule model with the corresponding R^2 values. We also show the force (loading and unloading) versus time profiles for each fixed mESC.

FIXED UNDIFFERENTIATED mESC

(a)

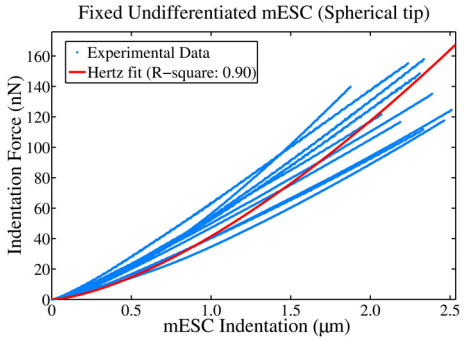

(b)

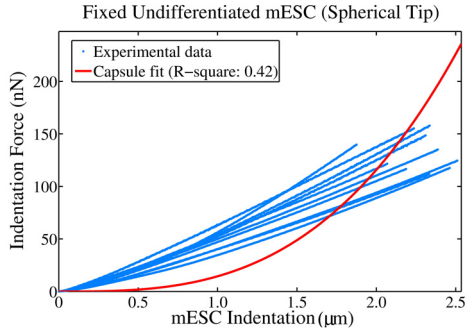

Figure 5.51: Force (F) versus cell indentation (δ) for 10 samples of fixed undifferentiated mESC: (a) Hertz fit; (b) Capsule fit. The R^2 value obtained with Hertz fit (0.90) is greater than capsule fit (0.42)

(a)

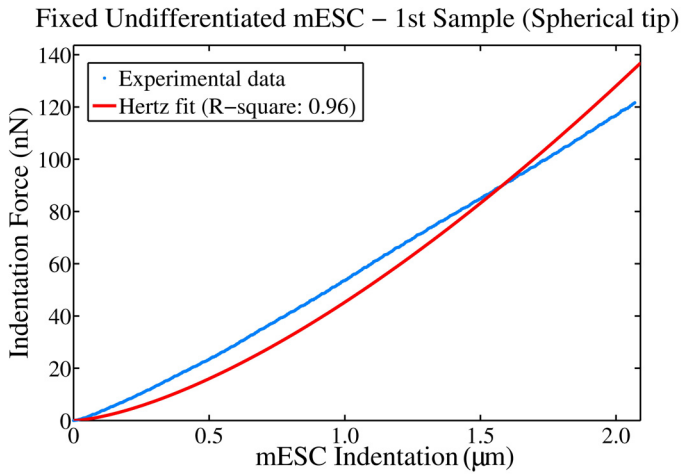

(b)

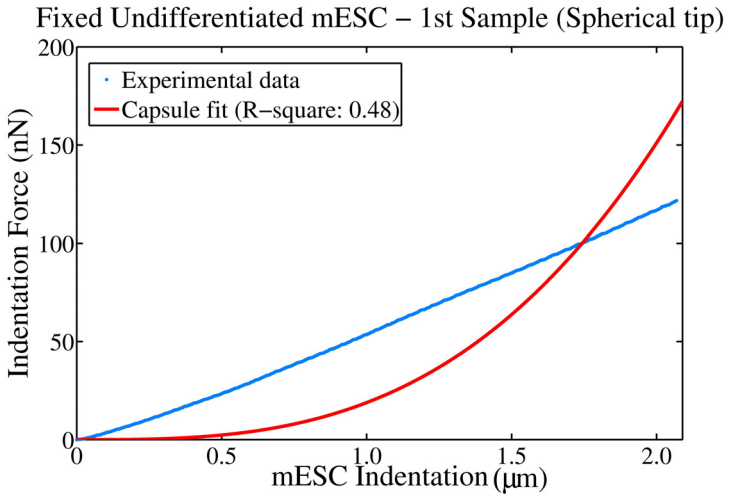

Figure 5.52: Force (F) versus cell indentation (δ) for 1st sample of fixed undifferentiated mESC: (a) Hertz fit; (b) Capsule fit. The R^2 value obtained with Hertz fit (0.96) is greater than capsule fit (0.48)

(a)

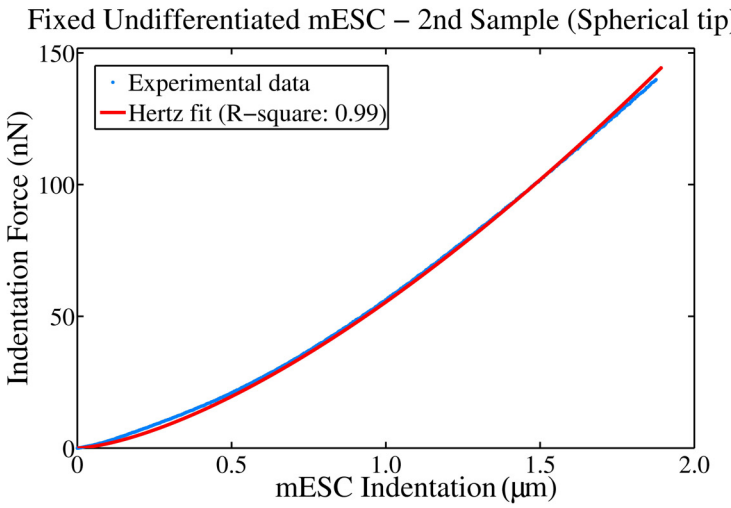

(b)

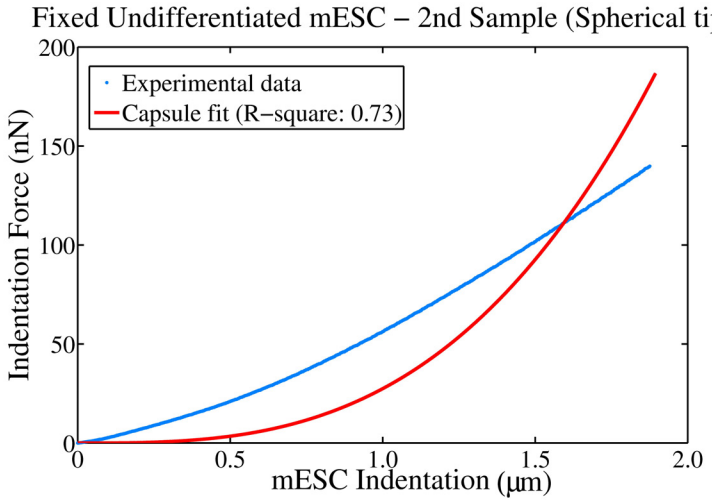

Figure 5.53: Force (F) versus cell indentation (δ) for 2nd sample of fixed undifferentiated mESC: (a) Hertz fit; (b) Capsule fit. The R^2 value obtained with Hertz fit (0.99) is greater than capsule fit (0.73)

(a)

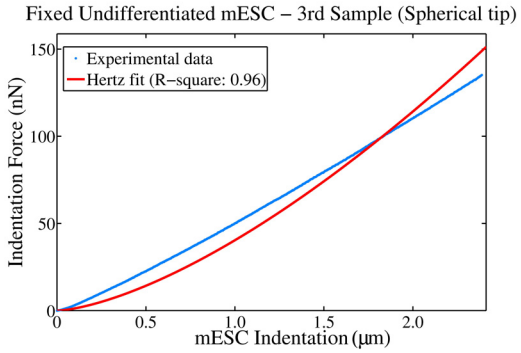

(b)

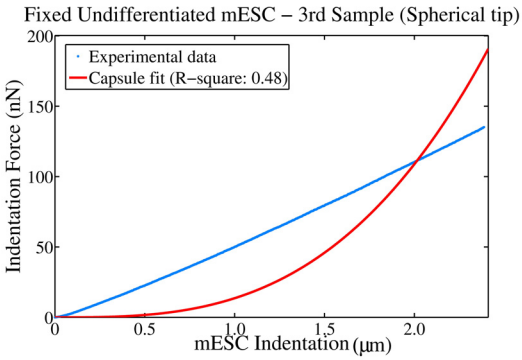

Figure 5.54: Force (F) versus cell indentation (δ) for 3rd sample of fixed undifferentiated mESC: (a) Hertz fit; (b) Capsule fit. The R^2 value obtained with Hertz fit (0.96) is greater than capsule fit (0.48)

Sample	1	2	3	4	5	6	7	8	9	10
R^2 (H)	0.96	0.99	0.96	0.99	0.98	0.96	0.98	0.98	0.95	0.97
R^2 (C)	0.48	0.73	0.48	0.67	0.58	0.52	0.59	0.61	0.46	0.57

Table 5.12: R^2 value obtained with the Hertz fit represented by R^2 (H) and capsule fit represented by R^2 (C) for 10 samples of fixed undifferentiated mESC. The R^2 value obtained with Hertz fit is greater than capsule fit.

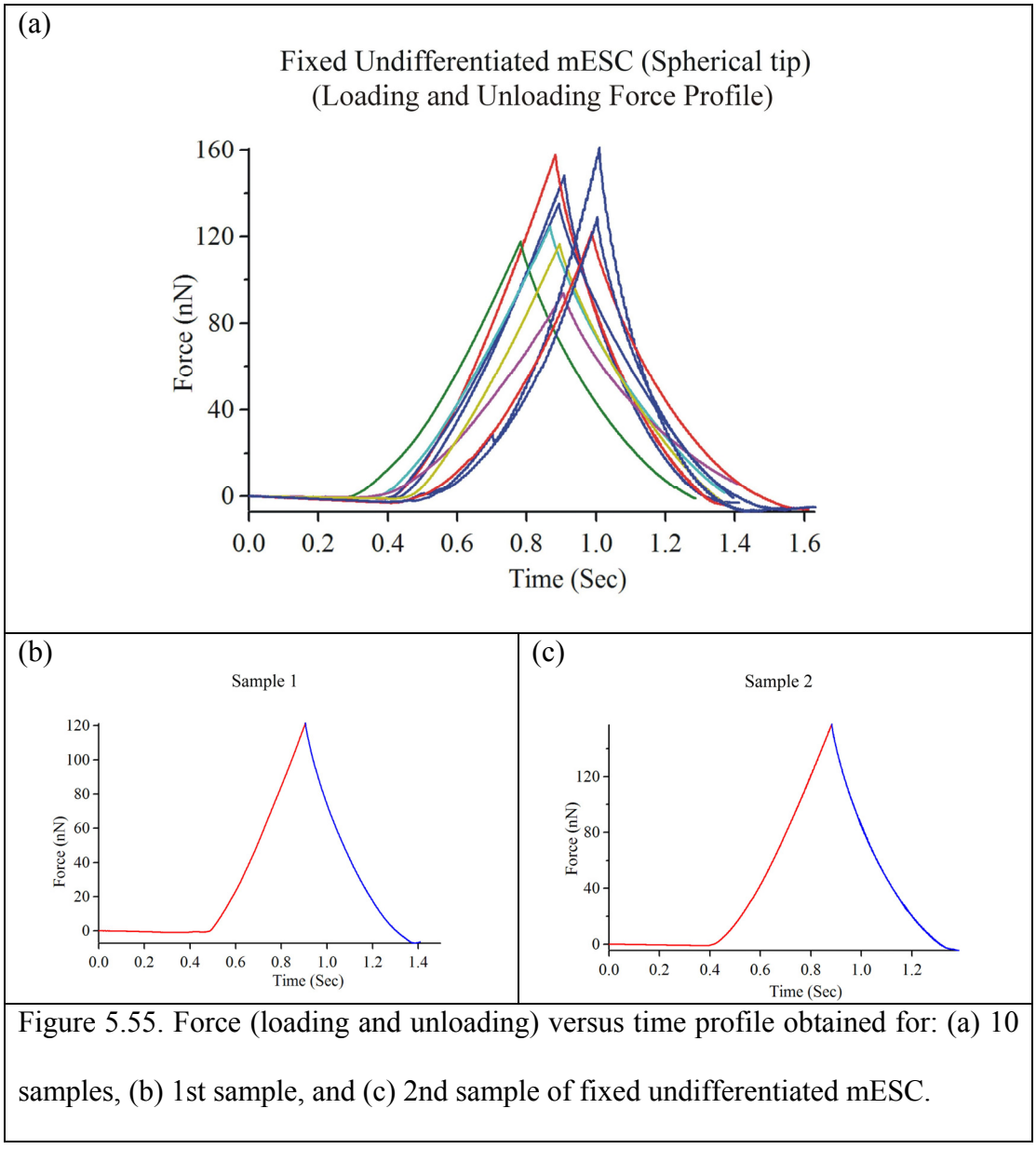

Figure 5.55. Force (loading and unloading) versus time profile obtained for: (a) 10 samples, (b) 1st sample, and (c) 2nd sample of fixed undifferentiated mESC.

We observe that the force of adhesion does not exist between the tip and the sample (figure 5.55). Hence, in this case we cannot use the JKR and DMT theory applicable to spherical indenter. From figures 5.51 – 5.54, we observe that the force-indentation curves of fixed undifferentiated mESC can be appropriately described by the Hertz model compared to the capsule model. The R^2 value obtained with the Hertz fit is

always greater than the capsule fit for any force versus indentation profile (table 5.12). Thus, we infer from the above analysis that the force-indentation curves for fixed undifferentiated mESC probed by a spherical indenter is best described by Hertz model.

FIXED DIFFERENTIATING (3rd day) mESC

(a)

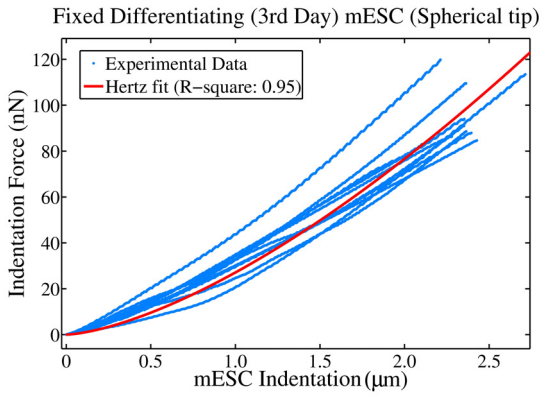

(b)

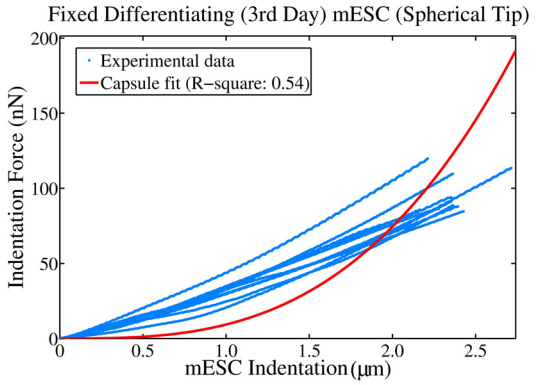

Figure 5.56: Force (F) versus cell indentation (δ) for 10 samples of fixed differentiating (3rd day) mESC: (a) Hertz fit; (b) Capsule fit. The R^2 value obtained with Hertz fit (0.95) is greater than capsule fit (0.54)

(a)

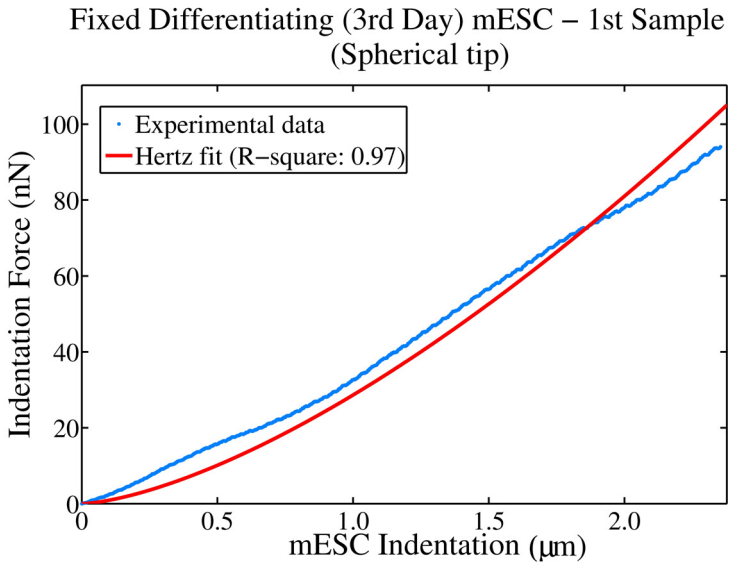

(b)

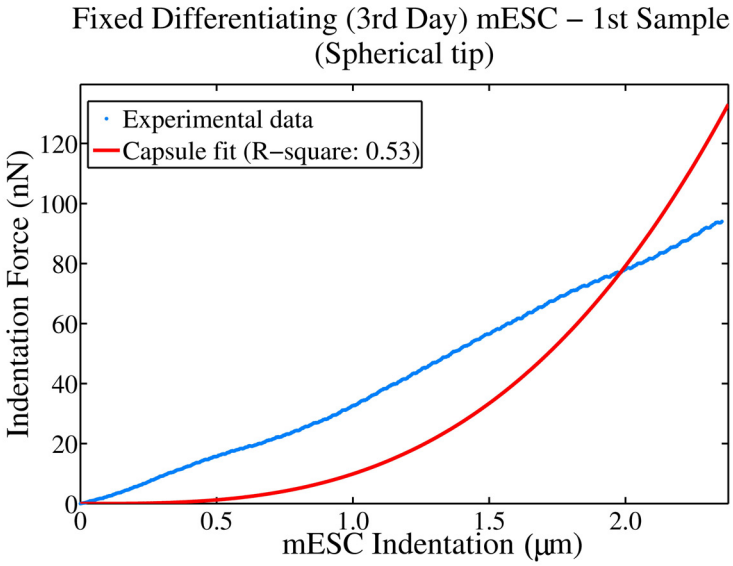

Figure 5.57: Force (F) versus cell indentation (δ) for 1st sample of fixed differentiating (3rd day) mESC: (a) Hertz fit; (b) Capsule fit. The R^2 value obtained with Hertz fit (0.97) is greater than capsule fit (0.53)

(a)

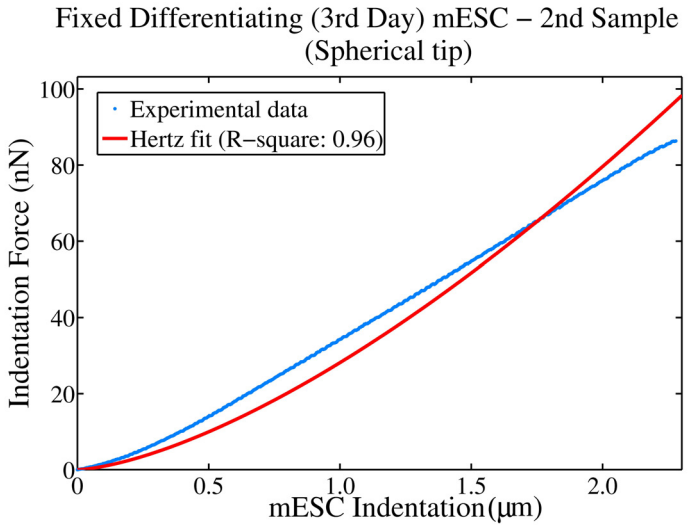

(b)

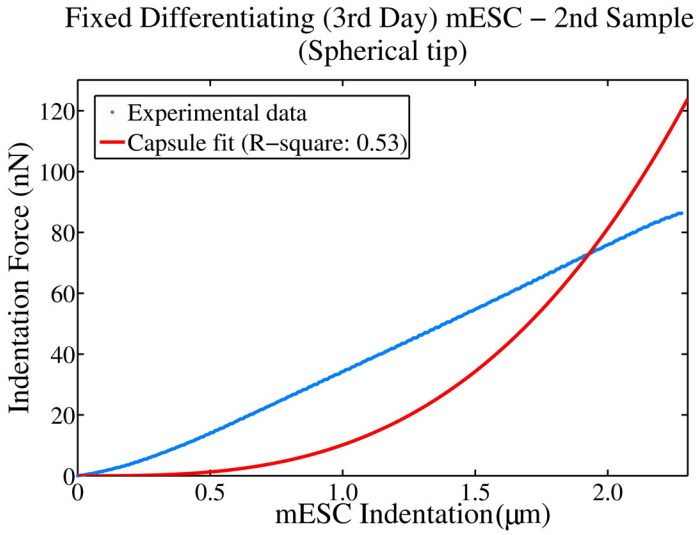

Figure 5.58: Force (F) versus cell indentation (δ) for 2nd sample of fixed differentiating (3rd day) mESC: (a) Hertz fit; (b) Capsule fit. The R^2 value obtained with Hertz fit (0.96) is greater than capsule fit (0.53)

(a)

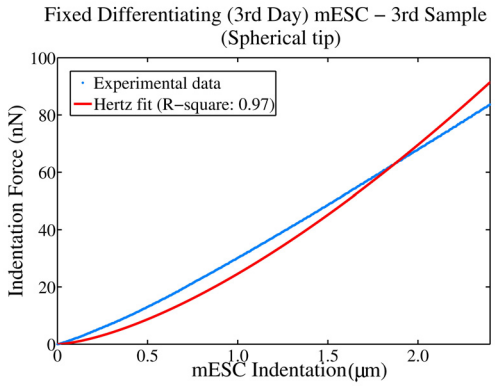

(b)

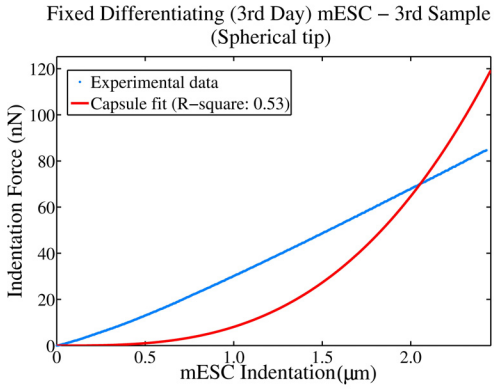

Figure 5.59: Force (F) versus cell indentation (δ) for 3rd sample of fixed differentiating (3rd day) mESC: (a) Hertz fit; (b) Capsule fit. The R^2 value obtained with Hertz fit (0.97) is greater than capsule fit (0.53)

Sample	1	2	3	4	5	6	7	8	9	10
R^2 (H)	0.97	0.96	0.97	0.97	0.97	0.99	0.99	0.99	0.97	0.98
R^2 (C)	0.53	0.53	0.53	0.53	0.56	0.72	0.71	0.83	0.57	0.59

Table 5.13: R^2 value obtained with the Hertz fit represented by R^2 (H) and capsule fit represented by R^2 (C) for 10 samples of fixed differentiating (3rd day) mESC. The R^2 value obtained with Hertz fit is greater than capsule fit.

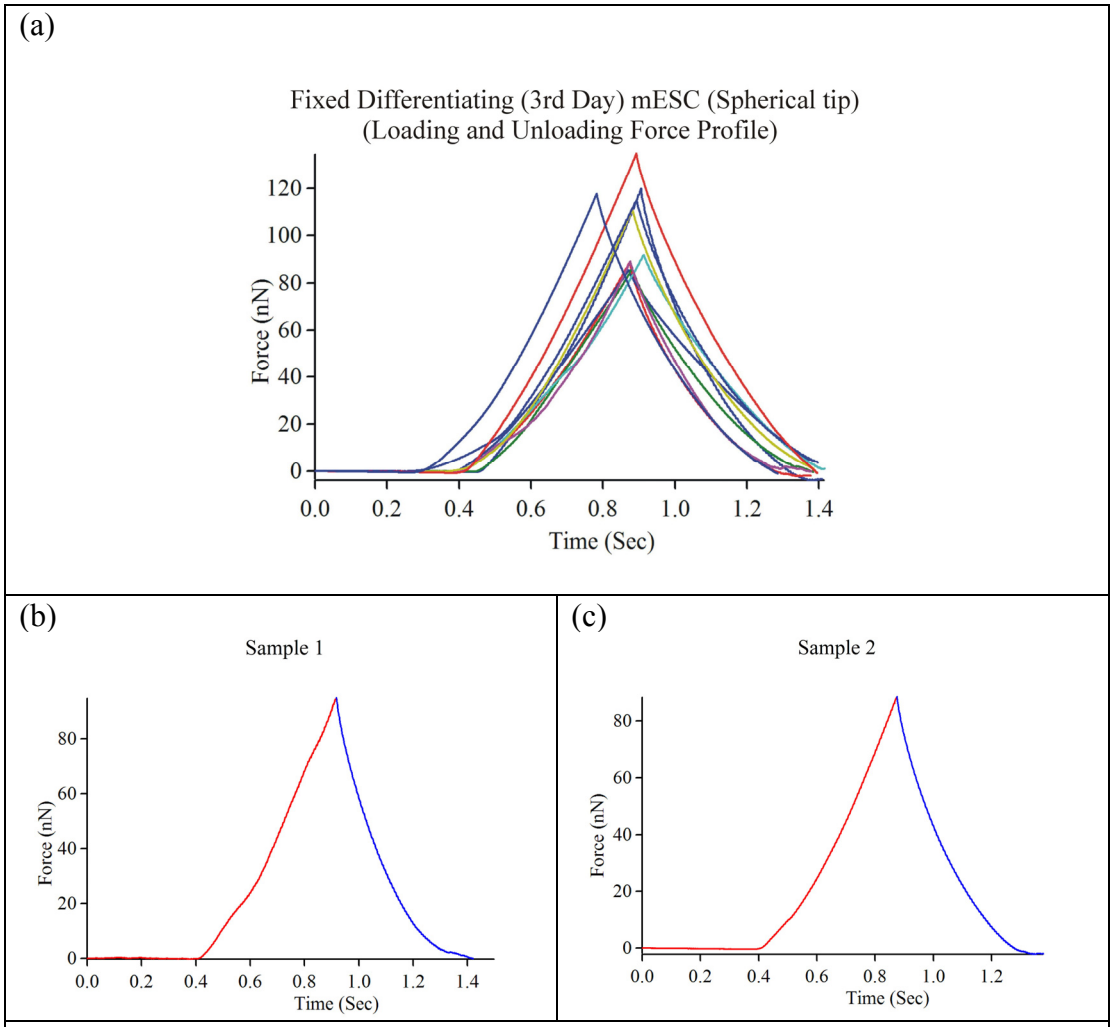

Figure 5.60. Force (loading and unloading) versus time profiles obtained for: (a) 10 samples, (b) 1st sample, and (c) 2nd sample of fixed differentiating (3rd day) mESC.

We observe that the force of adhesion does not exist between the tip and the sample (figure 5.60). Hence, in this case we cannot use the JKR and DMT theory applicable to spherical indenter. From figures 5.56 – 5.59, we observe that the force-indentation curves of fixed differentiating (3rd day) mESC can be appropriately described by the Hertz model compared to the capsule model. The R^2 value obtained with the Hertz fit is always greater than the capsule fit for any force versus indentation profile (table

5.13). Thus, we infer from the above analysis that the force-indentation curves for fixed differentiating (3rd day) mESC probed by a spherical indenter is best described by Hertz model.

FIXED DIFFERENTIATING (6th day) mESC

(a)

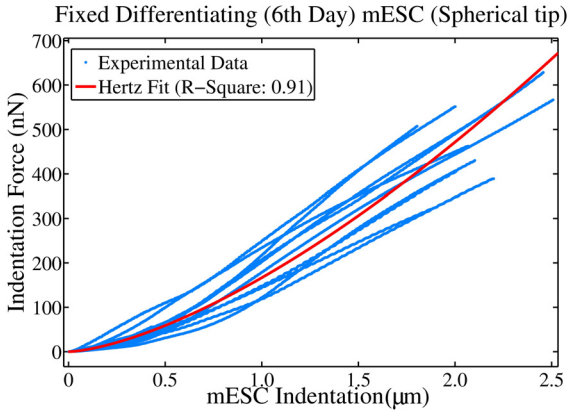

(b)

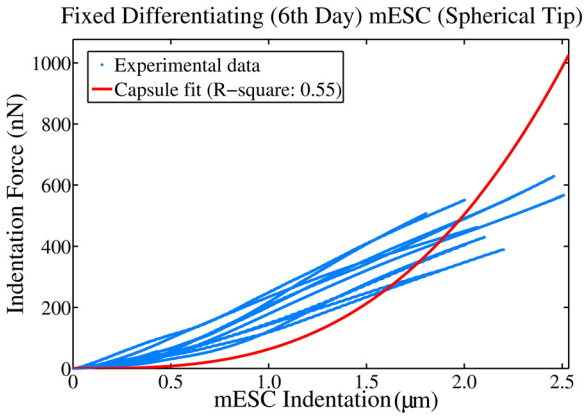

Figure 5.61: Force (F) versus cell indentation (δ) for 10 samples of fixed differentiating (6th day) mESC: (a) Hertz fit; (b) Capsule fit. The R^2 value obtained with Hertz fit (0.91) is greater than capsule fit (0.55)

(a)

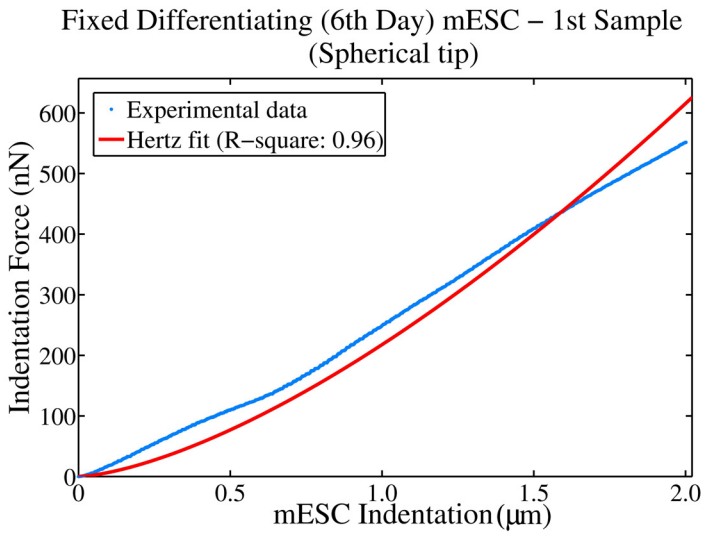

(b)

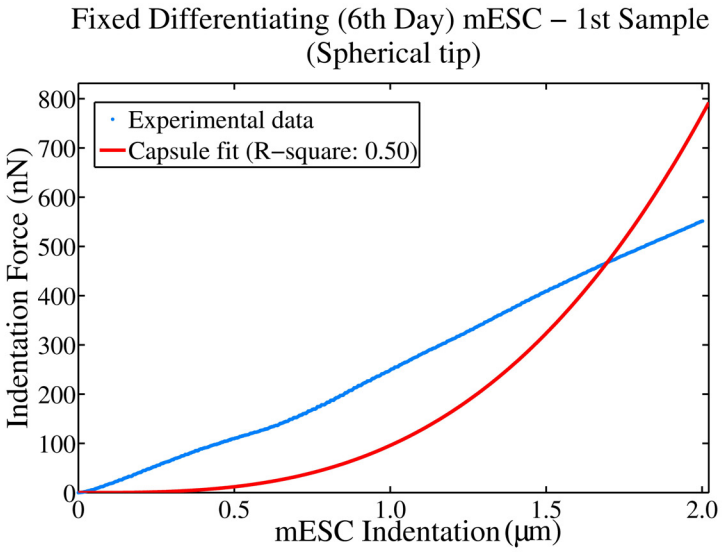

Figure 5.62: Force (F) versus cell indentation (δ) for 1st sample of fixed differentiating (6th day) mESC: (a) Hertz fit; (b) Capsule fit. The R^2 value obtained with Hertz fit (0.96) is greater than capsule fit (0.50)

(a)

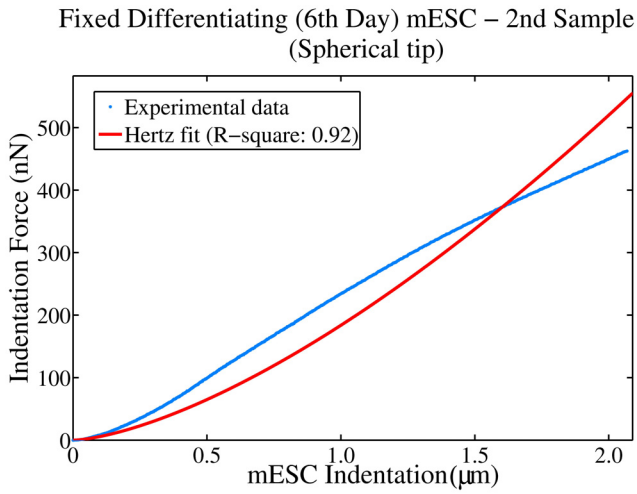

(b)

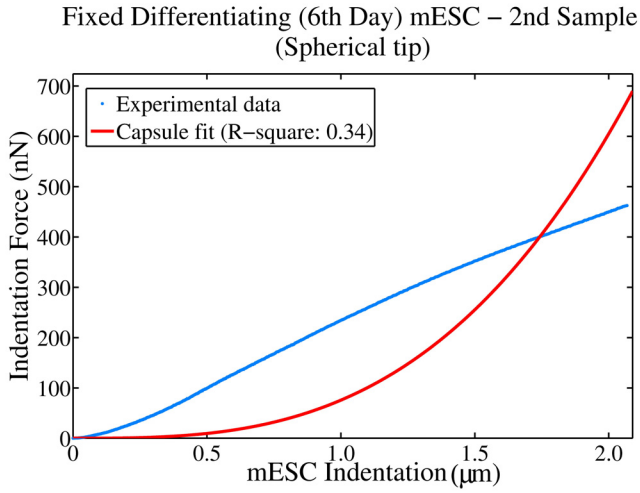

Figure 5.63: Force (F) versus cell indentation (δ) for 2nd sample of fixed differentiating (6th day) mESC: (a) Hertz fit; (b) Capsule fit. The R^2 value obtained with Hertz fit (0.92) is greater than capsule fit (0.34)

(a)

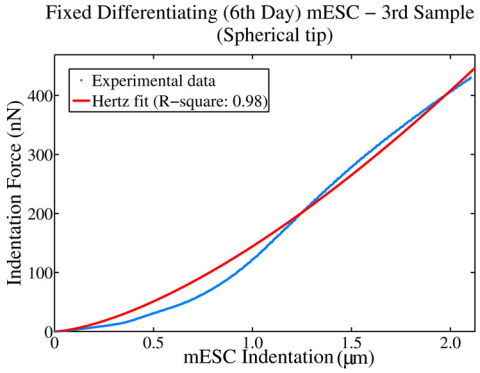

(b)

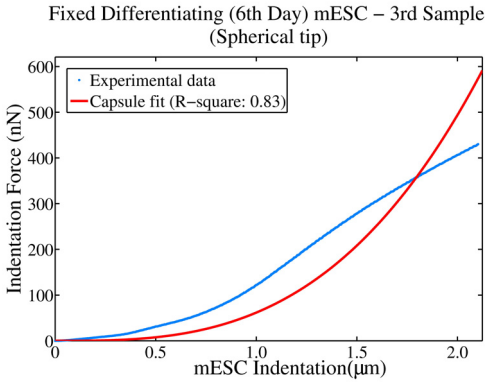

Figure 5.64: Force (F) versus cell indentation (δ) for 3rd sample of fixed differentiating (6th day) mESC: (a) Hertz fit; (b) Capsule fit. The R^2 value obtained with Hertz fit (0.98) is greater than capsule fit (0.83)

Sample	1	2	3	4	5	6	7	8	9	10
R^2 (H)	0.96	0.92	0.98	0.99	0.98	0.98	0.99	0.99	0.98	0.99
R^2 (C)	0.50	0.34	0.83	0.76	0.61	0.64	0.65	0.75	0.60	0.78

Table 5.14: R^2 value obtained with the Hertz fit represented by R^2 (H) and capsule fit represented by R^2 (C) for 10 samples of fixed differentiating (6th day) mESC. The R^2 value obtained with Hertz fit is greater than capsule fit.

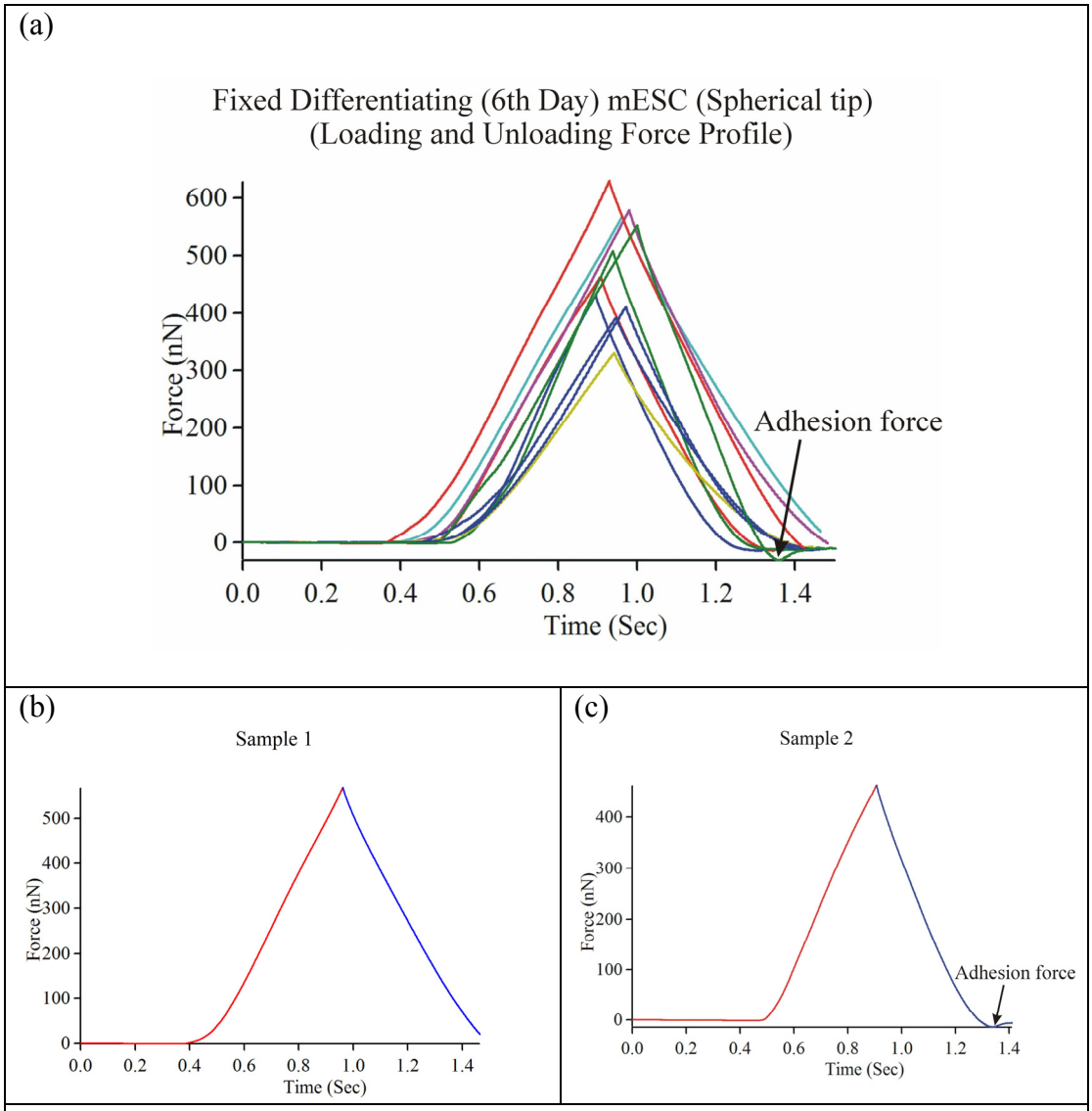

Figure 5.65. Force (loading and unloading) versus time profiles obtained for: (a) 10 samples, (b) 1st sample, and (c) 2nd sample of fixed differentiating (6th day) mESC. The adhesion force in (c) is 16 nN and in (b) is 8nN.

We observe that the force of adhesion does not exist between the tip and the sample except for two of them (figure 5.65a and 5.65c). The adhesion force is negligible (less than 0.05 times the maximum indentation force) compared to the adhesion force

(more than 0.1 times the maximum indentation force) observed by others for the JKR theory to be applicable [129, 149, 179]. The adhesion could be due to the wear of the spherical tip [179]. Hence, in this case we cannot use the JKR and DMT theory applicable to spherical indenter. From figures 5.61 – 5.64, we observe that the force-indentation curves of fixed differentiating (6^{th} day) mESC can be appropriately described by the Hertz model compared to the capsule model. The R^2 value obtained with the Hertz fit is always greater than the capsule fit for any force versus indentation profile (table 5.14). Thus, we infer from the above analysis that the force-indentation curves for fixed differentiating (6^{th} day) mESC probed by a spherical indenter is best described by Hertz model.

5.8.2.4. Discussion

We observe that the force-indentation curves of fixed mESC indented by a spherical tip can be appropriately described by the Hertz model compared to the capsule model. The R^2 value obtained with the Hertz fit is always greater than the capsule fit for any force versus indentation profile. In addition, the force of adhesion does not exist between the tip and the sample. Thus the JKR and DMT models applicable to spherical indenter do not describe the mechanical behavior of live mESC. We observe that the average maximum force attained for indenting (2 – 2.5 μm) 10 samples of fixed undifferentiated, 3^{rd} day differentiating and 6^{th} day differentiating mESC sample is approximately 133 nN, 96 nN and 475 nN respectively. The computation of elastic modulus and statistical analysis are presented in chapter 6. *As a first approximation,*

we conclude from the above analysis that the force-indentation curves for fixed mESC probed by a spherical indenter are appropriately described by Hertz model.

We have considered the analytical models presented in sections 5.2 – 5.7 of this chapter to predict the mechanical behavior of undifferentiated, 3rd day differentiating and 6th day differentiating mESC in both live and fixed states. The force-indentation profiles show that the force required to indent (2 – 2.5 μm) a differentiating (6th day) mESC sample (live and fixed) is greater than the undifferentiated mESC sample. *As a first approximation, the Bilodeau and Hertz model appropriately fit the force-indentation profiles of mESC indented by a pyramidal tip and spherical tip respectively. The models will aid in computing the elastic modulus and provide an understanding of the mechanical response of mESC and single indentation studies.*

5.9 Preliminary Studies on mESC

Our preliminary studies have involved indentation of live and fixed mESC. Experiments were performed on live as well as fixed cells to facilitate the use of fixed cells when logistics prove difficult to maintain live cells. We performed the indentation tasks with a peak trigger force for 1μm deflection of the AFM tip obtained from the previous study (please see section 4.5). We used a v-shaped Pyrex Nitride cantilever (PNP-DB, Nanoworld AG) in these studies. The spring constant and elastic modulus of the cantilever was 0.06 N/m and 222.22 GPa respectively. The opening angle (α) of the cantilever pyramidal tip was 35^0. Initially, we used the Sneddon model to compute the elastic modulus of mESC and later used the Bilodeau model. Referring to section 5.8, it can be seen the loading force (F) is directly

proportional to the square of indentation (δ) for both conical and pyramidal tip. Thus, the force-indentation profile obtained by both the tips is similar, but the value of constant (g) differs. Hence the elastic modulus value computed by Sneddon model (conical tip) will differ from the elastic modulus computed by Bilodeau model.

We present the computation of elastic modulus of live as well as fixed mESC in undifferentiated and 3rd day differentiating (very early in the differentiation process) states and the statistical analysis in the following sub-sections.

5.9.1 Live Cells

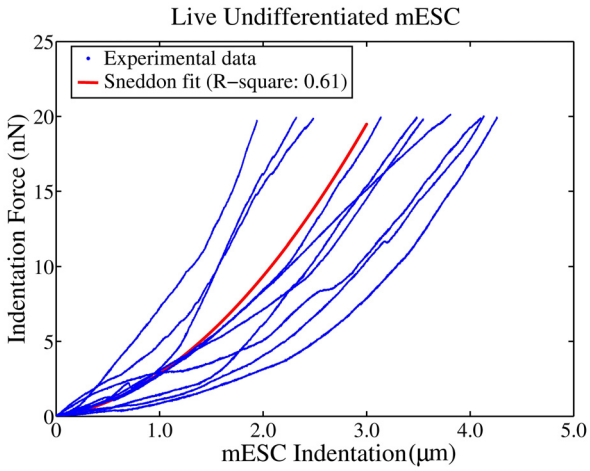

Figure 5.66. Force (F) versus cell indentation (δ) for live undifferentiated mESC. The R^2 value for the Sneddon fit is 0.6102.

Figure 5.66 and figure 5.67 shows the force versus cell indentation, δ, for live undifferentiated and differentiating mESC respectively. From the figures we observe that the undifferentiating mESC is supple cell compared to differentiated mESC. Based on the experimental data, we performed a Sneddon fit on the dataset and the corresponding Sneddon fit is shown in the figure. The R^2 value for live differentiating

mESC was found to be 0.5059 and R^2 value for live undifferentiated mESC was found to be 0.6102.

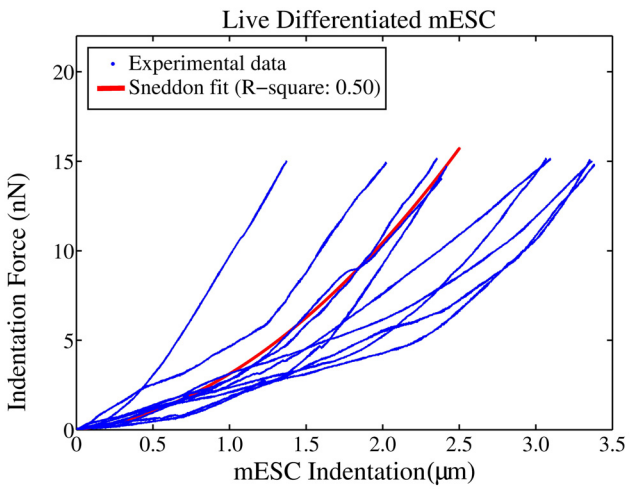

Figure 5.67. Force (F) versus cell indentation (δ) for live differentiating mESC. The R^2 value for the Sneddon fit is 0.5059.

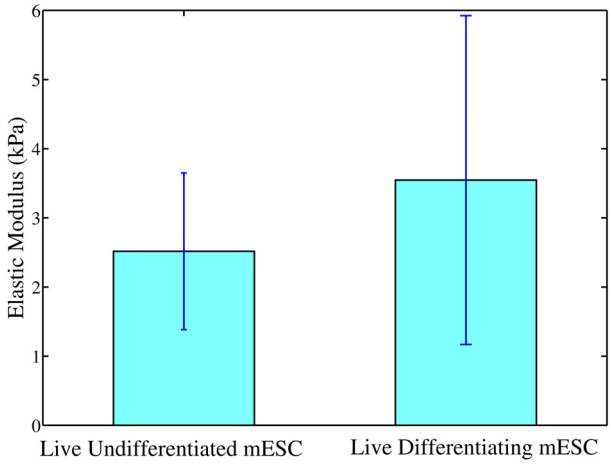

Figure 5.68. Elastic modulus of live mESC calculated from the Sneddon contact model along with the error bar.

Figure 5.68 shows the average elastic modulus of live differentiating and undifferentiated mESC. Sneddon model was used to compute the elastic modulus of mESC for each indentation task by assuming Poisson's ratio of 0.5. The average elastic modulus was found to be 2.5166 kPa and 3.546 kPa for live undifferentiated and differentiating mESC respectively. The standard deviation was 1.1332 kPa and 2.3771 kPa for live undifferentiated and differentiating mESC respectively. This may be explained based on the stage of cell cycle the live cells were indented by the AFM (please refer to the section 6.2.2). We also performed a non-parametric ANOVA analysis namely the Kruskal-Wallis test on the elastic modulus values for differentiating and undifferentiated live mESC and the p-value obtained was 0.3643. Since the p- value is more than the level of significance (α) i.e. 0.05 chosen in our studies, it implies that there is no significant statistical difference between the mechanical property (obtained by Sneddon model) of live undifferentiated and differentiating mESC.

The AFM tip used in our studies is a pyramid rather than a cone (Sneddon model). Thus we have also used the Bilodeau model (pyramidal tip) to compute the elastic modulus of live mESC. The force (F) versus indentation profile for both Sneddon and Bilodeau model is same (F is directly proportional to δ^2). Therefore, Sneddon fit (figures 5.66 and 5.67) is similar to Bilodeau fit. However, the elastic modulus computed by Bilodeau model will be different from the elastic modulus computed by Sneddon model. Figure 5.69 shows the average elastic modulus of live undifferentiated and differentiating mESC computed by Bilodeau model assuming Poisson's ratio of 0.5. The average elastic modulus was found to be 2.1362 kPa and

3.01 kPa for live undifferentiated and differentiating mESC respectively. The standard deviation was 0.9619 kPa and 2.0178 kPa for live undifferentiated and differentiating mESC respectively. The p-value obtained by Kruskal-Wallis test performed on the elastic modulus values for differentiating and undifferentiated live mESC was 0.3643 (same value obtained by Sneddon model). Hence there is no significant statistical difference between the mechanical property (obtained by Bilodeau model) of live undifferentiated and differentiating mESC as the p- value is more than α value (0.05). Referring to table 5.15, it is observed that the elastic modulus of live mESC obtained by Sneddon model is 17.8% more than the elastic modulus of live mESC obtained by Bilodeau model. This is due to the underestimation of the contact area in the Sneddon model (please refer to section 6.2.2).

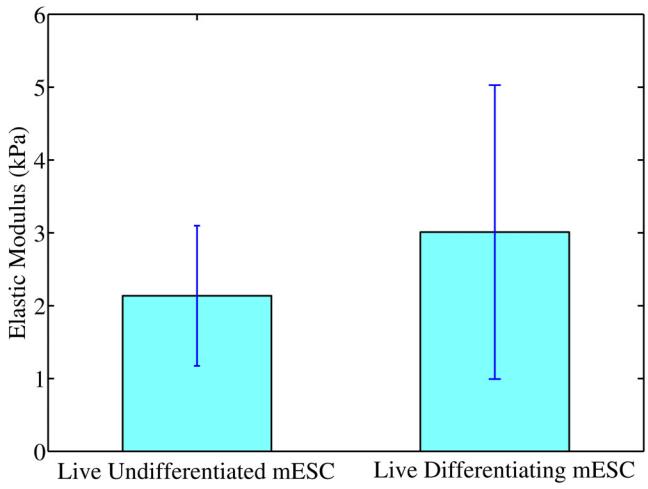

Figure 5.69. Elastic modulus of live mESC calculated from the Bilodeau contact model along with the error bar.

Statistics		Live Undifferentiated mESC	Live Differentiating mESC
Mean	Sneddon model	2.5166 kPa	3.546 kPa
	Bilodeau model	2.1362 kPa	3.01 kPa
Standard deviation	Sneddon model	1.1332 kPa	2.3771 kPa
	Bilodeau model	0.9619	2.0178 kPa
Relative deviation	Sneddon model	45.02%	67.03%
	Bilodeau model	45.02%	67.03%

Table 5.15: Elastic modulus of live undifferentiated and differentiating mESC computed by Sneddon as well as Bilodeau model. The elastic modulus computed by Sneddon model is 17.8% more than the elastic modulus computed by Bilodeau model. The relative deviation of modulus is high for both live undifferentiated and differentiating mESC.

5.9.2 Fixed Cells

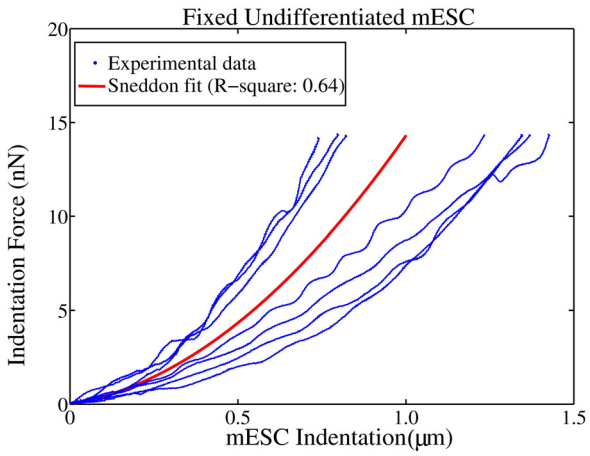

Figure 5.70. Force (F) versus cell indentation (δ) for fixed undifferentiated mESC. The R^2 value for the Sneddon fit is 0.6453.

Figure 5.70 and figure 5.71 shows the force versus cell indentation, δ, for fixed undifferentiated and differentiating mESC respectively.

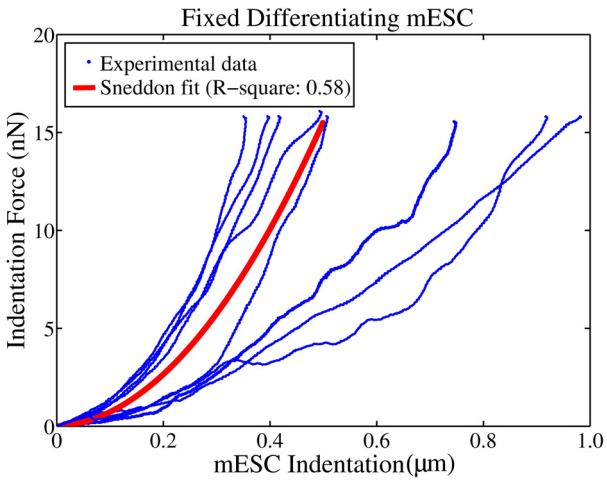

Figure 5.71. Force (F) versus cell indentation (δ) for fixed differentiating mESC. The R^2 value for the least square fit is 0.5816.

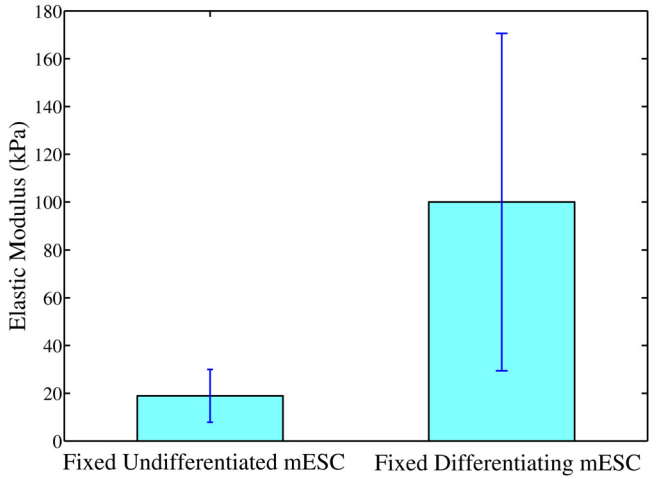

Figure 5.72. Elastic modulus of fixed mESC calculated from the Sneddon contact model along with the error bar.

From the figures we observe that the undifferentiated mESC is supple (e.g. cytoskeleton) compared to differentiating mESC. Based on the experimental data, we performed the Sneddon fit on the dataset and the corresponding Sneddon fit is shown in the figure. The R^2 value for fixed differentiating mESC was found to be 0.5816 and R^2 value for fixed undifferentiated mESC was found to be 0.6453. Figure 5.72 shows the average elastic modulus of fixed differentiating and undifferentiated mESC. Sneddon model was used to compute the elastic modulus of mESC for each indentation task by assuming Poisson's ratio of 0.5. The average elastic modulus was found to be 18.923 kPa and 100.01 kPa for live undifferentiated and differentiating mESC respectively. The standard deviation was 11.071 kPa and 70.581 kPa for live undifferentiated and differentiating mESC respectively. We also performed a non-parametric ANOVA analysis namely the Kruskal-Wallis test on the elastic modulus values for differentiating and undifferentiated fixed mESC and the p-value obtained was 0.0181. Since the p- value is less than the level of significance (α) i.e. 0.05 chosen in our studies, it implies that there is significant statistical difference between the mechanical property of fixed undifferentiated and differentiating mESC.

Figure 5.73 shows the average elastic modulus of fixed undifferentiated and differentiating mESC computed by Bilodeau model assuming Poisson's ratio of 0.5. The average elastic modulus was found to be 16.062 kPa and 84.891 kPa for fixed undifferentiated and differentiating mESC respectively. The standard deviation was 9.3976 kPa and 59.911 kPa for fixed undifferentiated and differentiating mESC respectively.

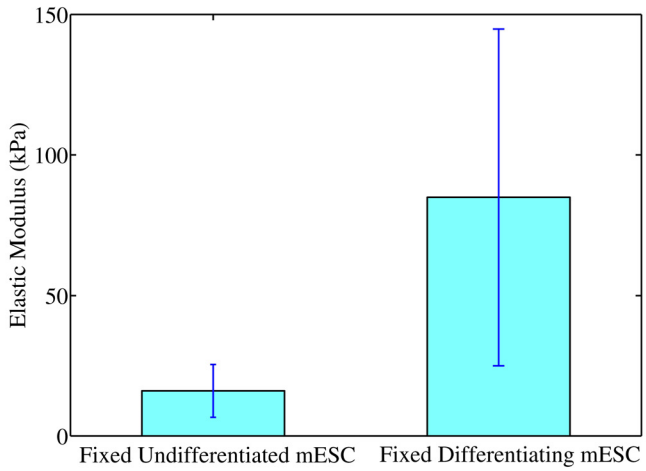

Figure 5.73: Elastic modulus of fixed mESC calculated from the Bilodeau contact model along with the error bar.

Statistics		Fixed Undifferentiated mESC	Fixed Differentiating mESC
Mean	Sneddon model	18.923 kPa	100.01 kPa
	Bilodeau model	16.062 kPa	84.891 kPa
Standard deviation	Sneddon model	11.071 kPa	70.581 kPa
	Bilodeau model	9.3976 kPa	59.911 kPa
Relative deviation	Sneddon model	58.5%	70.57%
	Bilodeau model	58.5%	70.57%

Table 5.16: Elastic modulus of fixed undifferentiated and differentiating mESC computed by Sneddon as well as Bilodeau model. The elastic modulus computed by Sneddon model is 17.8% more than the elastic modulus computed by Bilodeau model. The relative deviation of modulus is high for both fixed undifferentiated and differentiating mESC.

The p-value obtained by Kruskal-Wallis test performed on the elastic modulus values for differentiating and undifferentiated fixed mESC was 0.0181 (same value obtained by Sneddon model). The p-value is less than α value (0.05). Hence, there is a significant statistical difference between the mechanical property (obtained by Bilodeau model) of fixed undifferentiated and differentiating mESC. Referring to table 5.16, it is observed that the elastic modulus of fixed mESC obtained by Sneddon model is 17.8% more than the elastic modulus of fixed mESC obtained by Bilodeau model.

The Sneddon model considers the geometry of the conical tip-sample contact area as a circle. The contact area of the circle (A) is given by [140]:

$$A = \frac{4(\delta \tan\theta)^2}{\pi} \tag{6.1}$$

where, θ is the half-opening angle of the conical tip and δ is the sample (mESC) indentation. On the other hand, the Bilodeau model assumes the geometry of the pyramidal tip-sample contact area to be a polygon of the same type as the base of the pyramid [141]. Thus for a quadrilateral pyramid, the contact geometry is a square, whose area (A) is given by [141]:

$$A = 1.579(\delta \tan\theta)^2 \tag{6.2}$$

where, θ is the half-apex angle of the lateral face (isosceles triangle) of the pyramid. Comparing (6.1) and (6.2), we observe that the tip-sample contact area calculated by Sneddon model is less than the area calculated by Bilodeau model. The geometry of the tip used in our studies (PNP-DB, NanoWorld AG) is a quadrilateral pyramid.

Hence use of the Sneddon model underestimates the contact area and hence overestimates the elastic modulus of mESC compared to Bilodeau model. Therefore Bilodeau model is the right approach to compute the elastic modulus of mESC indented by a pyramidal tip. We also observed that there was a large standard deviation of the elastic modulus values for mESC in both live and fixed cells. One of the reasons for the large variation in modulus can be attributed to the variation in the stage of the cell cycle (M-phase or interphase) at the time of cell indentation. The cell cycle consists of four distinct phases: G1 phase, S phase, G2 phase, and M phase (see figure 5.74).

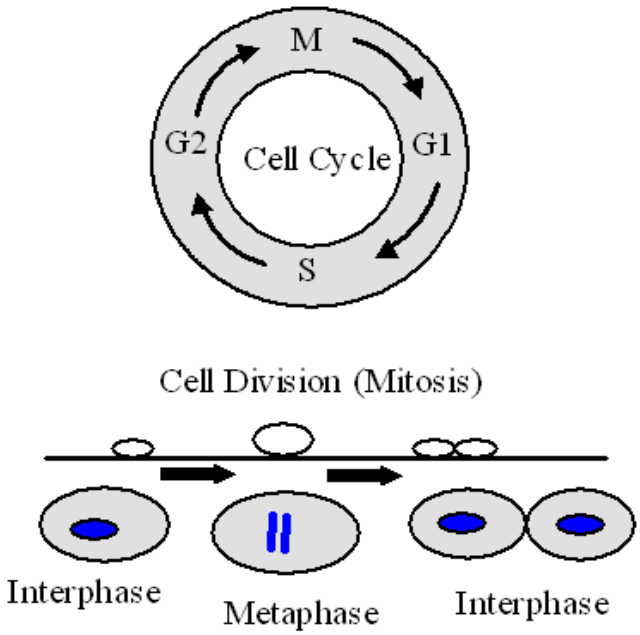

Figure 5.74. Various stages of cell cycle (Courtesy of Dr. Carol Keefer). The blue color represents a particular stain (Hoechst 33342) used to distinguish between interphase (elliptical shape) and metaphase (lines)

G1, G2, and S phases are considered the interphase, while M phase comprises the process of mitosis and cytokinesis (cell division) which results in the formation of two daughter cells. During cell indentation studies, it is difficult to ascertain the stage of cell cycle. This could explain the large variation in the elastic modulus value for live cells. In addition, the variation could be due to the mixed population of undifferentiated and differentiating mESC in a particular cell culture. For, fixed cells, similar reasoning could be applied, since the cells could be fixed at various stages of cell cycle. The variation in the stage of the cell cycle and the mixed population of mESC at the time of cell indentation could also explain a higher p-value (0.36) obtained by the Kruskal-Wallis test performed on the elastic modulus values for live undifferentiated and differentiating mESC. A similar reasoning could be applied to the low R^2 value obtained by the Sneddon fit for live and fixed cells (For an ideal fit, $R^2 = 1$). Thus, further studies are required to understand the changes in cell modulus that may occur during various phases of the cell cycle. These studies are feasible and we present them in chapter 6.

5.10 Discussion

We have presented various analytical models proposed in the literature to characterize the mechanical behavior of an individual biological cell namely: (a) Hertz theory (spherical indenter) [138], (b) Sneddon theory (cylindrical and conical indenter) [139, 140], (c) Bilodeau theory (pyramidal indenter) [141], (d) JKR (spherical and blunt conical indenter) and DMT (spherical indenter) theory [147, 166], and (e) capsule model (cylindrical and spherical indenter) [166, 178]. In addition, we have also

presented the extension of Sneddon and Bilodeau theory to blunt conical and pyramidal indenter respectively [142, 143]. Single indentation studies were performed on mESC by a pyramidal as well as spherical tip. For a pyramidal tip indenter we did not consider the following models because of indenter geometry: Hertz theory (spherical indenter), Sneddon theory (cylindrical and conical indenter), and capsule model (cylindrical and spherical indenters). We used a sharp pyramidal tip in all our experiments, therefore the blunt conical and pyramidal indenter models will not be applicable. Thus we considered the Bilodeau theory and performed an exhaustive analysis to predict whether it is an appropriate model for characterizing the mechanical behavior of mESC. We also scrutinized the force (loading and unloading) profiles to determine whether force of adhesion exists between the tip and the sample. The R^2 value obtained with Bilodeau fit for each mESC was approximately 0.9 or greater. The fit for 10 samples of live undifferentiated, 3^{rd} day differentiating and 6^{th} day differentiating was 0.90, 0.93 and 0.85. Also, the fit for 10 samples of fixed undifferentiated, 3^{rd} day differentiating and 6^{th} day differentiating was 0.83, 0.88 and 0.80. We observed that the force of adhesion existed between the tip and one sample of live undifferentiated mESC (see figure 5.13) and did not exist for all other samples of live undifferentiated, 3^{rd} day differentiating and 6^{th} day differentiating mESC. Further we also observed that the force of adhesion did not exist for fixed mESC. Thus the JKR model does not describe the mechanical behavior of mESC indented by a pyramidal tip. As a first approximation, we inferred that the Bilodeau model is appropriate for characterizing the mechanical behavior of mESC probed by a pyramidal tip. For a spherical tip, we did not consider the following

models: Sneddon theory (cylindrical and conical indenter) and the Bilodeau model (Pyramidal tip) because of the indenter geometry. In addition, the blunt conical and pyramidal indenter models are also not applicable due to tip geometry. Thus, we have considered the Hertz and the capsule model. In case of spherical tip, we also determined the loading and unloading force profiles to check whether force of adhesion exists between the tip and the sample. The R^2 value obtained with Hertz fit for each mESC was approximately 0.9 or greater. The Hertz fit averaged for 10 samples of live undifferentiated, 3rd day differentiating and 6th day differentiating was 0.95, 0.90 and 0.87. Also, the Hertz fit averaged for 10 samples of fixed undifferentiated, 3rd day differentiating and 6th day differentiating was 0.90, 0.95 and 0.91. On the other hand, the R^2 value obtained with capsule fit for each mESC was less than the Hertz fit. The capsule fit for 10 samples of live undifferentiated, 3rd day differentiating and 6th day differentiating was 0.64, 0.58, and 0.55. Also, the capsule fit for 10 samples of fixed undifferentiated, 3rd day differentiating and 6th day differentiating was 0.42, 0.54 and 0.55. We also observed that the force of adhesion did not exist for all mESC probed by a spherical tip. Thus the JKT and DMT theory do not characterize the mechanical behavior of mESC. As a first approximation, we inferred that the Hertz model is appropriate for characterizing the mechanical behavior of mESC probed by a spherical tip.

We have observed that the average force (10 samples) required to indent (2 – 2.5 μm) differentiating (6th day) mESC is greater than the average force (10 samples) required to indent undifferentiated mESC for both live and fixed cells (for both spherical and

pyramidal indenter). However in case of spherical indenter, the average force (10 samples) required to indent (2 – 2.5 μm) differentiating (3rd day) mESC is not greater than the average force (10 samples) required to indent undifferentiated mESC for both live and fixed cells indented. In addition, the force required to indent fixed cells are greater than live cells. This is because during the fixation process, aldehyde groups from the fixative react with primary amines in the cell membrane and cytoskeleton proteins, forming covalent imine bonds. The cross linking proteins dramatically increases the force response compared to live cells. As a first approximation, the mechanical response of mESC is appropriately described by solid models namely: Bilodeau model and Hertz model for pyramidal and spherical indenter respectively. We have observed that the capsule model fails in characterizing the mechanical behavior of mESC indented by spherical indenter. One of the reasons could be that the mESC mechanics is influenced by the compression of the cell interior (see figure 5.1) rather than that of the cell membrane (capsule model considers the stretching and the bending of the cell membrane). Thus, we infer that the mechanical response of mESC could be mainly due to the cell interior e.g. cytoskeleton and is not influenced by the cell membrane.

In our preliminary studies on mESC, we used Sneddon model (conical tip) as well as Bilodeau model (pyramidal tip) to compute the elastic modulus of each mESC from the force (F) and indentation (δ) data obtained from the experiments. The elastic modulus computed from Sneddon model was higher than the elastic modulus computed from Bilodeau model. This is because the former model underestimates the

contact area compared to the latter model and thus overestimates the elastic modulus of mESC. Hence, as a first approximation, we reconfirmed that Bilodeau model is appropriate for characterizing the mechanical behavior of mESC indented by a pyramidal tip. A significant statistical difference was observed between the elastic modulus of undifferentiated and differentiating mESC in fixed cells (p-value < 0.05) but not in live cells (p-value > 0.05). In addition, we also observed that the variation in elastic modulus of undifferentiated and differentiating cells was very high in both live and fixed states. Thus, we present our further studies on mESC in one particular stage of the cell cycle process in chapter 6.

However, the limitations of the present study are:

- We have assumed that the cell is elastic as well as isotropic. We did not study the viscoelastic behavior of cell [144, 180, 181].
- We have assumed that the strain induced in the cell is small during the indentation studies. We did not consider large deformation (> 20%) of the cell in our experiments.
- We have assumed that the cell is homogeneous. However, the cell surface is heterogeneous having different mechanical properties over different areas [182].

Chapter 6: Mechanical Characterization of Mouse Embryonic Stem Cell (mESC)

6.1 Introduction

We hypothesize that the mechanical property of undifferentiated mouse embryonic stem cell (mESC) differs from differentiating mESC. To address this hypothesis, we conducted indentation studies on undifferentiated and early differentiating (6 days under differentiation conditions) mESC. Experiments were performed on live as well as fixed cells to validate the hypothesis which would facilitate the use of fixed cells when logistics prove difficult to maintain live cells. The single indentation studies on multiple live and fixed mESC- undifferentiated and differentiating will determine the elastic modulus of the cells. This chapter focuses on the computation of mESC elastic modulus based on the appropriate analytical model chosen in chapter 5. The elastic modulus of undifferentiated and differentiating mESC is then analyzed using a statistical test. The test generates a p-value (probability) for the null hypothesis (H_0) and thus a probability for the research hypothesis (H_1) to be tested. The lower the p-value, the smaller the probability for the null hypothesis to be true and consequently higher is the probability that there is a significant statistical difference between the data sets (or the research hypothesis H_1 is true). The level of significance (α-value) for our statistical analysis was chosen to be 0.05, meaning that our research hypothesis would be considered true if $p < \alpha$.

6.2 Mechanical Characterization Studies on mESC in Interphase Stage (Pyramidal tip)

As described in the previous section, we observed a large standard deviation of the elastic modulus for mESC. This could be explained due to the variation in the stage of the cell cycle (M-phase or interphase) at the time of cell indentation. The large variation of elastic modulus could also be due to the mixed population of mESC (undifferentiated/differentiating) in a particular cell culture. As a result, we decided to conduct further studies to understand the change in mechanical behavior of mESC during one particular phase i.e. interphase stage of cell cycle. We implemented phase contrast module in the experimental set up (see figure 6.1) which enables imaging low contrast, transparent cells in fluid via an inverted microscope (Model: Nikon TE2000U, Optical Apparatus Co. Inc., Ardmore, PA) as shown in figure 6.2.

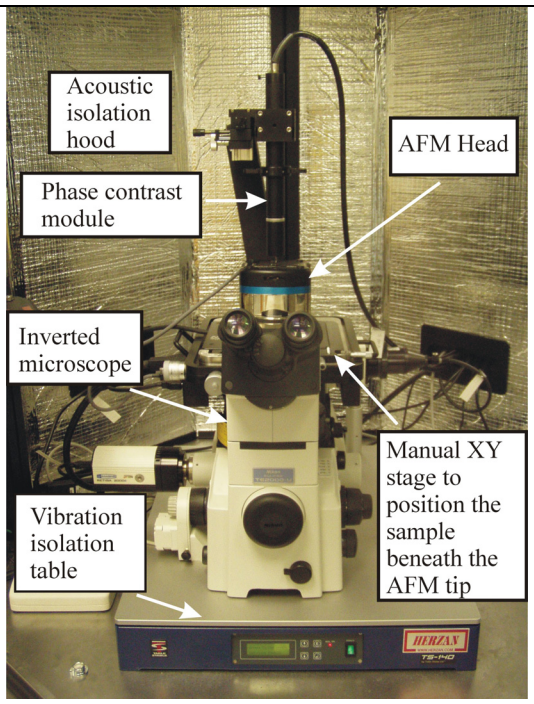

Figure 6.1. Experimental set up for mESC indentation studies in interphase stage.

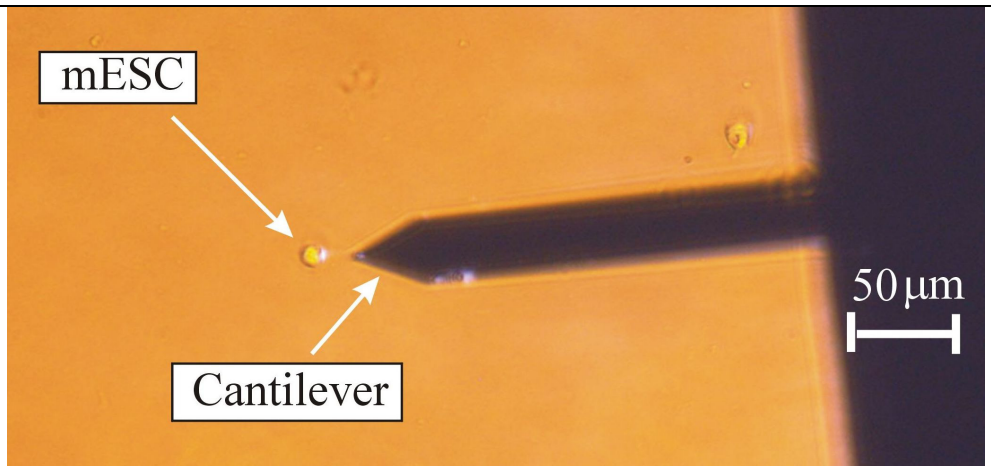

Figure 6.2. Phase contrast image of fixed differentiating (3rd day) mouse embryonic stem cells (mESC) and AC240TS cantilever (Olympus, Inc). The diameter of mESC is approximately 10 µm.

We were interested in quantifying the outcome of mESC progression during differentiation. Thus we chose to perform indentation studies on live and fixed mESC: undifferentiated and early differentiating. *In particular, we chose to perform indentation studies on undifferentiated, third day differentiating and sixth day differentiating mESC for both live as well as fixed cells.* The 3rd day and 6th day differentiating mESC are very early stages in the differentiation process. We performed initial studies on mESC in interphase stage with an AFM cantilever having pyramidal tip. Depending upon the elasticity of live and fixed mESC, we employed three types of cantilevers: (a) v-shaped Pyrex nitride cantilever (long) with a spring constant of 0.06 N/m (PNP-DB) for live cells, (b) v-shaped Pyrex nitride cantilever (short) with a spring constant of 0.48 N/m (PNP-DB) for live cells, and (c) silicon cantilever with a spring constant of 2.00 N/m (AC240TS, Olympus, Inc) for fixed cells. All the experiments were performed on mESC in one stage of the cell cycle i.e.

interphase. The cells were stained with Hoechst 33342 and were visualized by fluorescence microscopy (FM). In this microscopy, an individual cell in interphase is characterized by a blue circle (figure 6.3). Thus, the FM allowed us to perform single indentation studies on fixed mESC in interphase. We performed experiments on 60 samples of mESC as shown in table 5.1 and the cell indentation range was 2 – 2.5 μm.

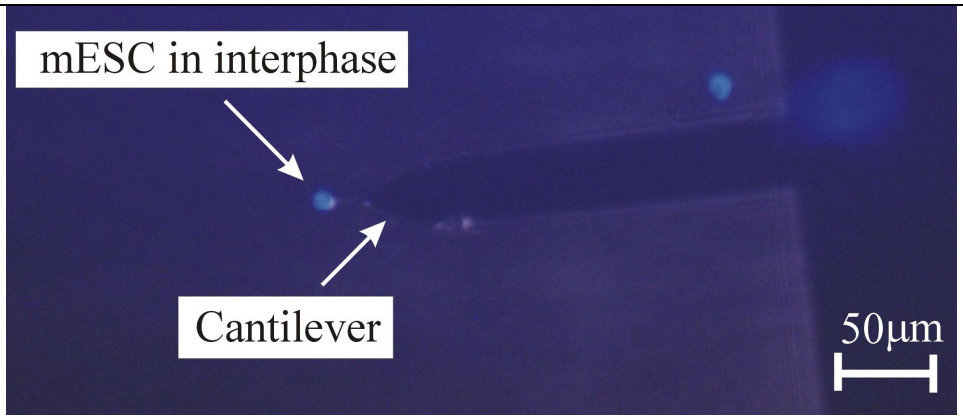

Figure 6.3. Fluorescence image (FM) of fixed differentiating mESC (3rd day) in interphase stage of the cell cycle process stained with Hoechst 33342.

6.2.1 Live Cells (Pyramidal Tip)

Figures 6.4, 6.5 and 6.6 show the force (F) versus cell indentation (δ) for live undifferentiated mESC, 3rd day differentiating mESC and 6th day differentiating mESC respectively. From the figures, we observe that the live undifferentiated mESC and 3rd day differentiating mESC are supple compared to the 6th day differentiating mESC. Based on the experimental data and the analysis shown in section 5.8, we performed a Bilodeau fit on the dataset and the corresponding Bilodeau fit is shown in the figure.

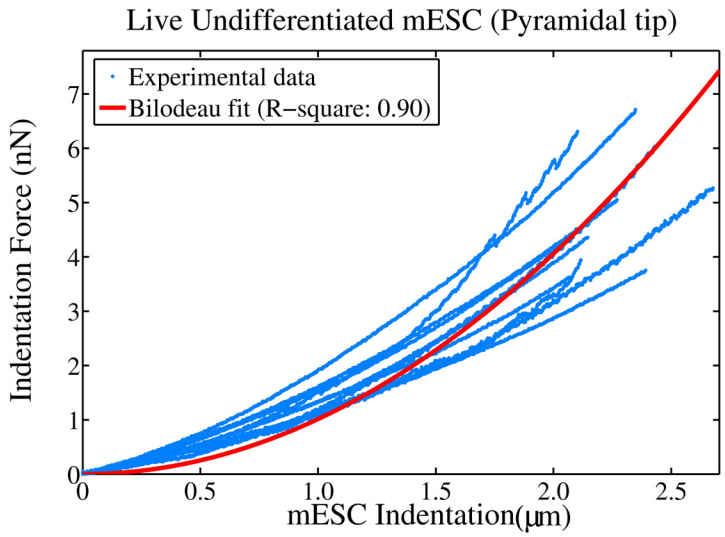

Figure 6.4. Force (F) versus cell indentation (δ) for live undifferentiated mESC. The R^2 value for the Bilodeau fit is 0.90.

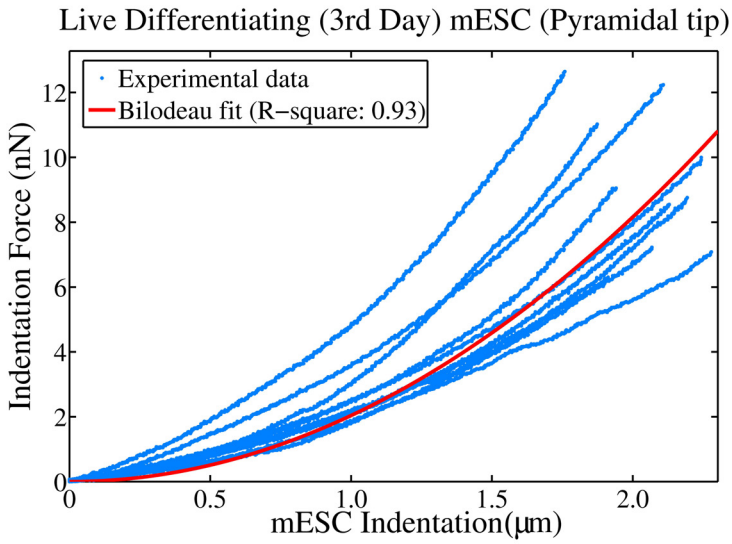

Figure 6.5. Force (F) versus cell indentation (δ) for live differentiating (3rd day) mESC. The R^2 value for the Bilodeau fit is 0.93.

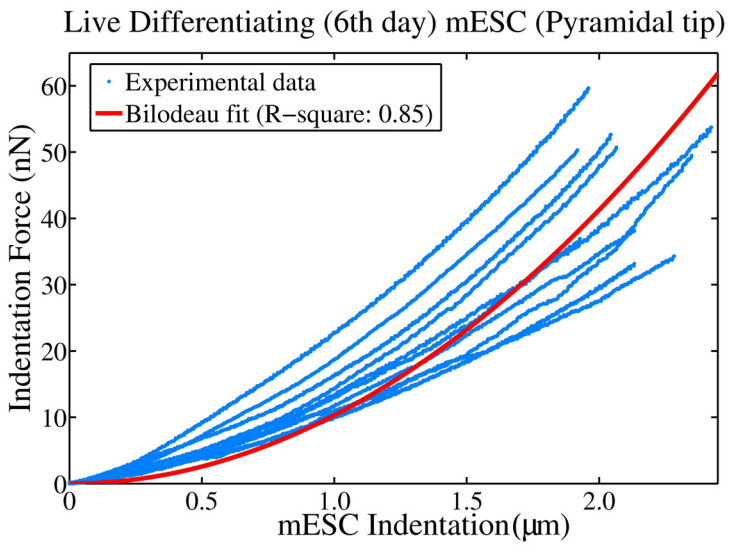

Figure 6.6. Force (F) versus cell indentation (δ) for live differentiating (6th day) mESC. The R^2 value for the Bilodeau fit is 0.85.

The R^2 value was found to be 0.90, 0.93, and 0.85 for live undifferentiated, 3rd day differentiating and 6th day differentiating mESC respectively. Bilodeau model was used to compute the elastic modulus of each live mESC sample from the force (F) versus indentation (δ) obtained from the experiments by assuming Poisson's ratio of 0.5. The average elastic modulus was found to be 1.4955 kPa, 3.374 kPa, and 16.069 kPa for live undifferentiated, 3rd day differentiating, and 6th day differentiating mESC respectively as shown in figure 6.7. The standard deviation was 0.3141 kPa, 1.2457 kPa, and 4.7052 kPa for live undifferentiated, 3rd day differentiating and 6th day differentiating mESC respectively (see figure 6.7). The statistics are summarized in table 6.1. The elastic modulus provides us a quantitative measurement of the cell membrane stiffness. Thus the data is useful for mechanical characterization of live mESC indented by a pyramidal tip.

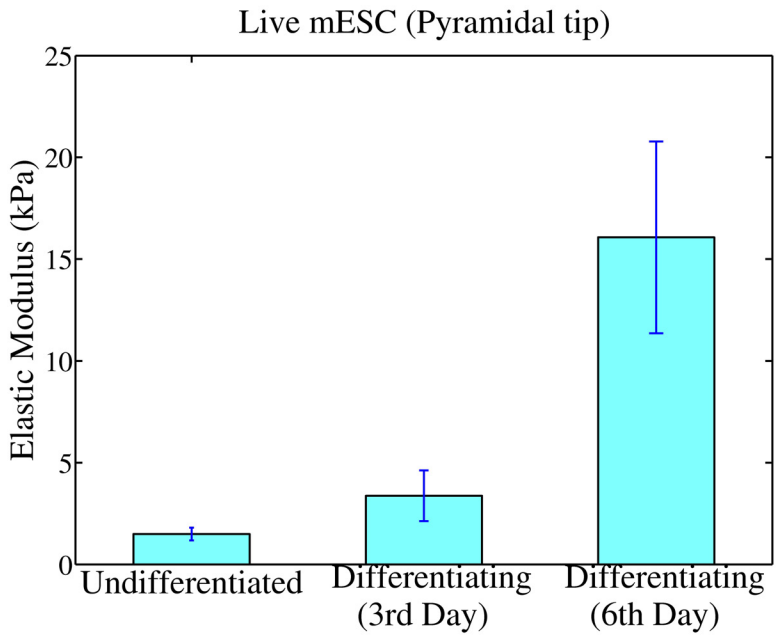

Figure 6.7. Elastic modulus of live undifferentiated, 3rd day differentiating, and 6th day differentiating mESC calculated from the Bilodeau contact model along with error bar.

Statistics	Live Undifferentiated mESC	Live Differentiating (3rd day) mESC	Live Differentiating (6th day) mESC
Mean (kPa)	1.4955	3.374	16.069
Standard deviation (kPa)	0.3141	1.2457	4.7052
Relative deviation	21%	36.9%	29.8%

Table 6.1. Elastic modulus of live mESC computed by the Bilodeau model. The variation of modulus (relative deviation) for live mESC is less than the values obtained for live mESC in our preliminary studies (section 5.9: table 5.15)

We also performed a non parametric ANOVA analysis (i.e., the Kruskal-Wallis test) on the elastic modulus values for live undifferentiated, 3rd day differentiating and 6th day differentiating mESC. The p-value obtained was less than 0.0001, leading to a probability of greater than 99.99% that there was a significant difference between the data sets. The p-value obtained on the elastic modulus values for different states of mESC is shown in table 6.2. Thus there is a probability of greater than 99.98% that there is a significant statistical difference between: (a) live undifferentiated and 3rd day differentiating mESC, (b) live undifferentiated and 6th day differentiating mESC, and (c) live 3rd day differentiating and 6th day differentiating. From the results, we infer that live undifferentiated mESC are supple compared to live 3rd day differentiating mESC. We also infer that the live 3rd day differentiating mESC is supple compared to live 6th day differentiating mESC.

Statistics	Live undiff, 3rd day diff and 6th day diff mESC	Live undiff and 3rd day diff mESC	Live undiff and 6th day mESC	Live 3rd day diff and 6th day diff
p-value (Kruskal-Wallis test)	0.00000249	0.0002	0.0002	0.0002

Table 6.2: Statistical analysis on the elastic modulus values for live undifferentiated (undiff), 3rd day differentiating (3rd day diff), and 6th day differentiating (6th day diff) mESC. A significant statistical difference exists for all data sets ($p < \alpha = 0.05$)

6.2.2 Fixed Cells

Figures 6.8, 6.9 and 6.10 show the force (F) versus cell indentation (δ) for fixed undifferentiated mESC, 3rd day differentiating mESC and 6th day differentiating mESC respectively. From the figures, we observe that the fixed undifferentiated

mESC and 3rd day differentiating mESC are supple compared to the 6th day differentiating mESC. Based on the experimental data and the analysis performed in section 5.8, we performed a Bilodeau fit on the dataset and the corresponding Bilodeau fit is shown in the figure. The R^2 value was found to be 0.83, 0.88, and 0.80 for fixed undifferentiated mESC, 3rd day differentiating mESC and 6th day differentiating mESC respectively. Bilodeau model was used to compute the elastic modulus of each live mESC sample from the force (F) versus indentation (δ) obtained from the experiments by assuming Poisson's ratio of 0.5.

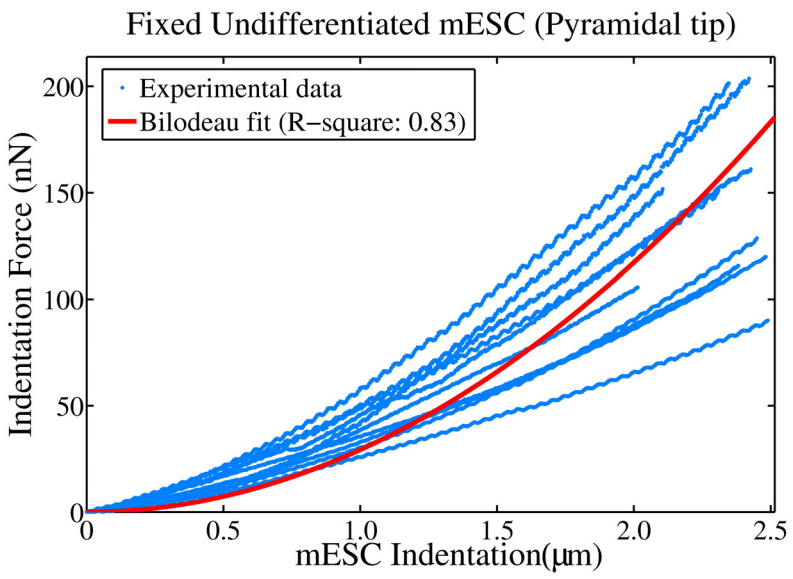

Figure 6.8: Force versus (F) cell indentation (δ) for fixed undifferentiated mESC. The R^2 value for the Bilodeau fit is 0.83.

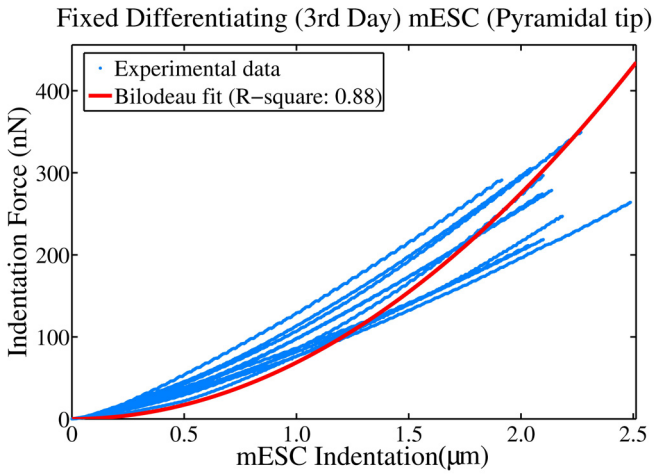

Figure 6.9 Force versus (F) cell indentation (δ) for fixed differentiating (3rd day). The R^2 value for the Bilodeau fit is 0.88.

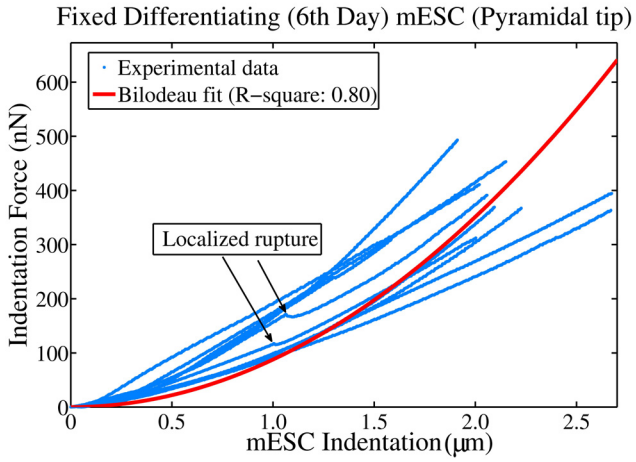

Figure 6.10 Force versus (F) cell indentation (δ) for fixed differentiating (6th day). The R^2 value for the Bilodeau fit is 0.88. The localized rupture may be due to the puncturing of the cell membrane.

The average elastic modulus was found to be 35.185 kPa, 83.344 kPa, and 120.87 kPa for fixed undifferentiated, 3rd day differentiating, and 6th day differentiating mESC respectively as shown in figure 6.11. The standard deviation was 9.626 kPa, 16.394 kPa, and 36.796 kPa for fixed undifferentiated, 3rd day differentiating and 6th day differentiating mESC respectively (see figure 6.11). The statistical results are summarized in table 6.3. The elastic modulus provides us a quantitative measurement of the cell stiffness. Thus the data is useful for mechanical characterization of fixed mESC indented by a pyramidal tip.

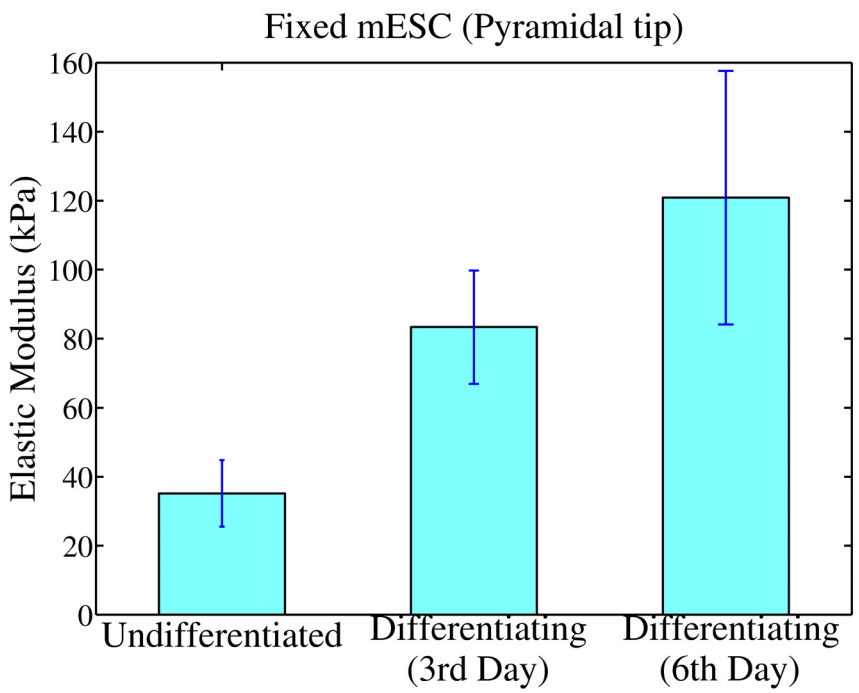

Figure 6.11. Elastic modulus of fixed undifferentiated, 3rd day differentiating, and 6th day differentiating mESC calculated from the Bilodeau contact model along with error bar.

Statistics	Fixed Undifferentiated mESC	Fixed Differentiating (3^{rd} day) mESC	Fixed Differentiating (6^{th} day) mESC
Mean (kPa)	35.185	83.344	120.87
Standard deviation (kPa)	9.626	16.394	36.796
Relative deviation	27%	19.6%	13.4%

Table 6.3. Elastic modulus of fixed mESC computed by the Bilodeau model. The variation of modulus (relative deviation) for fixed mESC is less than the values obtained for fixed mESC in our preliminary studies (section 5.9: table 5.16)

We also performed a non parametric ANOVA analysis (i.e., the Kruskal-Wallis test) on the elastic modulus values for fixed undifferentiated, 3^{rd} day differentiating and 6^{th} day differentiating mESC. The p-value obtained was less than 0.001, leading to a probability of greater than 99.9% that there was a significant difference between the data sets. The p-value obtained on the elastic modulus values for different states of mESC is shown in table 6.4. Thus there is a probability of greater than 99.98% that there is a significant statistical difference between: (a) fixed undifferentiated and 3^{rd} day differentiating mESC and (b) fixed undifferentiated and 6^{th} day differentiating mESC. There is also a probability of greater than 98.74% that there is a significant statistical difference between fixed 3^{rd} day differentiating and 6^{th} day differentiating mESC. From the results, we infer that fixed undifferentiated mESC is supple compared to fixed 3^{rd} day differentiating mESC. We also infer that the fixed 3^{rd} day differentiating mESC is supple cell compared to fixed 6^{th} day differentiating mESC.

Statistics	Fixed undiff, 3rd day diff and 6th day diff mESC	Fixed undiff and 3rd day diff mESC	Fixed undiff and 6th day mESC	Fixed 3rd day diff and 6th day diff
p-value (Kruskal-Wallis test)	0.0000153	0.0002	0.0002	0.0126

Table 6.4: Statistical analysis on the elastic modulus values for fixed undifferentiated (undiff), 3rd day differentiating (3rd day diff), and 6th day differentiating (6th day diff) mESC. A significant statistical difference exists for all data sets ($p < \alpha = 0.05$)

We have conducted indentation studies on mESC (interphase stage of the cell cycle process) with a pyramidal tip on undifferentiated, 3rd day differentiating and 6th day differentiating mESC in both live and fixed states. Experiments were conducted on 60 samples of mESC with a cell indentation range of 2 – 2.5 μm. Based on the analysis performed in section 5.8 and 6.2, we chose Bilodeau contact model to compute the elastic modulus of mESC indented by a pyramidal tip. We observed that the elastic modulus of 6th day differentiating mESC is higher than 3rd day differentiating mESC and the elastic modulus of 3rd day differentiating is higher than undifferentiated mESC in both live and fixed cells. Thus the results obtained using live cells parallel that of fixed cells. We also observed that the variation in elastic modulus values (undifferentiated and differentiating) for mESC is low compared to the elastic modulus values (undifferentiated and differentiating) obtained in our preliminary work (section 6.2) in both live and fixed states. Kruskal-Wallis test was performed on the elastic modulus values for undifferentiated, 3rd day differentiating and 6th day differentiating mESC in both live and fixed cells. We found that the p-value is less

than the level of significance ($\alpha = 0.05$). Thus we confirmed our research hypothesis that the mechanical property of undifferentiated mESC differs from early differentiating mESC in both live and fixed state.

6.3 Mechanical Characterization Studies on mESC in Interphase Stage (Spherical Tip)

In the previous section we performed experiments on mESC with a pyramidal tip. However, such cantilever induces large stress concentration in the vicinity of the tip apex [182]. This can lead to nonlinearity in the material response. The second major drawback with pyramidal tips is the relatively small area of contact. Cells can have inhomogeneous surfaces [182]. When the area of contact is small, the tip measures local elastic modulus of the cell which could vary over the cell surface. On the other hand, spherical probe causes lower stress concentration. The large area of probe-cell contact results in averaging local variation in elastic modulus compared to that measured with a regular pyramidal tip. Hence, we conducted experiments with a spherical probe to further confirm our research hypothesis that the mechanical property of undifferentiated mESC differs from early differentiating mESC.

Depending upon the elasticity of live and fixed mESC, we employed two types of cantilevers attached with a spherical probe (5 μm in diameter): (a) silicon nitride cantilever with a spring constant of 0.06 N/m (Novascan Technologies, Inc., Ames, IA) for live cells, (b) silicon cantilever with a spring constant of 1.75 N/m (Novascan Technologies, Inc) for fixed cells. The experimental set up shown in figure 6.1 was

used to indent live and fixed mESC in undifferentiated as well as differentiating state. The cells were 10 – 15 µm in diameter. The phase contrast module enabled imaging low contrast, transparent cells in fluid via an inverted microscope (Model: TE2000U, Nikon, Inc) as shown in figure 6.12. All the experiments were performed on mESC in one stage of the cell cycle i.e. interphase. The cells were stained with Hoechst 33342 and were visualized by fluorescence microscopy (FM) as shown in figure 6.13. We performed experiments on 60 samples of mESC as shown in table 5.1 and the cell indentation range was 2 – 2.5 µm.

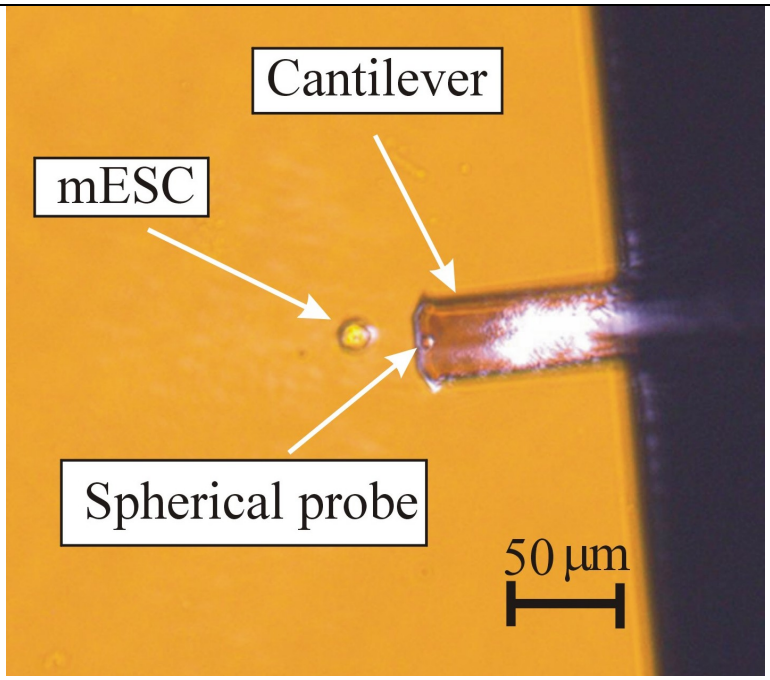

Figure 6.12. Phase Contrast image of fixed differentiating mouse embryonic stem cell (mESC) and silicon cantilever (k = 1.75 N/m) attached with a spherical probe (5 µm in diameter). The diameter of mESC is approximately 12 µm in diameter.

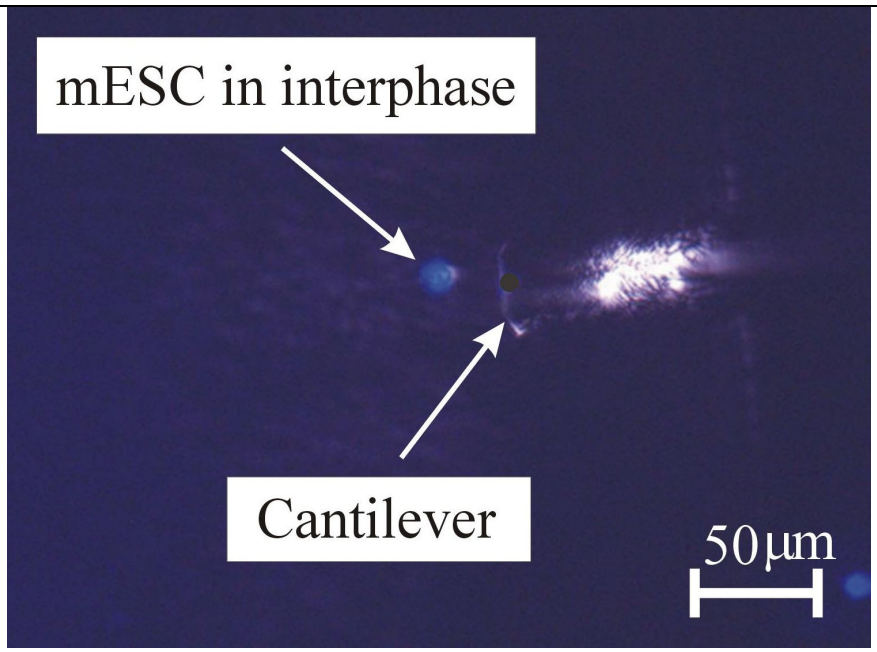

Figure 6.13. Fluorescence image (FM) of fixed differentiating mESC in interphase stained with Hoechst 33342.

6.3.1 Live Cells (Spherical Tip)

Figures 6.14, 6.15 and 6.16 show the force (F) versus cell indentation (δ) for live undifferentiated mESC, 3rd day differentiating mESC and 6th day differentiating mESC respectively. From the figures, we observe that the live undifferentiated mESC and 3rd day differentiating mESC are supple compared to the 6th day differentiating mESC. Based on the experimental data and the analysis shown in section 5.8, we performed a Hertz fit on the dataset and the corresponding Hertz fit is shown in the figure. The R^2 value was found to be 0.95, 0.90, and 0.87 for live undifferentiated, 3rd day differentiating and 6th day differentiating mESC respectively.

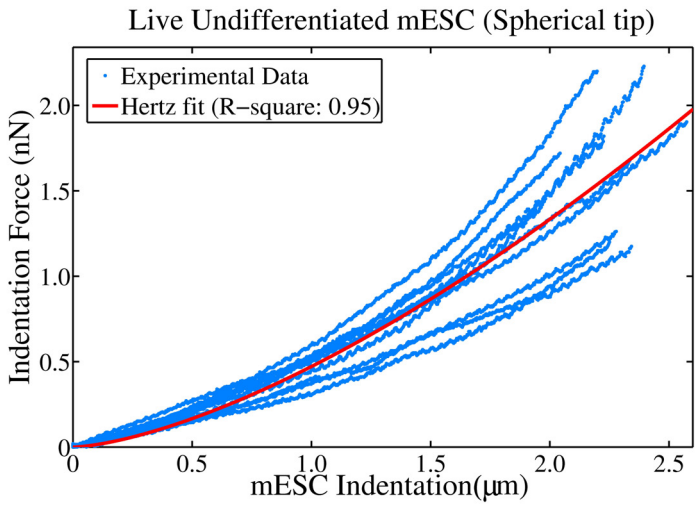

Figure 6.14. Force (F) versus cell indentation (δ) for 10 samples of live undifferentiated mESC. The R^2 value obtained with Hertz fit is 0.95.

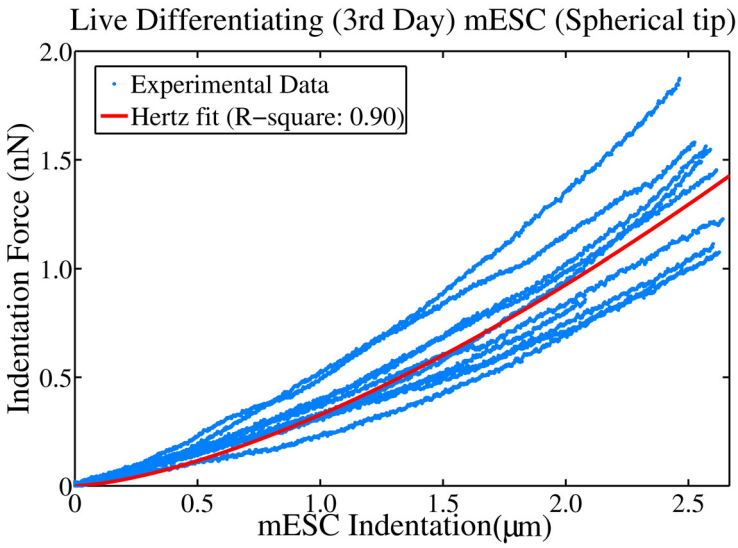

Figure 6.15. Force (F) versus cell indentation (δ) for 10 samples of live differentiating (3^{rd} day) mESC. The R^2 value obtained with Hertz fit is 0.90.

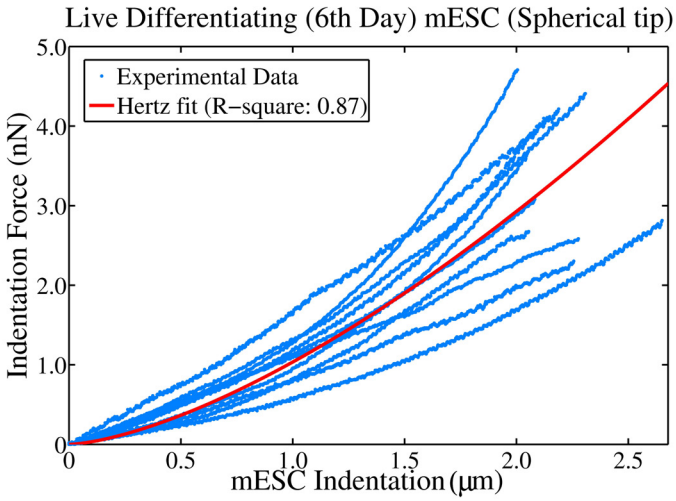

Figure 6.16. Force (F) versus cell indentation (δ) for 10 samples of live differentiating (6^{th} day) mESC. The R^2 value obtained with Hertz fit is 0.87.

Sample	1	2	3	4	5	6	7	8	9	10
Radius (μm)	3.7	3.65	3.9	4.1	3.2	3.4	4.4	3.7	4.7	3.7

Table 6.5: Radius of each live undifferentiated mESC sample.

Sample	1	2	3	4	5	6	7	8	9	10
Radius (μm)	5.67	5.42	5.42	5.37	5.02	5.52	6.02	6.02	5.65	5.9

Table 6.6: Radius of each differentiating (3^{rd} day) mESC sample.

Sample	1	2	3	4	5	6	7	8	9	10
Radius (μm)	4.49	4.84	5.49	4.75	5.4	7.52	8.72	8.47	6.97	4.47

Table 6.7: Radius of each differentiating (6^{th} day) mESC sample.

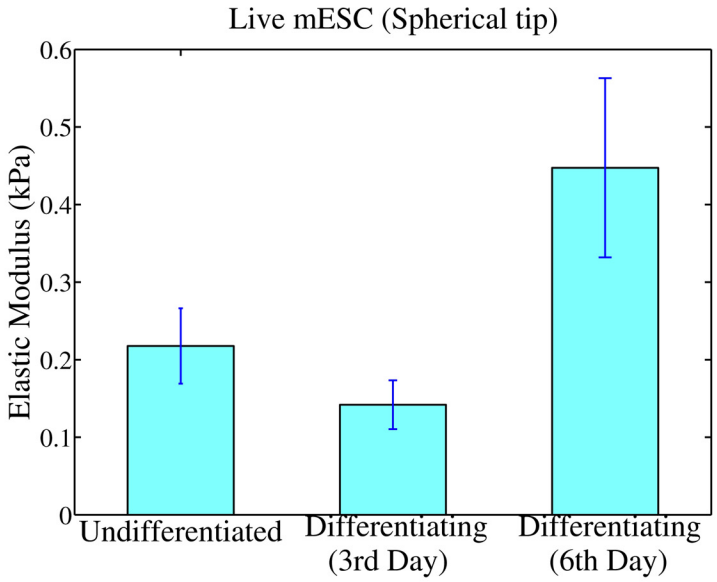

Figure 6.17. Elastic modulus of live undifferentiated, 3rd day differentiating, and 6th day differentiating mESC calculated from the Hertz contact model along with error bar.

Hertz model [138] was used to compute the elastic modulus of each live mESC sample from the force (F) versus indentation (δ) obtained from the experiments by assuming Poisson's ratio of 0.5. Table 6.5, 6.6, and 6.7 show the radius of each live undifferentiated, differentiating (3rd day) and differentiating (6th day) mESC sample respectively used to compute the elastic modulus. The average elastic modulus was found to be 0.2176 kPa, 0.1419 kPa, and 0.4473 kPa for live undifferentiated, 3rd day differentiating, and 6th day differentiating mESC respectively as shown in figure 6.17. The standard deviation was 0.048 kPa, 0.031 kPa, and 0.115 kPa for live undifferentiated, 3rd day differentiating and 6th day differentiating mESC respectively (see figure 6.17). We also performed the Kruskal-Wallis test on the elastic modulus values for live undifferentiated, 3rd day differentiating and 6th day differentiating

mESC. The p-value obtained was less than 0.0001, leading to a probability of greater than 99.99% that there was a significant difference between the data sets. The p-value obtained on the elastic modulus values for different states of mESC is shown in table 6.8. Thus there is a probability of greater than 99.98% that there is a significant statistical difference between: (a) live undifferentiated and 6th day differentiating mESC, and (b) live 3rd day differentiating and 6th day differentiating. From the results, we infer that live undifferentiated and 3rd day differentiating mESC are supple compared to live 6th day differentiating mESC. Unlike the results obtained with the pyramidal tip, the live undifferentiated mESC is not supple compared to the 3rd day differentiating mESC. This might be due to a different live mESC culture used for indentation studies with spherical tip.

Statistics	Live undiff, 3rd day diff and 6th day diff mESC	Live undiff and 3rd day diff mESC	Live undiff and 6th day mESC	Live 3rd day diff and 6th day diff
p-value (Kruskal-Wallis test)	0.00000944	0.0019	0.0003	0.0002

Table 6.8: Statistical analysis on the elastic modulus values for live undifferentiated (undiff), 3rd day differentiating (3rd day diff), and 6th day differentiating (6th day diff) mESC. A significant statistical difference exists for all data sets ($p < \alpha = 0.05$)

6.3.2 Fixed Cells (Spherical tip)

Figures 6.18, 6.19 and 6.20 show the force (F) versus cell indentation (δ) for fixed undifferentiated mESC, 3rd day differentiating mESC and 6th day differentiating mESC respectively.

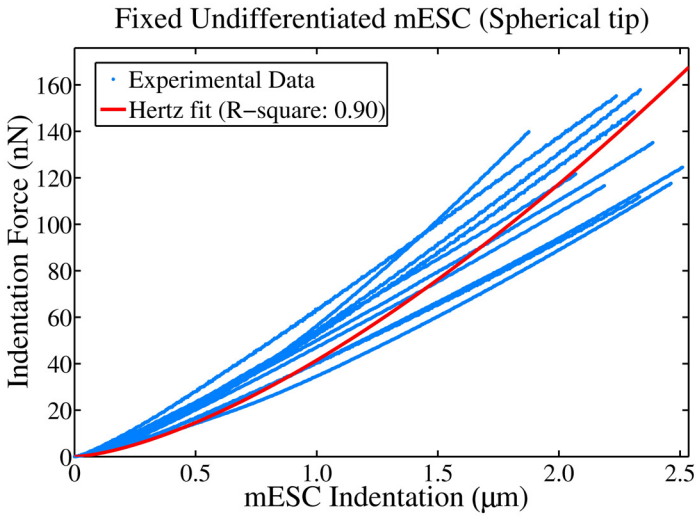

Figure 6.18. Force (F) versus cell indentation (δ) for 10 samples of fixed undifferentiated mESC. The R^2 value obtained with Hertz fit is 0.90.

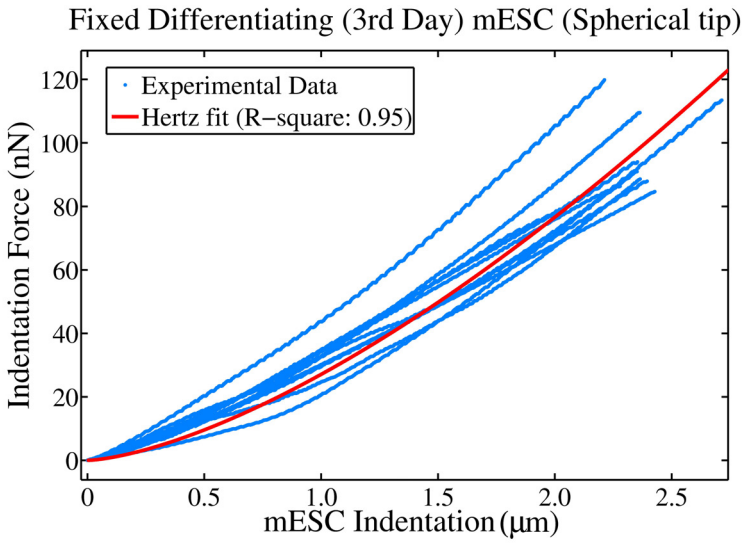

Figure 6.19. Force (F) versus cell indentation (δ) for 10 samples of fixed differentiating (3rd day) mESC. The R^2 value obtained with Hertz fit is 0.95.

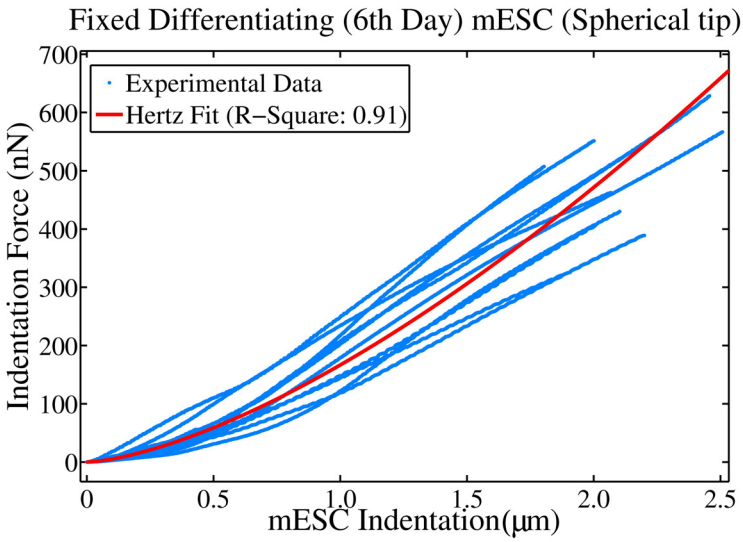

Figure 6.20. Force (F) versus cell indentation (δ) for 10 samples of fixed differentiating (6th day) mESC. The R^2 value obtained with Hertz fit is 0.91.

From the figures, we observe that the fixed undifferentiated mESC and 3rd day differentiating mESC are supple compared to the 6th day differentiating mESC. Based on the experimental data and the analysis performed in section 5.8, we performed a Hertz fit on the dataset and the corresponding Hertz fit is shown in the figure. The R^2 value was found to be 0.90, 0.95, and 0.91 for fixed undifferentiated, 3rd day differentiating and 6th day differentiating mESC respectively.

Hertz model was used to compute the elastic modulus of each fixed mESC sample from the force (F) versus indentation (δ) obtained from the experiments by assuming Poisson's ratio of 0.5. Table 6.9, 6.10, and 6.11 shows the radius of each fixed undifferentiated, differentiating (3rd day) and differentiating (6th day) mESC sample respectively used to compute the elastic modulus.

Sample	1	2	3	4	5	6	7	8	9	10
Radius (μm)	5.7	7.2	6.7	6.1	6.05	7.6	6.77	6.27	5.22	5.62

Table 6.9: Radius of each fixed undifferentiated mESC sample.

Sample	1	2	3	4	5	6	7	8	9	10
Radius (μm)	3.9	6.15	5.4	3.9	3.35	5.82	6.32	3.95	6.85	6.50

Table 6.10: Radius of each fixed differentiating (3^{rd} day) mESC sample.

Sample	1	2	3	4	5	6	7	8	9	10
Radius (μm)	5.63	7.33	4.05	4.69	5.56	3.8	4.05	4.3	5.55	4.85

Table 6.11: Radius of each fixed differentiating (6^{th} day) mESC sample.

The average elastic modulus was found to be 17.869 kPa, 12.271 kPa, and 73.519 kPa for fixed undifferentiated, 3^{rd} day differentiating, and 6^{th} day differentiating mESC respectively as shown in figure 6.21. The standard deviation was 3.37 kPa, 1.75 kPa, and 13.55 kPa for fixed undifferentiated, 3^{rd} day differentiating and 6^{th} day differentiating mESC respectively (see figure 6.21). We also performed the Kruskal-Wallis test on the elastic modulus values for fixed undifferentiated, 3^{rd} day differentiating and 6^{th} day differentiating mESC. The p-value obtained was less than 0.0001, leading to a probability of greater than 99.99% that there was a significant difference between the data sets. The p-value obtained on the elastic modulus values for different states of mESC is shown in table 6.12.

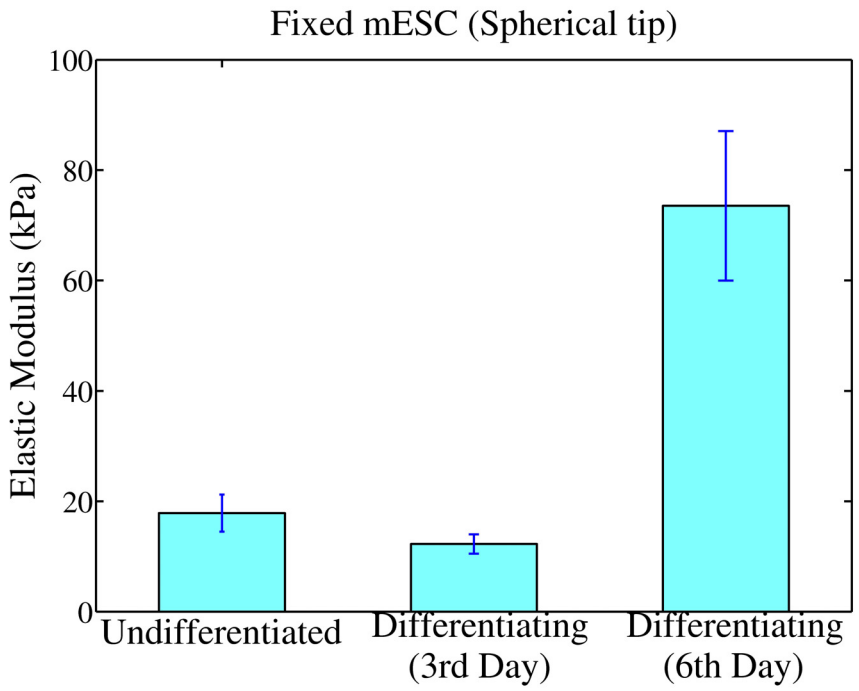

Figure 6.21. Elastic modulus of fixed undifferentiated, 3rd day differentiating, and 6th day differentiating mESC calculated from the Hertz contact model along with error bar.

Statistics	Fixed undiff, 3rd day diff and 6th day diff mESC	Fixed undiff and 3rd day diff mESC	Fixed undiff and 6th day mESC	Fixed 3rd day diff and 6th day diff
p-value (Kruskal-Wallis test)	0.00000362	0.0005	0.0002	0.0002

Table 6.12: Statistical analysis on the elastic modulus values for fixed undifferentiated (undiff), 3rd day differentiating (3rd day diff), and 6th day differentiating (6th day diff) mESC. A significant statistical difference exists for all data sets ($p < \alpha = 0.05$)

Thus there is a probability of greater than 99.95% that there is a significant statistical difference between: (a) fixed undifferentiated and 6^{th} day differentiating mESC, and (b) fixed 3^{rd} day differentiating and 6^{th} day differentiating. From the results, we infer that fixed undifferentiated and 3^{rd} day differentiating mESC are supple compared to fixed 6^{th} day differentiating mESC. Unlike the results obtained with the pyramidal tip, the fixed undifferentiated mESC is not supple compared to the 3^{rd} day differentiating mESC. This might be due to a different fixed mESC culture used for indentation studies with spherical tip.

We have conducted indentation studies on mESC (interphase stage of the cell cycle process) with a spherical tip on undifferentiated, 3^{rd} day differentiating and 6^{th} day differentiating mESC in both live and fixed states. Experiments were conducted on 60 samples of mESC with a cell indentation range of 2 – 2.5 μm. Based on the analysis performed in section 5.8, we chose Hertz contact model to compute the elastic modulus of mESC indented by a spherical tip. We observed that the elastic modulus of 6^{th} day differentiating mESC is higher than 3^{rd} day differentiating mESC as well as undifferentiated mESC in both live and fixed cells. Thus the results obtained using live cells parallel that of fixed cells. We also observed that the mean elastic modulus obtained with a spherical tip is less than the mean elastic modulus obtained with a pyramidal tip for undifferentiated, 3^{rd} day differentiating and 6^{th} day differentiating mESC in both live and fixed cells. The decrease in mean value could be due to the high stress concentration in the cell induced by sharper tip [182]. The larger area of spherical tip – cell contact results in averaging local variation in modulus compared

to that measured with a pyramidal tip. Thus we hypothesize that the elastic modulus obtained with a spherical tip truly predicts the mechanical property of mESC. Kruskal-Wallis test was performed on the elastic modulus values for undifferentiated, 3rd day differentiating and 6th day differentiating mESC in both live and fixed cells. We found that the p-value is less than the level of significance ($\alpha = 0.05$). Thus we confirmed our research hypothesis that the mechanical property of undifferentiated mESC differs from early differentiating mESC in both live and fixed state.

We performed experiments with spherical tip on one independent culture of mESC. However, we need to confirm that the variation in mechanical properties of mESC between undifferentiated and differentiating state is not an artifact and does occur for any independent culture of mESC. Thus, we repeated the indentation studies with a spherical tip on second independent culture of undifferentiated, 3rd day differentiating and 6th day differentiating mESC.

6.3.3 Live Cells (Second Independent Culture): Spherical Tip

Figures 6.22, 6.23 and 6.24 shows the force (F) versus cell indentation (δ) for second independent culture of live undifferentiated mESC, 3rd day differentiating mESC and 6th day differentiating mESC respectively. From the figures, we observe that the live undifferentiated mESC and 3rd day differentiating mESC are supple compared to the 6th day differentiating mESC. We performed a Hertz fit on the dataset and the corresponding Hertz fit is shown in the figure. The R^2 value was found to be 0.93, 0.89, and 0.92 for live undifferentiated, 3rd day differentiating and 6th day differentiating mESC respectively.

SECOND INDEPENDENT CULTURE OF mESC

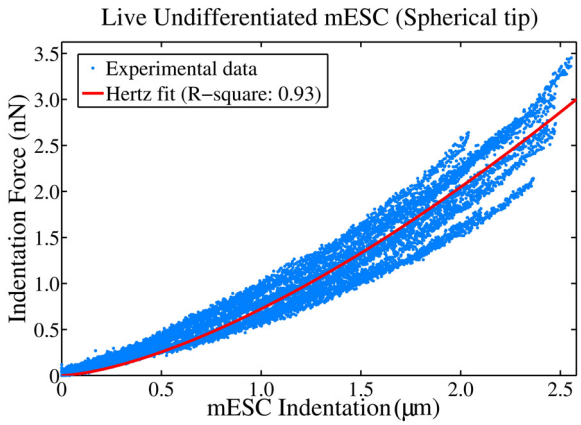

Figure 6.22. Force (F) versus cell indentation (δ) for 10 samples of live undifferentiated mESC (second independent culture). The R^2 value obtained with Hertz fit is 0.93.

SECOND INDEPENDENT CULTURE OF mESC

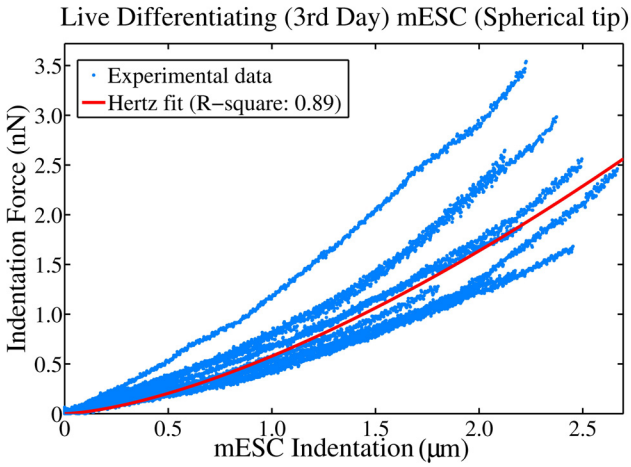

Figure 6.23. Force (F) versus cell indentation (δ) for 10 samples of live 3rd day differentiating mESC (second independent culture). The R^2 value obtained with Hertz fit is 0.89.

SECOND INDEPENDENT CULTURE OF mESC

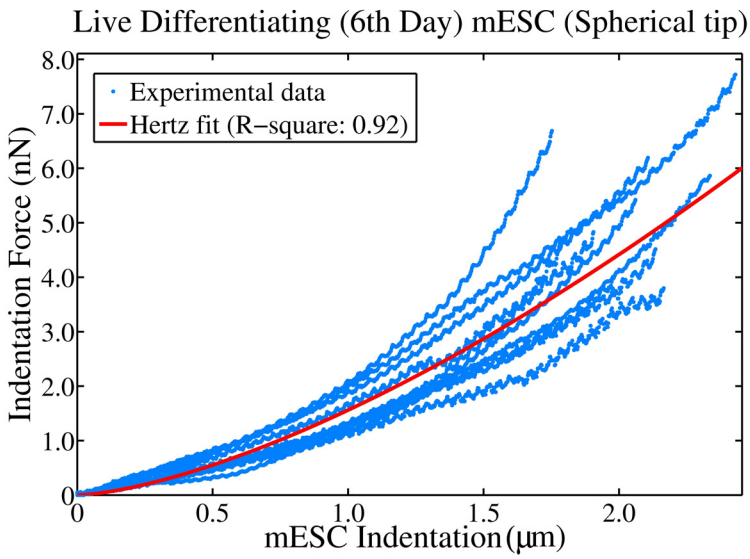

Figure 6.24. Force (F) versus cell indentation (δ) for 10 samples of live 6th day differentiating mESC (second independent culture). The R^2 value obtained with Hertz fit is 0.92.

Hertz model was used to compute the elastic modulus of each live mESC sample (second independent culture) from the force (F) versus indentation (δ) by assuming Poisson's ratio of 0.5. Table 6.13, 6.14, and 6.15 show the radius of each live undifferentiated, differentiating (3rd day) and differentiating (6th day) mESC sample respectively used to compute the elastic modulus.

Sample	1	2	3	4	5	6	7	8	9	10
Radius (μm)	4.85	3.85	4.6	3.6	4.6	4.35	4.85	6	6.25	6.75

Table 6.13: Radius of each live undifferentiated mESC sample (second independent culture)

Sample	1	2	3	4	5	6	7	8	9	10
Radius (μm)	3.9	4.15	6.45	6.45	6.45	6.5	4.72	4.17	5.62	4.65

Table 6.14: Radius of each live 3rd day differentiating mESC sample (second independent culture)

Sample	1	2	3	4	5	6	7	8	9	10
Radius (μm)	4.25	6.25	5.25	4	5.95	4.1	3.85	6.3	3.55	4.7

Table 6.15: Radius of each live 6th day differentiating mESC sample (second independent culture)

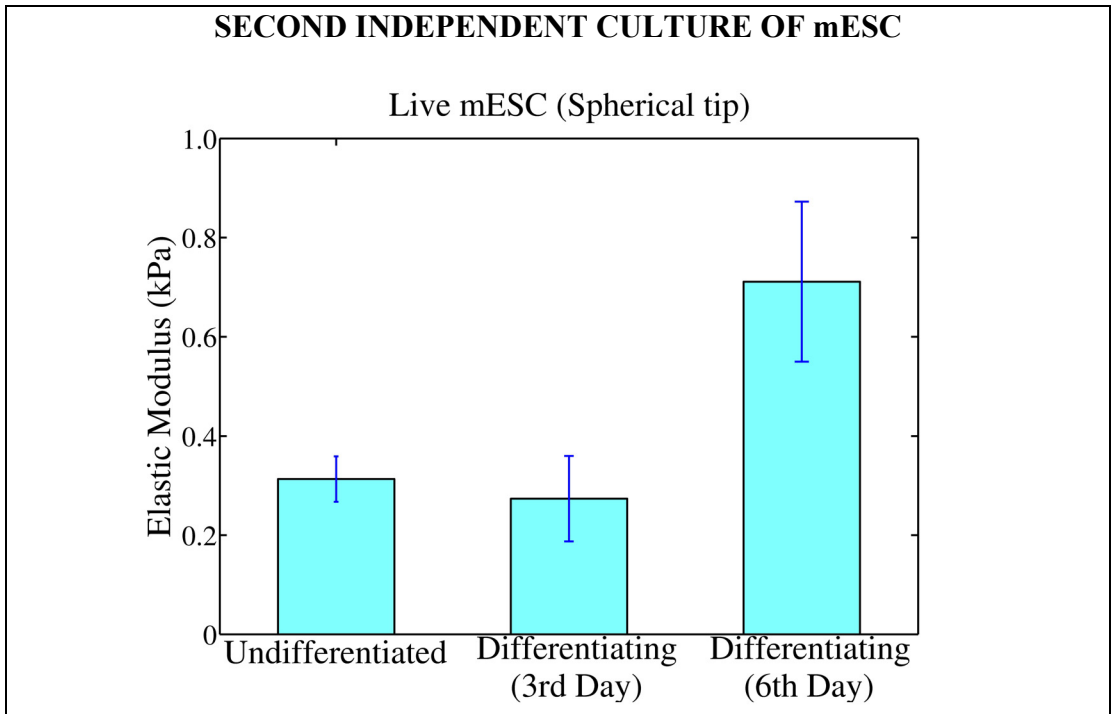

Figure 6.25: Elastic modulus of live undifferentiated, 3rd day differentiating, and 6th day differentiating mESC (second independent culture) calculated from the Hertz contact model along with error bar.

The average elastic modulus was found to be 0.3133 kPa, 0.2736 kPa, and 0.7111 kPa for second independent culture of live undifferentiated, 3rd day differentiating, and 6th day differentiating mESC respectively as shown in figure 6.25. The standard deviation was 0.046 kPa, 0.086 kPa, and 0.161 kPa for live undifferentiated, 3rd day differentiating and 6th day differentiating mESC respectively (see figure 6.25). We also performed the Kruskal-Wallis test on the elastic modulus values for the second independent culture of live undifferentiated, 3rd day differentiating and 6th day differentiating mESC. The p-value obtained was less than 0.0001, leading to a probability of greater than 99.99% that there was a significant difference between the data sets. The p-value obtained on the elastic modulus values for different states of mESC is shown in table 6.16.

Statistics	Live undiff, 3rd day diff and 6th day diff mESC	Live undiff and 3rd day diff mESC	Live undiff and 6th day mESC	Live 3rd day diff and 6th day diff
p-value (Kruskal-Wallis test)	0.000033	**0.15**	0.0002	0.0002

Table 6.16: Statistical analysis on the elastic modulus values for second independent culture of live undifferentiated (undiff), 3rd day differentiating (3rd day diff), and 6th day differentiating (6th day diff) mESC. A significant statistical difference exists for all data sets ($p < \alpha = 0.05$) except live undifferentiated and 3rd day differentiating mESC

Thus there is a probability of greater than 99.98% that there is a significant statistical difference between the second independent cultures of: (a) live undifferentiated and 6th day differentiating mESC, and (b) live 3rd day differentiating and 6th day

differentiating. From the results, we infer that the second independent culture of live undifferentiated and 3rd day differentiating mESC are supple compared to live 6th day differentiating mESC. Unlike the results obtained with the pyramidal tip, the live undifferentiated mESC is not supple compared to the 3rd day differentiating mESC. Thus the results obtained with second independent culture of live mESC parallel that of the results obtained with first independent culture of live mESC (section 6.4.1).

6.3.4 Fixed mESC (Second Independent Culture): Spherical Tip

Figures 6.26, 6.27 and 6.28 shows the force (F) versus cell indentation (δ) for second independent culture of fixed undifferentiated mESC, 3rd day differentiating mESC and 6th day differentiating mESC respectively.

SECOND INDEPENDENT CULTURE OF mESC

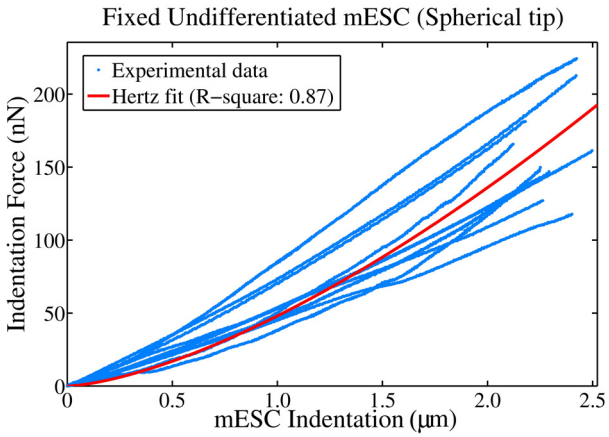

Figure 6.26: Force (F) versus cell indentation (δ) for 10 samples of fixed undifferentiated mESC (second independent culture). The R^2 value obtained with Hertz fit is 0.87.

SECOND INDEPENDENT CULTURE OF mESC

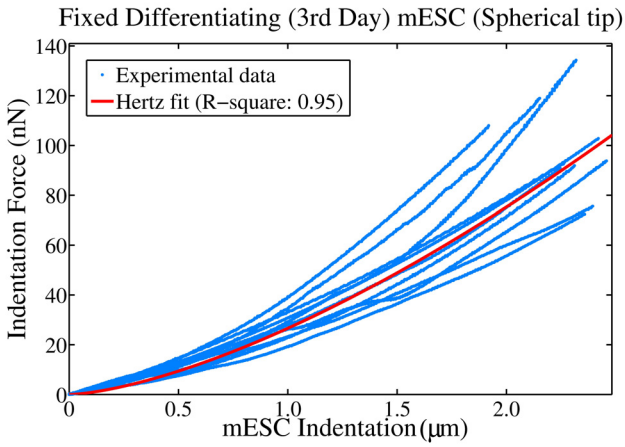

Figure 6.27: Force (F) versus cell indentation (δ) for 10 samples of fixed differentiating (3rd day) mESC (second independent culture). The R^2 value obtained with Hertz fit is 0.95.

SECOND INDEPENDENT CULTURE OF mESC

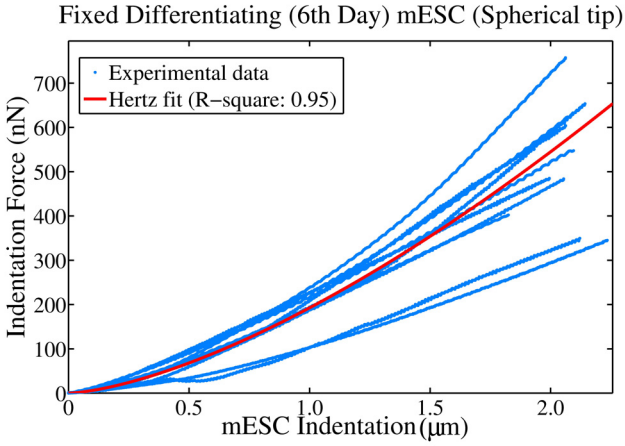

Figure 6.28: Force (F) versus cell indentation (δ) for 10 samples of fixed differentiating (6th day) mESC (second independent culture). The R^2 value obtained with Hertz fit is 0.95.

From the figures, we observe that the fixed undifferentiated mESC and 3rd day differentiating mESC are supple compared to the 6th day differentiating mESC. We performed a Hertz fit on the dataset and the corresponding Hertz fit is shown in the figure. The R^2 value was found to be 0.87, 0.95, and 0.95 for live undifferentiated, 3rd day differentiating and 6th day differentiating mESC respectively.

Sample	1	2	3	4	5	6	7	8	9	10
Radius (μm)	6.39	4.45	6.32	7.75	8	6.25	5.75	7.15	7.65	6.9

Table 6.17: Radius of each fixed undifferentiated mESC sample (second independent culture)

Sample	1	2	3	4	5	6	7	8	9	10
Radius (μm)	3.97	5.07	6.82	5.47	4.32	6.07	5.92	5.72	3.72	4.47

Table 6.18: Radius of each fixed 3rd day differentiating mESC sample (second independent culture)

Sample	1	2	3	4	5	6	7	8	9	10
Radius (μm)	4.6	4.0	3.5	3.6	5.4	5.5	4.8	3.25	3.7	6.0

Table 6.19: Radius of each fixed 6th day differentiating mESC sample (second independent culture)

Hertz model was used to compute the elastic modulus of each fixed mESC sample (second independent culture) from the force (F) versus indentation (δ) by assuming Poisson's ratio of 0.5. Table 6.17, 6.18, and 6.19 show the radius of each fixed

undifferentiated, differentiating (3rd day) and differentiating (6th day) mESC sample (second independent culture) respectively used to compute the elastic modulus. The average elastic modulus was found to be 20.509 kPa, 12.311 kPa, and 82.595 kPa for the second independent culture of fixed undifferentiated, 3rd day differentiating, and 6th day differentiating mESC respectively as shown in figure 6.29. The standard deviation was 4.75 kPa, 2.80 kPa, and 21.55 kPa for fixed undifferentiated, 3rd day differentiating and 6th day differentiating mESC respectively (see figure 6.29).

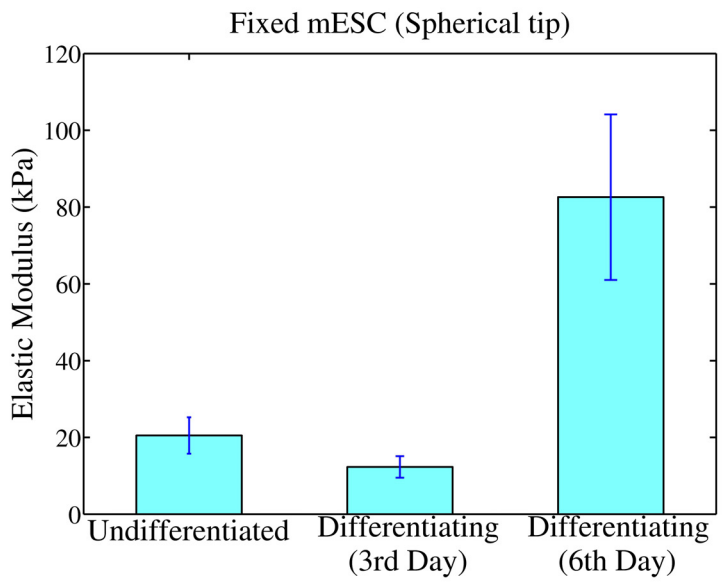

Figure 6.29: Elastic modulus of fixed undifferentiated, 3rd day differentiating, and 6th day differentiating mESC (second independent culture) calculated from the Hertz contact model along with error bar.

We also performed the Kruskal-Wallis test on the elastic modulus values for fixed undifferentiated, 3rd day differentiating and 6th day differentiating mESC. The p-value obtained was less than 0.0001, leading to a probability of greater than 99.99% that

there was a significant difference between the data sets. The p-value obtained on the elastic modulus values for different states of mESC is shown in table 6.20. Thus there is a probability of greater than 99.98% that there is a significant statistical difference between the second independent cultures of: (a) fixed undifferentiated and 6th day differentiating mESC, and (b) fixed 3rd day differentiating and 6th day differentiating. From the results, we infer that the second independent cultures of fixed undifferentiated and 3rd day differentiating mESC are supple compared to fixed 6th day differentiating mESC. Unlike the results obtained with the pyramidal tip, the fixed undifferentiated mESC is not supple compared to the 3rd day differentiating mESC. Thus the results obtained with second independent culture of fixed mESC parallel that of the results obtained with first independent culture of fixed mESC (section 6.4.2).

Statistics	Fixed undiff, 3rd day diff and 6th day diff mESC	Fixed undiff and 3rd day diff mESC	Fixed undiff and 6th day mESC	Fixed 3rd day diff and 6th day diff
p-value (Kruskal-Wallis test)	0.00000362	0.0004	0.0002	0.0002

Table 6.20: Statistical analysis on the elastic modulus values for fixed undifferentiated (undiff), 3rd day differentiating (3rd day diff), and 6th day differentiating (6th day diff) mESC (second independent culture). A significant statistical difference exists for all data sets ($p < \alpha = 0.05$)

Thus, the experimental results obtained with second independent culture of mESC confirm our research hypothesis that there is a significant statistical difference

between the mechanical property of undifferentiated and early differentiating (6^{th} day) mESC in both live and fixed cells.

6.4 Mechanical Characterization Studies on D3 mESC line (Differentiation Method: LIF Removal)

In the previous sections (6.2 - 6.4) of this chapter we performed experiments on R1 mESC cell line and the mESC was allowed to differentiate by the removal of leukemia inhibitory factor (LIF) from undifferentiated mESC culture. However, the results obtained in sections 6.2 – 6.4 could be a characteristic oddity of R1 mESC cell line. Thus, it is crucial to validate our findings with another cell line. Hence we conducted further indentation studies on two independent cultures of D3 mESC line and the method of differentiation was LIF removal. We observed in sections 6.2 – 6.4 that the results obtained with live cells parallel that with fixed cells. Therefore we conducted studies only on fixed D3 mESC line with a spherical tip to confirm our research hypothesis.

6.4.1 First Independent Culture (Fixed D3 mESC cell line)

Figures 6.30, 6.31 and 6.32 shows the force (F) versus cell indentation (δ) for the first independent culture of fixed undifferentiated, 3^{rd} day differentiating and 6^{th} day differentiating D3 mESC line respectively.

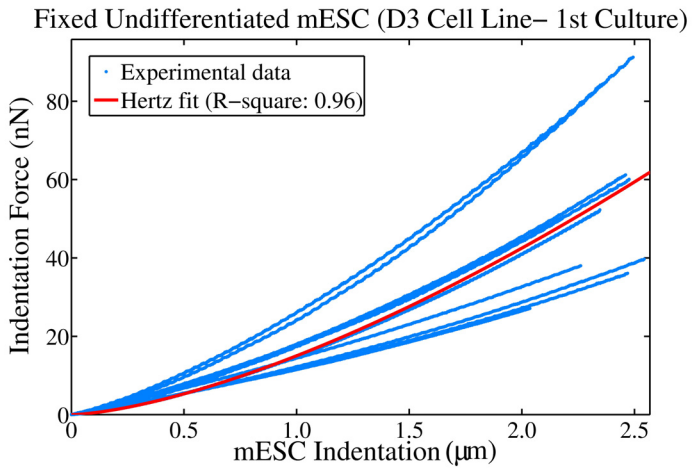

Figure 6.30: Force (F) versus cell indentation (δ) for 10 samples of fixed undifferentiated mESC (D3 cell line – first independent culture). The R^2 value obtained with Hertz fit is 0.96.

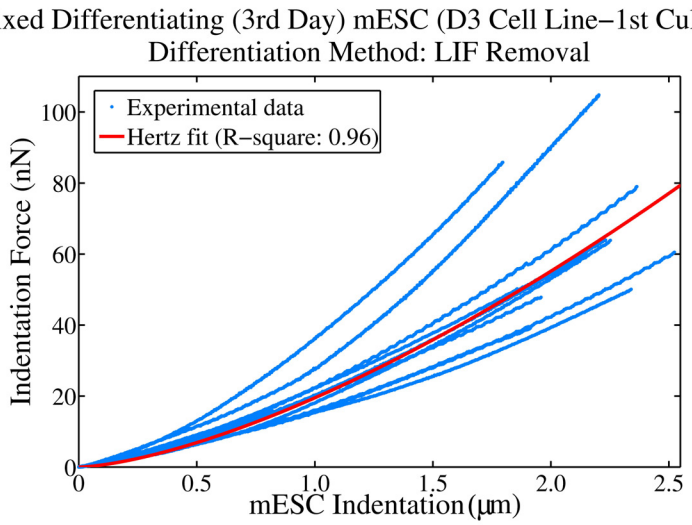

Figure 6.31: Force (F) versus cell indentation (δ) for 10 samples of fixed 3rd day differentiating mESC (D3 cell line – first independent culture). The R^2 value obtained with Hertz fit is 0.96.

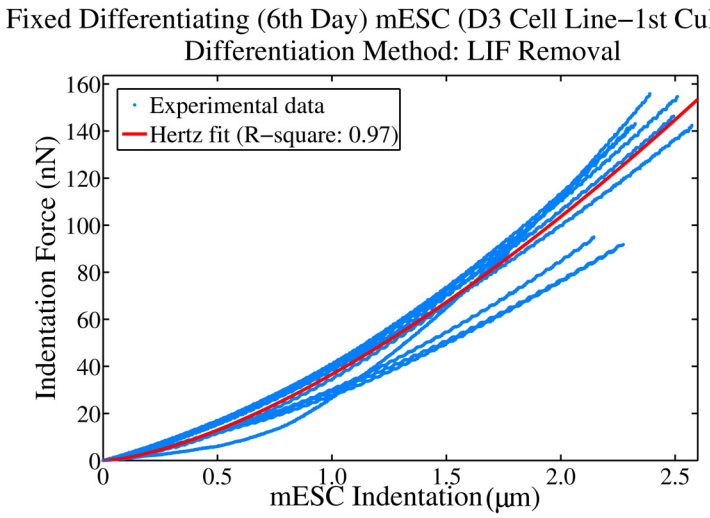

Figure 6.32: Force (F) versus cell indentation (δ) for 10 samples of fixed 6th day differentiating mESC (D3 cell line – first independent culture). The R^2 value obtained with Hertz fit is 0.97.

From the figures, we observe that the first independent cultures of fixed undifferentiated mESC and 3rd day differentiating mESC are supple compared to the 6th day differentiating mESC (D3 cell line). We performed a Hertz fit on the dataset and the corresponding Hertz fit is shown in the figure. The R^2 value was found to be 0.96, 0.96, and 0.97 for fixed undifferentiated, 3rd day differentiating and 6th day differentiating mESC respectively.

Sample	1	2	3	4	5	6	7	8	9	10
Radius (μm)	6.93	6.93	6.95	6.20	6.35	7.87	5.87	7.02	5.02	5.62

Table 6.21: Radius of each sample of fixed undifferentiated mESC (D3 mESC line: first independent culture).

Sample	1	2	3	4	5	6	7	8	9	10
Radius (μm)	5.15	5.75	5.65	5.35	5.07	5.15	5.12	5.60	5.15	6.55

Table 6.22: Radius of each sample of fixed 3rd day differentiating mESC (D3 mESC line: first independent culture).

Sample	1	2	3	4	5	6	7	8	9	10
Radius (μm)	4.0	4.22	4.22	5.26	5.5	5.0	5.0	6.25	5.32	5.52

Table 6.23: Radius of each sample of fixed 6th day differentiating mESC (D3 mESC line: first independent culture).

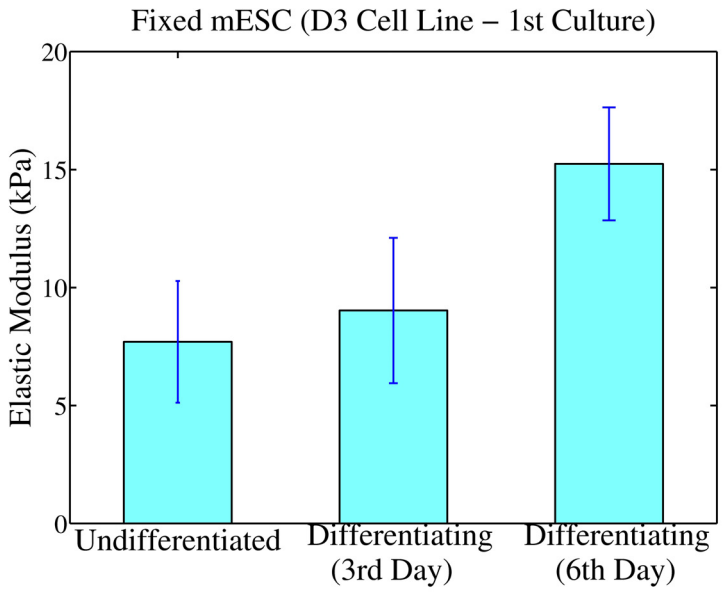

Figure 6.33: Elastic modulus of fixed undifferentiated, 3rd day differentiating, and 6th day differentiating mESC (D3 cell line: first independent culture) calculated from the Hertz contact model along with error bar.

Hertz model was used to compute the elastic modulus of each fixed mESC sample (D3 cell line: first independent culture) from the force (F) versus indentation (δ) by assuming Poisson's ratio of 0.5. Table 6.21, 6.22, and 6.23 shows the radius of each fixed undifferentiated, differentiating (3^{rd} day) and differentiating (6^{th} day) mESC sample (D3 cell line: first independent culture) respectively used to compute the elastic modulus. The average elastic modulus was found to be 7.7003 kPa, 9.0263 kPa, and 15.243 kPa for the fixed undifferentiated, 3^{rd} day differentiating, and 6^{th} day differentiating mESC respectively as shown in figure 6.33. The standard deviation was 2.57 kPa, 3.08 kPa, and 2.393 kPa for fixed undifferentiated, 3^{rd} day differentiating and 6^{th} day differentiating mESC respectively (see figure 6.33).

We also performed the Kruskal-Wallis test on the elastic modulus values for fixed undifferentiated, 3^{rd} day differentiating and 6^{th} day differentiating D3 mESC line. The p-value obtained was 0.0003, leading to a probability of greater than 99.97% that there was a significant difference between the data sets. The p-value obtained on the elastic modulus values for different states of mESC is shown in table 6.24. Thus there is a probability of greater than 99.88% that there is a significant statistical difference between the first independent cultures (D3 cell line) of: (a) fixed undifferentiated and 6^{th} day differentiating mESC, and (b) fixed 3^{rd} day differentiating and 6^{th} day differentiating. From the results, we infer that the first independent cultures of fixed undifferentiated and 3^{rd} day differentiating D3 mESC line are supple compared to fixed 6^{th} day differentiating D3 mESC line which parallel with R1 cell line (sections 6.3 and 6.4).

Statistics	Fixed undiff, 3rd day diff and 6th day diff mESC	Fixed undiff and 3rd day diff mESC	Fixed undiff and 6th day mESC	Fixed 3rd day diff and 6th day diff
p-value (Kruskal-Wallis test)	0.0003	**0.5191**	0.0004	0.0012

Table 6.24: Statistical analysis on the elastic modulus values for fixed undifferentiated (undiff), 3rd day differentiating (3rd day diff), and 6th day differentiating (6th day diff) D3 mESC line (first independent culture). A significant statistical difference exists for all data sets ($p < \alpha = 0.05$) except for fixed undifferentiated and 3rd day differentiating mESC

6.4.2. Second Independent Culture (Fixed D3 mESC line)

Figure 6.34, 6.35, and 6.36 shows the force (F) versus cell indentation (δ) for the second independent culture of fixed undifferentiated, 3rd day differentiating and 6th day differentiating D3 mESC line respectively. Similar to the first independent culture of D3 mESC cell line, we observe that second independent cultures of the fixed undifferentiated D3 mESC line and 3rd day differentiating D3 mESC line are supple compared to the 6th day differentiating D3 mESC line. We performed a Hertz fit on the dataset and the corresponding Hertz fit is shown in the figure. The R^2 value was found to be 0.87, 0.95, and 0.93 for fixed undifferentiated, 3rd day differentiating and 6th day differentiating D3 mESC line respectively.

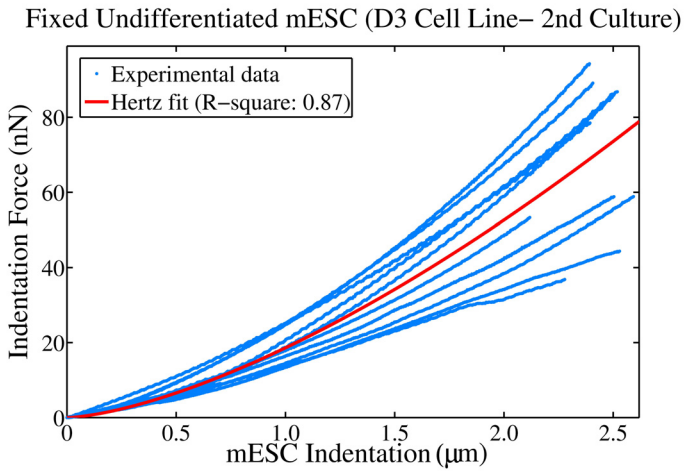

Figure 6.34: Force (F) versus cell indentation (δ) for 10 samples of fixed undifferentiated mESC (D3 cell line – second independent culture). The R^2 value obtained with Hertz fit is 0.87.

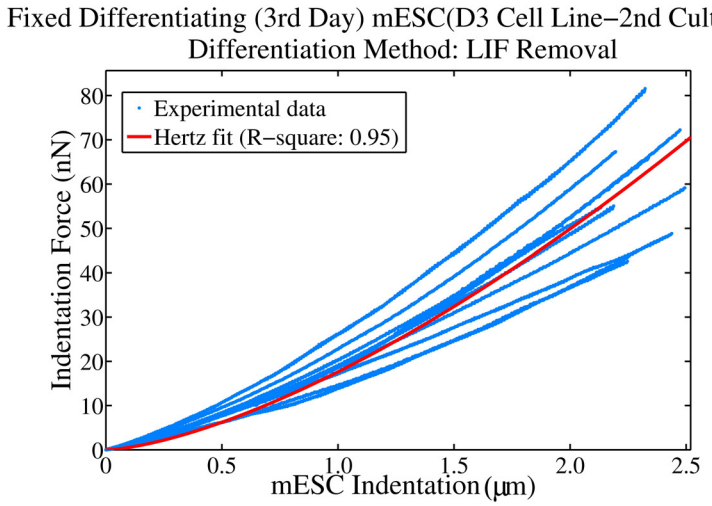

Figure 6.35: Force (F) versus cell indentation (δ) for 10 samples of fixed 3rd day differentiating mESC (D3 cell line – second independent culture). The R^2 value obtained with Hertz fit is 0.95.

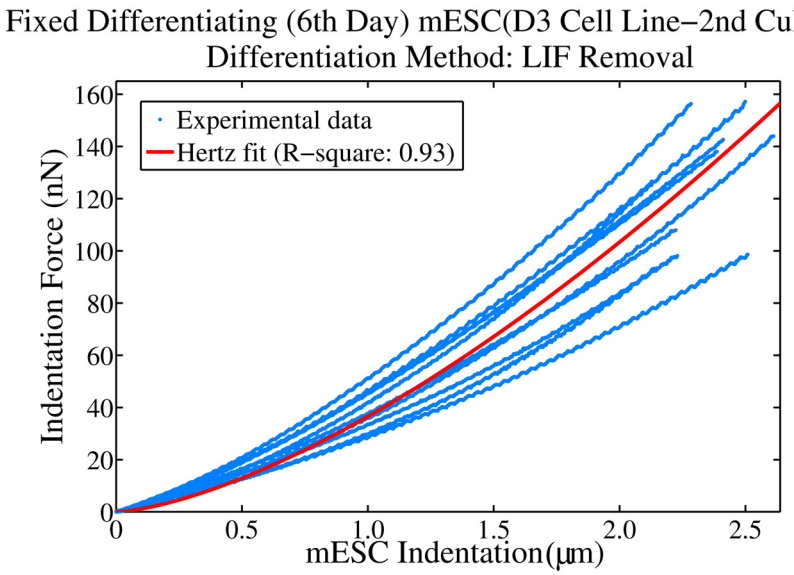

Figure 6.36: Force (F) versus cell indentation (δ) for 10 samples of fixed 6th day differentiating mESC (D3 cell line – second independent culture). The R^2 value obtained with Hertz fit is 0.93.

Sample	1	2	3	4	5	6	7	8	9	10
Radius (μm)	6.47	6.54	4.45	4.65	4.6	4.3	3.6	4.1	5.6	6.2

Table 6.25: Radius of each sample of fixed undifferentiated D3 mESC line (second independent culture).

Sample	1	2	3	4	5	6	7	8	9	10
Radius (μm)	4.7	4.45	3.25	3.5	3.2	6.7	4.9	4.5	4.25	4.15

Table 6.26: Radius of each sample of fixed 3rd day differentiating D3 mESC line (second independent culture).

Sample	1	2	3	4	5	6	7	8	9	10
Radius (μm)	5.0	4.9	4.2	4.6	6.2	4.15	5.9	3.62	4.25	3.5

Table 6.27: Radius of each sample of fixed 6th day differentiating D3 mESC line (second independent culture).

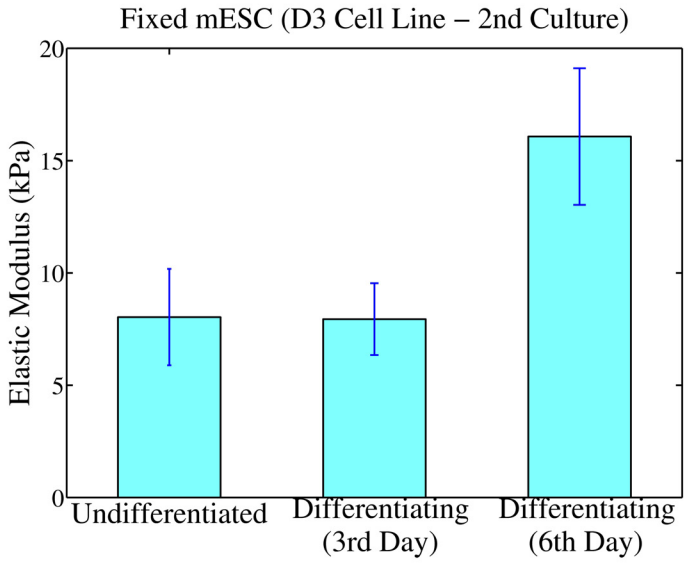

Figure 6.37: Elastic modulus of fixed undifferentiated, 3rd day differentiating, and 6th day differentiating D3 mESC line (second independent culture) calculated from the Hertz contact model along with error bar.

Hertz model was used to compute the elastic modulus of each fixed mESC sample (D3 cell line: second independent culture) from the force (F) versus indentation (δ) by assuming Poisson's ratio of 0.5. Table 6.25, 6.26, and 6.27 shows the radius of each fixed undifferentiated, 3rd day differentiating and 6th day differentiating mESC sample (D3 cell line: second independent culture) respectively used to compute their elastic

modulus. The average elastic modulus was found to be 8.032 kPa, 7.9433 kPa, and 16.073 kPa for the fixed undifferentiated, 3rd day differentiating, and 6th day differentiating D3 mESC line (second independent culture) respectively as shown in figure 6.37. The standard deviation was 2.14 kPa, 1.59 kPa, and 3.04 kPa for fixed undifferentiated, 3rd day differentiating and 6th day differentiating D3 mESC line respectively (see figure 6.37).

Statistics	Fixed undiff, 3rd day diff and 6th day diff mESC	Fixed undiff and 3rd day diff mESC	Fixed undiff and 6th day mESC	Fixed 3rd day diff and 6th day diff
p-value (Kruskal-Wallis test)	0.000091	**0.9397**	0.0002	0.0002

Table 6.28: Statistical analysis on the elastic modulus values for fixed undifferentiated (undiff), 3rd day differentiating (3rd day diff), and 6th day differentiating (6th day diff) D3 mESC line (second independent culture). A significant statistical difference exists for all data sets ($p < \alpha = 0.05$) except for fixed undifferentiated and 3rd day differentiating mESC.

We also performed the Kruskal-Wallis test on the elastic modulus values for fixed undifferentiated, 3rd day differentiating and 6th day differentiating mESC. The p-value obtained was less than 0.0001, leading to a probability of greater than 99.99% that there was a significant difference between the data sets. The p-value obtained on the elastic modulus values for different states of mESC is shown in table 6.28. Thus there is a probability of greater than 99.98% that there is a significant statistical difference between the second independent cultures (D3 cell line) of: (a) fixed undifferentiated

and 6th day differentiating mESC, and (b) fixed 3rd day differentiating and 6th day differentiating. However, there is no significant statistical difference between the elastic modulus of undifferentiated and 3rd day differentiating mESC cell line (p-value = 0.9397) in the second independent cultures. From the results, we infer that the second independent cultures of fixed undifferentiated and 3rd day differentiating D3 mESC line are supple compared to fixed 6th day differentiating D3 mESC line. The results parallel with first independent culture of D3 mESC cell line (section 6.5.1). Hence, we confirm our research hypothesis that the mechanical property of undifferentiated mESC differs significantly from differentiating mESC (6th day) irrespective of the cultures and mESC lines: R1 and D3.

6.5 Mechanical Characterization Studies on R1 mESC line (Differentiation Method: Ascorbic Acid)

LIF removal from undifferentiated mESC culture is one of the differentiation methods. One of the other ways to differentiate mESC is: ascorbic acid treatment towards cardiac cells [175]. We were also interested in validating our research hypothesis on mESC which have undergone differentiation via ascorbic acid treatment. Thus we performed experiments on undifferentiated, 3rd day differentiating and 6th day differentiating R1 mESC line via ascorbic acid treatment. The results obtained with live mESC paralleled with the results obtained with fixed mESC using R1 cell line and LIF removal differentiation method. Hence, we decided to conduct experiments only on fixed mESC, as it is easy to maintain them compared to live

mESC. In addition, we performed experiments on two independent cultures of R1 mESC line treated by ascorbic acid to confirm our research hypothesis.

6.5.1. First Independent Culture (Fixed R1 mESC Line, Differentiation method: Ascorbic Acid)

Figures 6.38, 6.39 and 6.40 shows the force (F) versus cell indentation (δ) for the first independent culture of fixed undifferentiated, 3rd day differentiating and 6th day differentiating R1 mESC line respectively via the ascorbic acid treatment.

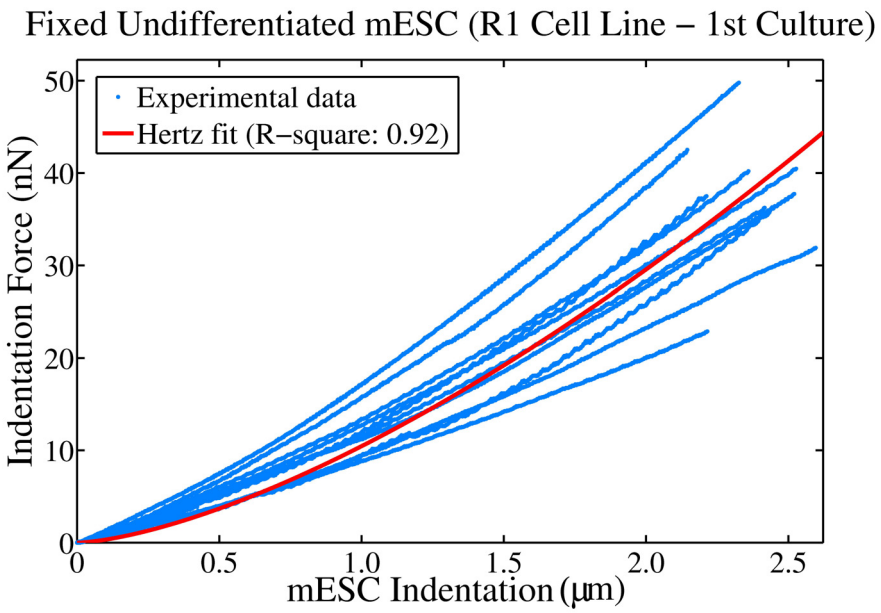

Figure 6.38: Force (F) versus cell indentation (δ) for 10 samples of fixed undifferentiated R1 mESC line (first independent culture). The R^2 value obtained with Hertz fit is 0.92.

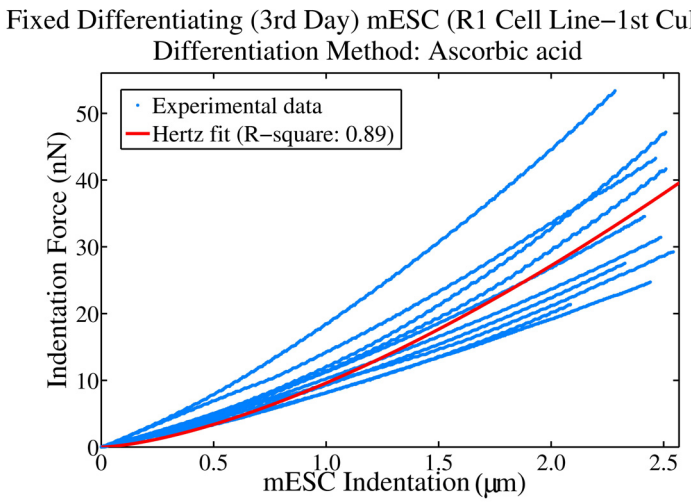

Figure 6.39: Force (F) versus cell indentation (δ) for 10 samples of fixed 3rd day differentiating R1 mESC line (first independent culture). The R^2 value obtained with Hertz fit is 0.89.

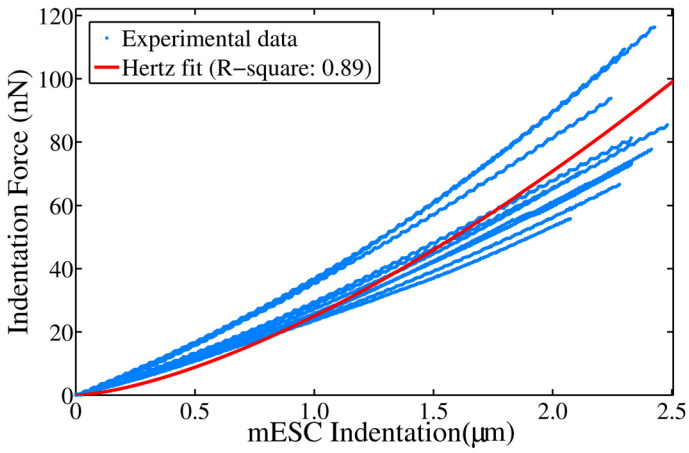

Figure 6.40: Force (F) versus cell indentation (δ) for 10 samples of fixed 6th day differentiating R1 mESC line (first independent culture). The R^2 value obtained with Hertz fit is 0.89.

From the figures, we observe that the first independent cultures of fixed undifferentiated mESC and 3rd day differentiating mESC are supple compared to the 6th day differentiating mESC (R1 cell line). We performed a Hertz fit on the dataset and the corresponding Hertz fit is shown in the figure. The R^2 value was found to be 0.92, 0.89, and 0.89 for fixed undifferentiated, 3rd day differentiating and 6th day differentiating R1 mESC line respectively.

Sample	1	2	3	4	5	6	7	8	9	10
Radius (μm)	7.5	7	7.25	6	7.3	7.5	6.5	6.23	3.25	3.75

Table 6.29: Radius of each sample of fixed undifferentiated mESC (R1 mESC line: first independent culture).

Sample	1	2	3	4	5	6	7	8	9	10
Radius (μm)	5.0	7.2	7.25	5.4	5.9	5.25	7.7	7.5	6.5	6.5

Table 6.30: Radius of each sample of fixed 3rd day differentiating mESC (R1 mESC line: first independent culture).

Sample	1	2	3	4	5	6	7	8	9	10
Radius (μm)	5.0	7.2	7.25	5.4	5.9	5.25	7.7	7.5	6.5	6.5

Table 6.31: Radius of each sample of fixed 6th day differentiating mESC (R1 mESC line: first independent culture).

Hertz model was used to compute the elastic modulus of each fixed mESC sample (R1 cell line: first independent culture) from the force (F) versus indentation (δ) by

assuming Poisson's ratio of 0.5. Table 6.29, 6.30, and 6.31 shows the radius of each fixed undifferentiated, differentiating (3rd day) and differentiating (6th day) mESC sample (R1 cell line: first independent culture) respectively used to compute the elastic modulus. The average elastic modulus was found to be 4.5839 kPa, 4.159 kPa, and 10.524 kPa for first independent culture of fixed undifferentiated, 3rd day differentiating, and 6th day differentiating R1 mESC line respectively as shown in figure 6.41. The standard deviation was 0.9904 kPa, 1.2579 kPa, and 1.9901 kPa for the first independent culture of fixed undifferentiated, 3rd day differentiating and 6th day differentiating R1mESC line respectively (see figure 6.41).

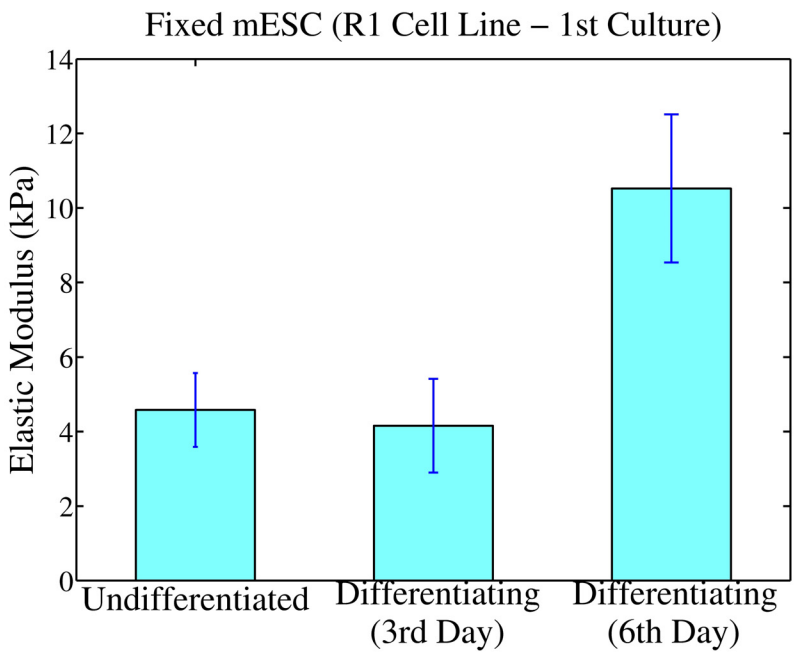

Figure 6.41: Elastic modulus of fixed undifferentiated, 3rd day differentiating, and 6th day differentiating R1 mESC line calculated from the Hertz contact model along with error bar. The differentiation was induced by ascorbic acid treatment.

We also performed the Kruskal-Wallis test on the elastic modulus values for the first independent culture of fixed undifferentiated, 3rd day differentiating and 6th day differentiating R1 mESC line. The p-value obtained was less than 0.0001, leading to a probability of greater than 99.99% that there was a significant difference between the data sets. The p-value obtained on the elastic modulus values for different states of mESC is shown in table 6.32. Thus there is a probability of greater than 99.98% that there is a significant statistical difference between the first independent cultures (R1 cell line) of: (a) fixed undifferentiated and 6th day differentiating mESC, and (b) fixed 3rd day differentiating and 6th day differentiating. However, there is no significant statistical difference between the elastic modulus of undifferentiated and 3rd day differentiating R1 mESC cell line (p-value = 0.2568). From the results, we infer that the first independent cultures of fixed undifferentiated and 3rd day differentiating R1 mESC line are supple cell compared to fixed 6th day differentiating R1 mESC line.

Statistics	Fixed undiff, 3rd day diff and 6th day diff mESC	Fixed undiff and 3rd day diff mESC	Fixed undiff and 6th day mESC	Fixed 3rd day diff and 6th day diff
p-value (Kruskal-Wallis test)	0.0000469	**0.2568**	0.0002	0.0002

Table 6.32: Statistical analysis on the elastic modulus values for fixed undifferentiated (undiff), 3rd day differentiating (3rd day diff), and 6th day differentiating (6th day diff) R1 mESC line (first independent culture). The differentiation was induced by ascorbic acid treatment. A significant statistical difference exists for all data sets ($p < \alpha = 0.05$) except for fixed undifferentiated and 3rd day differentiating mESC (p-value = 0.2568).

6.5.2. Second Independent Culture (Fixed R1 mESC line, Differentiation Method: Ascorbic Acid)

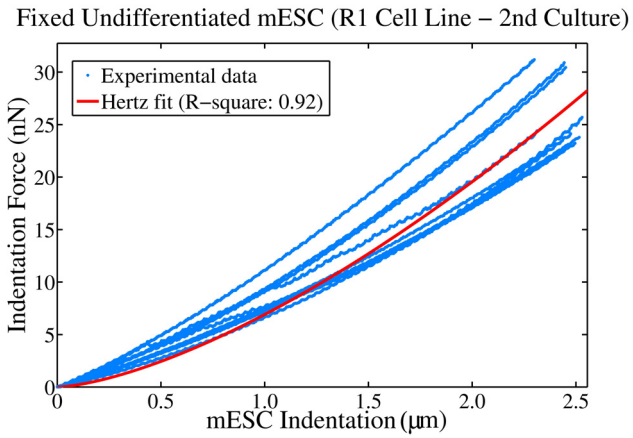

Figure 6.42: Force (F) versus cell indentation (δ) for 10 samples of fixed undifferentiated R1 mESC line (second independent culture). The R^2 value obtained with Hertz fit is 0.92.

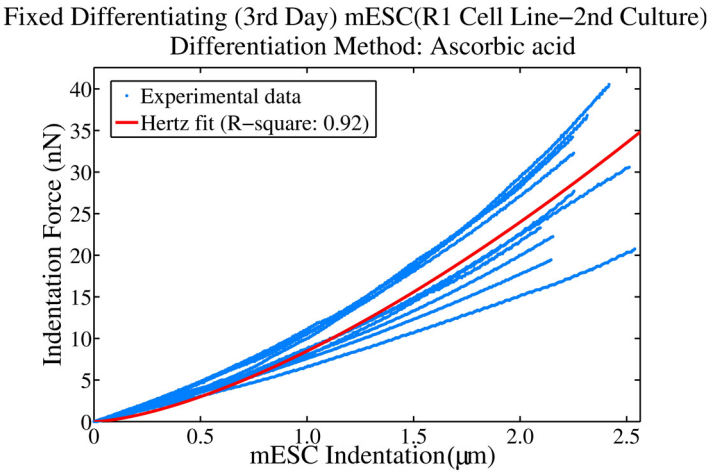

Figure 6.43: Force (F) versus cell indentation (δ) for 10 samples of fixed 3rd day differentiating R1 mESC line (second independent culture). The R^2 value obtained with Hertz fit is 0.92.

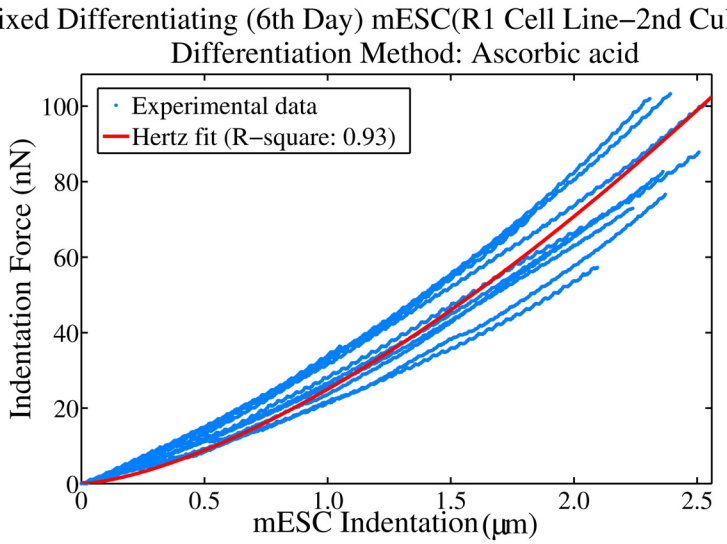

Figure 6.44: Force (F) versus cell indentation (δ) for 10 samples of fixed 6th day differentiating R1 mESC line (second independent culture). The R^2 value obtained with Hertz fit is 0.93.

Figure 6.42, 6.43, and 6.44 shows the force (F) versus cell indentation (δ) for the second independent culture of fixed undifferentiated, 3rd day differentiating and 6th day differentiating R1 mESC line respectively. Similar to the first independent culture of R1 mESC line in section 6.6.1, we observe that second independent cultures of the fixed undifferentiated R1 mESC line and 3rd day differentiating R1 mESC line are supple compared to the 6th day differentiating R1 mESC line using ascorbic acid treatment. We performed a Hertz fit on the dataset and the corresponding Hertz fit is shown in the figure. The R^2 value was found to be 0.92, 0.92, and 0.93 for the second independent culture of fixed undifferentiated, 3rd day differentiating and 6th day differentiating R1 mESC line respectively.

Sample	1	2	3	4	5	6	7	8	9	10
Radius (μm)	6.85	5.3	5.5	6.85	7.22	7.17	6.22	5.97	4.97	4.92

Table 6.33: Radius of each sample of fixed undifferentiated mESC (R1 mESC line: second independent culture).

Sample	1	2	3	4	5	6	7	8	9	10
Radius (μm)	5.15	7.9	7.1	8.4	4.2	5.2	3.5	5.7	4.7	6.6

Table 6.34: Radius of each sample of fixed 3rd day differentiating mESC (R1 mESC line: second independent culture).

Sample	1	2	3	4	5	6	7	8	9	10
Radius (μm)	7.04	6.21	7.0	4.2	6.2	6.3	6.6	6.3	6.8	7.1

Table 6.35: Radius of each sample of fixed 6th day differentiating mESC (R1 mESC line: second independent culture).

Hertz model was used to compute the elastic modulus of each fixed mESC sample (R1 cell line: second independent culture) from the force (F) versus indentation (δ) by assuming Poisson's ratio of 0.5. Table 6.33, 6.34, and 6.35 shows the radius of each fixed undifferentiated, differentiating (3rd day) and differentiating (6th day) R1 mESC line sample (second independent culture) respectively used to compute the elastic modulus. The average elastic modulus was found to be 3.018 kPa, 3.617 kPa, and 10.476 kPa for second independent culture of fixed undifferentiated, 3rd day differentiating, and 6th day differentiating R1 mESC line respectively as shown in

figure 6.45. The standard deviation was 0.534 kPa, 0.841 kPa, and 1.502 kPa for the second independent culture of fixed undifferentiated, 3rd day differentiating and 6th day differentiating R1mESC line respectively (see figure 6.45).

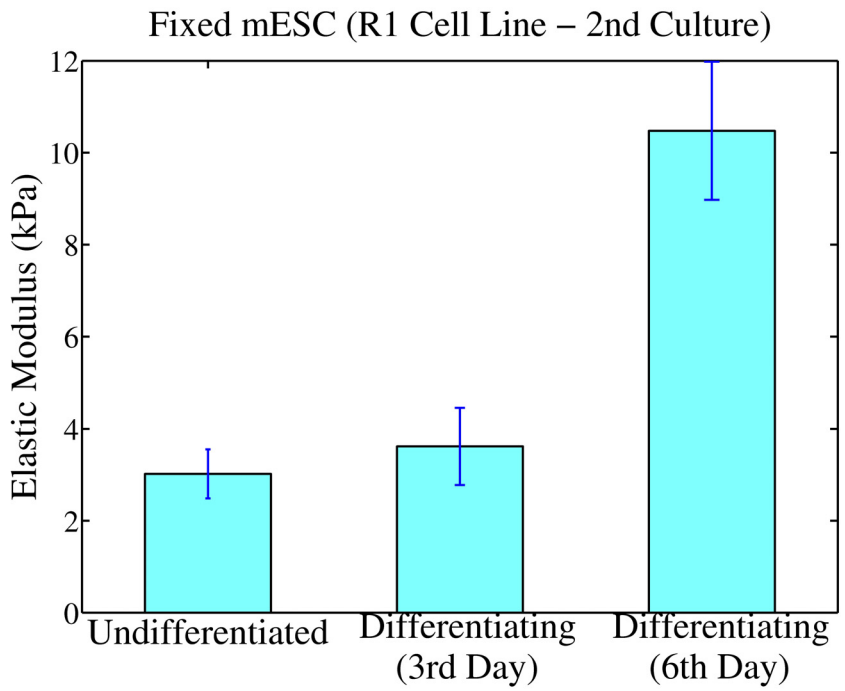

Figure 6.45: Elastic modulus of fixed undifferentiated, 3rd day differentiating, and 6th day differentiating R1 mESC line (second independent culture) calculated from the Hertz contact model along with error bar. The differentiation was induced by ascorbic acid treatment.

We also performed the Kruskal-Wallis test on the elastic modulus values for the second independent culture of fixed undifferentiated, 3rd day differentiating and 6th day differentiating R1 mESC line. The p-value obtained was less than 0.0001, leading to a probability of greater than 99.99% that there was a significant difference between the data sets. The p-value obtained on the elastic modulus values for different states

of mESC is shown in table 6.36. Thus there is a probability of greater than 99.98% that there is a significant statistical difference between the second independent cultures (R1 cell line) of: (a) fixed undifferentiated and 6th day differentiating mESC, and (b) fixed 3rd day differentiating and 6th day differentiating. However, there is no significant statistical difference between the elastic modulus of undifferentiated and 3rd day differentiating mESC cell line (p-value = 0.1124) in the second independent culture (similar to the first independent culture). From the results, we infer that the second independent cultures of fixed undifferentiated and 3rd day differentiating R1 mESC line are supple cell compared to fixed 6th day differentiating D3 mESC line. The results parallel with first independent culture of R1 mESC cell line (section 6.6.2). *Hence, we confirm our research hypothesis that the mechanical property of undifferentiated mESC differs significantly from early differentiating mESC (6th day) irrespective of the method of the culture and differentiation method.*

Statistics	Fixed undiff, 3rd day diff and 6th day diff mESC	Fixed undiff and 3rd day diff mESC	Fixed undiff and 6th day mESC	Fixed 3rd day diff and 6th day diff
p-value (Kruskal-Wallis test)	0.0000354	**0.1124**	0.0002	0.0002

Table 6.36: Statistical analysis on the elastic modulus values for fixed undifferentiated (undiff), 3rd day differentiating (3rd day diff), and 6th day differentiating (6th day diff) R1 mESC line (second independent culture). The differentiation was induced by ascorbic acid treatment. A significant statistical difference exists for all data sets ($p < \alpha = 0.05$) except for fixed undifferentiated and 3rd day differentiating mESC (p- value = 0.1124)

6.6 Discussion

In this chapter we conducted several indentation studies on mouse embryonic stem cells (mESC). The goal was to observe any mechanical property difference between undifferentiated and differentiating mESC. The statistical analysis was performed using a non-parametric ANOVA analysis namely the Kruskal-Wallis test. Initially, experiments were performed with a pyramidal tip on R1 mESC line in both live and fixed cells. The mESC was allowed to differentiate by LIF removal. In our preliminary studies on mESC presented in section 5.9, we observed a large variation in the modulus of mESC. This could be due to: (a) the variation in the stage of the cell cycle (M-phase or interphase) at the time of cell indentation, or (b) mixed population of undifferentiated and differentiating mESC in a particular cell culture. Hence we conducted further studies on mESC in one particular stage of the cell cycle process i.e. interphase. The indentation studies on R1 mESC line in interphase stage of the cell cycle process were performed with a pyramidal tip as well as spherical tip. In particular, we performed experiments on undifferentiated, third day differentiating (LIF removal) and sixth day differentiating mESC (LIF removal) for both live as well as fixed cells.

When experiments were performed with pyramidal tip, we observed that the 6th day differentiating mESC is stiffer compared to the 3^{rd} day differentiating mESC. Also the 3^{rd} day differentiating mESC was stiffer compared to the undifferentiated mESC in both live and fixed cells. In addition, a significant statistical difference (p-value < 0.05) was observed between the elastic modulus of undifferentiated and differentiating (3^{rd} and 6^{th} day) mESC. When experiments were performed with

spherical tip, we observed that the 6th day differentiating mESC was stiffer compared to the 3rd day differentiating as well as undifferentiated mESC. However, the 3rd day differentiating mESC was not stiffer compared to the undifferentiated mESC in both live and fixed cells. A significant statistical difference (p-value < 0.05) did exist between undifferentiated and early differentiating (6th day) mESC. We also observed that the variation in elastic modulus values of mESC in interphase stage of the cell cycle process is lower compared to the elastic modulus values obtained in our preliminary work with a pyramidal tip (section 5.9). The mean elastic modulus obtained with a spherical tip was less than the mean elastic modulus obtained with a pyramidal tip. The decrease in mean value could be due to the high stress concentration induced in the cell and the vicinity of the pyramidal tip apex [182]. The larger area of spherical tip – cell contact results in averaging local variation in modulus compared to that measured with a pyramidal tip. The high stresses induced in the cell with a pyramidal tip could also be the reason for 3rd day differentiating mESC to be stiffer compared to the undifferentiated mESC, which was not observed with a spherical tip. In addition, the pyramidal tip might be interacting with the mESC nucleus and reflecting its elastic modulus (high) as compared to the spherical tip. In order to validate the results, we repeated our experiments on second independent culture of R1 mESC cell line with a spherical tip. The mESC was allowed to differentiate by LIF removal. In this case, we observed that the 6th day differentiating mESC was stiffer compared to the 3rd day differentiating as well as undifferentiated mESC. However, the 3rd day differentiating mESC was not stiffer compared to the undifferentiated mESC. A significant statistical difference (p-value < 0.05) existed

between undifferentiated and differentiating (6^{th} day, LIF removal) mESC for the second independent culture of R1 cell line. Thus the results paralleled with the first independent culture of mESC obtained with spherical tip. Hence we infer that the elastic modulus obtained with a spherical tip truly predicts the mechanical property of mESC compared to a pyramidal tip and confirmed our research hypothesis that the mechanical property of undifferentiated mESC differs from early differentiating (6^{th} day, LIF removal) in both live and fixed cells.

The results obtained in sections 6.2 – 6.4 could be a characteristic oddity of the particular mESC line i.e. R1. In order to validate our results with another cell line, we conducted further indentation studies on two independent cultures of fixed D3 mESC cell line. Experiments on R1 mESC line (differentiation method: LIF removal) showed that the results obtained with live cells paralleled with fixed cells. Thus we performed experiments only on fixed D3 mESC line with a spherical tip. The results showed that the fixed 6th day differentiating D3 mESC line was stiffer compared to the 3^{rd} day differentiating as well as undifferentiated D3 mESC cell line for both cultures. However, no significant difference was observed between undifferentiated and 3^{rd} day differentiating D3 mESC line for both cultures. Also the elastic modulus of fixed 6^{th} day differentiating (LIF removal) D3 mESC cell line was approximately 80% less compared to the elastic modulus of fixed 6^{th} day differentiating (LIF removal) R1 mESC cell line. This could be due to a different cell line, but a significant statistical difference (p-value < 0.05) did exist between undifferentiated and differentiating (6^{th} day, LIF removal) mESC for both cultures of D3 mESC cell

line. Thus the results with fixed D3 mESC cell line parallel with fixed R1 mESC cell line by LIF removal.

We also conducted indentation studies on two independent cultures of fixed R1 mESC line differentiated by ascorbic acid treatment. In this study, we observed that the fixed 6th day differentiating R1 mESC line was stiffer compared to the 3rd day differentiating as well as undifferentiated R1 mESC cell line for both cultures. However, no significant difference was observed between undifferentiated and 3rd day differentiating (ascorbic acid treatment) R1 mESC cell line for both cultures. Also the elastic modulus of fixed 6th day differentiating (ascorbic acid treatment) R1 mESC cell line was approximately 31% and 85% less compared to the fixed 6th day differentiating (LIF removal) D3 mESC line and R1 mESC cell line respectively. This could be due to a different cell line and differentiation method, but a significant statistical difference (p-value < 0.05) did exist between undifferentiated and differentiating (6th day, ascorbic acid treatment) mESC for both cultures of R1 mESC cell line. Thus the results obtained with fixed R1 mESC cell line differentiated by ascorbic acid parallel with fixed R1 and D3 mESC line differentiated by LIF removal. Hence, we confirmed our research hypothesis that the mechanical property of undifferentiated mESC differs (supple) from early differentiating mESC (6th day) irrespective of the cell line (R1/D3) and method of differentiation (LIF removal/ascorbic acid treatment). Mechanical characterization of stem cells presented in this work can be used as a potential biological marker to distinguish differentiating stem cells from undifferentiated stem cells. However, the limitations of the work presented in this chapter are:

- We do not consider models which can take into account the influence of cell membrane, cytoplasm, cytoskeleton, and the nucleus on the mechanics of the cell.
- Finite element models or complex mechanical models may enable us to identify mechanical property differences between undifferentiated and 3rd day differentiating mESC.

Chapter 7: Concluding Remarks

7.1 Contributions

Manipulating individual biological cell is a common process involved in intracytoplasmic sperm injection (ICSI), pro-nuclei DNA injection, gene therapy, therapeutic and regenerative medicine and other biomedical areas. Potential application involves regional or target specific delivery of genetic material within a cell or an embryo. However, conventional cell manipulation techniques require long training and the success rate depends on the experience of the operator. Even for an experienced operator, the injection process results in low success rate and poor reproducibility. Further, the current techniques to distinguish between undifferentiated and differentiated stem cells are time consuming, cannot identify precursor stem cells and also involve genetic manipulation changing the characteristics of the stem cell. The potential applications of characterizing stem cells differentiating into a specialized cell type are: (a) drug development and toxicity tests, (b) replacement of diseased/damaged cells (tissue/cell therapy). In this dissertation, we addressed the drawbacks of conventional cell manipulation by incorporating force feedback in cell manipulation system. We showed that force feedback plays an important role in cellular level interactions. Further, we observed the change in force characterizing early stages of cell differentiation. Such characterization studies will enable the development of a high throughput system with force feedback capability. The following goals were achieved:

(1) Developed a force feedback interface for cell injection tasks [183]. The key component of a cell injection system with force feedback capability is a sensor capable of measuring forces in μN range. Therefore our research work focused on the development of a piezoelectric force sensor which has excellent sensitivity, high compliance and high signal to noise ratio. We showed a theoretical model for the force sensor and validated the model with experimental calibration. The developed sensor has the capability to measure forces in mN-μN range and was integrated with a cell manipulation system. The successful implementation of the system with force feedback capability was demonstrated by performing experiments on salmon fish and flying fish egg cells. In all the experiments the operator was able to feel the cell injection forces via PHANToM (haptic feedback device).

(2) Conducted human subject studies to evaluate the addition of force feedback for cell injection tasks [184, 185]. We performed experiments with 40 human subjects using two feedback scenarios: a) vision (V) feedback alone and b) vision + force (V+F) feedback on zebrafish egg cells (diameter: 600μm – 1mm). These cells are sensitive to mutagens and have low spontaneous malignancy rate, which makes it an ideal vertebrate animal model for understanding carcinogenesis, genetic functional screening, and drug discovery. The human subjects had a higher degree of success in injecting the desired material (trypan blue dye) into the cell with simultaneous vision + force feedback compared with vision feedback alone. Our findings confirmed that a system with force feedback capability when combined with vision feedback can lead

to potentially higher success rates in transgenesis, specifically where mechanical manipulation techniques are involved.

(3) Developed a haptics-enabled atomic force microscopy (AFM) for characterizing and manipulating mouse embryonic stem cells (mESC, diameter 10 – 15 μm) [186, 187]. Hence, we concentrated on achieving force feedback on smaller dimension cells compared to zebrafish egg cells. Stem cells have the unique capability to differentiate into specialized cell types e.g. bone, heart, nerve etc. These differentiated cells could be used for drug development/toxicity tests and for therapeutic medicine. Thus, the developed system aims to characterize the state of the cell via force feedback. We performed initial experiments on undifferentiated and early differentiating (3^{rd} day) mESC in both live and fixed states with a pyramidal tip. The force data obtained from the cell was reliable and the height of the cell was computed. In addition, it was shown that the stiffness of the cantilever plays an important role in the studies of live and fixed mESC. All the experiments were performed by indenting the cell without obtaining an AFM image and the user was able to feel the cell indentation forces in real time via PHANToM.

(4) Performed an exhaustive analysis to choose an appropriate analytical model to characterize the mechanical property of mouse embryonic stem cells. The analysis did not focus on complex mechanical and finite element models, because the first step is to observe whether there exists any difference in the mechanical behavior of mESC at various stages in the differentiation process. This was achieved by following an

analytical approach (calculated elastic modulus). The experimental data (force and indentation) obtained from the haptics-enabled AFM system was used to select the model. We inferred that the Bilodeau and Hertz model is appropriate for characterizing the mechanical behavior of mESC probed by a pyramidal and spherical tip respectively. From the analysis, we also concluded that the mESC mechanics could possibly be influenced by the compression of the cell interior (e.g. cytoskeleton) rather than that of the cell membrane.

(5) We conducted several indentation studies on mESC at undifferentiated and early differentiating (6 days under differentiation conditions) states. The appropriate analytical model chosen in chapter 5 was used to compute the elastic modulus of mESC. A statistical analysis was performed on all the data sets namely: undifferentiated, 3^{rd} day differentiating and 6^{th} day differentiating. In most of the studies we observed that there was no significant statistical difference between elastic modulus of undifferentiated and 3^{rd} day differentiating mESC. However in all the studies, we observed that there was a significant statistical difference between the elastic modulus of undifferentiated and 6^{th} day differentiating mESC. Also the 6^{th} day differentiating mESC was stiffer than the undifferentiated mESC. Hence we confirmed our research hypothesis that the mechanical property of undifferentiated mESC differs from early differentiating (6^{th} day) mESC irrespective of the cell line and the differentiation method.

However, there are certain limitations of the present work. They are:

(a) The force feedback interface developed for cell manipulation system can only perform cell injection. The system cannot perform other manipulation tasks e.g. grasping [165]. Moreover, the force feedback interface cannot be directly applied to inject smaller cells in the range of 10 – 50 μm diameter [166].

(b) We did not conduct indentation studies at specific locations of the cell surface because we were not able to obtain an AFM image of the cell in liquid (cell culture). We did obtain the image of an individual cell with optical microscopy. However, it was not possible to position the tip at specific locations on the cell surface because the end of the cantilever obstructs the clear visibility of the cell surface, when the tip is positioned on the cell. Indentation studies at specific locations of the cell would possibly determine the heterogeneity of the cell surface [182].

(c) In our analytical approach to characterize the mechanical behavior of mESC, we assumed that the cell is linear elastic, isotropic and homogeneous. We did not study the viscoelastic [144-146] and heterogeneous [182] behavior of the cell.

(d) We did not consider complex mechanical and finite element models to determine the mechanical property of mESC. In addition, we assumed that the mESC is incompressible (Poisson's ratio = 0.5).

7.2 Future Work

- Develop a microgripper for grasping cells with force feedback capability. This would address the poor control of pipette suction force to hold an individual cell which might rupture the cell membrane. Moreover, the microgripper could be used to grasp the cell while the AFM scans over the cell surface. This would solve the problem of cells dislodging from the substrate during AFM imaging.
- Develop a force feedback interface for injecting cells (trypan blue dye as a model for genetic material) of dimensions less than 100 μm. This could be achieved by following one of the two approaches: (a) develop a MEMS based force sensor integrated with microfluidic channels. This would involve integration of the MEMS sensor with the cell manipulation system and haptic device (b) develop an AFM cantilever integrated with microfluidic channels and then use the haptics-enabled AFM developed in this dissertation.
- Perform human factors studies with the haptics-enabled AFM developed in this dissertation to study the mESC stiffness change in real time at various stages of differentiation.
- Perform indentation studies on specific locations of the cell after obtaining the AFM image. This would determine the heterogeneous nature of the cell.
- Determine the viscoelastic behavior of mESC and subject the cell to large deformations. Develop a suitable model (complex analytical model or finite element model) for mESC which would neglect the assumptions made by the

Hertz and Bilodeau contact model. The developed model would be validated with experimental results.

- The finite element model of the cell could be integrated with a haptic device in a virtual environment. This could be used for training purposes.
- Conduct further studies on mouse embryonic stem cells (mESC) at later stages in the differentiation process (near the precursor cell stage and thereafter) leading to a particular cell lineage *in vitro* e.g. neurons. Later on the studies can be extended to mESC differentiating into other cell lineages e.g. heart. Such experiments will provide a better insight into the relationship between the mechanical properties of mESC at various stages of differentiation along a particular cell lineage.
- Develop a high throughput system for cell characterization with force feedback capability.

The findings of this research provide a foundation for incorporation of force feedback for cell manipulation and demonstrate the possibility of incorporating these technologies for therapeutic and regenerative medicine. The preliminary experimental work shows the potential advantages of mechanical manipulation and characterization of cells. The results of this research are an important first step towards efficient manipulation and characterization of cells for clinical applications.

Bibliography

[1] V. Korzh and U. Strahle, "Marshall Barber and the century of microinjection: from cloning of bacteria to cloning of everything," *Differentiation.*, vol. 70221 - 226, 2002.

[2] R. Briggs and T. J. King, "Transplantation of living nuclei from blastulla cells into enucleated frogs eggs," *Proc. Natl. Acad. Sci.*, vol. 38455-463, 1952.

[3] Y. Hiramoto, "Microinjection of the live spermatozoa into sea urchin eggs," *Experimental Cell Research*, vol. 27(3), pp. 416-426, 1962.

[4] A. Hanada and M. C. Chang, "Penetration of zona-free eggs by spermatozoa of different species," *Biol. Reprod*, vol. 6300-309, 1972.

[5] T. Uehera and R. Yanagimachi, "Microsurgical Injection of Spermatozoa into Hamster Eggs with Subsequent Transformation of Sperm Nuclei into Male Pronuclei," *Biol. Reprod.*, vol. 15467-470, 1976.

[6] J. Yovich and J. Stanger, "The limitations of in vitro fertilization from males with severe oligospermia and abnormal sperm morphology," *Journal of in Vitro Fertilization and Embryo Transfer*, vol. 1(3), pp. 172-179, 1984.

[7] G. Calderon, A. Veiga, J. Panella, and P. Barri, "Two years of assisted fertilization by partial zona dissection in male factor infertility patients," *Fertil. Steril.*, vol. 60(1), pp. 105-109, 1993.

[8] H. Malter and J. Cohen, "Partial zona dissection of the human oocyte: a nontraumatic method using micromanipulation to assist zona pellucida penetration," *Fertil. Steril.*, vol. 51(1), pp. 139-148, 1989.

[9] S. Fishel, S. Antinori, P. Jackson, J. Johnson, and L. Rinaldi, "Presentation of six pregnancies established by sub-zonal insemination (SUZI)," *Hum. Reprod.*, vol. 6(1), pp. 124-130, 1991.

[10] J. Lippi, D. Mortimer, and R. Jansen, "Sub-zonal insemination for extreme male factor infertility," *Hum. Reprod.*, vol. 8(6), pp. 908-915, 1993.

[11] G. Palermo, H. Joris, P. Devroey, and A. Steirteghem, "Pregnancies after intracytoplasmic injection of single spermatozoon into an oocyte," *Lancet.*, vol. 34017-18, 1992.

[12] J. Cohen, H. Malter, C. Fehilly, G. Wright, C. Elsner, H. Kort, and J. Massey, "Implantation of embryos after partial opening of oocyte zona pellucida to facilitate sperm penetration," *Lancet.*162, 1988.

[13] S.-C. Ng, A. Bongso, S. S. Ratnam, H. Sathananthan, C. L. K. Chan, P. C. Wong, L. Hagglund, C. Anandakumar, Y. C. Wong, and V. H. H. Goh, "Pregnancy after transfer of sperm under zona," *Lancet.*790, 1988.

[14] M. van Rumste, J. Evers, C. Farquhar, and D. Blake, "Intra-cytoplasmic sperm injection versus partial zona dissection, subzonal insemination and conventional techniques for oocyte insemination during in vitro fertilization.," *The Cochrane Database of Systematic Reviews*(2), pp. Art. No.: CD001301. DOI: 10.1002/14651858.CD001301, 2003.

[15] R. J. Wall, "Pronuclear microinjection," *Cloning. Stem. Cells*, vol. 3(4), pp. 209-220, 2001.

[16] M. Belting, S. Sandgren, and A. Wittrup, "Nuclear delivery of macromolecules: barriers and carriers," *Adv. Drug. Deliv. Rev.*, vol. 57(4), pp. 505-527, 2005.

[17] P. N. Moreira, "Efficient generation of transgenic mice with intact yeast artificial chromosomes by intracytoplasmic sperm injection.," *Biol. Reprod.*, vol. 71(6), pp. 1943-1947, 2004.

[18] T. Ogura, "In vivo electroporation: a new frontier for gene delivery and embryology," *Differentiation.*, vol. 70(4-5), pp. 163-171, 2002.

[19] D. Lechardeur and G. L. Lukacs, "Intracellular barriers to non-viral gene transfer," *Curr. Gene. Ther*, vol. 2(2), pp. 183-194, 2002.

[20] A. G. Smith, "Embryo-derived stem cells: of mice and men," *Annual review of cell and developmental biology*, vol. 17435-462, 2001.

[21] S. Assady, G. Maor, M. Amit, J. Itskovitz-Eldor, K. L. Skorecki, and M. Tzukerman, "Insulin production by human embryonic stem cells," *Diabetes*, vol. 50 1691 - 1697, 2001.

[22] H. Segev, B. Fishman, A. Ziskind, M. Shulamn, and J. Itskovitz-Eldor, "Differentiation of human embryonic stem cells into insulin producing clusters " *Stem Cells*, vol. 22 265 - 274, 2004.

[23] M. Li, L. Pevny, R. Lovell-Badge, and A. Smith, "Generation of purified neural precursors from embryonic stem cells by lineage selection," *Current Biology*, vol. 8 971 - 974, 1998.

[24] S. Okabe, K. Forsberg-Nilsson, A. C. Spiro, M. Segal, and R. D. Mackay, "Development of neuronal precursor cells and functional postmitotic neurons

from embryonic stem cells *in vitro*," *Mechanisms of Development*, vol. 59 89 - 102, 1996.

[25] M. G. Klug, M. H. Soonpaa, G. Y. Koh, and L. J. Field, "Genetically selected cardiomyocytes from differentiating embryonic stem cells from stable intracardiac grafts. ," *Journal of Clinical Investigation*, vol. 98 216 - 224, 1996.

[26] M. Muller, B. K. Fleischmann, and S. Selbert, "Selection of ventricular-like cardiomyocytes from ES cells *in vitro*," *The Journal of the Federation of American Societies for Experimental biology*, vol. 14 2540 - 2548, 2000.

[27] V. Sottile, J. A. Thomson, and J. McWhir, "*In vitro* osteogenenic differentiation of human ES cells," *Cloning Stem Cells*, vol. 5149 - 155, 2003.

[28] W. Ansorage, "Improved system for capillary microinjection into living cells," *Exp. Cell. Res*, vol. 14031-37, 1982.

[29] K. Viigipuu and P. Kallio, "Microinjection of Living Adherent Cells by using a Semi-automatic Microinjection System," *Twenty-first Scandivian Cell Toxicology Workshop*417-423, 2004.

[30] K. Kobayashi, K. Kato, M. Saga, M. Yamane, C. M. Rothman, and S. Ogawa, "Subzonal insemination of a single mouse spermatozoon with a personal computer-controlled micromanipulation system," *Mol. Reprod. Dev.*, vol. 33(1), pp. 81-88, 1992.

[31] Y. Kimura and R. Yanagimachi, "Intracytoplasmic Sperm Injection in the Mouse," *Biology of Reproduction*, vol. 52(4), pp. 709-720, 1995.

[32] K. Yanagida, H. Katayose, H. Yazawa, Y. Kimura, K. Konnai, and A. Sato, "The usefulness of a piezo-micromanipulator in intracytoplasmic sperm injection in humans," *Human Reproduction*, vol. 14(2), pp. 448-453, 1998.

[33] Y. Sun and B. J. Nelson, "Microrobotic Cell Injection," *IEEE International Conference on Robotics and Automation*620 - 625, 2001.

[34] A. Ashkin, "Acceleration and Trapping of Particles by Radiation Pressure," *Physical Review Letters*, vol. 4156-159, 1970.

[35] W. H. Wright, G. J. Sonek, Y. Tadir, and M. W. Berns, "Laser Trapping in Cell Biology," *IEEE Journal of Quantum Electronics*, vol. 26(12), pp. 2148 - 2157, 1990.

[36] A. Ashkin and J. M. Dziedzic, "Optical trapping and manipulation of viruses and bacteria," *Science.*, vol. 235(4795), pp. 1517-1520, 1987.

[37] A. Ashkin, J. M. Dziedzic, and T. Yamane, "Optical trapping and manipulation of single cells using infrared laser beams," *Nature*, vol. 330769-771, 1987.

[38] K. Konig, H. Liang, M. W. Berns, and B. J. Tromberg, "Cell damage by near-IR microbeams," *Nature*, vol. 37720-21, 1995.

[39] T. N. Buican, M. J. Smyth, H. A. Crissman, G. C. Salzman, C. C. Stewart, and J. C. Martin, "Automated Single-cell Manipulation and Sorting by Light Trapping," *Applied Optics*, vol. 26(24), pp. 5311 - 5316, 1987.

[40] A. Ashkin, "History of Optical Trapping and Manipulation of Small-Neutral Particle, Atoms, and Molecules," *IEEE Journal on Selected Topics in Quantum Electronics*, vol. 6(6), pp. 841-856, 2000.

[41] H. A. Pohl, "The motion and precipitation of suspensoids in divergent electric fields," *Journal of Applied Physics*, vol. 22(7), pp. 869-871, 1951.

[42] M. Mischel, A. Voss, and H. A. Pohl, "Cellular spin resonance in rotating electric fields," *Journal of Biological Physics*, vol. 10(4), pp. 223-226, 1982.

[43] W. M. Arnold and U. Zimmermann, "Electro-rotation: development of a technique for dielectric measurements on individual cells and particles," *Journal of Electrostatics*, vol. 21(2-3), pp. 151-191, 1988.

[44] F. Arai, K. Morishima, T. Kasugai, and T. Fukuda, "Bio-Micro-Manipulation(New Direction for Operation Improvement)," *IEEE International Conference on Intelligent Robots and Systems*1300-1305, 1997.

[45] M. Washizu, Y. Kurahashi, H. Iochi, O. Kurosawa, S. I. Aizawa, S. Kudo, Y. Magariyama, and H. Hotani, "Dielectrophoretic Measurement of Bacterial Motor Characteristics," *IEEE Transactions on Industry Applications*, vol. 29(2), pp. 286-294, 1993.

[46] A. Mizuno, M. Imamura, and K. Hosoi, "Manipulation of single fine particle in liquid by electrical force in combination with optical pressure," *IEEE Transactions on Industry Applications*, vol. 27(1), pp. 140-146, 1991.

[47] M. Nishioka, S. Katsura, K. Hirano, and A. Mizuno, "Evaluation of Cell Characteristics by Step-Wise Orientational Rotation Using Optoelectrostatic Micromanipulation," *IEEE Transactions on Industry Applications*, vol. 33(5), pp. 1381-1388, 1997.

[48] F. Arai, M. Ogawa, T. Mizuno, T. Fukuda, K. Morishima, and K. Horio, "Teleoperated Laser Manipulator with Dielectrophoretic Assistance for

Selective Separation of a Microbe," *IEEE International Conference on Intelligent Robots and Systems*1872 - 1877, 1999.

[49] A. Docoslis, N. Kalogerakis, and L. A. Behie, "Dielectrophoretic forces can be safely used to retain viable cells in perfusion cultures of animal cells," *Cytotechnology*, vol. 30133-142, 1999.

[50] G. J. Garrisi, B. E. Talansky, L. Grunfeld, V. Sapira, D. Navot, and J. W. Gordon, "Clinical evaluation of three approaches to micromanipulation assisted fertilization," *Fertility and Sterility*, vol. 54(4), pp. 671-677, 1990.

[51] D. Payne, K. J. McLaughlin, H. T. Depyper, C. A. Kirby, G. M. Warnes, and C. D. Matthews, "Experience with zona drilling and zona cutting to improve fertlization rates of human oocytes *in vitro*," *Human Reproduction*, vol. 6(3), pp. 423-431, 1991.

[52] M. Germond, D. Nocera, A. Senn, K. Rink, G. Delacretaz, T. Pedrazzini, and J. P. Hornung, "Improved fertilization and implantation rates after non-touch zona pellucida microdrilling of mouse oocytes with a 1.48 μm diode laser system.," *Human Reproduction*, vol. 11(5), pp. 1043-1048, 1996.

[53] D. Palanker, S. Ohad, A. Lewis, A. Simon, J. Shenkar, S. Penchas, and N. Laufer, "Technique for cellular surgery using the 193-nm excimer laser," *Lasers in Surgery and Medicine*, vol. 11(6), pp. 580-586, 1991.

[54] N. Laufer, D. Palanker, Y. Shufaro, A. Safran, A. Simon, and A. Lewis, "The efficacy and safety of zona pellucida drilling by a 193-nm excimer laser," *Fertility and Sterility*, vol. 59(4), pp. 889-895, 1993.

[55] R. E. Rasmussen, M. Hammer-Wilson, and M. W. Berns, "Mutation and sister chromatid exchange induction in chinese hamster ovary (CHO) cells by pulsed excimer laser radiation at 193 nm and 308 nm and continuous UV radiation at 254 nm.," *Photochemistry and Photobiology*, vol. 49(4), pp. 413-418, 1989.

[56] H. Strohmer and W. Feichtinger, "Successful clinical application of laser for micromanipulation in an in vitro fertilization program," *Fertility and Sterility*, vol. 58(6), pp. 212-214, 1992.

[57] W. Feichtinger, H. Strohmer, P. Fuhrberg, K. Radivojevic, S. Antinori, G. Pepe, and C. Versaci, "Photoablation of oocyte zona pellucida by erbium-yag laser for in-vitro fertilization in severe male infertility," *The Lancet*, vol. 339811, 1992.

[58] S. Antinori, C. Versaci, P. Fuhrberg, C. Panci, B. Caffa, and G. H. Gholami, "Andrology: seventeen live births after the use of an erbium-yytrium aluminium garnet laser in the treatment of male factor infertility.," *Human Reproduction*, vol. 9(10), pp. 1891-1896, 1994.

[59] M. Boada, M. Carrera, C. D. L. Iglesia, M. Sandalinas, P. N. Barri, and A. Veiga, "Successful use of a laser for human embryo biopsy in preimplantation genetic diagnosis: report of two cases.," *Journal of Assisted Reproduction and Genetics*, vol. 15(5), pp. 302-307, 1998.

[60] M. Montag, K. Ven, G. Delacretaz, K. Rink, and H. Ven, "Laser assisted microdissection of the zona pellucida facilitates polar body biopsy.," *Fertility and Sterility*, vol. 69(3), pp. 539-542, 1998.

[61] M. Montag, K. Rink, U. Dieckmann, G. Delacretaz, and H. Ven, "Laser assisted cryopreservation of single human spermatozoa in cell free zona pellucida.," *Andrologia*, vol. 3149-53, 1999.

[62] T. Ebner, C. Yaman, M. Moser, M. Sommergruber, J. Hartl, and G. Tews, "Laser assisted immobilization of spermatozoa prior to intracytoplasmic sperm injection in humans," *Human Reproduction*, vol. 16(12), pp. 2628-2631, 2001.

[63] S. Antinori, C. Panci, H. A. Selman, B. Caffa, G. Dani, and C. Versaci, "Zona thinning with the use of laser: a new approach to assisted hatching in humans," *Human Reproduction*, vol. 11(3), pp. 590-594, 1996.

[64] D. A. Blake, A. S. Forsberg, B. R. Johansson, and M. Wikland, "Laser zona pellucida thinning- an alternative approach to assisted hatching.," *Human Reproduction*, vol. 16(9), pp. 1959-1964, 2001.

[65] H. E. Malter, T. Schimmel, and J. Cohen, "Zona dissection by infrared laser: developmental consequences in the mouse, technical considerations, and controlled clinical trial.," *Reproductive Biomedicine Online*, vol. 3(2), pp. 117-123, 2001.

[66] F. H. C. Crick and A. F. W. Hughes, "The physical properties of cytoplasm: A study by means of the magnetic particle method," *Experimental Cell Research*, vol. 137-80, 1949.

[67] B. G. Hosu, K. Jakab, P. Banki, F. I. Toth, and G. Forgacs, "Magnetic tweezers for intracellular applications," *Review of Scientific Instruments*, vol. 74(9), pp. 4158-4163, 2003.

[68] A. H. B. de Vries, B. E. Krenn, R. van Driel, and J. S. Kanger, "Micro magnetic tweezers for nanomanipulation inside living cells," *Biophysical Journal*, vol. 882137-2144, 2005.

[69] C. Wilhelm, F. Gazeau, and J. C. Bacri, "Magnetic micromanipulation in the living cell," *Europhysics News*89-92, 2005.

[70] T. R. Strick, J. F. Allemand, D. Bensimon, A. Bensimon, and V. Croquette, "The elasticity of a single supercoiled DNA molecule," *Science*, vol. 271(5257), pp. 1835-1837, 1996.

[71] C. Haber and D. Wirtz, "Magnetic tweezers for DNA micromanipulation," *Review of Scientific Instruments*, vol. 71(12), pp. 4561-4570, 2000.

[72] J. Yan, D. Skoko, and J. F. Marko, "Near-field-tweezer manipulation of single DNA molecules.," *Physical Review E*, vol. 701-5, 2004.

[73] C. H. Chiou, Y. Y. Huang, M. H. Chiang, H. H. Lee, and G. B. Lee, "New magnetic tweezers for investigation of the mechanical properties of single DNA molecules," *Nanotechnology*, vol. 171217-1224, 2006.

[74] W. H. Guilford, R. C. Lantz, and R. W. Gore, "Locomotive forces produced by single leukocytes in vivo and in vitro," *The American Physiological Society*, vol. 268C1308-C1312, 1995.

[75] F. J. Alenghat, B. Fabry, K. Y. Tsai, W. H. Goldmann, and D. E. Ingber, "Analysis of Cell Mechanics in Single Vinculin-deficient Cells using a Magnetic Tweezer.," *Biochemical and Biophysical Research Communications*, vol. 27793-99, 2000.

[76] M. Boukallel, E. Piat, and J. Abadie, "Micromanipulation tasks using passive levitated force sensing manipulator," *International Conference on Intelligent Robots and Systems*529-534, 2003.

[77] M. Pesce and M. De Felici, "Purification of Mouse Primordial Germ Cells by Mini-MACS Magnetic Separation System," *Developmental Biology*, vol. 170722 -725, 1995.

[78] H. Lee, T. P. Hunt, and R. M. Westervelt, "Magnetic and Electric Manipulation of a Single Cell in Fluid," *Mat. Res. Soc. Symp. Proc*, vol. 8202.3.1 - 2.3.8, 2004.

[79] M. Barbie, "Single domain magnets in bio-medical applications," *European Cells and Materials*, vol. 3(2), pp. 132-134, 2002.

[80] E. Mirowski, J. Moreland, A. Zhang, and S. E. Russek, "Manipulation and sorting of magnetic particles by a magnetic force microscope on a microfluidic magnetic trap platform," *Applied Physics Letters*, vol. 86243901-1 - 3, 2005.

[81] T. Kozuka, T. Tuziuti, H. Mitome, T. Fukuda, and F. Arai, "Two-dimensional Acoustic Micromanipulation Using Three Ultrasonic Transducers," presented at International Symposium on Micromechatronics and Human Science, Nagoya, Japan, 201 - 204, 1998.

[82] T. Kozuka, T. Tuziuti, H. Mitome, F. Arai, and T. Fukuda, "Three-Dimensional Acoustic Micromanipulation Using Four Ultrasonic Transducers," presented at International Symposium on Micromechatronics and Human Science, 201-206, 2000.

[83] J. J. Hawkes, D. Barrow, and W. T. Coakley, "Microparticle manipulation in millimetre scale ultrasonic standing wave chambers," *Ultrasonics*, vol. 36925-931, 1998.

[84] A. Haake and J. Dual, "Micro-Manipulation of small particles by node position control of an ultrasonic standing wave," *Ultrasonics*, vol. 40317-322, 2002.

[85] D. H. Kim, A. Haake, Y. Sun, A. P. Neild, J. Ihm, J. Dual, J. A. Hubbell, B. K. Ju, and B. J. Nelson, "High Throughput Cell manipulation Using Ultrasound Fields," presented at Proceedings of the 26th Annual International Conference of the IEEE EMBS, San Fransisco, CA, USA, 2571-2574, 2004.

[86] E. W. H. Jager, O. Inganas, and I. Lundstrom, "Microrobots for Micrometer-Size Objects in Aqueous Media : Potential Tools for Single -Cell Manipulation," *Science*, vol. 2882335-2338, 2000.

[87] N. Chronis and L. P. Lee, "Electrothermally activated SU-8 microgripper for single cell manipulation in solution," *Journal of Microelectromechanical Systems*, vol. 14(4), pp. 857-863, 2005.

[88] P. K. Wong, U. Ulmanella, and C. Ho, "Fabrication process of microsurgical tools for single cell trapping and intracytoplasmic injection," *Journal of Microelectromechanical Systems*, vol. 13(6), pp. 940-946, 2004.

[89] B. Kim , D. Collard, M. Lagouge, F. Conseil, B. Legrand, and L. Buchaillot, "Thermally actuated probe arrays for manipulation and characterization of individual bio-cell.," *Transducers '03: The 12th IEEE International*

*Conference on Solid State Sensors, Actuators and Microsystems*1255-1258, 2003.

[90] E. W. H. Jager, C. Immerstrand, K. H. Peterson, K. Magnusson, I. Lundstrom, and O. Inganas, "The cell clinic: closable microvials for single cell studies," *Biomedical Microdevices*, vol. 4(3), pp. 177-187, 2002.

[91] N. Reeves, Y. Liu, N. M. Nelson, S. Malhotra, M. Loganathan, J. M. Lauenstein, J. Chaiyupatumpa, E. Smela, and P. A. Abshire, "Integrated MEMS structures and CMOS circuits for bioelectronic interface with single cells," *IEEE International Symposium on Circuits and Systems*673-676, 2004.

[92] K. Chun, G. Hashiguchi, H. Toshiyoshi, and H. Fujita, "Fabrication of array of hollow microcapillaries used for injcetion of genetic material into animal/plant cells.," *Jpn.J.Appl.Phys.Part 2*, vol. 38(3A), pp. 279-281, 1999.

[93] D. V. McAllister, M. G. Allen, and M. R. Prausnitz, "Microfabricated Microneedles For Gene and Drug Delivery," *Annu.Rev.Biomed.Eng*, vol. 2289-313, 2000.

[94] A. Codourey, R. Siegwart, W. Zesch, and R. Büchi, "A robot system for automated handling in micro-world," *IEEE International Conference on Intelligent Robots and Systems*, vol. 3185 - 190, 1995.

[95] P. Gao and S.-M. Swei, "A six-degree-of-freedom micro-manipulator based on piezoelectric translator," *Nanotechnology*, vol. 10447 - 452., 1999.

[96] M. Goldfarb and J. E. Speich, "Design of a minimum surface-effect three degree-of- freedom micro-manipulator," *IEEE International Conference on Robotics and Automation*1466 - 1471, 1997.

[97] Y. Ohya, T. Arai, Y. Mae, K. Inoue, and T. Tanikawa, "Development of 3-DOF finger module for micro manipulation," *IEEE International Conference on Intelligent Robots and Systems*894 - 899, 1999.

[98] T. Tanikawa and T. Arai, "Development of a micro-manipulation system having a two-fingered micro-hand," *IEEE Transactions on Robotics and Automation*, vol. 15(1), pp. 152 - 162, 1999.

[99] Y. H. Choi, C. C. Love, Y. G. Chung, D. D. Varner, M. E. Westhusin, R. C. Burghardt, and K. Hinrichs, "Production of nuclear transfer horse embryos by piezo-driven injection of somatic cell nuclei and activation with stallion sperm cytosolic extract.," *Biology of Reproduction*, vol. 67561-567, 2002.

[100] A. Kawaji, F. Arai, and T. Fukuda, "Calibration for Contact Type of Micro-manipulation," *IEEE International Conference on Intelligent Robots and Systems*715 - 720, 1999.

[101] G. Li and N. Xi, "Calibration of a Micromanipulation System," *IEEE International Conference on Intelligent Robots and Systems*1742 -1747, 2002.

[102] B. Vikramaditya and B. Nelson, "Visually Guided Microassembly Using Optical Microscopes and Active Vision Techniques," presented at IEEE International Conference on Robotics and Automation, Albuquerque, New Mexico, USA, 3172 - 3177, 1997.

[103] J. T. Feddema and R. W. Simon, "CAD-Driven Microassembly and Visual Servoing," presented at IEEE International Conference on Robotics and Automation, Leuven, Belgium, 1212 - 1219, 1998.

[104] X. Li, G. Zong, and S. Bi, "Development of Global Vision System for Biological Automatic Micro-Manipulation System," presented at IEEE International Conference on Robotics & Automation, Seoul, Korea, 127 - 132, 2001.

[105] H. Yamamoto and J. Sakiyama, "Stereoscopic Visual Servo System for Microinjec-tion," presented at IEEE Instrumentation and Measurement Technology Conference, Anchorage, USA, 1109 - 1112, 2002.

[106] Y. Mezouar and P. K. Allen, "Visual Servoed Micropositioning for Protein Manipulation Tasks.," presented at IEEE/RSJ International Conference on Intelligent Robots and Systems, Lausanne, Switzerland, 1766 - 1771, 2002.

[107] A. Georgiev, P. K. Allen, and W. Edstorm, "Visually-Guided Protein Crystal Manipulation Using Micromachined Silicon Tools," presented at International Conference on Intelligent Robots and Systems, Sendai, Japan, vol. 1, pp. 236-241, 2004.

[108] F. J. Sanchez-Marin, "Computerized Recognition of Biological Objects Using the Hotelling Transform," presented at 22nd Annual EMBS Internation Conference, Chicago, USA, 3067 - 3070, 2000.

[109] F. A. Arámbula Cosío, L. Vega, A. Herrera Becerra, Prieto Meléndez, R. and, and C. G., "A Neural Network Based Workstation for Automated Cell Proliferation Analysis," presented at 23rd Annual EMBS International Conference, Istanbul, Turkey, 2567 - 2570, 2001.

[110] T. Jiang and F. Yang, "An Evolutionary Tabu Search for Cell Image Segmentation," *IEEE Transactions on Systems, Man and Cybernetics - Part B: Cybernetics*, vol. 32(5), pp. 675 - 678, 2002.

[111] G. Binnig and C. F. Quate, "Atomic Force Micrscope," *Physical review Letters*, vol. 56(9), pp. 930-933, 1986.

[112] R. Lal and S. A. John, "Biological applications of atomic force microscopy," *The American Physiological Society*, vol. 266C1 - C21, 1994.

[113] W. Fritzsche, L. Takac, and E. Henderson, "Application of Atomic Force Microscopy to Visualization of DNA, Chromatin and Chromosomes," *Critical reviews in Eukaryotic Gene Expression*, vol. 7(3), pp. 231-240, 1997.

[114] C. Putman, K. O. Werf, B. D. Grooth, N. V. Hulst, and J. Greve, "Viscoelasticity of living cells allows high resolution imaging by tapping mode atomic force microscopy," *Biophysical Journal*, vol. 671749-1753, 1994.

[115] W. Harbele, J. K. H. Horber, F. Ohnesorge, D. P. E. Smith, and G. Binnig, "In Situ Investigations of single living cells infected by viruses," *Ultramicroscopy*, vol. 42-441161 - 1167, 1992.

[116] J. H. Hoh and C. Schoenenberger, "Surface morphology and mechanical properties of MDCK monolayers by atomic force microscopy," *Journal of Cell Science*, vol. 1071105-1114, 1994.

[117] S. S. Schaus and E. Henderson, "Cell Viability and probe-cell membrane interactions of XR1 glial cells imaged by atomic force microscopy," *Biophysical Journal*, vol. 731205 -1214, 1997.

[118] S. C. Minne, G. Yaralioglu, S. R. Manalis, J. D. Adams, J. Zesch, A. Atalar, and C. F. Quate, "Automated parallel high-speed atomic force microscopy," *Applied Physics Letters*, vol. 72(18), pp. 2340-2342, 1998.

[119] B. Rogers, T. Sulchek, K. Murray, D. York, M. Jones, L. Manning, S. Malekos, B. Beneschott, and J. D. Adams, "High Speed Tapping Mode Atomic Force Microscopy in Liquid using an Insulated Piezoelectric Cantilever," *Review of Scienetific Instruments*, vol. 74(11), pp. 4683-4686, 2003.

[120] H. K. Park, Y. K. Hong, S. Q. Lee, and K. S. Moon, "Design of a Compact Atomic Force Microscope to Enhance Scanning Speed," presented at Proceedings of the SPIE International Conference on Opto-mechatronic Actuators, Sensors and Control, Philadelphia, 2004.

[121] S. B. Andersson and J. Park, "Tip steering for Fast Imaging in AFM," presented at American Control Conference 2005.

[122] S. S. Wong, J. D. Harper, P. T. J. Lansbury, and C. M. Lieber, "Carbon Nanotubes : High -Resolution Probes for Imaging Biological Systems," *J.Am.Chem.Soc*, vol. 120603-604, 1998.

[123] S. S. Wong, A. T. Woolley, T. W. Odom, J. L. Huang, P. Kim , D. V. Vezenov, and C. M. Lieber, "Single-walled carbon nanotube probes for high-resolution nanostructure imaging," *Applied Physics Letters*, vol. 73(23), pp. 3465-3467, 1998.

[124] D. H. Kim, B. Kim, S. Yun, and S. Kwon, "Cellular force measurement for force reflected biomanipulation," *IEEE International Conference on Robotics and Automation*2412-2417, 2004.

[125] N. Ando, P. Korondi, and H. Hashimoto, "Development of micromanipulator and haptic interface for networkes micromanipulation," *IEEE/ASME Transactions on Mechatronics*, vol. 6(4), pp. 417 - 427, 2001.

[126] K. Takeo and K. Kosuge, "Implementation of the micro-macro teleoperation system without using slave-side force sensors," presented at IEEE International Conference on Robotics and Automation, Albuquerque, New Mexico, USA, 1600 - 1605, 1997.

[127] M. Guthold, M. R. Falvo, W. R. Matthews, S. Paulson, S. Washburn, D. A. Erie, S. R., F. P. Brooks, Jr., and R. I. Taylor, "Controlled Manipulation of Molecular samples with the nanoManipulator," *IEEE/ASME Transactions on Mechatronics*, vol. 5(2), pp. 189-197, 2000.

[128] W. Vogl, M. Sitti, and M. F. Zah, "Nanomanipulation with 3D visual and force feedback using atomic force microscope," in *4th IEEE Conference on Nanotechnology*, 2004, pp. 349-351.

[129] M. Girot, M. Boukallel, and S. Reigner, "Modeling soft contact mechanism of biological cells using an atomic force bio-microscope," presented at International Conference on Intelligent Robots and Systems, Beijing, China, 1831 - 1836, 2006.

[130] D. P. Perrin, C. R. Wagner, N. Geisse, R. D. Howe, and K. K. Parker, "Haptic interface for cardiac cell exploration using AFM," presented at World Haptics, Pisa, Italy, 2005.

[131] J. H. Hoh and C. A. Schoenenberger, "Surface morphology and mechanical properties of MDCK monolayers by atomic force microscopy," *Journal of Cell Science*, vol. 107 1105-1114, 1994.

[132] W. Xu, P. J. Mulhern, B. L. Blackford, M. H. Jericho, and I. Templeton, "A new atomic force microscopy technique for the measurement of the elastic properties of biological materials," *Scanning Microscopy*, vol. 8499-506, 1994.

[133] Q. H. Qin and M. V. Swain, "A micro-mechanics model of dentrin mechanical properties " *Biomaterials*, vol. 255081-5090, 2004.

[134] A. M. Collinsworth, S. Zhang, W. E. Kraus, and G. A. Truskey, "Apparent elastic modulus and hysteresis of skeletal muscle cells through differentiation," *American Journal of Physiology: Cell Physiology*, vol. 283 pp 1219 -1227, 2002.

[135] A. Touhami, B. Nysten, and Y. F. Dufrene, "Nanoscale mapping of the elasticity of microbial cells by atomic force microscopy," *Langmuir*, vol. 19 pp 4539 - 4543, 2003.

[136] A. Vinckier and G. Semenza, "Measuring elasticity of biological materials by atomic force microscopy," *FEBS Letters*, vol. 43012 - 16, 1998.

[137] A. L. Weisenhorn, M. Khorsandi, S. Kasas, V. Gotzos, and H. Butt, "Deformation and height anomaly of soft surfaces studied with an AFM," *Nanotechnology*, vol. 4106 - 113, 1993.

[138] K. L. Johnson, "One hundred years of Hertz contact," *Proc Instn Mech Engrs*, vol. 196, 1982.

[139] I. N. Sneddon, "Boussinesq's problem for a flat ended cylinder," *Mathematical Proceedings of the Cambridge Philosophical Society*, vol. 4229 - 39, 1946.

[140] I. N. Sneddon, "Boussinesq's problem for a rigid cone," *Mathematical Proceedings of the Cambridge Philosophical Society*, vol. 44492 - 507, 1948.

[141] G. G. Bilodeau, "Regular pyramid punch problem," *Journal of applied mechanics*, vol. 59519 - 523, 1992.

[142] B. J. Briscoe, K. S. Sebastian, and M. J. Adams, "The effect of indenter geometry on the elastic response to indentation," *Journal of Physics*, vol. 271157 - 1162, 1994.

[143] F. Rico, P. Roca-Cusachs, N. Gavara, R. Farre, M. Rotger, and D. Navajas, "Probing mechanical properties of living cells by atomic force microscopy with blunted pyramidal cantilever tips," *Physical Review E*, vol. 721 - 10, 2005.

[144] J. Alcaraz, L. Buscemi, M. Grabulosa, X. Trepet, B. Fabry, R. Farre, and D. Nevajas, "Microrheology of human lung epithelial cells measured by atomic force microscopy," *Biophysical Journal*, vol. 842071 - 2079, 2003.

[145] M. J. Rosenbluth, W. A. Lam, and D. A. Fletcher, "Force microscopy of nonadherent cells: a comparison of leukemia cell deformability," *Biophysical Journal*, vol. 902994 - 3003, 2006.

[146] A. B. Mathur, A. M. Collinsworth, W. M. Reichert, W. E. Kraus, and G. A. Truskey, "Endothelial, cardiac muscle and skeletal muscle exhibit different viscous and elastic properties as determined by atomic force microscopy," *Journal of Biomechanics*, vol. 341545 - 1553, 2001.

[147] D. Maugis, *Contact, Adhesion and Rupture of Elastic Solids*: Springer, 2000.

[148] D. Tabor, "Surface forces and surface interactions," *Journal of Colloid and Interface Science*, vol. 58(1), pp. 2 - 13, 1977.

[149] Y. Cao, D. Yang, and W. Soboyejoy, "Nanoindentation method for determining the initial contact and adhesion characteristics of soft polydimethylsiloxane," *Journal of Materials Research*, vol. 20(8), pp. 2004 - 2011, 2005.

[150] V. Lulevich, T. Zink, H. Chen, F. Liu, and G. Liu, "Cell mechanics using atomic force microscopy-based single cell compression," *Langmuir*, vol. 228151 - 8155, 2006.

[151] S. Danti, M. D'Acunto, L. Trombi, S. Berrettini, and A. Pietrabissa, "A micro/nanoscale surface mechanical study on morpho-functional changes in multilineage-differentiated human mesenchymal stem cells.," *Macromolecular Bioscience*, vol. 7589-598, 2007.

[152] M. J. Evans and M. H. Kaufman, "Establishment in culture of pluripotential cells from mouse embryos," *Nature*, vol. 292154 - 156, 1981.

[153] G. R. Martin, "Isolation of a pluripotent cell line from early mouse embryos cultured in medium conditioned by teratocarcinoma stem cells," *Proceedings of the National Academy of Sciences*, vol. 787634 - 7638, 1981.

[154] S. Bourne, J. M. Polak, S. P. F. Hughes, and L. D. K. Buttery, "Osteognic differentiation of mouse embryonic stem cells: differential gene expression analysis by cDNA microarray and purification of osteoblasts by cadherin-11 magnetically activated cell sorting," *Tissue Engineering*, vol. 10796 - 806, 2004.

[155] K. Prelle, I. M. Vassiliev, S. G. Vassilieva, E. Wolf, and A. M. Wobus, "Establishment of pluripotent cell lines from vertebrate species - present status and future prospects," *Cells Tissues Organs*, vol. 165220 - 236, 1999.

[156] J. McWhir, A. E. Schnieke, and R. Ansell, "Selective ablation of differentiated cells permits isolation of embryonic stem cell lines from murine embryos with a non-permissive genetic background," *Nature Genetics*, vol. 14 223 - 226, 1996.

[157] P. Mountford, J. Nichols, B. Zevnik, C. O' Brien, and A. Smith, "Maintainance of pluripotential embryonic stem cells by stem cell selection," *Reproduction, Fertility and Development*, vol. 10 527 - 533, 1998.

[158] T. Kenny, "Nanometer-scale force sensing with MEMS devices," *IEEE Sensors Journal*, vol. 1(2), pp. 148-157, 2001.

[159] Y. Sun, B. J. Nelson, D. P. Potasek , and E. Enikov, "A bulk microfabricated multi-axis capacitive cellular force sensor using transverse comb drives,"

Journal of Micromechanics and Microengineering, vol. 12(6), pp. 832-840, 2002.

[160] C. K. M. Fung, I. Elhajj, W. J. Li, and N. Xi, "A 2-D PVDF Force Sensing System For Micro-manipulation and Micro-assembly," *International Conference on Robotics & Automation*1489-1494, 2002.

[161] C. K. M. Fung, W. J. Li , I. Elhajj, and N. Xi, "Internet-Based Remote Sensing and Manipulation in Micro Environment," *International Conference on Advanced Intelligent Mechatronics*695-700, 2001.

[162] M. S. Inc, "Piezo film sensors technical manual," *Internet Version*, 1999.

[163] Y. Shen, N. Xi, W. J. Li, and J. Tan, "A High Sensitivity Force Sensor for Microassembly:Design and Experiments," *International Conference on Advanced Intelligent Mechatronics*703-708, 2003.

[164] G. A. Poleo, R. S. Denniston, B. C. Reggio, R. A. Godke, and T. R. Tiersch, "Fertilization of eggs of zebrafish, danio rerio, by intracytoplasmic sperm injection," *Biol. Reprod.*, vol. 65961-966, 2001.

[165] A. Pillarisetti, E. Steager, M. Pekarev, A. D. Brooks, and J. P. Desai, "Micro robotic gripper for cell manipulation," presented at International symposium on experimental robotics, Rio de Janeiro, Brazil, 2006.

[166] Y. Sun, K. T. Wan, K. P. Roberts, J. C. Bischof, and B. J. Nelson, "Mechanical Property Characterization of Mouse Zona Pellucida," *IEEE Transactions on Nanobioscience*, vol. 2(4), pp. 279-286, 2003.

[167] A. Alessandrini and P. Facci, "AFM: a versatile tool in biophysics," *Measurement science and technology*, vol. 16R65-R92, 2005.

[168] W. R. Bowen, R. W. Lovitt, and C. J. Wright, "Application of atomic force microscopy to the study of micromechanical properties of biological materials," *Biotechnology Letters*, vol. 22893-903, 2000.

[169] M. Sitti and H. Hashimoto, "Tele-Nanorobotics Using Atomic Force Microscope," presented at International Conference on Inteligent Robots and Systems, Victoria, B.C.,Canada, 1739-1746, 1998.

[170] J. Brufau, M. P. Vidal, J. L. Sanchez, and J. Samitier, "MICRON: Small autonomous robot for cell manipulation applications," presented at International Conference on Robotics and Automation, Barcelona, Spain, 2005.

[171] J. L. Hutter and J. Bechhoefer, "Calibration of atomic force microscope tips," *Review of Scientific Instruments*, vol. 64(7), pp. 1868 -1873, 1993.

[172] R. Fuierer, "Basic Operation Procedures for Asylum MFP3D," 2006.

[173] F. Braet and E. Wisse, "Imaging surface and submembranous structures in living cells with the atomic force microscope," *Methods in Molecular Biology*, vol. 242201-216, 2004.

[174] K. El Kirat, I. Burton, V. Dupres, and Y. F. Dufrene, "Sample preparation procedures for biological atomic force microscopy," *Journal of Microscopy*, vol. 218 199-207, 2005.

[175] T. Takahashi, B. Lord, P. S. Schulze, R. M. Fryer, S. S. Sarang, S. R. Gullans, and R. T. Lee, "Ascorbic acid enhances differentiation of embryonic stem cells into cardiac myocytes," *Basic Science Reports*, vol. 1071912 - 1916, 2003.

[176] T. S. Lanero, O. Cavalleri, S. Krol, R. Rolandi, and A. Gliozzi, "Mechanical properties of single living cells encapsulated in polyelectrolyte matrixes," *Journal of Biotechnology*, vol. 124723-731, 2006.

[177] Y. Sun, B. Akhremitchev, and G. C. Walker, "Using the adhesive interaction between atomic force microscopy tips and polymer surfaces to measure the elastic modulus of compliant samples," *Langmuir*, vol. 205837 - 5845, 2004.

[178] V. V. Lulevich, D. Andrienko, and O. I. Vinogradova, "Elasticity of polyelectrolyte multilayer microcapsules," *Journal of Chemical Physics*, vol. 120(8), pp. 3822 - 3826, 2004.

[179] E. Kwon, Y. Kim, J. Park, D. Kim, and H. Jung, "Measurement of pull-off forces by atomic force microscope in liquids used for biological applications," *Experimental Techniques* 40-45, 2007.

[180] R. Ananthakrishnan, J. Guck, and J. Kas, "Cell mechanics: recent advances with a theoretical perspective," *Recent Research Developments in Biophysics*, vol. 539 - 69, 2006.

[181] R. E. Mahaffy, C. K. Shih, F. C. MacKintosh, and J. Kas, "Scanning probe based frequency dependent microrheology of polymer gels and biological cells," *Physical Review Letters*, vol. 85(4), pp. 880 - 883, 2000.

[182] T. K. Berdyyeva, C. D. Woodworth, and I. Solokov, "Human epithelial cells increase their rigidity with ageing in vitro: direct measurements," *Physics in Medicine and Biology*, vol. 5081-92, 2005.

[183] A. Pillarisetti, W. Anjum, J. P. Desai, G. Friedman, and A. Brooks, "Force Feedback Interface for Cell Injection," *World Haptics Conference*391-400, 2005.

[184] A. Pillarisetti, M. Pekarev, A. Brooks, and J. P. Desai, "Evaluating the Role of Force Feedback for Biomanipulation Tasks," presented at 14th Symposium on Haptic Interfaces for Virtual Environment and Teleoperator Systems, Alexandria, Virginia, USA, 11 - 18, 2006.

[185] A. Pillarisetti, M. Pekarev, A. D. Brooks, and J. P. Desai, "Evaluating the Effect of Force Feedback in Cell Injection," *IEEE Transactions on Automation Science and Engineering*, vol. 4(3), pp. 322-331, 2007.

[186] A. Pillarisetti, C. Keefer, and J. P. Desai, "Mechanical Response of embryonic stem cells using haptics-enabled atomic force microscopy," in *Interntational Sympoisum on Experimental Robotics* Athens, Greece, 2008

[187] A. Pillarisetti, C. Keefer, and J. P. Desai, "Mechanical Characterization of Fixed Undifferentiated and Differentaited mESC," in *International Conference on Biomedical Robotics and Biomechatronics* Scottsdale, Arizona, 2008 (accepted).